Power Line Sensor Networks for Enhancing Power Line Reliability and Utilization

A Dissertation
Presented to
The Academic Faculty

By

Yi Yang

In Partial Fulfillment
Of the Requirements for the Degree
Doctor of Philosophy in the
School of Electrical and Computer Engineering

Georgia Institute of Technology
August 2011

Copyright © Yi Yang 2011

Power Line Sensor Networks for Enhancing Power Line Reliability and Utilization

Approved by:

Dr. Deepak Divan, Advisor
School of ECE
Georgia Institute of Technology

Dr. Santiago Grijalva
School of ECE
Georgia Institute of Technology

Dr. Ronald G. Harley, Co-Advisor
School of ECE
Georgia Institute of Technology

Dr. Ying Zhang
School of ECE
Georgia Institute of Technology

Dr. Thomas G. Habetler
School of ECE
Georgia Institute of Technology

Dr. J. Rhett Mayor
School of ME
Georgia Institute of Technology

Date Approved: April 26, 2011

Dedicated to my dear parents

Mr. Yin Yang
Mrs. Qiuping Zheng

for their love and support...

ACKNOWLEDGEMENTS

My PhD at Georgia Tech has helped me immensely to lay a foundation for my future professional life. I have received invaluable support from my teachers, colleagues, and friends, without whom this journey would not have been possible.

First, I would first like to express sincere gratitude for my advisor Professor Deepak M. Divan. His guidance and support has always helped me to think creatively and instigated a philosophy of "being an independent thinker." I am also extremely grateful for the support and invaluable guidance and help from my co-advisor Professor Ronald G. Harley throughout the entire process. I am also thankful to Dr. Thomas G. Habetler and Dr. A. P. Sakis Meliopoulos for their knowledge and experience in my interactions with them, and especially for their suggestions and guidance on my research work. I would like to extend my gratitude to Dr. Santiago Grijalva, Dr. Yi Zhang, and Dr. J. Rhett Mayor for serving on my PhD defense committee and for their support in completion of this work.

I would like to thank Ms. Deborah King for always being so patient with me, and helping me with the lab orders and organization of events. This thesis work was supported under research contract from the National Science Foundation (NSF). I would like to acknowledge their financial support for my graduate studies.

I would like to acknowledge the Eaton Corporation, and especially thank Dr. Thomas Schoepf, Tom Pier, Susan Hopkins, Charles J. Luebke, Peter J. Theisen, Dr. Peter Liu, and Dr. Tiefu Zhao at the Eaton Corp. Innovation Center for their valuable inputs and constant support.

Additionally, I would like to thank all my family and friends who have always helped me and have been a source of inspiration. I would especially like to thank my friends Dr. Ping Wang, Jia Li, Man Yu, Dr. Chunyan Bai, Dr. Yongge Gan, Yi Li, and Dr. Zhenyu Fan for their support and for always being there for me. I would also like to thank all of my

fellow graduate students in the electric power group at the Georgia Institute of Technology for their friendship and company throughout my study. Among them, I wish to especially thank Dr. Bin Lu, Dr. Long Wu, Dr. Wei Qiao, Dr. Harjeet Johal, Dr. Jyoti Sastry, Anish Prasai, Dr. Jean Carlos Hernandez, Dr. George Stefopoulos, Dr. Salman Mohagheghi, Jing Dai, Dr. Wei Zhou, Dr. Zhi Gao, Dr. Pinjia Zhang, Jiaqi Liang, Siwei Cheng, Yi Du, Dr. Yao Duan, Liang Du, Rohit Moghe, Debrup Das, and Frank Kreikebaum for their wonderful friendship. It was a pleasure for me to be with you all.

Most of all, I owe the greatest debt of gratitude to my parents for their unconditional love, support, and confidence. My parents have always been the source of encouragement and support that have always helped me through difficult times.

TABLE OF CONTENTS

ACKNOWLEDGEMENTS ..... **iv**

LIST OF TABLES ..... **xii**

LIST OF FIGURES ..... **xiii**

SUMMARY ..... **xviii**

CHAPTER 1 INTRODUCTION **1**

1.1 Overview of Electric Power System Issues 1

1.2 Challenges and Opportunities of Distributed Power Grid Monitoring 3

1.3 Potential Applications of Distributed Sensor Networks for Power Grid Monitoring 5

1.3.1 Real-time Thermal Capacity Evaluation of Overhead Power Lines 6

1.3.2 Overhead Power Line Vicinity Monitoring for Incipient Faults Detection 8

1.4 Problem Statement 10

1.5 Dissertation Outline 11

CHAPTER 2 SUMMARY OF EXISTING SENSING TECHNOLOGIES FOR THE POWER GRID **13**

2.1 Real-time Thermal Capacity Evaluation for Overhead Power Lines 13

2.1.1 Weather-Model-Based Real-Time Line Rating Evaluation 14

2.1.2 Conductor Temperature Model-based Real-Time Line Rating Evaluation 15

2.1.3 TSM-Based Real-Time Line Rating Evaluation 16

2.2 Thermal Condition Monitoring of Overhead Power Lines 18

2.2.1 Overhead Conductor Temperature Measurement 18

2.2.2 Overhead Conductor Sag/Tension Measurement 20

2.3 Overhead Power Line Vicinity Monitoring 21
2.3.1 Overhead Power Conductor Contact with Vegetation and Animals 21
2.3.2 Overhead Power Conductor Clearance to Ground 22
2.3.3 Overhead Power Conductor Gallop 23
2.3.4 Insulation Failure Detection of Underground Cables 23
2.4 Chapter Summary 25

CHAPTER 3 SUMMARY OF EXISTING TECHNOLOGIES OF COMMUNICATIONS AND ENERGY SCAVENGING 27
3.1 Communications Technologies for Power System Applications 27
3.1.1 Wireless Communication for Power Systems 27
3.1.2 Power Line Communications (PLC) 30
3.1.3 Wireless Sensor Networks (WSN) 31
3.2 Energy Scavenging Technologies 35
3.3 Chapter Summary 38

CHAPTER 4 POWER LINE SENSOR NETWORK -- A NEW CONCEPT FOR POWER GRID MONITORING 39
4.1 Conceptual Power Line Sensor Network 39
4.2 Principles of Power Line Sensor Operation 41
4.2.1 Power Line Sensor Module Introduction 41
4.2.2 Target Applications of Power Line Sensor Networks 41
4.3 Impact of Power Line Sensor Networks 43
4.4 Chapter Summary 44

CHAPTER 5 EVALUATION OF REAL-TIME DYNAMIC THERMAL RATINGS OF OVERHEAD POWER LINES VIA MULTILAYER PERCEPTRON NEURAL NETWORK 45

5.1 Overhead Power Line Thermal Dynamics and Safe Operating Margin 46
5.1.1 Overhead Power Line Thermal Dynamics 46
5.1.2 Overhead Power Line Thermal Limit Curve 48
5.2 Simplified Conductor Thermal Model and Direct Solution of Line Dynamic Thermal Rating 53
5.3 MLPN-based Thermal Model Parameters Estimation 56
5.3.1 Design of the MLPN based Parameter Estimator 56
5.3.2 On-line Adaptive Training of MLPN Parameter Estimator 59
5.4 Simulation Results 63
5.5 Identification of Overhead Power Line Thermal Dynamics 65
5.6 Chapter Summary 67

CHAPTER 6 EVALUATION OF REAL-TIME DYNAMIC THERMAL RATINGS OF OVERHEAD POWER LINES VIA ECHO STATE NETWORKS 69
6.1 Overview of the Proposed Method 69
6.2 Echo State Networks Dynamics 71
6.2.1 ESN Structure 72
6.2.2 Echo State Properties and Training of ESNs 74
6.3 ESN based Overhead Conductor Thermal Dynamics Identification/Prediction 75
6.3.1 ESN-based Identification and Prediction 77
6.3.2 Simulation Validation of Performance of ESN-Idf and ESN-Prd 78
6.4 Online Adaptation of Echo State Networks 83
6.4.1 Issues and Challenges in Online Adaptation with ESNs 85
6.4.2 Online Adaptation of ESN-based Conductor Thermal Dynamics Identifier 88
6.4.3 Performance Validation of the Online Adaptation of ESN-Idf/ESN-Prd . 90
6.5 Real-Time Dynamic Thermal Rating Evaluation and On-line Update of I-T Thermal Limit Curve 95
6.5.1 Overhead Power Line I-T Thermal Limit Curve 95
6.5.2 Online Adaptation of I-T Thermal Limit Curve 97
6.5.3 Real-time Thermal Rating over a Pre-allotted Overload Duration 100

6.6 Experimental Validation 102
6.7 Chapter Summary 106

CHAPTER 7 POWER LINE VICINITY MONITORING VIA ELECTRIC FIELD DETECTION..... 107
7.1 Dielectric Coupling between Overhead Conductors to Ground 108
7.2 Multiple Displacement Current Sensor (mDCS) Scheme 110
7.3 Introducing the Concept of Distributed Capacitance Density (D_cap) 114
7.3.1 Introduction to Distributed Capacitance Density..... 114
7.3.2 mDCS Surface Charge Density in a Two-Conductor System 115
7.4 mDCS Surface Charge Density in a 3-Φ Power Line System..... 118
7.4.1 Common-Mode mDCS Surface Charge Density (E-field Distribution). 121
7.4.2 The Space-Phasor Model of Differential-Mode mDCS Surface Charge Density (E-field Distribution)..... 122
7.5 Information Extraction from mDCS Surface E-field Distribution 126
7.5.1 E-field Distribution Approximation by mDCS..... 126
7.5.2 Rotational Reference Frame Transformation from 1~6-axis to DQ-axis Coordinates 128
7.5.3 Maxwell™ Electrostatic 2D Simulation Validation of DQ-axis Decomposition 130
7.5.4 Line Voltage and Conductor Ground Clearance Indicators..... 133
7.6 Displacement Current Measurement and Experimental Validation 139
7.6.1 Displacement Current Sensing around an Overhead Power Conductor . 140
7.6.2 Displacement Current Sensor Experimental Validation in a Scaled-Down 160 V Single-Phase System..... 142
7.7 Chapter Summary 149

CHAPTER 8 PROTOTYPE POWER LINE SENSOR NETWORK AND EXPERIMENTAL VALIDATION..... 151

8.1 Power Line Sensor Module Design and Its Implementation 151
8.1.1 Energy Scavenging and Voltage Regulation Unit 153
8.1.2 Sensing and Signal Conditioning Unit..... 155
8.1.3 IEEE 802.15.4 RF Unit..... 156
8.1.4 DSP Unit 157
8.2 Prototype PLSN and Experimental Validation 159
8.2.1 Prototype PLS Module..... 159
8.2.2 PLS Module Stand-alone Performance Test..... 160
8.2.3 IEEE 802.15.4 Data Transfer Performance 161
8.2.4 IPIC Laboratory PLSN and Experimental Validation 162
8.3 Chapter Summary 164

CHAPTER 9 CONCLUSIONS AND CONTRIBUTIONS 165
9.1 Overview..... 165
9.2 Conclusions..... 165
9.3 Contributions..... 168

CHAPTER 10 RECOMMENDATIONS FOR FUTURE WORK 172
10.1 Distributed Sensing for Overhead Power Lines and Utility Assets..... 172
10.2 Overhead Power Line Real-time Thermal Rating Evaluation 173
10.3 Power Line Vicinity Monitoring via Overhead Conductor E-field Analysis .. 174
10.4 Power Line Vicinity Monitoring via Overhead Line EM Wave Propagation . 175
10.4.1 Motivation of Detecting EM Wave Propagation along Overhead Lines and Proposed Method 176
10.4.2 Thevenin Equivalent of a 3-Φ Power Line at the Point of PLS Module Signal Injection 184
10.4.3 Simulation Validation of the Proposed Method..... 193
10.4.4 Summary 198

APPENDIX A **201**

APPENDIX B **203**

APPENDIX C **204**

APPENDIX D **205**

APPENDIX E **212**

APPENDIX F **215**

APPENDIX G **220**

APPENDIX H **230**

BIBLIOGRAPHY **232**

LIST OF TABLES

Table 2.1 Overhead Conductor Sag Measurement 20

Table 3.1 Most Common Standards for Wireless Communications..... 28

Table 3.2 Sensor Networks' General Features and Requirements..... 32

Table 3.3 Sensor Nodes Development..... 33

Table 3.4 Energy Scavenging for Sensor Operating Power Supply 35

Table 5.1 System Data Sampling and MLPN Updating Rate..... 59

Table 6.1 Proposed Echo State Networks Structure 78

Table 6.2 System Data Sampling and ESN Updating Rate 88

Table 7.1 Proposed mDCS Dimension 110

Table 7.2 mDCS Surface Charge Density $\rho_C(\varphi,t)$ 125

Table 7.3 Analogy between AC Machine M-field and mDCS E-field in a 3-Φ Power Line System 125

Table 8.1 Line Parameters [126]..... 152

Table 8.2 Transformer Core Geometry [126] 153

Table 8.3 PLS Module Power Requirement 154

Table 8.4 PLS Module Functionalities 160

Table 8.5 IEEE 802.15.4 Performance Test in HC Environment (Indoor)..... 161

Table 8.6 IEEE 802.15.4 Performance Test in Outdoor (@GT Campus) 162

Table 8.7 IPIC Laboratory Power Line Sensor Network Performance 162

Table 10.1 Line Configuration under Study 194

LIST OF FIGURES

Figure 1.1 Line Real-Time Thermal Capacity Distribution [6]. 7

Figure 2.1 WM-based Line Rating System 14

Figure 2.2 CTM-based Line Rating System..... 15

Figure 2.3 TM-based line rating system..... 18

Figure 2.4 Sag measurement devices 21

Figure 3.1 Overview cost/complexity vs. data rates of wireless technologies [59]. .. 29

Figure 3.2 Commercial sensor nodes 33

Figure 3.3 Cluster-tree topology 34

Figure 4.1 Conceptual Power Line Sensor Network (PLSN) 40

Figure 4.2 PLS Module Schematic..... 41

Figure 5.1. A generic representation of overhead conductor thermal behavior. 46

Figure 5.2. Overhead conductor thermal model in lumped thermal parameters 48

Figure 5.3. Conductor temperature response following a step change in current under various ambient weather conditions..... 49

Figure 5.4. Conductor temperature response subject to a series of step changes in current under a certain weather conditions 50

Figure 5.5. A typical I-T Thermal Limit Curve (ITLC) of a power line segment 51

Figure 5.6. MLPN based DRTR evaluation. 56

Figure 5.7. MLPN parameters estimation system 58

Figure 5.8. Online adaptive algorithm flowchart 62

Figure 5.9. Thermal conditions of a power line segment for six days 63

Figure 5.10. MLPN on-line estimation of thermal model parameters 65

Figure 6.1. Echo State Network Structure..... 73

Figure 6.2. ESN based Identification/Prediction for Overhead Conductor Thermal Dynamics 76

Figure 6.3. ESN step response under variant weather conditions: (a) Wind velocity; (b) Heat capacitance. 81
Figure 6.4. Steady state and time constant evaluation of and weather condition estimation based on ESN identifier output. 83
Figure 6.5. Online Adaptive Algorithm Flow Chart. 90
Figure 6.6. Time-varying weather and loading conditions of the conductor for two days: (a) Joule heat gain; (b) ambient temperature Ta; (c) wind velocity; (d) conductor heat capacity; (e) solar radiation. 91
Figure 6.7. The RLS algorithm's tracking performance with ESN-Idf in I-Mode: (a) the ESN-Idf's output vs. Tc; (b) Normalized Mean Square Error in (6.18). 92
Figure 6.8. The RLS algorithm's performance with ESN-Prd in P-Mode: (a) the ESN-Prd's s output vs. Tc; (b) Normalized Mean Square Error in (13). 93
Figure 6.9. The SW algorithm's tracking performance with ESN-Idf in I-Mode: (a) the ESN-Idf's output vs. Tc; (b) Normalized Mean Square Error in (6.18). 93
Figure 6.10. The SW algorithm's performance with ESN-Prd in P-Mode: (a) the ESN-Prd's s output vs. Tc; (b) Normalized Mean Square Error in (6.18). 95
Figure 6.11. ESN identifier behaviors under various overload conditions. 96
Figure 6.12. I-T Thermal Limit curve of one line segment..... 97
Figure 6.13. Flow Chart of Online Updating of the I-T Thermal Limit Curve..... 97
Figure 6.14. I-T thermal limit curve updating through time 99
Figure 6.15. Dynamic thermal rating I-T curve for multiple line segments 99
Figure 6.16. Real-time dynamic thermal rating over an allotted overload duration: (a) tol = 20 minutes; (b) tol = 10 minutes. 101
Figure 6.17. IPIC Lab set-up for experimental testing: (a) 795 kcmil 26/7 ACSR (Drake) conductor experimental test set-up; (b) Prototype PLS module.103

Figure 6.18. Time-varying weather and loading conditions of the conductor for two days: (a) ambient temperature Ta; (b) conductor temperature; (c) conductor current. 104
Figure 6.19. I-T thermal limit curve updating through time 105
Figure 6.20. Real-time dynamic thermal rating over an allotted overload duration: (a) tol = 20 minutes; (b) tol = 10 minutes. 105
Figure 7.1. Multiple Displacement Sensor (mDCS) as a part of the PLS Module mounted around a Overhead Conductor 111
Figure 7.2. Overhead conductor E-field distribution approximation via mDCS measurement 113
Figure 7.3. Electric charge density (E-field distribution) over mDCS surface subject to (a) conductor B; (b) earth..... 117
Figure 7.4. Cross-section of a 3-Φ Power Line System with mDCS installed on Conductor C. 119
Figure 7.5. Differential-mode mDCS surface charge density distribution..... 124
Figure 7.6. Overhead power line voltage and conductor ground clearance measurement based on mDCS scheme 126
Figure 7.7. DQ-axis components subject to conductor-to-ground clearance variation... 131
Figure 7.8. DQ-axis components subject to conductor separation variation..... 132
Figure 7.9. DQ-axis components variation subject to conductor-to-ground clearance variation 133
Figure 7.10. Conductor-to-ground clearance varying from 5 to 16 meters; (b) line phase voltage magnitude varying sinusoidally at 0.0233 Hz..... 135
Figure 7.11. $\rho_i(t)$, for i = 1, …, 6: (a) $\rho_m(t)$; (b) $\Delta\rho_i(t)$. 136
Figure 7.12. Conductor voltage Estimation with the reference of (7.34)..... 137

Figure 7.13. Conductor voltage estimation accuracy assessment with respect to conductor-to-ground clearance variation. 138
Figure 7.14. Conductor-to-ground clearance estimation. 138
Figure 7.15. D_cap of mDCS subject to ground v.s. conductor-to-ground clearance: (a) Common-mode component c_{Cg_m}; (b) Differential-mode component Δc_{Cg} (Maxwell Eletrostatic 2D)..... 140
Figure 7.16. Generic representation of mDCS sensing scheme in an overhead power line system, with i_{d1} measurement as an example..... 141
Figure 7.17. Laboratory testing arrangement for displacement current measurement.144
Figure 7.18. Schematic of the exeperimental setup and the displacement current sensing scheme..... 145
Figure 7.19. C_t evaluated by the direct displacement current measurement v.s. C_t simulated in the Maxwell electrostatic 2D environment 147
Figure 7.20. DCS's output voltage V_{out} v.s parallel plates distance 148
Figure 8.1. Power Line Sensor (PLS) Module Schematic 152
Figure 8.2. PLS Module power supply circuit 155
Figure 8.3. CPU Multi-Task Handler..... 158
Figure 8.4. Prototype Power Line Sensor Module in IPIC lab..... 159
Figure 8.5. IPIC Laboratory Prototype Power Line Sensor Network 162
Figure 8.6. IPIC Prototype PLSN Experimental Results 163
Figure 10.1 General representation of a 3-Φ overhead power line with earth return: (a) Schematic representation and notation; (b) equivalent circuits of an infinitesimal length. 176
Figure 10.2 TDR based PLS power line vicinity monitoring..... 180
Figure 10.3 "Anti-Chirp" process for information extraction..... 182
Figure 10.4 General representation of the induced current distribution subject to the V_{sB} injection 184

Figure 10.5 Thevenin equivalent network of a 3-Φ power line (in sequence networks) at the point of PLS voltage source injecting: (a) Generic representation; (b) Single-phase equivalent circuit of right side of zero-sequence network with respect to the voltage injection point. 190

Figure 10.6 Illustration of the Symmetrical Components on a 3-Φ Power Line 191

Figure 10.7 Injected voltage signal V_{sB} and reflected current signal I_{sB} in Time Domain..... 195

Figure 10.8 Frequency spectrum of the reference equivalent impedance $Z_{eq,Ref}$ seen by the PLS module *M*. 195

Figure 10.9 $\Delta Z_{eq}(l)$ subject to line disturbances with respect to shunt admittance variation. 196

Figure 10.10 Sensitivity Analysis: $|\Delta Z_{eq}(l)|$ vs. conductor-to-ground clearance. ... 197

Figure 10.11 $\Delta Z_{eq}(l)$ subject to line disturbances with respect to both shunt admittance and series impedance variation. 198

SUMMARY

Over the last several decades, electricity consumption and generation have continually grown. Investment in the Transmission and Distribution (T&D) infrastructure has been minimal and it has become increasingly difficult and expensive to permit and build new power lines. At the same time, a growing increase in the penetration of renewable energy resources is causing an unprecedented level of dynamics on the grid. Consequently, the power grid is congested and under stress.

To compound the situation, the utilities do not possess detailed information on the status and operating margins on their assets in order to use them optimally. The task of monitoring asset status and optimizing asset utilization for the electric power industry seems particularly challenging, given millions of assets and hundreds of thousands of miles of power lines distributed geographically over millions of square miles. The lack of situational awareness compromises system reliability, and raises the possibility of power outages and even cascading blackouts.

To address this problem, a conceptual Power Line Sensor Network (PLSN) is proposed in this research. The main objective of this research is to develop a distributed PLSN to provide continuous on-line monitoring of the geographically dispersed power grid by using hundreds of thousands of low-cost, autonomous, smart, and communication-enabled Power Line Sensor (PLS) modules thus to improve the utilization and reliability of the existing power system.

The proposed PLSN specifically targets the use of passive sensing techniques, focusing on monitoring the real-time dynamic capacity of a specific span of a power line under present weather conditions by using computational intelligence technologies. An ancillary function is to detect the presence of incipient failures along overhead power lines via monitoring and characterizing the electromagnetic fields around overhead

conductors. This research integrates detailed modeling of the power lines and the physical manifestations of the parameters being sensed, with pattern recognition technologies. Key issues of this research also include design of a prototype PLS module with integrated sensing, power and communication functions, and validation of the Wireless Sensor Network (WSN) technology integrated to this proposed PLSN.

CHAPTER 1

INTRODUCTION

1.1 Overview of Electric Power System Issues

Geographically spanning the entire continent, most of the U.S. power grid is in excess of 50-60 years old. Over the past several decades, electricity consumption and generation have continually grown. The U.S. Department of Energy (DOE) reports in [1] that, during the 1960s, the generating capacity of the U.S. electric power industry almost doubled, growing from 175 to 325 GW. By the end of the last century, it had reached 700 GW. It is expected that over 210 GW of new capacity will be required by 2011, which brings the U.S. capacity for the first time into the TW range.

At the same time, the increasing penetration of dynamic sources and loads, such as renewable energy from wind and photovoltaic panels, and plug-in electric vehicles (PHEV/EVs), has dramatically changed the existing usage patterns of transmission. The new transmission patterns that were not envisioned in the regulated environment [2], such as the demands for "open access" transmission, uncertain future circuit loading due to load growth and dispatch changes, and the new patterns of wheeling power to achieve economic energy transfers, further stresses the Transmission and Distribution (T&D) infrastructure.

Even as the demand for electricity has increased dramatically, investment in the T&D infrastructure, on the other hand, has steadily declined. Uncertain regulations and policies make it difficult to attract investment capital, and it has become increasingly difficult and expensive to permit and build new power lines. Moreover, it has become increasingly difficult to site new conventional overhead power lines, particularly in urban and suburban areas which are experiencing the greatest load growth. Since 1982, growth in

peak demand for electricity has exceeded transmission growth by almost 25% every year [1]. As a result, it has become extremely important for the U.S. electric power industry to know how to accurately assess the actual capacity of utility assets in order to improve the utilization of the existing system.

With the growing complexity and stress on the power grid, reliability is of vital importance in the operation of the power system. It is generally admitted that, it becomes more and more expensive for the system or the customers to handle system outages. The economic impact of these interrupts is significant, and is estimated to cost American business more than $100 billion on average each year [1]. The existing reliability of the system, which approaches 99.999%, can not be degraded in any way.

The U.S. power grid represents perhaps the most complicated and largest network built by man, but has a minimal level of monitoring and automation. The high cost and complexity of monitoring high voltage and high current, and the high cost of communications have limited the level of information that is available to grid operators. Most of the work that has been done on the monitoring of utility assets is still limited to expensive sensors located in substations, which are connected back to control rooms via SCADA systems. In many areas of the United States, the status of utility assets is normally unknown until a failure triggers a manual inspection or until a regular maintenance patrol discovers a problem. The lack of operational and situational awareness compromises system reliability, and raises the possibility of power outages and even cascading blackouts. There have been five massive blackouts reported over the past 40 years; three have occurred in the past 9 years [1]. Therefore, how to increase the situational awareness in order to improve the reliability of the existing system is another critical issue faced by today's electric power industry.

Experience with modern networks has shown that high system reliability and availability can be realized through redundancy, low-cost communications and distributed sensing solutions [3]. Developing a cost-effective, massively deployed, widely

distributed and intelligent sensing scheme for the power grid becomes one of the critical needs of the U.S. electric power industry today.

1.2 Challenges and Opportunities of Distributed Power Grid Monitoring

The task of monitoring the status of utility asset and optimizing asset utilization for the power grid, given millions of assets and hundreds of thousands of miles of power lines distributed geographically over millions of square miles, seems particularly challenging. For a typical utility, with 75,000 km of power lines, and thousands of transformers, capacitors and breakers, this could require the monitoring of over 200,000 distinct and distributed sensors or sources of data spread over 20-80,000 km^2 of area. Implementation of a distributed, grid-wide monitoring system using conventional sensors and communications technologies would be prohibitively expensive. Cost is one of the main reasons that little prior work has been done to explore the concept of distributed sensing for the grid. Developing low-cost sensor devices is therefore the most critical challenge for a successful implementation of such a distributed sensing scheme for power system applications.

The need for a consistent highly-reliable power supply is another reason that the electric power industry always tends to be conservative and reluctant to accept new technologies. It is therefore difficult and challenging to implement distributed monitoring across the power grid. The installation of any new control and monitor devices can be expensive, if it requires physical modification of a line or other utility assets. Especially, if the installation requires a line outage, this outage might be hard or impossible to obtain. Therefore, the design and deployment of distributed sensor devices must consider the requirements that their installation should have the least impact on the existing system. In addition, the implementation of such sensor devices should require the least additional maintenance and minimal human intervention. Non-intrusive, in-service sensing

techniques and condition monitoring methods have to be developed and deployed. Those sensors should also be unattended, self-powered, rust corrosion resistant and fault-tolerated.

Although techniques for distributed power grid monitoring have been studied for decades, and some of them are already in operation, the work is often focused on developing individual devices. Combining data from a large number of dispersed sensors and extracting important actionable information to the existing SCADA/EMS system are still open areas to be explored. New communications technologies need to be deployed to facilitate the complex and frequent real-time information transferred between utility assets and control centers.

Communications technologies have already revolutionized many application areas, such as telecommunication, banking and certain manufacturing industries. Networks that have been built and upgraded recently are much smarter. Among them, Wireless Sensor Networks (WSNs) have been identified as one of the most important technologies for the 21st century. Cheap, smart devices with multiple sensors, networked through wireless links and deployed in large numbers, provide unprecedented opportunities for many different applications, including air traffic control, traffic surveillance, video surveillance, industrial and manufacturing automation, distributed robotics, environment monitoring, and building and structures monitoring [3]. Its unique networking characteristics, i.e. self-organizing, self-healing, and optimized network routing, are particularly developed for the applications where data connectivity is required in harsh, uncertain, and dynamic environments.

As a large geographically distributed system, the U.S. power grid, with many monitoring devices, can be viewed as one large sensor network. Some monitoring systems were developed with specialized computers and communication capabilities several decades ago, even before the term “sensor networks” came into vogue. However, the state of the art at that time in sensors, computers, and communication networks made

the concept of distributed sensor networks for power grid monitoring more of a vision than a technology ready to be exploited. Fortunately, technological advances in the past decades have completely changed the situation. Reduction in costs of sensors, microProcessors, computation and communications, coupled with enhanced performance, has raised the possibility of realizing a massively deployed, widely distributed, robust, and intelligent sensor network across the power grid. The successful implementation of such a sensor network can drastically enhance the operational and situational awareness of the system thus to improve the system utilization and reliability.

1.3 Potential Applications of Distributed Sensor Networks for Power Grid Monitoring

To explore the potential needs of distributed sensor networks for power grid monitoring from an end-use perspective, a survey project "Potential Applications for Sensor Networks in Power Delivery" funded by NEETRAC was conducted [4]. Working with utility advisors and other interested experts in the T&D community, the results of the survey provide a good understanding of the full scope of potential applications, concerns, constraints and issues for the wide-scale deployment of such a distributed sensor network.

For overhead power lines, the important parameters that govern reliable operation of power lines include: a) real-time information on the actual static and dynamic thermal capacity of lines; b) possible violation of conductor-to-ground clearance caused by conductor sagging; c) imminent tree limb contact with power lines; d) 'galloping' lines; and e) incipient failure of insulators and towers.

The target applications of distributed sensor networks for power grid monitoring are discussed mainly in two aspects in the rest of this section: a) the estimation of the real-time thermal capacity of an overhead line considering ambient weather conditions; and b)

power line vicinity monitoring to identify and locate the presence of incipient faults along the line.

1.3.1 Real-time Thermal Capacity Evaluation of Overhead Power Lines

The thermal capacity of an overhead power line is determined by the maximum current that the line can carry without overheating, which is dramatically influenced by ambient weather conditions of the line. In the U.S. electric power industry, this maximum allowable current is often denoted as the "static" steady state thermal ratings (SSTR) of the line, which is determined in the design stage based on the following set of conservative weather parameters [5]:

- Ambient temperature = 40 ^{o}C;
- Wind speed = 1.4 mph;
- Solar radiation = 1000 W/m^2.

This particular set of weather parameters is generally selected according to historical worst case weather conditions common to a region; the probability level selected to evaluate the worst case condition is 0.02% [6]. However, weather conditions are never constant. During favorable weather conditions when the ambient temperature is lower than the assumed maximum or the wind speed is higher than the assumed minimum, or during cloudy sky conditions, higher thermal rating is possible without overheating line conductors. Figure 1.1 shows a distribution of the actual thermal capacity of an overhead power line based on the real-time ambient weather conditions over a whole year. The conventional SSTR of the line is 920 A. Consider the cumulative probability that the actual line thermal capacity is larger than the SSTR value, Figure 1.1 indicates that, for 90-98% of the time, the power line can carry 10-30% more current than that defined by the SSTR of the line.

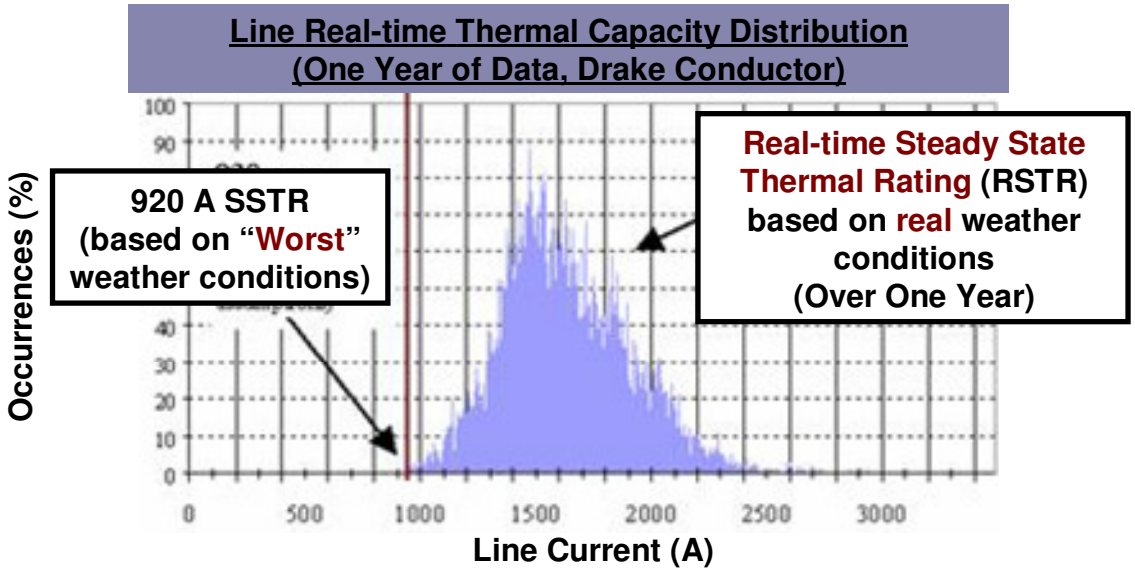

Figure 1.1 Line Real-Time Thermal Capacity Distribution [6].

The fact that the inherent conservatisms in conventional line ratings result in underutilization of the power grid has been widely recognized by utilities. Since the 1960's [7], utilities have started in monitoring and coordinating the real-time weather conditions to evaluate the Real-time Steady State Thermal Rating (RSTR) of overhead power lines, and thus to increase the utilization of the existing lines. With the actual thermal limits of operation, a utility may also be able to re-route power through uncongested lines and thus earn more revenue. The problem is exacerbated by lines spread out over large geographic areas with different ambient conditions. Sometimes, when contingencies arise, an operator may be able to seize opportunities to overload a line for a short duration by taking into consideration the thermal inertia of the conductors, thereby avoiding unnecessary load shedding The maximum allowable short-term overload of a line is normally called the Real-time Dynamic Thermal Rating (RDTR) of the line.

Overhead power lines often extend several hundred miles in length. It is recognized that the thermal rating of each span along a power line will be different even at the same point in time due to variations of weather conditions along the line, and it is deemed

economically impractical to monitor the thermal conditions of every span along a power line. In present systems [8] [9], the centralized monitoring equipment is normally placed at/near a predetermined "critical span", where the line experiences the highest average temperature. Sometimes, a need exists to select the optimal monitoring sites that can best represent the thermal conditions of "critical spans" along the length of a line. Since weather conditions always vary with time and space, the location of the "critical span" is not necessarily spatially fixed, but often shifts with time [10]. Clearly, the existing techniques based on a fixed, predetermined "critical span" are not able to provide an accurate assessment of the thermal conditions of the whole line as micro-climate variations along the line are ignored. Utilities therefore have to operate with conservative loading values, or large safety margins.

If large amounts of low-cost sensors are distributed along the length of a power line, it would allow the collection of local thermal condition information from each sensor down to a "per-span" level of granularity. A more realistic assessment of the thermal capacity of the whole line can be obtained.

1.3.2 Overhead Power Line Vicinity Monitoring for Incipient Faults Detection

For overhead power lines, it is generally believed that incipient faults are associated with the gradual intrusion of tree limbs as they grow into and toward the lines [11], and with the violation of conductor separation caused by galloping conductors [12]. Moreover, the recent practice by utilities to utilize the real-time thermal ratings of power lines via taking the real-time weather conditions into account potentially increases conductor temperatures, and thus the amount of conductor sag [13]. This may violate conductor-to-ground clearance requirements, which must always be maintained under all operating conditions.

All these phenomena may not immediately cause the insulation breakdown between a phase conductor and ground or between any phase conductors. However, they raise serious safety problems, and present a challenge to power system protection engineering. The anticipation and location of such incipient faults are important to improve system reliability and to reduce the possibility of power outages.

Developing a sensitive detector to detect and locate incipient faults has received much attention. Some of the techniques use standard relaying inputs and others require special equipment [14]. However, this kind of fault normally has a high-impedance path and does not cause excessive change of current in the affected feeder, which is generally difficult for conventional over-current protection devices to detect. The conventional fault detection devices are therefore not able to provide sufficient sensitivity. Another approach for the detection of such high-impedance, incipient faults is based on the identification of arcing current signatures that are typically associated with fallen conductors. However, these techniques have not been proven to always be effective [15].

For overhead lines, there are strong electromagnetic (EM) fields around the conductors, which are affected by insulation conditions between conductors and ground. There has recently been much interest to develop sensing technologies to detect and characterize local EM signatures around line conductors, and thus to detect the health of power lines and to predict the high-impedance, incipient faults as discussed above [16]. It would be useful and important to develop new, low-cost sensing techniques and devices that are distributed along an overhead power line down to a “per-span” level of granularity if necessary, by which unprecedented sensitivity in monitoring the presence of incipient faults along the line can be achieved.

1.4 Problem Statement

To address the issues in implementing distributed sensor networks across the power grid, a conceptual Power Line Sensor Network (PLSN) project has been funded by NSF, called "Power Line Sensornet for Enhancing Line Reliability and Utilization" [17].

The PLSN proposes to provide continuous on-line monitoring of the geographically dispersed power grid by using hundreds of thousands of low-cost, autonomous, smart, and communication-enabled Power Line Sensor (PLS) modules. Each individual PLS module is designed to sense and characterize the line thermal conditions and health conditions in the vicinity of the sensor module. Each PLS module also operates as a communication node, and communication occurs between adjacent working nodes. The local information sensed by each PLS module can be transmitted peer-to-peer back to a remote control center via the WSN technology.

The main objective of this research is to develop a distributed PLSN and to investigate the underlying technologies for implementing the PLSN that can enhance the utilization of the existing power grid and improve system reliability. The focus of this research centers on the following major thrusts:

Characterization of Line Thermal Behavior and Evaluation of Real-time Line Thermal Rating: The thermal model of an overhead conductor in the presence of different ambient weather conditions and electrical conditions is developed and validated. With the PLS module as the platform, the ability of a neural network to estimate the heat-removal capability of the line span where the module is mounted is validated. The capability of the PLSN to evaluate the real-time thermal rating of a whole line is also validated.

Power Line Vicinity Monitoring to Measure Line Local Disturbances and Characterize Incipient Failures: The design of the PLS module to sense and analyze the EM environment around an overhead power line, in the vicinity of the sensor module, is

another major objective of this research. The potential for measuring the changes in the shunt impedances to ground for line conductors is explored in order to detect and locate incipient faults along the line. Signal conditioning and extraction for maximum signal to noise ratio is applied to enhance sensing performance.

Integration of Power, Sensing and Communications Functions: An optimized design of a PLS module to achieve functions of power management, sensing and communications is novel and is the key to realizing low-cost implementation of the proposed PLSN. The commercially available WSN technology is integrated to the PLSN, and its performance is tested in a high electrical noise environment.

Experimental Validation of Key Concepts: Key concepts such as the thermal-behavior identification of an overhead conductor, the ability to sense line incipient faults in the vicinity of the PLS module, and the operation of an integrated prototype PLS module, is validated experimentally, showing a close agreement with theoretical expectations.

1.5 Dissertation Outline

Chapter 2 summarizes the previous work on power grid monitoring, with a focus on the existing sensing technologies that have been developed and deployed for enhancing system utilization and reliability. Chapter 3 presents a survey of the existing communications technologies for power system applications. The existing energy scavenging technologies are also summarized in this chapter.

The concept of the proposed PLSN is overviewed in Chapter 4.

Chapter 5 presents a Multilayer Perceptron Neural Network (MLPN) based method to estimate the heat-removal capability of line conductors under present line loading and

weather conditions, and thus to evaluate the thermal capacity of an overhead power line in real time. To eliminate the need for an analytical model and relieve the difficulties to measure and quantify metrological parameters as required by traditional methods as well as the MLPN based method, a novel strategy of dynamic thermal rating evaluation by using an Echo State Network (ESN) is proposed and presented in Chapter 6.

Chapter 7 introduces a novel Multiple Displacement Current Sensor (mDCS) scheme, as a part of the Power Line Sensor (PLS) module, to capture the spatial mapping of the electric field distribution around overhead conductors, the analysis of which allows independent measurements of conductor-to-ground clearance and conductor voltage.

Chapter 8 introduces the design and implementation of an integrated prototype PLS module and a laboratory PLSN, with preliminary experimental results validating the basic operation of the proposed PLSN.

Conclusions, contributions, and recommendations for future work are presented in Chapters 9 and 10. Several parts of this thesis have already been published [4] [17] [106] [132] [135] [136] [137] [138] [139].

CHAPTER 2

SUMMARY OF EXISTING SENSING TECHNOLOGIES FOR THE POWER GRID

This chapter summarizes the previous work on power grid monitoring, with a focus on the existing sensing technologies to enhance system utilization and reliability.

2.1 Real-time Thermal Capacity Evaluation for Overhead Power Lines

Based on ambient weather conditions, the issue of real-time dynamic thermal ratings of overhead power lines is a subject which has been exhaustively studied for decades in the electric industry. The problem can be stated as follows [18]. Based on ambient weather conditions along a line route, the maximum current that can be passed through the line at a given time is determined such that the conductor temperature at any section of the line does not exceed some maximum value, or the conductor-to-ground clearance at any line segment does not violate safety regulations.

The most important parameter in establishing real-time line ratings for overhead conductors is the temperature of the conductor, which can be obtained either by direct measurement or thermal inference. The line rating systems developed so far can be classified into three categories: Weather Model (WM); Conductor-Temperature Model (CTM); and Tension/Sag Model (TSM). The difference between these methods mainly relies on how the conductor temperature is obtained.

2.1.1 Weather-Model-Based Real-Time Line Rating Evaluation

WM-based methods have been proposed by several researchers [19]-[23], and are the most widely accepted means to evaluate real-time thermal ratings of overhead power lines. Figure 2.1 shows a typical WM-based line rating system, where the weather conditions are directly measured from one or multiple weather stations along a line on a continuous basis. These real-time meteorological parameters are utilized to calculate a conductor overall heat-transfer coefficient which in turn is used to predict conductor temperature, and thus to evaluate the real-time thermal rating of the line based on an analytical conductor thermal model, e.g. the IEEE Standard 738-2006 model [24].

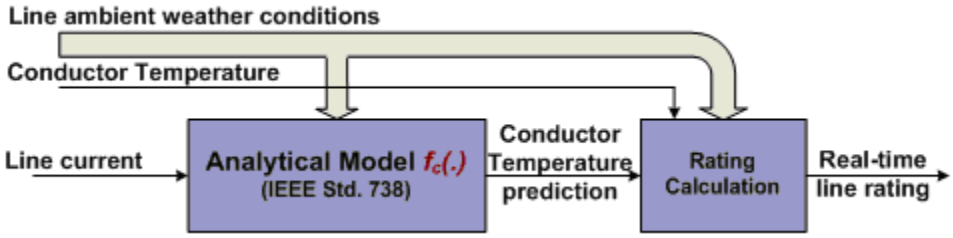

Figure 2.1 WM-based Line Rating System

The WM-based method usually uses standard weather instruments, such as anemometers, atmospheric pressure sensors, and thermal sensors, etc, which are often expensive. The accuracy of a WM-based rating system is highly dependent on the accuracy of weather condition monitoring. If the weather stations are positioned appropriately to measure the weather actually experienced by the line, this method is generally considered to be accurate. Unfortunately, the weather stations can not always accurately reflect the weather conditions of the line. In a WM-based system, the weather conditions can only be measured from a limited number of locations, and the weather stations are normally far away from the line itself. The measured meteorological parameters can not provide sufficient information to capture the thermal conditions of the

whole line as micro-climate variations along the line are ignored, and give inaccurate assessment of the actual line thermal capacity.

Moreover, at low wind speeds, where an accurate measurement is the most desirable, rotating wind speed sensors stall, and the wind direction becomes variable due to wind turbulence [21]. The convection cooling effect on the conductor rating becomes difficult to measure. Moreover, in most WM-based systems, those meteorological conditions (e.g. wind velocity, rain, snow, or ice) that are not easily measured and accurately quantified are simply ignored. These weather conditions, on the other hand, normally have a significant effect on the thermal capacity of overhead lines.

The WM-based method is in general expensive, and the weather monitoring instruments are in need of frequent calibration.

2.1.2 Conductor Temperature Model-based Real-Time Line Rating Evaluation

The development of the CTM-based method is driven by the need that the meteorological variables, which are difficult to quantify and measure, can be inferred from the measured conductor temperature and a mathematical thermal model. In [25], Foss suggests that, if real-time conductor temperature, ambient temperature and conductor current are available, a total conductor heat-removal coefficient (or cooling coefficient) can be inferred mathematically without direct measurements of wind speed and wind direction in real-time. Figure 2.2 shows a typical CTM-based line rating system as suggested by Foss.

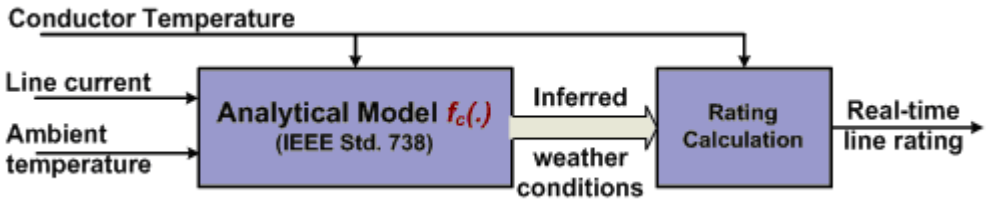

Figure 2.2 CTM-based Line Rating System

This CTM-based method overcomes the difficulties that the WM-based method encounters. It avoids the need for wind and other meteorological parameter measurements as needed in a typical WM-based system, and provides more accurate estimation of line thermal rating at low wind speeds than a WM-based system. Because only low-cost temperature and current sensors are needed in the CTM-based line rating systems, it becomes possible that the sensor devices are mounted on every span of the line. Thus, the micro-climate variations along the line can be captured, and the assessment of the conductor thermal conditions down to a "per-span" level of granularity can be obtained. Therefore, the CTM-based method becomes the most promising candidate to evaluate the real-time thermal ratings of overhead power lines based on a distributed monitoring scheme.

However, there are several challenges that need to be addressed, when this method is implemented. First of all, the accuracy of the rating calculation is sensitive to errors in the measured conductor temperature rise above the ambient temperature, especially under light load conditions [26] [27]. Besides, the implementation of a CTM-based system normally requires physical contact with a power conductor, and consequently increases the difficulty and cost of device installation.

2.1.3 TSM-Based Real-Time Line Rating Evaluation

In WM- and CTM-based line rating systems, a maximum allowable conductor temperature is used to determine the line thermal rating. However, for overhead power lines, the operating current capacity limits of most lines actually depend on the available clearance to ground of predefined "Ruling Spans" [28] along the line, which must always be maintained under all operating conditions. When the line geometry and the conductor properties are known, a well-defined mathematical relation exists between the average

conductor temperature and the conductor sag [29]. Thus, if the **average conductor temperature** is maintained within prescribed limits, i.e. maximum allowable conductor temperature, all safety considerations can be maintained.

Seppa suggests in [30] that, the average temperature of a conductor is a more accurate and realistic indicator to conductor sag than the one-spot temperature of the conductor. Since average conductor temperature is a function of conductor tension, Seppa [30] proposes an on-line tension monitoring system, where conductor tension at tension towers along the line are measured in real time. This TSM-based method is able to observe the average temperature of the conductor, and thus provides a more accurate assessment of line rating to meet the line safety requirement than the WM- and CTM-based methods. Figure 2.3 shows the block diagram of a TSM-based line rating system.

One of the main drawbacks to this method is the difficulty and the cost needed for installation. Although a tension monitor is theoretically possible to install live, many utilities have rules preventing such work. It may be feasible to install such devices on certain heavily loaded lines, but it is impractical and expensive to install tension monitors on all transmission and distribution lines for line rating evaluation.

Three line rating approaches have been introduced above. The most appropriate method needs to be selected depending on various issues including accuracy, cost, and installation factors, and there is no overall “best” solution. However, when a large area, distributed sensing scheme is considered, the CTM-based method shows the most potential. Because only low-cost sensors are required in a CTM-based system, it allows the sensor devices to be scattered along a line almost along every span, by which the micro-climate variations along the line can be captured and the actual thermal capacity of the whole line can be accurately evaluated. Admittedly, the success of this CTM-based method greatly relies on the accuracy of the measured conductor temperature, and the proper hardware design of sensor devices that can support low-cost and convenient installation.

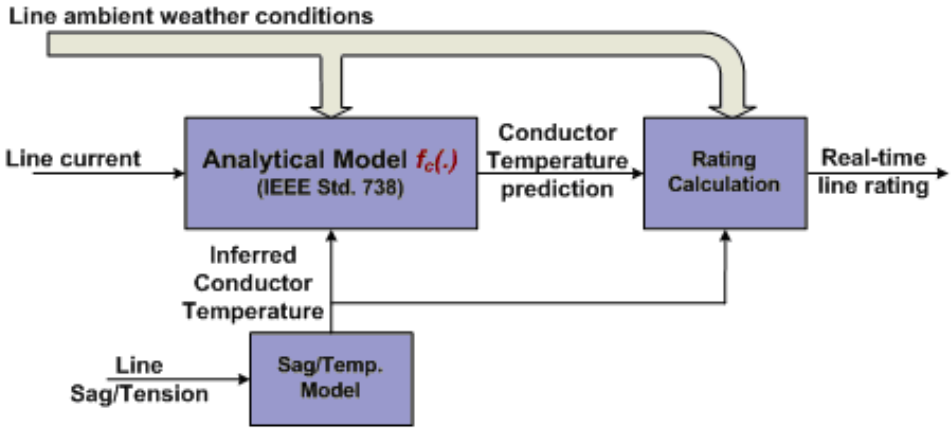

Figure 2.3 TM-based line rating system

2.2 Thermal Condition Monitoring of Overhead Power Lines

All the line rating systems introduced above require direct measurements of line parameters on a continuous basis, such as conductor temperature, overhead conductor sag, conductor tensions, etc. In this section, the state-of-the-art of the existing technologies to monitor thermal conditions of overhead conductors is summarized.

2.2.1 Overhead Conductor Temperature Measurement

The conventional thermal sensors, such as thermocouples, thermistors, and Resistance Thermal Detectors (RTDs), have been widely used for conductor surface temperature measurement [31]. They provide the most cost-effective solution for one-spot temperature measurement. However, if a temperature sensor is placed on the surface of a conductor, it becomes a heat sink and can also shield a part of the conductor from wind or solar radiation. Consequently, for existing sensor types, the error caused by the heat sink effect is typically on the order of $\pm 5 \sim 10\%$ of the temperature rise over the ambient [32],

which depends on the type of sensor, conductor properties as well as conductor ambient cooling conditions.

With the development of power line communications through the use of a fiber optic cable integrated with a power line conductor, it is now possible to have a distributed system of fiber optic conductor temperature sensors (FODT) that can span the entire length of the power line [33][36]. The commercial available instruments offer a range of 10 km with 1 m resolution, whereas experimental systems have demonstrated a range of over 30 km [34] [35]. This distributed temperature sensing approach is immune to electromagnetic interference, and provides a small-size, geometrically flexible sensing solution. However, the distributed fibers are impractical for retrofit installations. A special dead-end assembly and an optical insulator are required when the fiber optic transmission conductor is installed.

Recently, a low-cost Infrared (IR) based conductor temperature system has been developed, where the IR conductor measurement is performed remotely and continuously (about every 10 minutes), and logged [36]. This method allows for a direct, non-contact, and reliable means to monitor conductor temperature on energized overhead conductors. However, this system requires the presence of a trained IR camera operator, and therefore is not a solution to unattended and continuous monitoring.

For the grid-wise, distributed monitoring scheme being exploited in this research, installing or fitting the sensor devices for use in/on an existing structure is an important factor to be considered. The conventional one-spot temperature sensors are still the most promising candidates to measure the conductor surface temperature for this thermal rating evaluation application mainly because of their low costs. Given the experience of deploying this one-spot thermal sensor in many other applications, it allows to design flexible and convenient installation schemes to fulfill the requirements in this application.

2.2.2 Overhead Conductor Sag/Tension Measurement

The maximum allowable temperature of conductors in an overhead line may be limited to maintain minimum required clearances between energized conductors and ground or other conductors, or to avoid annealing of aluminum or copper strands. Therefore, accurate assessment of overhead conductor sag is critical to determine power line thermal capacity as well as to maintain the system security.

Table 2.1 summarizes several direct sag measurement methods, which are either available in the market or still under development. Figure 2.4 shows some sag measurement devices related to the methods depicted in Table 2.1.

Most of the sag measurement methods introduced above require sophisticated and complex hardware design of the sensor devices, and are often expensive and difficult to install. This fact prevents them from being utilized as a cost-effective, massively deployed and widely distributed sensing solution.

Table 2.1 OVERHEAD CONDUCTOR SAG MEASUREMENT

Methods	Functionality	Features
GPS [37]	Conductor sag is directly measured by using differential GPS technology.	Around 20cm accuracy
Inclinometer [38]	The phase conductor angle with respect to horizontal is measured to indicate conductor sag.	Precise angle measurement is required.
Resistive wires [39] [40]	Conductor sag is evaluated by the E-field near a power line, which is measured by the current induced on a high resistance grounded wire by the E-field near the high-voltage conductor.	Sensitive to external disturbances, e.g. wind. Induced and actual currents are difficult to be distinguished.
Tension Measurement [28] [30]	Conductor sag is indirectly measured by the tension of the conductor within the ruling span sections.	Average conductor temperature is monitored.
Sagometer [41][42]	The sagometer unit is mounted on one of the supporting structures, and provides video-based sag measurement.	Around ±2 inches accuracy
Laser Distance Measurement [41]	As an associated project to Sagometer evaluation, a laser distance sensor is used to measure the distance from line conductors to ground.	Around ±2 inches accuracy

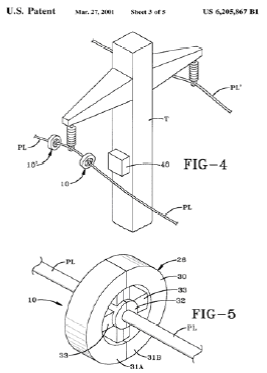

Inclinometer [38]

Sagometer [41] [42]

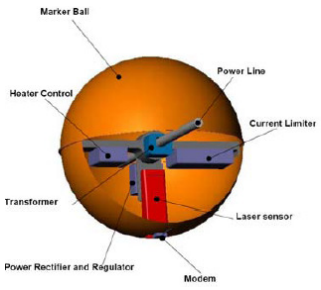

LDM Sensor [41]

Tension Sensor [28] [30]

Figure 2.4 Sag measurement devices

2.3 Overhead Power Line Vicinity Monitoring

For overhead power lines, there are strong electromagnetic (EM) fields around the high-voltage conductors, which are influenced by insulation conditions between conductors and the ground. There has been much interest in developing sensing technologies to detect and characterize EM signatures around power conductors, and thus to detect the health of power lines and to predict the presence of incipient faults or momentary line contact with tree-limbs or high-resistivity soil.

In this section, the state of the art in the field of overhead power line vicinity monitoring is reviewed, with a focus on the technologies for sensing and analyzing conductor EM field signatures. To give a complete overview of the effort that has been spent to improve power system reliability, the technologies for underground cable fault detection are also summarized.

2.3.1 Overhead Power Conductor Contact with Vegetation and Animals

The Transmission and Distribution (T&D) systems are likely to experience contact with branches of trees or some animals. Detection of these phenomena could provide vital predictive maintenance information.

In [43], the electric field near a 400 kV transmission line is investigated. The study shows that the electric field is dampened by nearby spruce trees of different sizes and heights. The reduction effect starts when a spruce forest is 15 meters away from the lines. For smaller trees, the effect starts at around 5 meters.

The research in [44] characterizes the phenomenon of tree contact with energized conductors through field experiments, visual observations, and computer data analysis. The results suggest that further examination of conductor current by high frequency harmonic analysis is likely to provide more and better insight of the characteristics of the current flowing into trees to detect the occurrence of tree contact phenomenon.

Even though some studies have been conducted to analyze and characterize the electric field around overhead conductors subject to conductor contact with trees and/or animals, no practical and effective solution has been found to detect incipient faults caused by these phenomena, especially for real-time implementation.

2.3.2 Overhead Power Conductor Clearance to Ground

Little work has been reported on monitoring the clearance to ground for overhead conductors via direct field measurement around the conductors. The scheme presented in [39] [40] involves attaching two ends of a grounded wire of high electrical resistance to an appropriate location on each of two transmission line towers. The current induced on the wire by the electric field near high-voltage line conductors is then measured with a simple ammeter. Since the phase and amplitude variation of the electric field near a high-voltage transmission line depend upon the clearance to ground for line conductors, the induced current on the wire is able to indicate the variations either in conductor sag or in conductor-to-ground clearance.

The study in [39] shows that, changes in conductor sag of 1% produces nearly a 19% change in the induced current. The entire system can be installed while the line is

energized and the package can be made simple and, hence relatively inexpensive. However, this method requires complex calibration upon installation, which is affected by the non-uniform terrain under the power line.

2.3.3 Overhead Power Conductor Gallop

Conductor gallop is a high-amplitude, low-frequency oscillation of overhead power lines due to wind. The swings in the wires occur most commonly in the vertical plan, although horizontal or rotational motion is also possible. It is a periodic motion with a natural frequency mode that tends to be around 1 Hz. The oscillations can exhibit amplitudes well in excess of a meter, and the displacement is sometimes sufficient for the phase conductors to infringe on operating clearances, and to cause flashover. It may even cause mechanical failure of the conductor or structure of overhead power lines. How to effectively detect conductor gallop and vibration is an important issue. However, little work has been reported on the detection of galloping conductors. The effort seems to have only been focused on avoiding conductor galloping by using certain anti-vibration or damping schemes [45] [46].

2.3.4 Insulation Failure Detection of Underground Cables

While underground power lines experience fewer interruptions than overhead lines, there are a variety of failures that do affect underground cables especially in joints and terminations. In-service/conditioning monitoring and diagnosis of underground cables have drawn significant attention from electric utilities, and the insulation failure detection technologies have accordingly been better developed and are more mature than those for overhead power lines. This is mainly because service interruptions in underground

systems can last much longer than those in overhead systems, before faults are located and service is restored.

The presence of Partial Discharge (PD) is one of the most prominent indicators to defects and ongoing degradation processes in underground cable insulation systems. PD causes the transmission of acoustic, electrical and optical energy, which can be detected and analyzed using various coupling techniques [128].

The most commonly used method involves a coupling capacitor that is placed in parallel with the test object, and the discharge signals are measured across external impedance. The external impedance usually consists of a resonant circuit that is used to expand the discharge-current pulses in the time domain so they are easier to detect. However, tests based on this method are generally performed offline within a well-screened laboratory, which don't provide sufficient sensitivity under operating conditions when noise and interference are severe [47]. Besides the PD detector, additional HV components like a test-voltage supply and a coupling capacitor are heavy, expensive and not suitable for on-site tests.

To overcome the problems mentioned above, two non-conventional testing methods have been recently developed, i.e. coaxial cable sensors and inductive sensors. Coaxial cable sensors are essentially capacitive sensors. Typically, additional metal foils are applied on cable joints as pick-up electrodes [48] [49], or the existing metallic structures within a cable joint are used as the electrode [50]. The sensor and the cable dielectric form a high-frequency voltage divider consisting of the capacitance of the cable section and the sensor. The PD pulse may be detected between the metal foil and cable shield, or across an interruption in the metal earth screen of the cable [51]. This type of sensor can be easily installed in joints or terminations, which shows the potential for continuous on-line detection. However, the sensor sensitivity is affected by the resistance formed between sensors and the ground sheath.

Recently, three types of inductively coupled sensors have been developed and widely used for underground PD detection: high-frequency current transformer [52]; radio-frequency current transducer [53] [54]; and loop antenna attached to the cable jacket. These inductive coupling techniques are less expensive with less heavy equipment required. They are easy to use and no modification of the cable is necessary. However, the detection sensitivity may be affected by the rate-of-change of the magnetic flux; and sophisticated signal processing, such as wavelets [55] or high-frequency spectrum analysis [52], are often needed to distinguish between external noise and PD signals, especially in the very high frequency (VHF) range.

2.4 Chapter Summary

An extensive survey of literature in the area of power grid monitoring has been presented in this chapter, with a focus on the existing sensing technologies for enhancing the utilization and reliability of the electric power system.

Much work has been done to address the issue of real-time dynamic thermal ratings of overhead power lines in the electric industry. Three kinds of line rating systems have been developed and even utilized in several applications. Among them, the Conductor Temperature Model (CTM) -based method shows the most potential, when a large-area, distributed sensing scheme is considered. However, the accurate measurement of conductor temperature and the proper hardware design of the sensor devices for low-cost and convenient installation are two main challenges for the success of this CTM-based method.

Even though there has lately been much interest to development sensing technologies to monitor overhead power lines, little work has been reported to develop practical and effective solutions to detect the health and wellness of overhead power lines and to predict incipient faults, especially for real-time implementation. Compared to the mature

technologies that have been developed for monitoring and diagnostics of underground cables, the vicinity monitoring of overhead power lines through the use of new, cost-effective sensing technologies is truly in great demand.

The next chapter presents a survey of the existing communications technologies for power system applications, and the existing energy scavenging technologies for distributed sensors.

CHAPTER 3

SUMMARY OF EXISTING TECHNOLOGIES OF COMMUNICATIONS AND ENERGY SCAVENGING

This chapter reviews and summarizes the existing communications technologies that could potentially be implemented for power system applications. The review includes wireless communications and power line communications, with a focus on the Wireless Sensor Network (WSN) communications technology. In addition, existing energy scavenging technologies are also been reviewed as a critically important component of important technologies to successfully implement distributed sensor networks.

3.1 Communications Technologies for Power System Applications

3.1.1 Wireless Communication for Power Systems

Wireless communication offers the most flexible and easiest interconnection between devices without relying on any physical connection. The electric power industry has long used wireless data communication for power system operation, including microwave systems, multiple address radio (MAS), spread spectrum radio systems, 450 MHz short range systems, limited satellite applications (including VSAT, paging, and GPS), and mobile radio systems for limited data exchange [59]. These wireless systems have generally been used outside the substation or between the substation and other sites, often for Supervisory Control and Data Acquisition (SCADA) functions.

Over the last few years, great progress has been made in new types of wireless systems, such as public cellular networks (e.g. text messaging and Internet access) and private wireless LANs (e.g. WiFi). Personal and commercial wireless data communication systems are becoming widespread, with increasingly mature technologies

and standards, as well as decreasing cost. In addition, these wireless systems are being considered by many industries, as they offer the benefits of inexpensive products, rapid deployment, low cost installations, widespread access, and mobile communications which wired technologies and even the older wireless technologies often cannot provide. Table 3.1 summarizes the wireless communications technologies that have been recently developed and at present most commonly used, and Figure 3.1 compares cost, complexity and data rates of these technologies.

Table 3.1 MOST COMMON STANDARDS FOR WIRELESS COMMUNICATIONS

Standard	Features	Target Applications
IEEE 802.11b (WiFi) [60]	Data Rate: 11Mbps @2.4GHz Range: 100 ~ 500 m Power: 150 ~ 400 mW Price: $20.0	A standard for infrastructure-based Wireless Local Area Networks (WLANs), providing high capacity, full connectivity among attached stations, and broadcast capability with a communication range typical of a single building, which is the most popular and cheapest wireless standard.
IEEE 802.11g (Enhanced WiFi) [60]	Data Rate: 54Mbps @2.4GHz Range: 100 ~ 500 m Power: 150 ~ 400 mW Price: $20.0	An enhanced WiFi standard.
IEEE 802.15.1 (Bluetooth) [61]	Data Rate: 1.5Mbps @2.4GHz Range: 10m Power: 40 ~ 100 mW Price: $5.0	A standard for low-traffic Wireless Personal Area Networks (WPAN), used in devices like cell phones, Personal Digital Assistants (PDAs) and other mobile wireless devices, primarily for communicating with computers, headsets, and other hands-free systems.
IEEE 802.15.4 (ZigBee Meshed Networks) [62]	Data Rate: 250 kpbs @2.4GHz Range: ~100 m Power: <50 mW Price: $2.0	A standard for Low-Rate Wireless Personal Area Networks (LR-WPAN), designed for applications requiring low-data-rate, low-power wireless connectivity among inexpensive fixed, portable, and moving devices as in an ad hoc sensor network.
IEEE 802.16 (WiMax) [63]	Data Rate: 10Mbps @<66 GHz Range: ~1 km Power: > 200 mW Price: >$100.0	A standard for "first-mile/last-mile" connection in Broadband Wireless Access (BWA), designed to connect Wi-Fi hotspots to the Internet, providing a wireless alternative to cable and DSL series.
Global System for Mobile communications (GSM) [64]	Data Rate: 100 Mbit/s (4G) @0.85/0.9/1.8/1.9/2.1 GHz Range: 35 km Power: 1~2 W Price: ~$100.0	A standard for a mobile cellular radio system, which also allows cell phone users to "roam" across many cell phone systems and between most countries world-wide. New generations of cell phone technologies are termed 2.5G, 3G, and 4G.

Among these new wireless technologies, IEEE 802.15.4 is a standard specifically for low-rate WPANs often termed “meshed networks” as opposed to point-to-point. The main features of the standard are network flexibility, ultra-low cost and ultra-low power consumption. This standard is suitable for many applications requiring low-data-rate wireless connectivity among inexpensive fixed, portable, and moving devices as in an ad hoc self-organizing sensor network [65]. ZigBee builds upon this 802.15.4 standard to define application profiles that can be shared among different manufacturers to provide system-to-system interoperability [66].

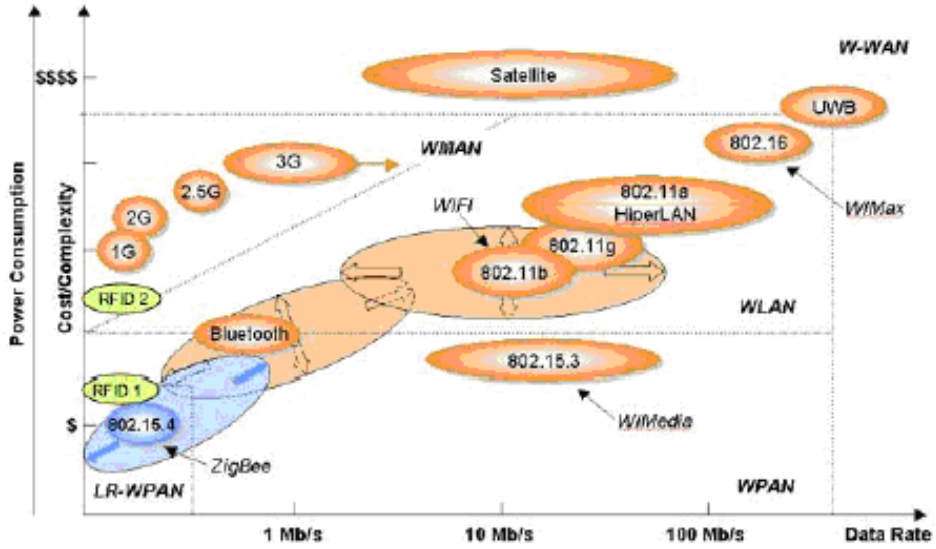

Figure 3.1 Overview cost/complexity vs. data rates of wireless technologies [59].

The potential advantages of new wireless technologies for power system operations have been widely recognized. It is generally admitted that, given the advances of new wireless communications, additional condition monitoring, safety monitoring, security management, and other new functions can be added to the arsenal for enhancing power system reliability. However, the use of wireless technologies in power system environments also presents a number of security and reliability concerns, such as eavesdropping on non-secured channels; wireless signal disruption due to

electromagnetic interference (EMI); faded signals due to long distance transmission or obstacles in the line-of-sight; overloading of bandwidth; immaturity of wireless lower layer protocols, and the need for testing in power system environments [59].

To help the industry address the potential of these technologies, the IEEE has started working on a new standard to create functional, performance, security and on-site testing practices for wireless technologies in power system operations. New standard, IEEE P1777(TM) [67], "Using Wireless Data Communications in Power System Operations", focuses on newer technologies, such as WiFi, Bluetooth, ZigBee, WiMax and cellular phones. The standard will define the potential uses of wireless technologies at many levels of power system operations, including substations, underground vaults, transmission and distribution circuits, generation and distributed generation plants, and customer electrical and metering equipment [67].

3.1.2 Power Line Communications (PLC)

It is generally admitted by utilities that, it would be highly desirable if the electric power lines could be used to deliver both electric power and communications signals. Therefore, PLC becomes a promising alternative for sensor network implementation.

Using the power lines for communications is not a new concept. PLC technologies have tremendous potential for growth in providing a networking infrastructure to support the concept of distributed sensor networks for power delivery. However, use of PLC technologies, particularly over HV or MV power lines, presents several concerns such as [68] [69],

- It is a challenge to design a cost-effective PLC coupler over HV power lines.
- Signals must pass through or around transformers, or other T & D equipment.
- Line connections and branches cause signal reflection and attenuation.

- At high frequencies power lines act as antennas both for emitting and receiving electromagnetic radiation, which makes reliable data communication via this medium difficult. Encryption must be used to prevent the interception of sensitive data by unauthorized personnel.

3.1.3 Wireless Sensor Networks (WSN)

The development of WSNs is motivated by the need to coordinate a large number of sensors into a higher-level sensing task (e.g., reporting with greater accuracy and more information than possible with a single sensor).

Research on WSNs was originally driven by military applications. However, the availability of low-cost sensors and communication networks has resulted in the development of many other potential applications, such as infrastructure security [70], environment and habitat monitoring [71] and industrial sensing. Because of potentially harsh, uncertain, and dynamic environments, along with energy and bandwidth constraints, WSNs pose many technical challenges [72]. Even though WSNs are different for different applications, they share several common features and requirements, as summarized in Table 3.2.

Much research has been conducted to develop schemes that fulfill the requirements as listed in Table 3.2. The technologies generally originate from three different research areas: sensor node hardware; networking and communications; networked information processing.

Sensor Nodes:

A sensor node is made up of four basic components: a sensing unit, a processing unit, a transceiver unit and a power unit. Thanks to advances in modern technologies, sensors, processors and communication devices are all getting smaller and cheaper. All the

subunits can typically fit into a matchbox-sized module with a relatively low product cost [75].

Table 3.2 SENSOR NETWORKS' GENERAL FEATURES AND REQUIREMENTS

Features	**Requirements**
Sensor Nodes	
Sensor nodes are in large numbers and densely deployed.	Cost-effective and small size
Power source is limited and generally irreplaceable. (Less power constraint with energy scavenging.)	Low power consumption
Performance is limited in power, computational capacities, and memory.	Simple network protocols and algorithms
Networking	
Position of sensor nodes need not to be engineered or pre-determined.	Self-organizing capability
Topology of a WSN may change frequently, due to system upgrade, or geographic expansion requirements.	
Sensors nodes are prone to failure due to hostile environments.	Self-healing capability
Short distance communication between sensor nodes requires multi-hop communication.	Optimized network routing
Information processing	
Sensor nodes may not have global identification (ID) because of a large number of sensors.	Localized computation
A cooperative effort of sensor nodes is needed.	Data aggregation and collaborative signal processing
Information concentration and extraction are needed to prevent data overload.	

Table 3.3 summarizes some hardware constraints and technical solutions for a network of small and embedded sensor nodes. Much effort has been put into developing and commercializing wireless sensor network technologies, and the ZigBee Alliance [66] is an association of companies working together to enable reliable, cost-effective, low-power, wirelessly networked, monitoring and control products based on IEEE Standard 802.15.4. Figure 3.2 shows three examples of ZigBee products available in the market.

Networking and Communications

A WSN is generally organized in the form of a star, cluster tree, mesh, or ring topology depending on the application [65]. Many protocols and algorithms have been

proposed thus far for WSNs to fulfill their special networking requirements, such as network discovery, network self-organization, and network control and routing [72]. Among them, ZigBee technology enables low-cost, low-power networking of sensors, controllers and other such devices in a self-configuring and self-healing WSN. ZigBee features allow for communication in a point-to-point, point to multipoint, or peer-to-peer configuration. These features are helpful in organizing a WSN by a cluster tree topology as shown in Figure 3.3 , which is more suitable to networks that cover larger physical areas, e.g. the geographically distributed power grid.

Table 3.3 SENSOR NODES DEVELOPMENT

Constraints	**Technical solutions**
Sensing Unit: - Low power - Low product cost - Fault tolerant	Many commercially available sensors are suitable for WSNs applications: SUNX Sensors, Keyence, Turck, UE Systems (ultrasonic), Leake (IR), CSI (vibration), etc. MEMS sensors are developed and are available for many sensing applications, such as 'Smart Dust sensors' from Dust Inc [74].
Processing Unit: - Limited power - Computation - Memory capacity	Memory storage: - Larger flash memory on a separate chip, up to several megabytes; - Tiny multi-threading distributed operating systems requiring less OS code space: Tiny-OS, µ-OS operating system [72].
Transceiver Unit: - Worldwide - Low power - Low cost	Optical devices: Smart dust motes [74]; Radio frequency devices: Most of the ongoing sensor node products are using 915 MHz and 2.4 GHz ISM bands [72].

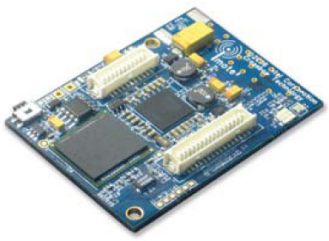

Crossbow[75]

MicroStrain

Digi International [76]

Figure 3.2 Commercial sensor nodes

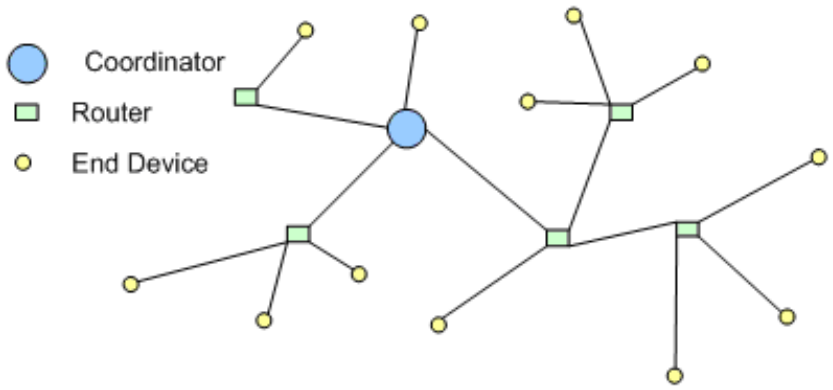

Figure 3.3 Cluster-tree topology [65]

The ZigBee protocol defines three types of nodes: Coordinator, Routers and End Devices, with a requirement of one Coordinator per network [65], as shown in Figure 3.3. In general, the Coordinator acts as a central RF (radio frequency) module that is configured to provide synchronization services through the transmission of beacons, and the establishment of membership between End Devices and a Coordinator. With its help, a large cluster tree network can self-organize into smaller subnets, each of which has a Coordinator. ZigBee networking is a powerful way to route data. Transmission range is extended by allowing data to hop from node to node, where data flows from an End device to its Coordinator node, through a Router node to a higher subnet, and continues upward until reaching a central collection device. At the same time, the network's reliability is increased by "self-healing", and the ability to create alternate paths when one node fails or a connection is lost.

Networked Information Processing

Collaborative signal and information processing over a WSN is a new area of research and is related to distributed information fusion. Important technical issues generally include two aspects [3]: processing data from more sensors generally results in better performance but also requires more communication resources; the more information is transmitted from each sensor, the more bandwidth is required. Therefore, the multiple tradeoffs between performance and resource utilization need to be

considered. Examples of recent research results can be found in [78], where localized algorithms and directed diffusion are developed.

3.2 Energy Scavenging Technologies

The implementation of a distributed sensor network for power grid monitoring should require the minimum of maintenance from the utility. Although battery technology has continued to improve, it would be impossible or impractical to frequently replace batteries especially in a high-voltage area. Therefore, exploring practical and useful energy scavenging technologies is critical in electric power utility applications for powering distributed sensor devices.

The existing energy scavenging technologies can be categorized depending on the energy sources utilized: solar energy, mechanical/kinetic energy, thermal energy, and electromagnetic energy, as summarized in Table 3.4.

Table 3.4 ENERGY SCAVENGING FOR SENSOR OPERATING POWER SUPPLY

Power Source	Principles	Performance
Solar Energy	Photovoltaic (PV) cells [79]	136 mW/cm^2 (sunny day); 10 mW/cm^2 (indoor); Efficiency: 10~20%
Mechanical /Kinetic Energy (Vibration)	Piezoelectric: Pressure on piezoelectric material causes voltage [80] [81];	200uW/cm^3 @ 120Hz [82]
	Inductive: Coil current induced by moving magnet	830uW [83]
	Capacitive/Electrostatic: Distance between plates or plate area changes	50uW/0.1cm^3 @ 980Hz [84]
Thermal Sources	Thermo-electric Generator [85] Thermo elements [86]	20~60 μW/cm^2 @ ΔT=20 ^{o}C
Capacitive Energy around Power Lines	50 m long antenna stretched between towers @ 6 m below the line [87]	10 μW/kg
Inductive Energy around Power Lines	High-permeability current transformer clamped around a power conductor [88]	1~3 W/g @ I=200 A
	Air-core current transformer near a power conductor [89]	9 μW/mm^2 @ I = 200 A
	50 m long loop @ 7 m below the line [87]	5 W/kg
E.M. Source (RF Waves)	Wireless power supply received via a range of RF radiation across a collection of frequencies [90]	1-2W @902-928 MHz/2.4-2.5 GHz

The power requirement of most of the wireless sensors available in the market is on the order of a few mill watts during transmit/receive operation and a few microwatts during sleep mode [75] [76]. The power required for communications varies depending on the distance of communication and the noise present in the environment, and is governed by the Federal Communications Commission (FCC) rules [91]. The scale of data transmission range for power grid monitoring applications is typically on the order of several hundred meters, which may bring the power requirement to a scope of x0 mill watts.

Technological advances in the electronics industry during the last decade have made it possible to reduce many electronic devices' size as well as the power required for them to operate. This power reduction has created an interest in developing new methods of scavenging ambient energy sources, i.e. mechanical energy and/or thermal energy, and converting it into electric energy [92] [93] [94]. However, as indicated in Table 3.4, these energy sources do not appear to provide sufficient energy for the sensor devices in power system applications with reasonable scale of device size.

An extensive study is conducted in [89] to evaluate the feasibility and performance of piezoelectric materials to scavenge energy in a high-current power line environment. The testing setup consists of a magnet attached to the edge of a piezoelectric bimorph bender, and is located next to a conductor carrying a current of up to 1000 A at 60 Hz. The magnetic field energy around the conductor is then converted to electrical energy through the vibration kinetic energy of the piezoelectric bender. The study shows that piezoelectric bimorph is able to provide a continuous average power of 100 μW with a current of 1000 A in the conductor. Its inability to provide power continuously is one of the major drawbacks to this technique. Besides, the design of a piezoelectric sensor to scavenge energy requires moving parts, which potentially degrades the efficiency of energy conversion.

The solar-cell based power supply [79] has features of low cost and simple structure, and provides sufficient power for most sensor applications with acceptable scale of size, e.g. 136 mW/cm^2 in a sunny day. However, solar cells are dependent on weather conditions, and it is difficult for sensors based on this technology to sustain good operation in bad weather or in an indoor environment.

The large electric field and magnetic field present around utility assets are the most promising energy sources that can be harnessed for distributed, unattended sensors. Studies in both [87] and [89] show that the small amount of capacitive energy coupled from electric fields near utility assets does not appear to warrant further consideration and investigation. Even though this technique shows that theoretically sufficient amount of energy can be harvested from the electric field to power a sensor device, the size of such a device may be quite large, which does not appear as a practical solution in most applications.

Magnetic field around power assets, on the other hand, has been proven to be the most promising and convenient energy source that is available for the distributed sensors in power system applications. Traditional high-permeability current transformer (CT) based method has been used in many occasions to provide energy for unattended sensor devices. This method provides sufficient amount of energy, requires simple structure, and is easy to implement. However, this scheme requires the sensor devices clamped around power assets, which potentially creates installation difficulty. To overcome this drawback, a novel concept to harness inductive energy from utility assets is proposed in [89], where a flux-concentrator sticks on to the surface of an asset. By loosely coupling the magnetic field through the use of the flux-concentrator, inductive energy is converted into useful electrical energy. The preliminary study in [89] shows that a maximum power of 257 mW can be obtained with a primary current of 200 A. This scheme comprises the amount of energy that can be harnessed from the magnetic field around power assets, but it greatly simplifies the device installation and reduces the sensor cost.

3.3 Chapter Summary

The potential advantages of new communications technologies for power industry operation have been wide recognized. It is generally admitted that, given the advances of new wireless communications, additional condition monitoring, safety monitoring, security management, and other new functions can be added to the arsenal for enhancing power system reliability.

The ZigBee WSN technology may not be the final answer to the data connectivity among the sensor modules in the proposed Power Line Sensor Network (PLSN). However, the development of ZigBee networks that has been driven by the needs for low-data-rate wireless connectivity among inexpensive fixed, portable, and moving devices as in an ad hoc self-organizing sensor network, make the WSN technology a promising solution to provide grid-wide monitoring across the power grid. Consider the target applications of the proposed PLSN as discussed in Chapter 1, a sensor module may need to report the real-time thermal capacity and/or the health conditions of the line only a few times per hour. These applications are excellent candidates for a low-data-rate, low-cost wireless communications link between sensor modules.

Even though both 802.11 and Bluetooth technologies are also good candidates to provide low-cost and robust wireless connectivity for a distributed sensor network, they are both complex in technology and unsuitable for low-power-consumption applications.

In this research, the existing WSN technology will be integrated to the PLSN, and its performance will be tested in a high electrical noise environment.

For energy scavenging to power distributed, unattended sensor devices, the availability of large electric and magnetic fields around utility assets greatly encourages the wide-area distribution and massive deployment of distributed sensor networks in power system applications.

CHAPTER 4

POWER LINE SENSOR NETWORK -- A NEW CONCEPT FOR POWER GRID MONITORING

This chapter introduces the concept of the proposed Power Line Sensor Network (PLSN), including the principles of the sensor network and the Power Line Sensor (PLS) module operation. Three functions of the PLSN from the end-user perspective are also described briefly.

4.1 Conceptual Power Line Sensor Network

The main objective of the proposed PLSN is to provide continuous on-line monitoring of power lines using hundreds of thousands of low-cost, autonomous, smart, and communications-enabled PLS modules. As shown in Figure 4.1, the PLS modules are clamped onto the overhead power lines where they float on the line both electrically and mechanically, and scavenge power from the line for both sensing and communications tasks.

Wireless Sensor Network (WSN) technology is deployed for this proposed PLSN, where each PLS module operates as a communication node, and communication occurs between adjacent working nodes. Self-organizing techniques ensure that failure of single or multiple nodes would not affect the ability of the network to continue operating. The distance between peer adjacent sensor nodes can range from 100 meters to several kilometers depending on the transmission power provided by the sensor nodes and the noise present in the environment. Local information from each PLS module is transmitted peer-to-peer back to a “master communication node”, which is normally several miles away from local sensor modules. The master communication node serves as a data-collector and provides a simplified interface with existing utility SCADA/EMS systems.

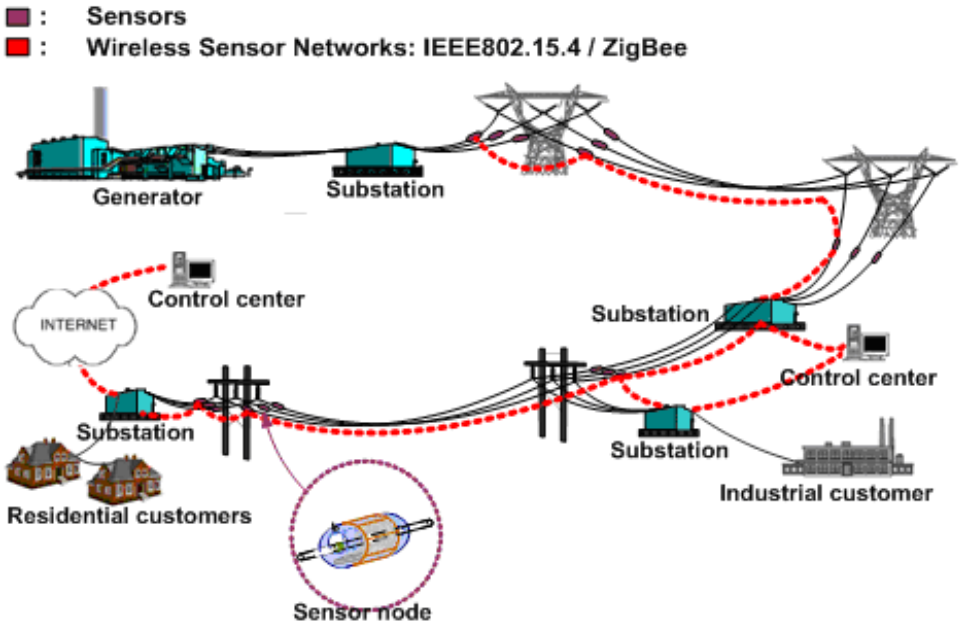

Figure 4.1 Conceptual Power Line Sensor Network (PLSN)

The use of PLS modules that float electrically and mechanically on the power line eliminates the need for high voltage isolation. By deploying low cost sensing technologies, and exploiting the cost effective communications technologies, i.e. WSN, it is possible to realize the dramatic reductions in cost that are required to achieve grid-wise, distributed deployment of such sensor modules.

If the PLSN could be implemented as planned, the PLS modules would provide continuous monitoring of diverse parameters associated with the real-time thermal conditions and/or health conditions of a power line down to a “per span” level of granularity if necessary. Gathering local information from all PLS modules, the sensor network should be able to provide the system operators with information that helps them optimally utilize the power line capacity, and makes them cognizant of the potential problems that can result in cascading failures, such as the August 2003 blackout.

4.2 Principles of Power Line Sensor Operation

This section introduces the principles of the basic PLS module operation. It also briefly describes the three functions of the proposed PLSN from the end-use perspective.

4.2.1 Power Line Sensor Module Introduction

Each PLS module has four core functions: sensing and measurement of critical line parameters in the immediate vicinity of the sensor module; local computation to continuously evaluate the real-time thermal capacity of the line and to detect the presence of incipient faults along the line in a changing environment; operation as a communication node in the WSN system; power and fault management while allowing sensing and communication functions. Figure 4.2 shows the configuration and block schematic of a PLS module that can provide these functions and communicate the information via the proposed PLSN.

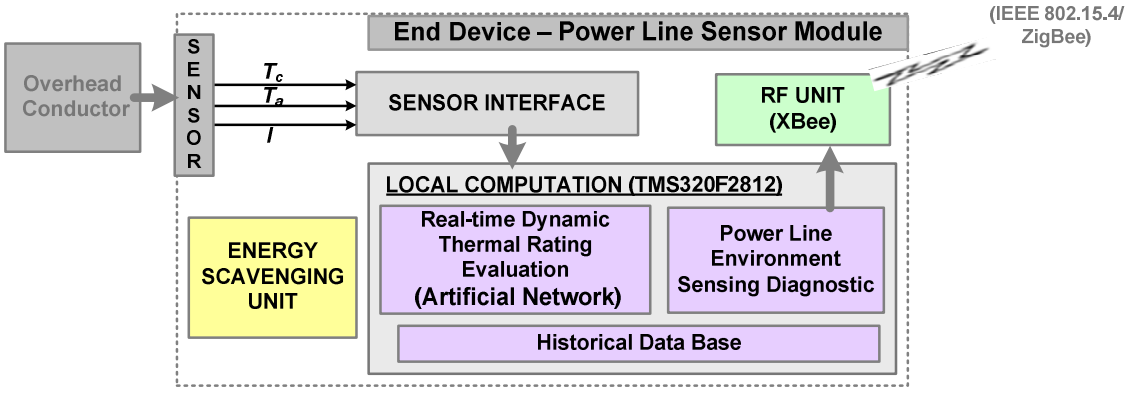

Figure 4.2 PLS Module Schematic

4.2.2 Target Applications of Power Line Sensor Networks

Based on the present state of knowledge in the field of distributed monitoring for utility assets as presented in Chapters 2 and 3, a detailed discussion and comprehensive

investigation is needed about the underlying technologies for the implementation of such a PLSN. The proposed PLSN will specifically target the use of passive sensing techniques, focusing on sensing the real-time capacity of a specific span of the power line under present weather conditions. An ancillary application would be to sense the presence of incipient faults along overhead power lines.

The two applications of the PLSN investigated in this research are detailed in the following sections:

1. Evaluation of Real-time Dynamic Thermal Rating of Overhead Power Lines

One of the main functions of this proposed PLSN is to evaluate the real-time dynamic thermal capacity of an overhead power line considering the ambient weather conditions.

In this work, the PLS model is proposed to take only conductor temperature, ambient temperature, and conductor current as inputs, and use computational intelligence technologies to estimate the heat-removal capacity of the conductor under present line loading and weather conditions. Together with the knowledge of loading history for the conductor, the true dynamic capacity of the particular span where the PLS module is mounted could then be estimated. As a typical Conductor-Temperature Model (CTM) based method, as introduced in Chapter 2, this proposed method avoids the need for weather condition measurements, and only requires low-cost temperature and current sensors. It allows the sensors to be mounted on every span of the line, thus to capture the micro-climate variations along the line and to assess the conductor thermal conditions down to the "per-span" level of granularity. Data from a large number of such modules gives a clear and dynamic picture of the thermal conditions along the whole line and indicates the critical span at any given time.

2. Power Line Vicinity Monitoring via Electric Field (E-field) Analysis

For this function of the PLSN, a novel Multiple Displacement Current Sensor (mDCS), as a part of the PLS module, is proposed to capture the spatial mapping of the E-field distribution around the overhead conductor where the mDCS is mounted, and thus to detect the presence of incipient insulator failure between the conductor and the ground, and/or other conducting objects in vicinity of the line.

The E-field distribution around overhead conductors is affected by both conductor voltage and line geometry variations, such as conductor-to-ground clearance, or proximity of tree limbs to conductors. The importance of this work is that the analysis of the E-field distribution around the conductor with the mDCS mounted enables the separation of the capacitive coupling effects between the conductor and its adjacent conducting objects in different directions, and thus allows independent and accurate measurements of both conductor voltage and line geometry variations.

4.3 Impact of Power Line Sensor Networks

Implementation of a PLSN across the power grid can have a significant beneficial impact for the utility industry. Most of the $225 billion in utility assets are aging and do not have any online monitoring. Coupled with the inability to control power flows on the network and the inability to store electricity, the power grid is congested, poorly utilized and has significant reliability problems. Uncertainties in T&D investment recovery delays the high cost of new lines and a semi-regulated utility industry have exacerbated the problems.

The most significant issues of the existing system are asset utilization, reliability, security and continued operation under contingency conditions. Improved real-time situational awareness of the power grid will allow improvement of grid operations against all the metrics listed above, resulting in higher reliability and lower cost of electricity. Accurate real-time information on dynamic capacity of lines will allow safe operation at

higher capacity, thereby reducing brownouts and transmission loading relief calls. Information on the location and timing of incipient failures, such as imminent line-tree contact or a failing insulator, will allow corrective action in a timely manner. Poor situational awareness, poor tree trimming practices, poor understanding of dynamic line loading and capacity, ineffective knowledge of location and significance of transmission breaker operations, and failure of the SCADA alarm system, were the primary contributors to the August 14, 2003 blackout. Implementation of the proposed PLSN would have addressed all these issues, and could possibly have averted the cascading failure.

4.4 Chapter Summary

This chapter has introduced the concept of a PLSN, a distributed approach for continuous monitoring of power lines through the use of large numbers of low-cost, communication-enabled sensors. Principles of the PLSN operation are introduced. Three functions of the PLSN from the end-user perspective are described briefly. In addition, the impact of such a PLSN on an existing power system is also stated.

The detailed discussion and comprehensive investigation on the underlying technologies to implement such a PLSN are presented in Chapters 5-8.

CHAPTER 5

EVALUATION OF REAL-TIME DYNAMIC THERMAL RATINGS OF OVERHEAD POWER LINES VIA MULTILAYER PERCEPTRON NEURAL NETWORK

To assist utilities in utilizing the overhead power lines more effectively and thus to optimize the utilization of the existing system, it is important to know how to accurately assess the real-time dynamic overload current capacity of lines down to a 'per span' level of granularity. One of the main functions of the proposed PLSN is to evaluate the Real-time Dynamic Thermal Rating (RDTR) of an overhead power line. Formulation of the RDTR requires the accurate assessment of the ambient weather conditions along the line (either directly measured or indirectly inferred), and the prediction of conductor temperature ahead of time under different ambient weather conditions. This task is often complex and difficult for real-time implementation.

This chapter proposes a Conductor-Temperature Model (CTM) based line rating method, where a Multilayer Perceptron Neural Network (MLPN) based parameter estimation scheme is used to estimate the heat-removal capability of a power line under present line loading and weather conditions and to evaluate the RDTR of the line. As a typical CTM-based line rating system, this method requires only conductor temperature, ambient temperature and conductor current as inputs, with no direct measurement of line ambient weather conditions needed. The proposed MLPN model is capable of estimating two weather-related parameters in real time, and tracking the time-varying ambient weather conditions with acceptable accuracy. The validity of the proposed method is examined on a typical overhead conductor (Drake ACSR) by simulations in the MATLAB environment.

5.1 Overhead Power Line Thermal Dynamics and Safe Operating Margin

5.1.1 Overhead Power Line Thermal Dynamics

The thermal behavior of overhead conductors is dramatically affected by the conductor heating, and the conductor ambient weather conditions, such as ambient temperature, wind velocity/direction, rain, ice, sun intensity, and the emissivity and absorptivity of the conductor surface, etc. Figure 5.1 shows a generic representation of the conductor heat balance.

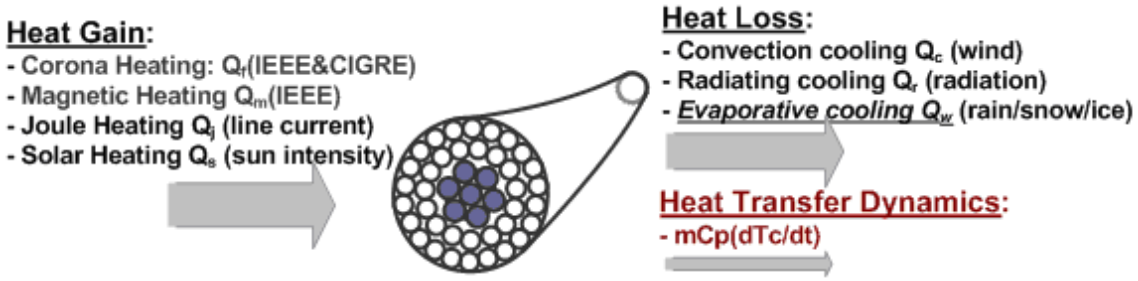

Figure 5.1. A generic representation of overhead conductor thermal behavior.

The heat balance equation is given [95] by,

$$mCp\frac{dT_c}{dt} = Q_j + Q_m + Q_s + Q_f - Q_c - Q_r - Q_w \tag{5.1}$$

where,

Q_j = Joule heating, including the frequency-dependent "skin effect" of the conductor;

Q_m = Magnetic heating, current density dependent magnetic core effects;

Q_s = Solar heating, the energy received from the sun depending upon the condition of the sky and the position of the sun with respect to the conductor;

Q_f = Corona heating, which is significant when there are high surface voltage gradients, a condition that would normally only occur during heavy precipitation and high wind. This heating term is usually much smaller than the high convective and evaporative cooling terms under the same meteorological conditions, and therefore is often ignored;

Q_c = Convective cooling, cooling effect from air flow around the conductor: wind movement; natural convection, which is the most significant cooling effect;

Q_r = Radiation cooling, heat emitted directly from the conductor;

Q_w = Evaporative cooling, which is generally not significant from air born water vapor or from water droplets flowing around the conductor but can be when the conductor is entirely wetted;

$mCp\frac{dT_c}{dt}$ = Heat transfer capacity, the product of the mass and specific heat of the conductor. T_c is the conductor temperature.

Figure 5.2 shows a generic overhead conductor thermal dynamic model in terms of lumped thermal parameters, where the thermal capacitor and resistor are associated with the overhead conductor and the ambient weather conditions. The thermal resistor $R_{Tr}(t) = 1/K_{cool}(t)$ represents the heat dissipation capacity of the conductor through the combined effects of radiation, convection and evaporation. $K_{cool}(t)$ is defined as the total cooling factors, given by $K_{cool}(t) = (Q_c + Q_r + Q_w)/(T_c - T_a)$, where Q_c, Q_r, and Q_w are the convection, radiating and evaporating cooling effects respectively. The effective thermal capacitance $C_{Tr}(t) = mC_P(t)$ is a function of the type of the conductor, as well as the conductor surface coating conditions affected by ambient conditions such as snow/rain.

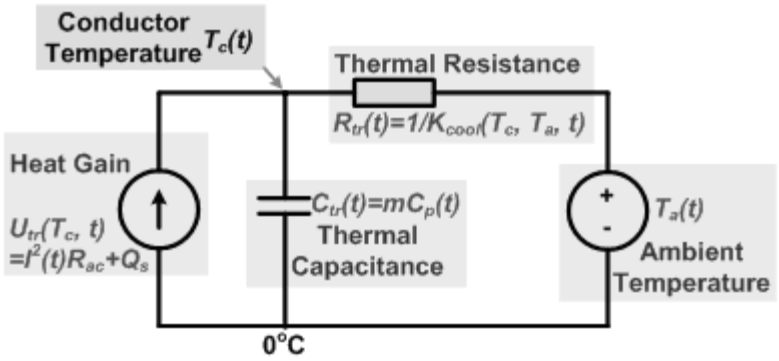

Figure 5.2. Overhead conductor thermal model in lumped thermal parameters

The total heat gain $U_{Tr}(t)$ is associated directly with joule heating/magnetic heating Q_j and Q_m, and solar heating Q_s, given by $U_{Tr}(t) = Q_j + Q_s$. Joule/magnetic heating is given by $Q_j = I^2 \cdot R_{ac}(T_c)$, where I is the conductor current. R_{ac} is the conductor ac resistance, which is a function of conductor temperature T_c.

Therefore, the conductor thermal behavior can be formulated by the following differential equation,

$$\frac{dT_c}{dt} = \frac{U_{Tr}(T_c,t)}{C_{Tr}(t)} - \frac{T_c(t) - T_a(t)}{R_{Tr}(T_c,T_a,t) \cdot C_{Tr}(t)} \qquad (5.2)$$
$$= f_c(T_c,\ I, \text{Ambient Weather Conditions})$$

Considering the time-varying affects from ambient weather conditions, the overhead conductor thermal dynamics essentially represents a time-varying, non-linear, first-order differential dynamic system.

5.1.2 Overhead Power Line Thermal Limit Curve

As a result of the large thermal capacitance $C_{Tr}(t)$ of the conductor, the conductor temperature changes gradually over a period of time after a change in current. Figure 5.3 shows typical conductor temperature responses following a step change in conductor

current for three different wind velocities, based on IEEE Std. 738-2006 conductor thermal model [24]. For the analysis and results which follow, it is assumed that initially the conductor with a temperature T_{c0} carries a preload current of I_i and that at time $t_0=0$ minutes the conductor is subjected to a step change in current to I_f.

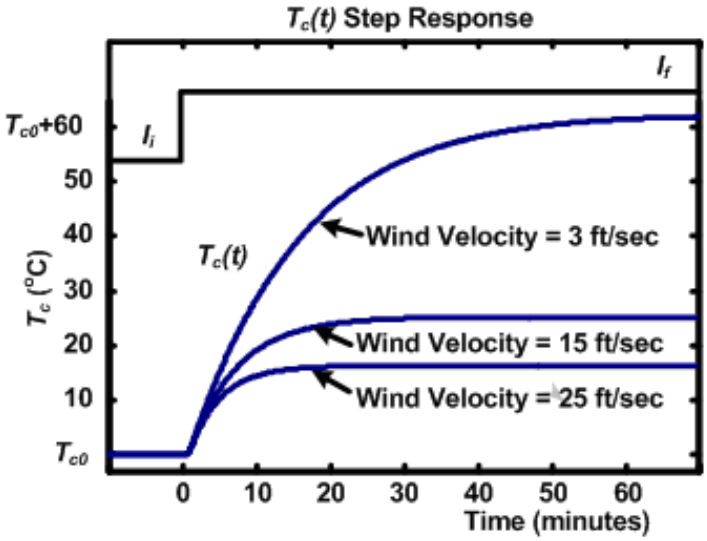

Figure 5.3. Conductor temperature response following a step change in current under various ambient weather conditions.

Because both the thermal resistance and capacitance of overhead conductors are strongly affected by ambient weather conditions, the temperature rising time delay is a function of environmental factors, and typically ranges from 5 to 30 minutes. The conductor thermal inertia allows overloading the power line for short **time durations** before the conductor reaches to its maximum allowable temperature.

For instance, as depicted in Figure 5.4, three T_c responses when subjected to a step change in conductor current from a preload value I_i to three different overload values I_f of say 1300, 1100 and 1050 A respectively. For each overload current there is a time duration needed for T_c to reach its maximum allowable temperature T_{cMax}. This means

the shorter the overload time duration, the higher the allowable short term overload current without overheating the conductor.

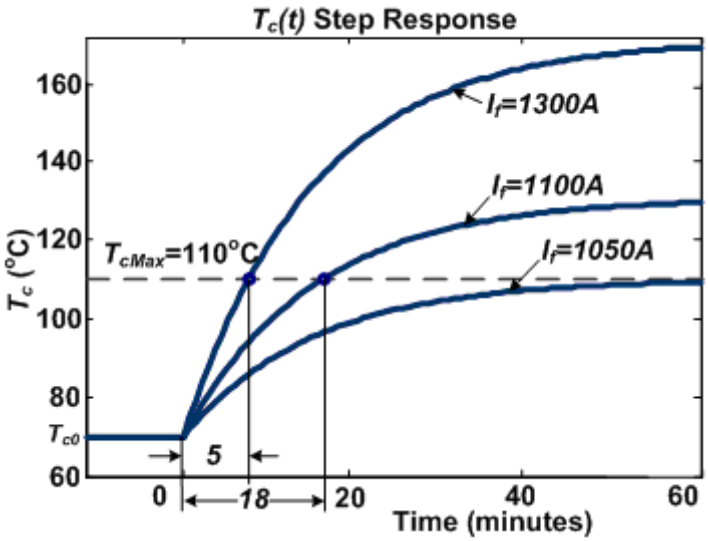

Figure 5.4. Conductor temperature response subject to a series of step changes in current under a certain weather conditions

This allowable short term overload current is also called the **Real-time Dynamic Thermal Rating** (RDTR) of the line for allotted duration. For instance, in Figure 5.4, 1300 A is the dynamic thermal rating I_{dyn} for an overload duration of t_o=5 minutes, and similarly 1100 A is the dynamic thermal rating I_{dyn} for a duration of t_o=18 minutes. Note that the overload current 1050A is actually the real-time steady state thermal rating I_{rs} (e.g. RSST as introduced in Chapter), since T_c eventually rises to T_{cMax} only at steady state.

The RDTR of a line is therefore not a **single value**, but **a series of short term overload capacities** associated with a series of short term durations, whose relationship can be represented in the form of an I-T Thermal Limit Curve (ITLC), as shown in Figure 5.5. Any point (I_{dyn}, t_o) on the I-T curve means that, for t_o period of time, I_{dyn} is the allowable short term overload current the conductor can withstand before T_c reaches

T_{cMax}. This ITLC defines the Safe Operating Area of the line segment where the PLS module is installed. It is not a fixed curve but variant through time, subject to continuously changing weather conditions nearby the overhead conductors.

At the same time, the ITLC for each line segment is different from others, since the line ambient weather conditions vary greatly along the line. Therefore, the resultant dynamic thermal rating of the whole line is actually a composite worst case thermal limit I-T curve capturing the weather conditions along the whole line and varying in real-time. This composite worst case I-T curve provides utilities the safe operating margin of a power line under a certain conductor ambient weather condition, in terms of increased short term (transient) and long term (steady state) line capacity. This is important, especially under system emergencies, for the operator to make efficient energy management decisions.

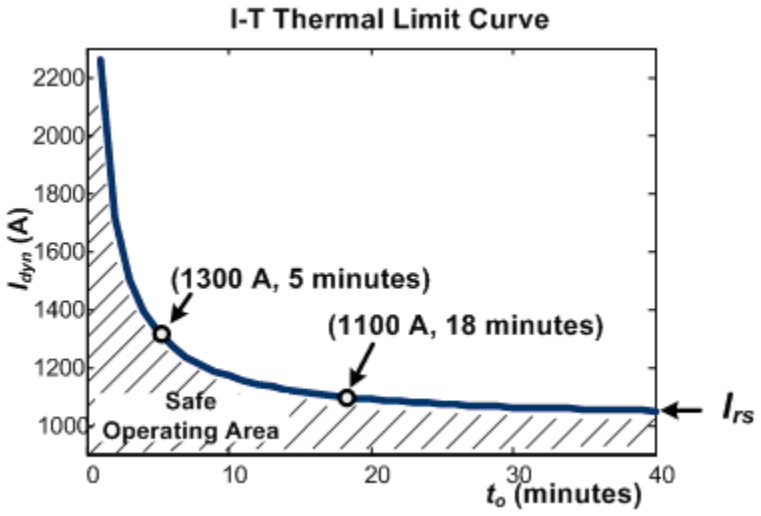

Figure 5.5. A typical I-T Thermal Limit Curve (ITLC) of a power line segment

However, determining an ITLC for a line segment is not an easy task. It requires repeated calculation to accurately **predict** how T_c will vary in the future, based on a certain conductor thermal model and driven by a range of assumed overload conductor

currents. For an accurate prediction of the conductor temperature, an analytical conductor thermal model that can precisely describe the conductor thermal behavior and can be used to solved for T_c is often needed [96] [97]. Two well known mathematical models describing overhead conductor thermal behavior appear in the IEEE Standard 738-2006 [24] and the CIGRE's Standard [98]. To simplify the heat balance equation in (5.1) and thus to simplify the calculation for line ratings, both IEEE and CIGRE methods remove several thermal effects from the equation, such as magnetizing heating, corona heating and evaporating cooling effects, which are generally considered to have little impact on the determination of line thermal ratings [95]. However, the resultant models still do not avoid the numerical complexity associated with computing the conductor temperature, and this has discouraged some utility engineers from attempting to use it in real time. Besides, these models normally require real-time measurements of weather conditions, and it makes the solutions generally expensive and difficult to implement.

To overcome these problems, this research adopts the CTM-based rating method as introduced in Chapter 2, where there is no additional measurement of line ambient weather conditions needed other than conductor temperature, ambient temperature and conductor current as inputs. A multi-layer-perceptron neural network (MLPN) model is proposed to estimate in real time the two parameters that are closely associated with line ambient weather conditions, i.e. wind speed, rain/snow, etc. To calculate the line RDTR through the use of these two estimated parameters, a simplified conductor thermal model is adopted with reference to the work presented in [99]. The continuous adaptation of the MLPN model due to changes in weather conditions allows the estimation of heat-removal capability of the conductor in real-time, which in turn helps evaluate the line thermal capacity under different ambient weather conditions.

5.2 Simplified Conductor Thermal Model and Direct Solution of Line Dynamic Thermal Rating

As the most commonly accepted model, IEEE Standard 738-2006 includes joule heating Q_j and solar radiation Q_s into the total heat gain. At the same time, only the convection and radiation cooling effects, Q_c and Q_r, are considered. The resulting heat balance equation of an overhead conductor is given by [24],

$$\begin{aligned} mC_P(t)\frac{dT_c}{dt} = I^2(t)\cdot R_{ac} + Q_s(t) - K_{\text{cov}}(t)\cdot(T_c(t)-T_a(t)) \\ -K_{rad}\cdot((T_c(t)+274)^4-(T_a(t)+274)^4) \end{aligned} \tag{5.3}$$

where the conductor ac resistance R_{ac} is expressed as a linear function of conductor temperature T_c, given by $R_{ac} = R_0 + K_R \cdot T_c$, where R_0 is the ac resistance at 0°C and K_R is the temperature coefficient of resistance. $K_{\text{cov}}(t)$ is the cooling factor associated only with convection cooling effect, and $K_{rad}(t)$ is the radiation cooling factor. The effective thermal capacitance $mC_P(t)$ is a function of the type of the conductor, as well as the conductor surface coating conditions affected by ambient conditions such as snow/rain.

To predict the conductor temperature T_c, (5.3) is can be used to solve for T_c. Unfortunately this equation is non-linear, as a result mainly of the radiation heat loss term, especially when wind velocity is low. Therefore, a simple, closed-form solution to (5.3) is not practical. In [99], Black and Rehberg propose a simplified conductor thermal model that is derived from (5.3). In this simplified model, the radiation cooling term Q_r is linearized to be $Q_r(t) = K_{rad}\cdot E\cdot(T_c(t)-T_a(t))$, where $E = k1 + k2\cdot T_a$. Parameters, *k1* and *k2*, are constants associated with the conductor type under study [99].

Therefore, (5.3) can now be reformulated as,

$$mC_P(t)\frac{dT_c}{dt} = (K_{cool}(t) - I^2(t)\cdot K_R)\cdot T_c(t) + I^2(t)\cdot R_o + K_{cool}(t)\cdot T_a(t) + Q_s(t) \qquad (5.4)$$

where $K_{cool}(T_a,t) = K_{\mathrm{cov}}(t) + K_{rad}\cdot(k1 + k2\cdot T_a)$.

Since the two terms $(K_{cool}(t) - I^2(t)\cdot K_R)$ and $(I^2(t)\cdot R_o + K_{cool}(t)\cdot T_a(t) + Q_s(t))$ are independent from T_c, (5.4) results in a **linear, ordinary differential** equation. The transient response of T_c therefore can be predicted by the following exponential equation, when the conductor is subjected to a step change in current from a preload current of I_i to an overload value of I_f,

$$T_c(t) = T_{css} - (T_{css} - T_{c0})\cdot\exp(-t/\tau_{tr}) \qquad (5.5)$$

where $\tau_{tr} = \dfrac{mC_p}{K_{cool} - I_f^2\cdot K_R}$ is the time constant, and $T_{css} = \dfrac{I_f^2\cdot R_0 + K_{cool}\cdot T_a + Q_s}{K_{cool} - I_f^2\cdot K_R}$ is the steady state conductor temperature under overload current I_f and present ambient weather conditions. The initial steady state conductor temperature is T_{c0} at time $t = 0$.

Now assume that, under an overload current I_{dyn}, the conductor temperature rises to its maximum allowable temperature T_{c_Max} at time $t = t_o$, and the following relationship can be obtained,

$$T_{c\_Max} = T_{css} - (T_{css} - T_{c0})\cdot\exp(-t_o/\tau_{tr}) \qquad (5.6)$$

Rearranging above equation, the overload current I_{dyn} is related to its minimum allowable overload duration t_o as follows,

$$t_o = f_{DYN}(I_{dyn}) = -\tau_{tr} \cdot \ln(\frac{f_1(T_{c\_Max}, I_{dyn})}{f_1(T_{c0}, I_{dyn})}) \tag{5.7}$$

where $f_1(T_c, I_{dyn}) = I_{dyn}^2(R_0 + T_c \cdot K_R) - K_{cool}(T_c - T_a) + Q_s$.

This overload current I_{dyn} is then called the *dynamic thermal rating* for the overload duration of t_o. If all the parameters in (5.7) are available, I_{dyn} can directly be solved through the use of (5.7).

In (5.7), the parameters, K_R, R_0, *k1*, *k2*, and K_{rad}, are closely related to the type of the conductor under study, and independent from ambient weather conditions. References [99] and [100] both give comprehensive descriptions on how to determine these parameters. The other two parameters, $K_{\text{cov}}(t)$ and mC_p, however, are highly dependent on the line ambient weather conditions, which are time-varying, and normally unknown or difficult to measure.

To calculate the dynamic thermal rating I_{dyn} based on (5.7), accurately estimating $K_{\text{cov}}(t)$ and mC_p becomes important. A novel idea in this research is to use a MLPN model to continuously estimate K_{cov} and mC_p in real-time under various line ambient weather conditions. The proposed MLPN receives the conductor and ambient temperatures, T_c and T_a, and conductor current I as inputs, which are directly measured from the proposed PLS module. Its outputs are the estimated $\hat{K}_{\text{cov}}$ and $m\hat{C}_p$. The neural network mapping is represented by $[\hat{K}_{\text{cov}}, m\hat{C}_p] = f_{MLP}(T_c, I, T_a)$. These two estimated parameters are then fed to a Dynamic Thermal Rating Solver, as illustrated in (5.7), to calculate the dynamic thermal rating of the line. The proposed line thermal rating method is summarized in Figure 5.6.

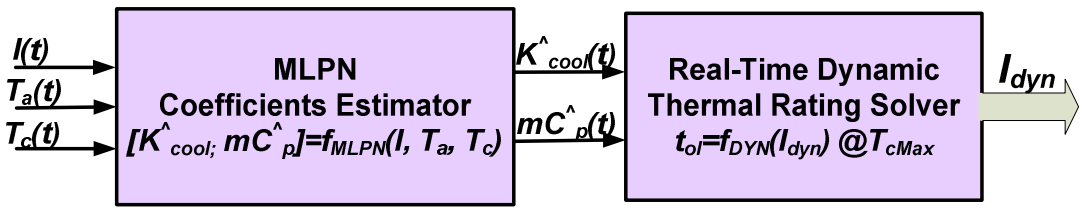

Figure 5.6. MLPN based DRTR evaluation.

5.3 MLPN-based Thermal Model Parameters Estimation

MLPNs have been widely accepted to learn complex and unknown non-linear mapping from inputs to outputs [101]. In this section, design and implementation issues of the proposed MLPN based parameters estimation scheme are presented. Developing an adaptive on-line learning algorithm for the neural network is one of the challenges for this application. A generalized Back-propagation (BP) learning algorithm is proposed to train the MLPN model.

5.3.1 Design of the MLPN based Parameter Estimator

In this research, a three-layer MLPN is used. The network input vector consists of k = *3* previous samples of conductor and ambient temperatures, T_c and T_a, and conductor current I, given by, $U_N(n) = [I(n-1), \ldots, I(n-k), T_a(n-1), \ldots, T_a(n-k), T_c(n-1), \ldots, T_c(n-k)]'$. The MLPN outputs are the estimated convection cooling factor and the effective heat capacitance, $Y_N(n) = [\hat{K}_{\text{cov}}(n) \quad m\hat{C}_P(n)]'$. The number of neurons in the hidden layer is chosen on a trial and error basis to be 20. A tan-sigmoid activation function, $f(\underline{n}) = 2/(1+e^{-2\cdot\underline{n}}) - 1$, is used in the hidden layer. A linear activation function is used in the output layer.

When the MLPN model is trained, an algorithm must be used to modify the weights and biases of the network to minimize a performance function (cost function). One of the key issues is to define a cost function for the MLPN based parameter estimator.

A commonly used cost function is the mean-squared error (MSE) between the outputs of the MLPN model and its desired outputs. In this specific application, however, the desired outputs of the MLPN model $K_{\text{cov}}(t)$ and $mC_P(t)$ are closely associated with the ambient weather conditions. Among them, $K_{\text{cov}}(t)$ is greatly affected by wind speed, and rain/snow etc. The thermal capacitance $mC_P(t)$ is a function of the conductor type, as well as the conductor coating conditions affected by ambient conditions such as snow/rain. Both of them are not available or difficult, if not impossible, to measure. Hence, the cost function cannot be defined directly in terms of the errors between the neural network's estimated outputs and the desired outputs.

A Parameter Estimation Tester (PET), $Y(n) = f_{Tr}(U(n))$, is therefore proposed in this research as a cascade to the MLPN model, as shown in Figure 5.7, to provide a new definition of the cost function, when the MLPN model is updated. The inputs of the PET consist of the MLPN's outputs at the nth instant of time, $\hat{K}_{\text{cov}}(n)$ and $m\hat{C}_P(n)$, and one previous sample of conductor current and ambient temperature, *I(n-1)* and $T_a(n-1)$, given by, $U(n) = [\hat{K}_{\text{cov}}(n) \quad m\hat{C}_P(n) \quad I(n-1) \quad T_a(n-1)]$. Its outputs are one-step ahead predictions of conductor temperature and its first derivative at the nth instant of time, $Y(n) = [\hat{T}_c(n) \quad \Delta\hat{T}_c(n)]$. Therefore, with reference to the MLPN based parameter estimation scheme depicted in Figure 5.7, the complete system can be described by,

$$Y(n) = f_{Tr}(\hat{K}_{\text{cov}}, m\hat{C}_P, I, T_a) \cdot f_{MLP}(U_N(t), \underline{x}) \tag{5.8}$$

where $f_{MLP}(U_N(t), \underline{x})$ represents the nonlinear function of the MLPN model, and $\underline{x}$ is the vector of coefficients of the MLPN model, including its weights and biases. $f_{Tr}(\hat{K}_{\text{cov}}, m\hat{C}_P, I, T_a)$ is the proposed PET, which is derived from the simplified conductor thermal model in (5.4) but in discrete time. Appendix A.1 presents the PET model in detail.

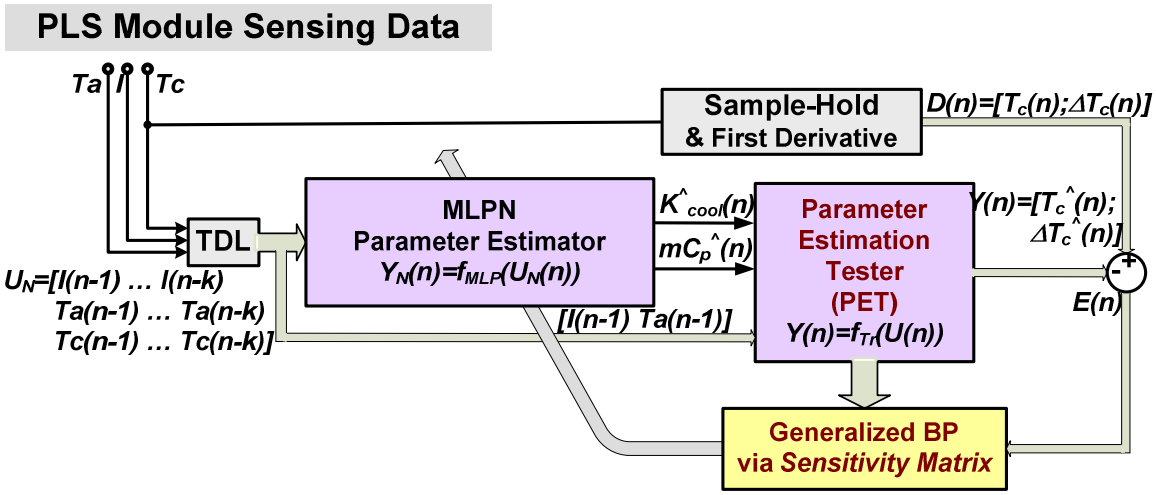

Figure 5.7. MLPN parameters estimation system

$D(n) = [T_c(n) \quad \Delta T_c(n)]$ can be obtained via direct measurement from the conductor temperature sensor embedded in the PLS module. Thus, in this particular application, with the help of the proposed PET, the cost function is defined in terms of the system errors, $E(n) = [e_{Tc}(n) \quad e_{\Delta Tc}(n)]$, where $e_{Tc}(n) = T_c(n) - \hat{T}_c(n)$ and $e_{\Delta Tc}(n) = \Delta T_c(n) - \Delta\hat{T}_c(n)$, rather than the neural network output errors normally deployed in conventional learning algorithms. In the following section, a new on-line adaptive learning algorithm is introduced to train the MLPN parameter estimator continuously in real-time.

5.3.2 On-line Adaptive Training of MLPN Parameter Estimator

The training goal of the MLPN parameter estimator is to determine the two parameters, $\hat{K}_{\text{cov}}(n)$ and $m\hat{C}_P(n)$, so that the system outputs *Y(n)* are able to track their desired values *D(n)* in real-time under different weather conditions. A continual on-line training algorithm of the MLPN has to be used, because the conductor thermal behavior are greatly affected by the line ambient weather conditions which vary widely over the course of the day, or even one hour.

During the on-line training procedure, the basic data sampling rate is selected to be 1 minute. Previous samples of current *I*, conductor and ambient temperatures, T_c and T_a (Q = 120 samples, 1 minute apart) from the last two hours are used to construct one set of training patterns with the size of Q. The sampling window slides along every 5 minutes, and the MLPN is only updated every 5 minutes based on the past two hours of training patterns. Table 5.1 summarizes the system data sampling rate and neural network updating rate.

Table 5.1 SYSTEM DATA SAMPLING AND MLPN UPDATING RATE

Training Data Sampling rate	1 minute
MLPN Updating Rate	5 minutes
Parameter Estimation Rate	5 minutes
MLP Training Pattern Size *Q*	120 samples (2 hours)

During each network updating interval, the cost function is evaluated in terms of the Mean Squared Error (MSE) between the actual system outputs *Y(n)* and the desired outputs *D(n)* for the given input sequences, given by,

$$V(n) = \frac{1}{2}\sum_{q=1}^{Q} \| E(q) \|^2 = \frac{1}{2}\sum_{q=1}^{Q} \| D(q) - Y(q) \|^2 \tag{5.9}$$

where $E(q)$ is the errors vector when the qth training pattern *(U(q), D(q))* is presented. Minimizing V using gradient descent methods for MLPNs, results in the well-known BP algorithm for training neural networks. In this work, a modified Back-Propagation (BP) algorithm, the Levenberg-Marquardt algorithm (LM) [101] given by,

$$\underline{x}_{n+1} = \underline{x}_n + [J'(\underline{x}_n) \cdot J(\underline{x}_n) + \mu I]^{-1} \cdot J'(\underline{x}_n) \cdot E_J(\underline{x}_n) \tag{5.10}$$

is used to update the network coefficients. I is a $(C \times C)$ identity matrix, and $J(\underline{x})$ is the $(T \times C)$ Jacobian matrix, which contains first derivatives of the system output errors with respect to the current neural network coefficients $\underline{x}$, including weights and biases in different layers. T is the product of the training pattern size Q and the system output dimension L. C is the total number of the MLPN network coefficients $\underline{x}$. $E_J(\underline{x})$ is a vector of system output errors for all Q training patterns with the size of $(T \times 1)$.

Using the LM updating rule, the critical step is the computation of the Jacobian Matrix, with a typical element given by $J_{t,c}(\underline{x}) = \partial e_t(\underline{x}) / \partial x_c$, for t=1,2,…,T and c=1,2,…,C. It is noted that, $e_t(\underline{x})$ could be the error between any component of the estimated and desired system outputs for any qth training pattern $(U(q), D(q))$.

Therefore, computing the partial derivatives of the system output errors *E(n)* with respect to $\underline{x}$, at any instant of time (every minute), becomes important, and is expressed by,

$$\frac{\partial E}{\partial \underline{x}}(n) = -\frac{\partial Y}{\partial \underline{x}}(n) = -\left[\frac{\partial \hat{T}_c}{\partial \underline{x}}(n) \quad \frac{\partial \Delta \hat{T}_c}{\partial \underline{x}}(n) \right]' \tag{5.11}$$

When the MLPN model is cascaded in series with the PET as shown in Figure 5.7, the partial derivatives $\partial Y(n)/\partial \underline{x}$ of the **system outputs** *Y(n)* with respect to $\underline{x}$, cannot be obtained directly, but have to be derived through an intermediate step.

Revisiting (5.8), the MLPN based parameter estimation system can be treated as a generalized neural network [102]. If taking the partial derivative of (5.7) with respect to $\underline{x}$ and using the chain rule, the following equations are obtained, in matrix form,

$$\frac{\partial Y(n)}{\partial \underline{x}} = \Pi_{RC}(n) \cdot \frac{\partial Y_N(n)}{\partial \underline{x}} \tag{5.12}$$

where $\frac{\partial Y_N(n)}{\partial \underline{x}} = \left[\frac{\partial \hat{K}_{\text{cov}}(n)}{\partial \underline{x}} \quad \frac{\partial m\hat{C}_P(n)}{\partial \underline{x}} \right]'$ is the partial derivative of the neural network outputs $Y_N(n)$ with respect to $\underline{x}$, which can be obtained directly using the conventional BP technique [101].

$$\Pi_{RC}(n) \equiv \begin{bmatrix} \delta_{TK}(n) & \delta_{TC}(n) \\ \delta_{\Delta TK}(n) & \delta_{\Delta TC}(n) \end{bmatrix} \tag{5.13}$$

is the **Sensitivity Matrix (SM)** (Refer to Appendix A.2 for details) and is closely associated with the PET model $f_{Tr}(\hat{K}_{\text{cov}}, m\hat{C}_P, I, T_a)$ (Refer to Appendix A.1 for detailed description of PET model). Because the PET is a dynamic system, the SM needs to be updated in a recursive manner through time, as follows,

$$\Pi_{RC}(n) \equiv A \cdot \Pi_{RC}(n-1) + B \tag{5.14}$$

Appendix A.3 gives a detailed description of A and B.

With help from the SM, the conventional BP learning algorithm is successfully extended to the generalized neural network described by (5.8), and the complete network training procedure is denoted as a generalized BP learning algorithm.

Figure 5.8 shows the flow chart of the MLPN model online adaptive training. The MLPN feed-forward calculation and the computation for the gradients of system outputs $\partial Y(n)/\partial \underline{x}$ are carried out at the basic sampling rate (1 minute). All the computed quantities are queued in a FIFO buffer with a size of Q = 120 to form the error vector $E_J(\underline{x})$ and the Jacobian Matrix $J(\underline{x})$. Every 5 minutes, the LM learning rule in (5.10) is calculated by retrieving the latest error vector E_j and Jacobian Matrix from the FIFO butter. Therefore, the MLPN is updated every 5 minutes based on the past two hours of information.

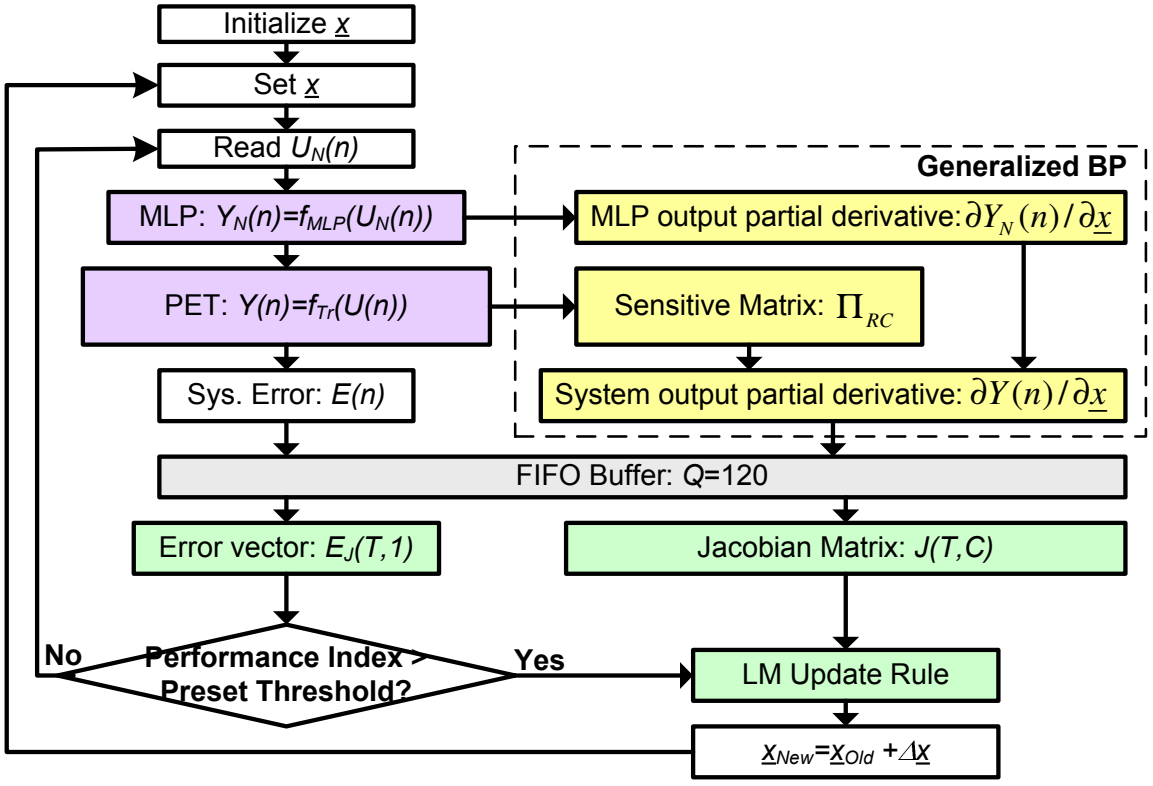

Figure 5.8. Online adaptive algorithm flowchart

5.4 Simulation Results

A 795 kcmil 26/7 ACSR (Drake) conductor is evaluated as the base case (Appendix B provides Drake conductor parameters). The conductor thermal model provided in IEEE standard 738-2006 [24] is used to prepare the training data. The assumed ambient conditions of the overhead power line appear in Appendix C. Figure 5.9 shows thermal conditions of an overhead line segment for 6 days, including joule heating gain Q_j, ambient temperature T_a, solar radiation Q_s, wind velocity V_w, conductor heat capacity mC_p (affected by conductor loading conditions, i.e. ice/rain), and conductor temperature T_c.

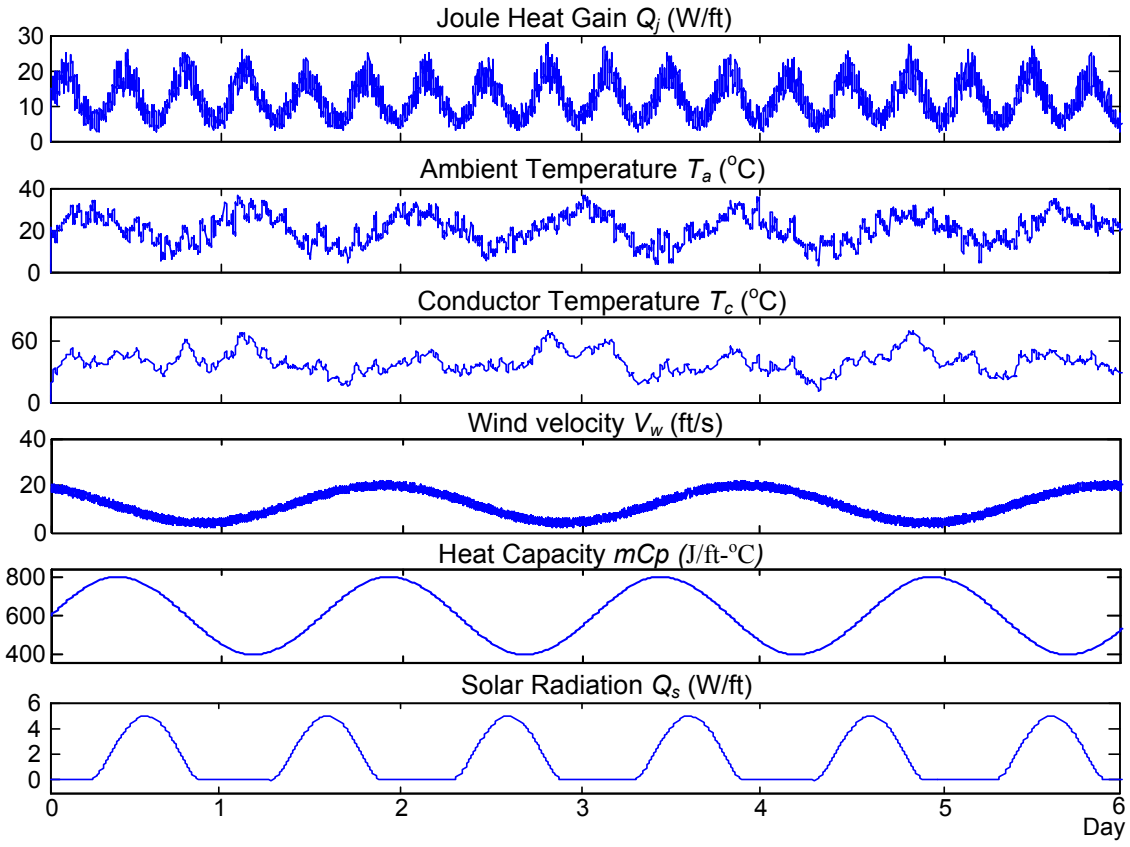

Figure 5.9. Thermal conditions of a power line segment for six days

Under time-varying weather conditions, both the MLPN based parameter estimation system in (5.8) and the IEEE model are driven by input sequences *U(n)* sampled from two hours of immediately preceding time-varying profiles of ambient temperature T_a and line current *I*. The MLPN coefficients $\underline{x}$ are adjusted to minimize the cost function defined in (5.9). In order to continuously adapt the MLPN model to the latest ambient conditions, the training data sampling window slides forward every 5 minutes, and the MLPN is updated every 5 minutes as well.

Figure 5.10 (a) and (b) show the estimated $\hat{K}_{\text{cov}}$ and $m\hat{C}_p$, as the outputs of the MLPN model. For comparison purposes, the analytical results based on the IEEE Standard 738 model are included in this figure. At the same time, Figure 5.10 (c) also depicts the evaluated maximum allowable overload current (RDTR) of the line for an overload duration of 10 minutes. Again, the RDTR calculated based on the IEEE Standard 738 model is also shown.

Figure 5.10 indicates that, outputs of the MLPN model are able to track the variation of ambient weather conditions with acceptable accuracy. However, large tracking errors are observed on $\hat{K}_{\text{cov}}$, when the solar radiation Q_s is high. The error is caused by the fact that solar radiation is not included into the MLPN based parameter estimation system, as depicted in Figure 5.7. However, it does not affect the accuracy of the evaluated RDTR of the line, as shown in Figure 5.10 (c). The results based on the two methods, i.e. the MLPN based method and the IEEE Standard based method, agree well.

This fact that the errors in the parameter estimation do not affect the accuracy of rating evaluation can be explained as follows. When the power line operates at its rated current, joule heating gain Q_j on the conductor is much larger than the heat gain obtained from solar radiation. The joule heating gain Q_j is 115 W/m with an overload current of 1500 A flowing through a Drake conductor [24]. On the other hand, the maximum sun radiation on a Drake conductor is around 15 W/m [24], which can be reasonably ignored

under overload conditions. Therefore, omitting solar radiation affects the accuracy of parameter estimation, but does not influence the performance of the line RDTR evaluation.

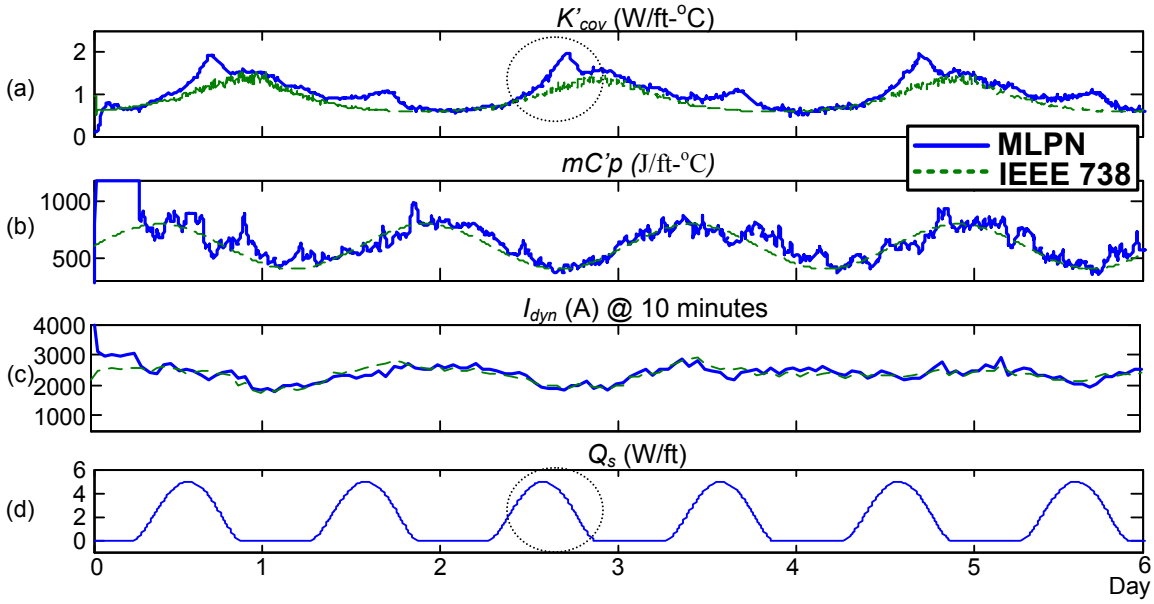

Figure 5.10. MLPN on-line estimation of thermal model parameters

5.5 Identification of Overhead Power Line Thermal Dynamics

In the previous sections, the capability of the proposed MLPN-based parameter estimator has been validated to estimate the heat-removal capability of the overhead conductor and to evaluate the dynamic thermal rating of an overhead power line on a continuous basis in the simulation environment.

However, there are several drawbacks to this method. First of all, as discussed in Section 5.3, the implementation of this MLPN based method still requires an analytical model of the conductor dynamics (i.e. the Parameter Estimation Tester (PET) shown in Figure 5.7) to assist the MLPN learning process and to calculate the line rating. Prior knowledge of the conductor analytical model is thus needed. At the same time, the

parameters appearing in (5.7), i.e. K_R, R_0, $k1$, $k2$, and K_{rad}, are closely related to the type of the conductor under study as well as the conductor surface conditions, which may change with time as the conductor ages and the conductor surface becomes heavily oxidized. The uncertainty in these parameters may affect the accuracy of the proposed method to evaluate line ratings.

The complexity associated with the MLPN on-line training algorithm is another drawback of this method. The generalized BP algorithm requires a Sensitivity Matrix that must be updated in a recursive manner through time, which increases the computation burden.

Last but not least, the conductor thermal model in (5.4) that is utilized in this work ignores several thermal effects on conductor thermal behavior, i.e. magnetizing heating, corona heating and evaporating cooling effects. Even though they are generally considered to have little impact when the line thermal ratings are determined [95], it is not always true especially for the evaporative cooling effects. Evaporative cooling is generally not significant from air born water vapor or from water droplets flowing around a conductor. However, its cooling effect can be significant when the conductor is entirely wetted. Moreover, in the cold and low-temperate regions of North America, Europe and Asia, the icing and snow build-up on high-voltage overhead power lines and conductors during winter storms is a serious problem. It compromises the reliability of power transmission. If the icing and snow built up on a line can be detected by evaluating the effective thermal capacitance, the joule heat gain can be used as de-icing and anti-icing techniques. Therefore, sometimes, the icing and snow effect is even expected to be detected and included in the evaluation process for line ratings. However, this adds more complexity to establish the line thermal rating, not only because the icing and snow effect is difficult to measure but also because it is difficult to quantify.

To overcome the above difficulties, in the following Chapter 6, a novel strategy of dynamic thermal rating evaluation by using an Echo State Network (ESN) is proposed.

The ESN is an alternative form of a Recurrent Neural Network (RNN), and a promising tool to learn and identify the complete transient behavior of a non-linear **dynamical** system [103], e.g. the overhead conductor thermal behavior studied in this research. The implementation of the ESN identification potentially removes the need for an analytical conductor thermal model, as well as the need for prior knowledge of the conductor. Besides, the dynamic thermal behavior of the conductor that is identified by the ESN model effectively reflects the heat-removal capability of the conductor caused by any cooling effects, i.e. convective cooling, radiative cooling and/or evaporative cooling (omitted in both the conventional methods and the MLPN method). This relieves the difficulty in measuring and quantifying the meteorological parameters especially associated with the evaporative cooling effect.

Moreover, the training of an ESN is simply a linear regression task [105], which is much simpler than the generalized BP algorithm needed in the MLPN method and makes it a promising solution for real-time implementation. In Chapters 6 and 7, the proposed ESN-based thermal rating evaluation scheme is presented in more details

5.6 Chapter Summary

In this chapter, an online adaptive MLPN model has been proposed to estimate two weather-related parameters, which are used to estimate the heat-removal capability of the conductor on a continuous basis under time-varying line loading and weather conditions. Preliminary simulation results have validated the proposed methods as a useful tool to evaluate the line real-time dynamic thermal rating with the proposed PLS module as the platform. However, the successful implementation of this proposed method still needs an analytical model of the conductor dynamics. The simplification of the model neglects several important conductor-thermal effects, and results in an inaccurate thermal rating

estimate. Besides, the complexity of the MLPN training process prevents the proposed method being a promising solution for real-time implementation.

To overcome the above difficulties, another real-time dynamic thermal ratings strategy, which uses an ESN-based identifier is proposed and presented in the following chapter.

CHAPTER 6

EVALUATION OF REAL-TIME DYNAMIC THERMAL RATINGS OF OVERHEAD POWER LINES VIA ECHO STATE NETWORKS

As presented in the previous chapter, accurate prediction of the conductor temperature ahead of time subject to various conductor overload conditions is the most critical and challenging step when determining the Real-time Dynamic Thermal Rating (RDTR) of an overhead power line. This chapter proposes another dynamic line rating method based on the identification technology of Echo State Networks (ESNs). Compared to the MLPN-based method proposed in Chapter 5, this new method eliminates the need for an analytical model and relieves the difficulties to measure and quantify metrological parameters as required by traditional methods and even the MLPN based method.

6.1 Overview of the Proposed Method

As discussed in the previous chapter, the most important parameter in establishing real-time dynamic thermal ratings for overhead conductors is the conductor temperature T_c. **Predicting** how T_c will behave ahead of time subject to various overload conditions under the present weather conditions is the most critical and challenging step to determine the dynamic thermal rating of a line.

Overhead conductor temperature depends on a complex relationship between the conductor temperature, current, and various meteorological factors such as ambient temperature, wind velocity and direction, rain and ice, sun intensity, and the emissivity and absorptivity of the conductor surface, etc. With reference to the first order differential model of the conductor thermal dynamics in (5.2), if the conductor current I and ambient

temperature T_a are the only two known external influences to the system, then the state space representation of the conductor thermal dynamics can be written as,

$$dT_c / dt = f_c(T_c, I, T_a) \tag{6.1}$$

The function $f_c(.)$ represents a non-linear combination of the output (i.e. T_c) and inputs (i.e. I and T_a), which is time-varying, and closely related to the ambient weather conditions around the conductor. To predict the conductor temperature T_c, $f_c(.)$ needs to be solved for T_c. However, as discussed in Section 5.1, even if this model were accurately known, the direct calculation of T_c is often complicated. Let alone that the values associated with the weather conditions would have to be measured or estimated which is often difficult, if not impossible. The numerical complexity associated with computing T_c has discouraged utilities from attempting to evaluate the RDTR in real time.

To remove the need for an analytical model of $f_c(.)$, e.g. the model in IEEE Std. 738-2006, in this chapter, an original, novel idea using an Echo State Network (ESN) model is proposed to identify the conductor thermal dynamics, denoted by $f_c(.)$ in (1), with I and T_a as inputs (directly measured from the PLS module [106]) and the estimated conductor temperature T_c^* as output. The state space representation of the ESN model can be written as,

$$dT_c^* / dt = f_{ESN}(T_c^*, I, T_a) \tag{6.2}$$

During the system identification, the network function $f_{ESN}(.)$ is trained to maintain a minimized error between T_c^* and the actual conductor temperature T_c.

After it is well trained, the ESN model is used as an emulator of the conductor thermal dynamics to predict the transient (dynamic) behavior of T_c under different overload conditions, and in turn to help evaluate the dynamic line rating in real time. This method requires no analytical model of conductor thermal dynamics, and needs no actual weather monitoring devices in the system.

6.2 Echo State Networks Dynamics

The ESN is an alternative form of Recurrent Neural Networks (RNNs) [105]. Given its inherent recurrent connectivity between neurons inside the network, an RNN (or an ESN) develops a self-sustained temporal activation dynamics even in the absence of inputs. Mathematically, this renders an RNN to be a dynamical system, and makes it a promising tool to identify nonlinear dynamical systems through the use of suitable training algorithms. A number of successful academic and practical applications have been reported [104] [107], however, the impact of RNNs in nonlinear modeling has remained limited for a long time mainly because of the difficulty to train the network, e.g. the famous Back-Propagation Through Time (BTT) [108] [109]. Besides, implementation complexity, slow convergence and suboptimal solutions remain obstacles for this type of neural network from being used widely in real-time implementations.

ESNs, on the other hand, overcome the above RNN problems. Besides, the ESN training algorithm is essentially a linear regression problem, which allows an ESN to continuously adapt itself to any changes in conductor ambient weather conditions without too much computation required, which makes it an attractive solution to real-time implementation.

6.2.1 ESN Structure

The ESN is a special case of fully connected RNNs in which only a fraction of recurrent connections exists among neurons in the internal layer. This fraction of neurons is sparsely interconnected with non-trainable weights $\boldsymbol{W}$, often called a "*Dynamic Reservoir*" (DR), and produces the dynamics of the whole network. Figure 6.1 depicts the structure of a typical ESN, with *K* inputs, *N* internal neurons and *L* output neurons, which can be formulated in the following discrete form [103],

$$X(n) = f(\boldsymbol{W}^{in}U(n) + \boldsymbol{W}X(n-1) + \boldsymbol{W}^{back}Y(n-1) + v(n)) \tag{6.3}$$

$$Y(n) = f_{out}(\boldsymbol{W}^{out}\left[U(n), \quad X(n), \quad 1\right]) \tag{6.4}$$

where *f(.)* is the neuron activation function of the internal layer. $\boldsymbol{W}^{in}(N \times K)$ is the weight matrix connecting the network inputs *U(n)* and the internal states *X(n).* The internal states *X(n)* with their connection weights $\boldsymbol{W}(N \times N)$ form the DR. The weight matrix $\boldsymbol{W}^{back}(N \times L)$ provides the feedback connections from the outputs *Y(n)*.

$f^{out}(.)$ is the neuron activation function of the output layer. $\boldsymbol{W}^{out}$ $(L \times (K + N + 1))$ is the output weight matrix. Both activation functions, *f(.)* and $f^{out}(.)$, consist of bipolar sigmoids or tanh, offering the nonlinear feature of the neural network. The term $[U(n) \;\; X(n) \;\; 1]$ is the concatenation of a bias, the input, and the internal state vectors. In a simplified form, the whole network can also be represented by,

$$Y(n) = f_{ESN}(Y(n-1), U(n)) \tag{6.5}$$

The novel idea behind ESNs is to separate the RNNs' architectures into two constituent parts: a **fixed** recurrent architecture, i.e. the DR, within the internal layer; and

an **adjustable** linear output layer, also called the readout neurons [107]. The recurrent architecture offers the system dynamics, and the related weight matrices $\boldsymbol{W}^{in}$, $\boldsymbol{W}^{back}$ and $\boldsymbol{W}$ are all randomly predetermined and remain unchanged during the training process. Therefore, the training of an ESN only involves updating the weights in the output layer, i.e. $\boldsymbol{W}^{out}$, which are adjusted to achieve the desired outputs $D(n)$. If the sigmoid output activation function is used, the training error to be minimized can be expressed by [103],

$$MSE = \frac{1}{T}\sum_{n=1}^{T} \| \tanh^{-1} D(n) - \tanh^{-1} Y(n) \|^2 \tag{6.6}$$

where T is the size of the training sequence. Because there are no cyclic dependencies between the trained readout connections, training an ESN becomes a simple linear regression task, for which numerous batch or adaptive online algorithms are available [105].

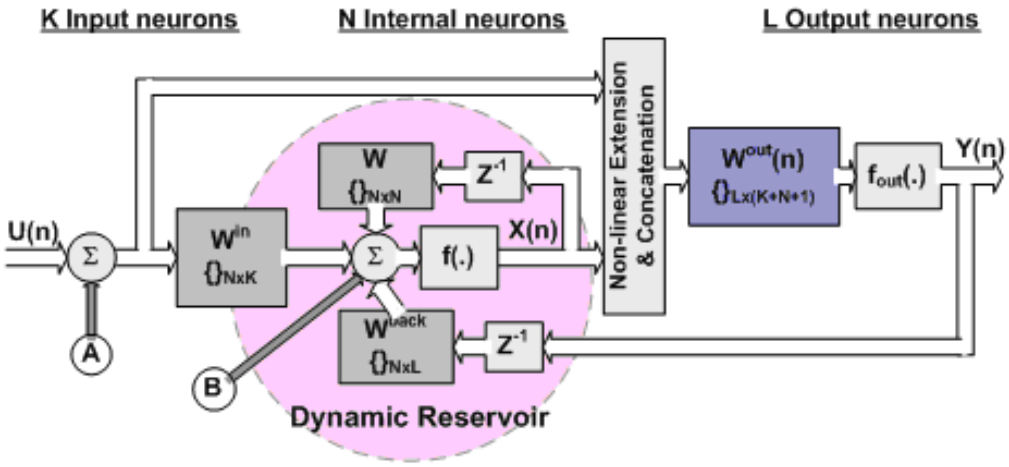

Figure 6.1. Echo State Network Structure.

6.2.2 Echo State Properties and Training of ESNs

The problem with a fixed recurrent architecture (i.e. DR), however, is that the randomly constructed DR might develop oscillatory or even chaotic activity even in the absence of external excitation. In [103], Jaeger suggests that proper selection of the above weight matrices, especially $\boldsymbol{W}$, is important to ensure a special property of an untrained, randomly constructed network, i.e. a so-called echo-state property.

There are several nontrivial alternative definitions of echo-state property and algebraic characterizations of which the matrix $\boldsymbol{W}$ leads to networks having this property. In [103], Jaeger provides a sufficient condition for the non-existence of echo states, which is not helpful for finding echo state networks. However, for practical purposes it suffices to limit the spectral radius of $\boldsymbol{W}$, α, to a value below unity to ensure the echo state property. According to Jaeger, it is sufficient to ensure that $\boldsymbol{W}$ has a maximum eigenvalue $|\lambda_{\max}| < 1$. The stability of the system can be ensured by a DR that is damped. This can be achieved by proper scaling of $\boldsymbol{W}$: the smaller the weights of $\boldsymbol{W}$, the stronger the damping. It is also important that the dynamics of the DR neurons be richly varied, which can be ensured by a sparse interconnectivity (1-20%) within the reservoir. This condition lets the reservoir decompose into many loosely coupled subsystems, establishing a richly structured reservoir of excitable dynamics.

Having an ESP prevents a chaotic and unbounded behavior of the network, and is particularly important if the ESN is expected to run independently after it is well trained. The current states of the ESN, *X(n)*, are therefore asymptotically independent of the initial conditions *X(0)*, which will wash out after some time, and are determined only by the inputs. This point is elaborated more in the following sections.

The main objective of the ESN training process is that, given a training input/output (I/O) sequence $(U(1), D(1)), ..., (U(T), D(T))$, a trained ESN output *Y(n)* is able to approximate the desired output *D(n)*, when the ESN is driven by *U(n)*. For convenience

of notation, the off-line batch training process of an ESN is summarized briefly as follows [103]:

- Given an I/O training sequence (*U(n)*, *D(n)*).

- Generate randomly the matrices (***W^in***, ***W***, ***W^back***), scaling ***W*** such that $|\lambda_{\max}| < 1$ with a spectral radius of α.

- Drive the network using the training I/O sequence, by computing $X(n) = f(W^{in} \cdot U(n) + W \cdot X(n-1) + W^{back} \cdot D(n-1))$.

- Collect at each time step the state *X(n)* as a new row into a state collecting matrix ***M***, and collect similarly at each time step the f^{out}-inverted teacher output $(f^{out})^{-1} D(n)$ into a teacher collection matrix ***Z***.

- Multiply the pseudoinverse of ***M*** with ***Z***, to obtain $W^{out} = (M^{-1}Z)^t$, where *t* indicates transpose operation.

- The ESN is now trained.

These unique characteristics of the ESN, including the ensured network stability and the simple learning algorithm, make it an ideal identification tool for real-time applications.

6.3 ESN based Overhead Conductor Thermal Dynamics Identification/Prediction

In this work, an ESN model is used to identify the conductor thermal dynamics under various ambient weather conditions. Figure 6.2 depicts the ESN based identification scheme where there are two individual ESN models in this scheme, but of identical structure: ESN Identifier (ESN-Idf) and ESN Predictor (ESN-Prd). As the hardware platform, the proposed PLS module provides continuous monitoring of line current *I*,

and ambient and conductor temperature, T_a and T_c, which form the inputs and desired outputs to the ESN-Idf and ESN-Prd.

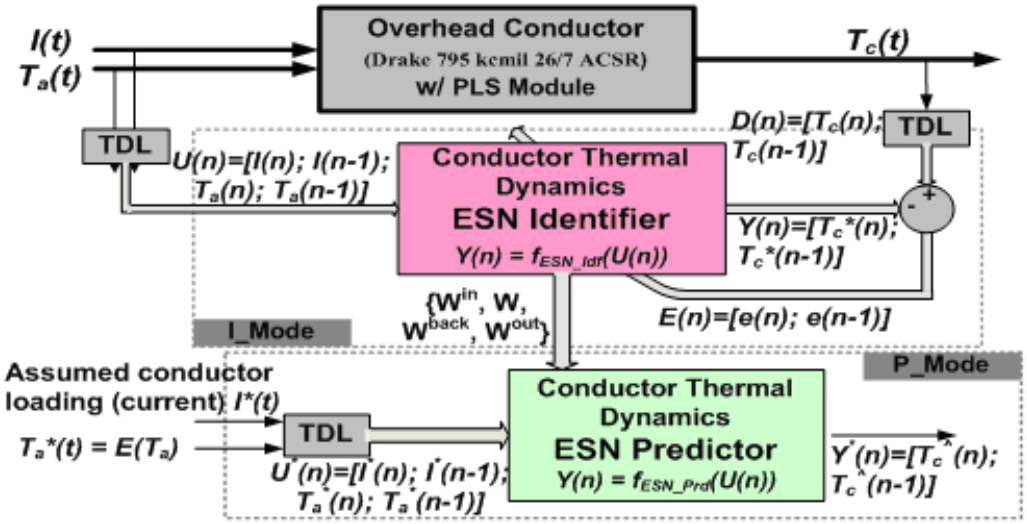

Figure 6.2. ESN based Identification/Prediction for Overhead Conductor Thermal Dynamics

ESN-Idf is used to continuously learn the conductor thermal dynamics, under various ambient weather conditions from historical data. This network learning process is normally denoted as the *Identification Mode* (I-Mode) of the ESN operation.

In typical ESN applications, once the ESN identifier has been properly trained in the *identification mode*, its weights are exported to a separate ESN model of an identical structure to the identifier (i.e., the ESN-Prd in this application), which is expected to run independently to **repeat/mimic** the dynamic behavior of the system, e.g. $f_c(.)$ in (6.1) for which it has been trained. More importantly, the ESN-Prd may often be needed to **predict** the system dynamics under a new set of inputs. This mimicking or predicting process is then denoted as the *Prediction Mode* (P-Mode) of the ESN operation.

In this application, the ESN operation in the P-Model is important, because a well-trained ESN-Prd needs to predict the conductor temperature up to 30 minutes ahead of time under a series of conductor overload conditions. The resultant predicted conductor temperature responses are in turn used to construct the I-T Thermal Limit Curve, as introduced in Section 5.1, and estimate the dynamic thermal ratings over allotted overload durations.

6.3.1 ESN-based Identification and Prediction

With reference to Figure 6.2, the ESN-Idf is driven by an input vector $U(n) = [I(n)\ I(n-1)\ T_a(n)\ T_a(n-1)]$ at time step n, and estimates two steps ahead of conductor temperature $Y(n) = [T_c^*(n)\ T_c^*(n-1)]$. The desired outputs $D(n) = [T_c(n)\ T_c(n-1)]$ are used to train the ESN to minimize the MSE as defined in (6.6).

The DR matrix size N of the ESN identifier should reflect both the length T of training data, and the difficulty of the task. A value of $N = 60$ is used initially. The model fails to identify the conductor thermal dynamics when the wind velocity is less than 5 ft/sec. As the radiation cooling dominates under low wind speed, the conductor thermal model becomes more nonlinear, which increases the identification difficulty. Therefore, an ESN with $N = 90$ internal neurons is selected in this work.

Improved identification for nonlinear systems can be obtained by using "augmented" network training and exploitation [103]. In addition to the original network states *X(n)* and inputs *U(n)*, the squares thereof are added to the network, which yields an output weight matrix W^{out} of size $L \times (2L + 2N + 1)$. Therefore the output equation is modified to

$$Y(n) = f^{out}(W^{out}[U(n)\ U(n)^2\ X(n)\ X(n)^2\ 1]) \tag{6.7}$$

The activation functions in the internal and the output layers are both selected to be sigmoid functions. The proposed ESN identifier structure is summarized in Table 6.1 as follows.

Table 6.1 PROPOSED ECHO STATE NETWORKS STRUCTURE

Input Layer	**Inner Layer**	**Feedback Layer**	**Output Layer**
K = 4	N = 90	L = 2	L = 2
$W^{in} = \{\}_{N\times K}$	$W^{in} = \{\}_{N\times N}$	$W^{back} = \{\}_{N\times L}$	$W^{out} = \{\}_{L\times(2K+2N+1)}$

The matrices $\boldsymbol{W^{in}}$, $\boldsymbol{W}$ and $\boldsymbol{W^{back}}$ should be selected cautiously to guarantee the model stability and the dynamic damping speed. A diligent choice of the spectral radius α of W is of crucial importance for the success of ESN training, as α is intimately connected to the intrinsic timescale of the dynamics of the DR state. Ref. [103] suggests the standard setting of α in a range between 0.7 and 0.98. The final value of α is manually tuned to 0.85 in this work.

The absolute size of input weights $\boldsymbol{W^{in}}$ may affect the network capability to identify system nonlinearities. Again, manual adjustment and repeated learning trials will often be required. Similar remarks hold for the absolute size of weights in $\boldsymbol{W^{back}}$. The weights of $\boldsymbol{W^{in}}$ and $\boldsymbol{W^{back}}$ are uniformly distributed on (0, 1) and (0, 0.01) respectively in this network.

6.3.2 Simulation Validation of Performance of ESN-Idf and ESN-Prd

To validate the ESN's capability to identify conductor thermal dynamics, a 795 kcmil 26/7 ACSR (Drake) conductor is evaluated as a base case. The conductor thermal model provided in IEEE standard 738 [24] is used to prepare the training data. This IEEE

standard model is simulated in the MATLAB environment. The conductor ambient conditions are listed in Appendix C.

The ESN-Idf and the IEEE thermal model are driven by input sequences *U(n)* sampled at every 6 seconds from the six-hour time-varying profiles of T_a and *I*. The output matrix $\boldsymbol{W^{out}}$ is adjusted to minimize the error between the output sequences of the ESN-Idf and the IEEE thermal model based on off-line batch learning process. For different weather conditions it is retrained to form a new $\boldsymbol{W^{out}}$. In reality, over a six-hour period, the conductor ambient weather condition can vary and the identified thermal dynamics are expected to reflect the average effects from the ambient conditions.

In order for the ESN-Idf to improve its learning capability for the conductor thermal dynamics, the pseudo-random binary signals (PRBSs) are added to the input sequences. The PRBS is a randomly generated external signal. In this work, a combination of two difference frequencies 1/60 Hz, 1/6 Hz, and 1 Hz is applied for the T_a input sequence, and a combination of three different frequencies 1/300 Hz, 1/30 Hz, and 1/5 Hz is applied for the *I* input sequence. The above frequencies are used to define the scenarios to represent hypothetical conductor current and ambient temperature variations that are close to realistic conditions. The PRBS signal magnitude is limited to $\pm 10\%$ of T_a and *I* base values. The signals are added as part of the inputs at point A in Figure 6.1.

At the same time, a small uniform white noise term $v(n)$ of size 0.001 is added at point B in Figure 6.3 to improve the stability of the trained network. Therefore, the update equation is modified to,

$$X(n) = f(W^{in} \cdot U(n) + W \cdot X(n-1) + W^{back} \cdot Y(n-1) + v(n)) \tag{6.8}$$

Note that, for output weights $\boldsymbol{W^{out}}$ update, not all the information from the initial period of time is used, because the effects from the network's arbitrary starting state need

to wash out over time. Therefore, the network states *X(n)* are stored into the state collecting matrix ***M***, and similarly, the f^{out}-inverted teacher output $(f^{out})^{-1}D(n)$ are collected into the teacher collection matrix ***Z***, only when time is larger or equal than an wash out time t_i. In this work, the washout time t_i = 10 minutes.

The network training process follows the same routine as introduced in Section 6.2.2, except for the modifications presented above for this specific application. Once the ESN-Idf is updated, the updated output weight matrixes $\boldsymbol{W^{out}}$ are exported to the ESN-Prd, which in turn operates in the P-Mode and is used to predict the conductor thermal dynamics (conductor temperature) under the present ambient weather conditions.

When this ESN-Prd is in use, T_a is set to the mean value over the training period, i.e., 6 hours for this case. The network continues from the last training network state *X(n)*, but the output weights $\boldsymbol{W^{out}}$ are fixed during this testing period. Figure 6.3 shows two typical examples of ESN-Prd responses when subjected to a step change in current from 500 A to 1200 A under various weather conditions. Figure 6.3 (a) shows the effect of wind velocity over a range from 3 to 25 ft/sec. The effect of the conductor thermal capacitance, ranging from 400 to 800 J/m-^{o}C, is depicted in Figure 6.3 (b). The thermal model provided by IEEE Std. 738 model is used for comparison purposes. The maximum test error of the predicted conductor temperature is found to be $\pm 5\%$ of its actual value.

For further validation, the ESN-Prd dynamic behavior for each value of $\boldsymbol{W^{out}}$ (for the various weather conditions) is evaluated in terms of the thermal time constant and the temperature's steady state value. With reference to the model depicted in (5.2), the time constant $\tau_{tr}(t)$ and the conductor steady state temperature $T_{c(\infty)}$ of the thermal model can be expressed by,

$$\tau_{tr}(t) = mC_p / (K_{cool} - I_f^2 \cdot K_R) \tag{6.9}$$

$$T_{c(\infty)} = (I_f^2 \cdot R_0 + K_{cool} \cdot T_a + Q_s) / (K_{cool} - I_f^2 \cdot K_R) \tag{6.10}$$

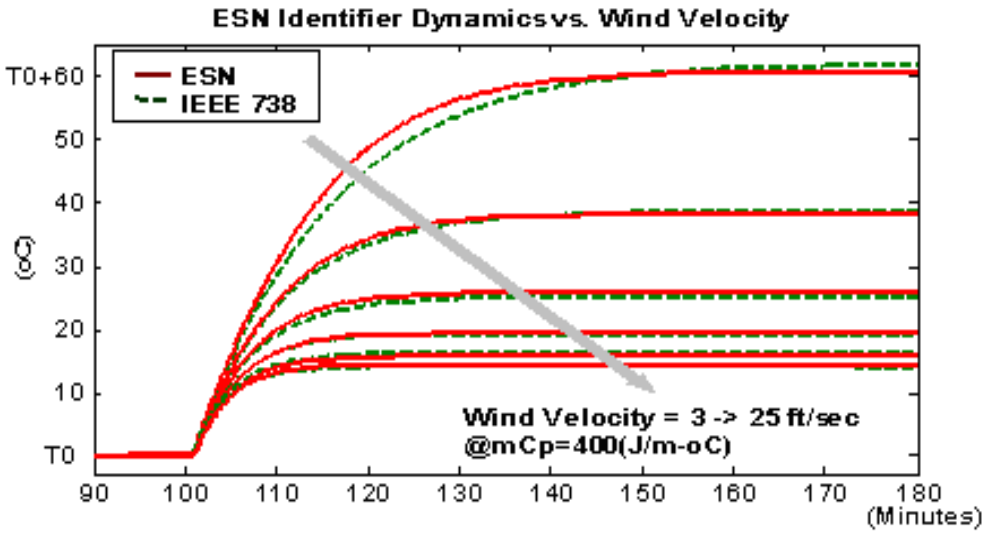

(a)

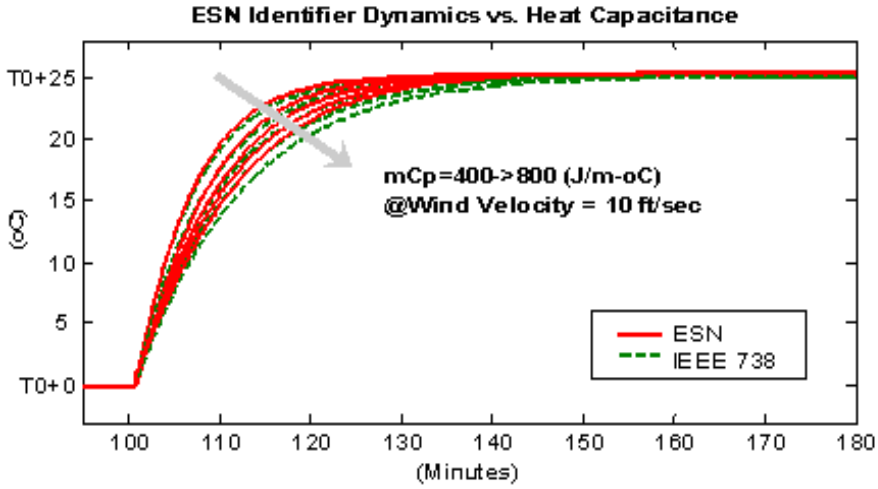

(b)

Figure 6.3. ESN step response under variant weather conditions: (a) Wind velocity; (b) Heat capacitance.

Figure 6.4 shows the ESN results compared with the analytical results based on the IEEE model. The effects of wind velocity, heat capacitance and final conductor current are studied. The parameter, which proves to be the most critical in determining $\tau_{tr}(t)$ and T_c, is the wind velocity, as shown in Figure 6.4 (a). $\tau_{tr}(t)$ is not a function of the preload

current I_i, but it is the final value I_f, which increases as the wind velocity decreases and as I_f increases. However $\tau_{tr}(t)$ is practically independent of current for moderate wind velocities above about 3 m/s (10 ft/sec) [99], as illustrated in Figure 6.4 (c). At the same time, the larger conductors with their greater thermal inertia provide for greater time constants, as depicted in Figure 6.4 (b). Similarly, the snow/rain coating around the conductor surface also increases thermal inertia, and consequently slows down the temperature response.

The comparison shows an encouraging match between the results of the IEEE and the ESN models. The ESN based thermal dynamics identifier therefore permits the correct prediction of conductor temperature ahead of time, as well as the calculation of the thermal time constant and the steady state temperature with acceptable accuracy over a wide variety of ambient weather conditions.

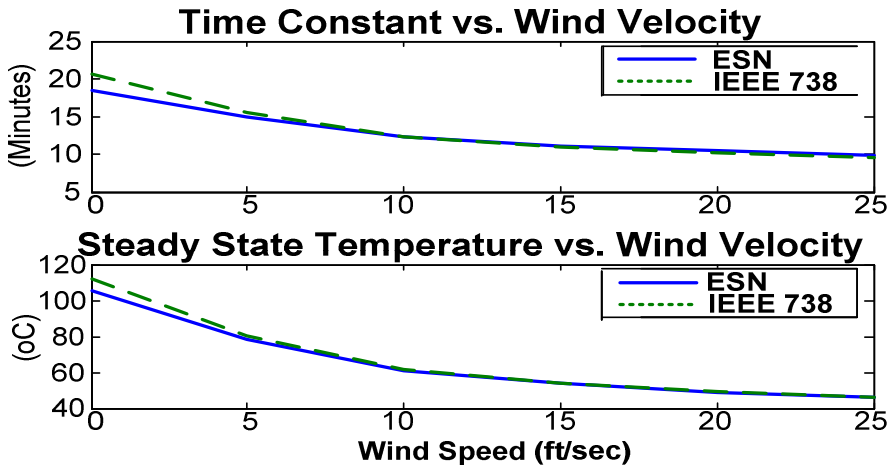

(a)

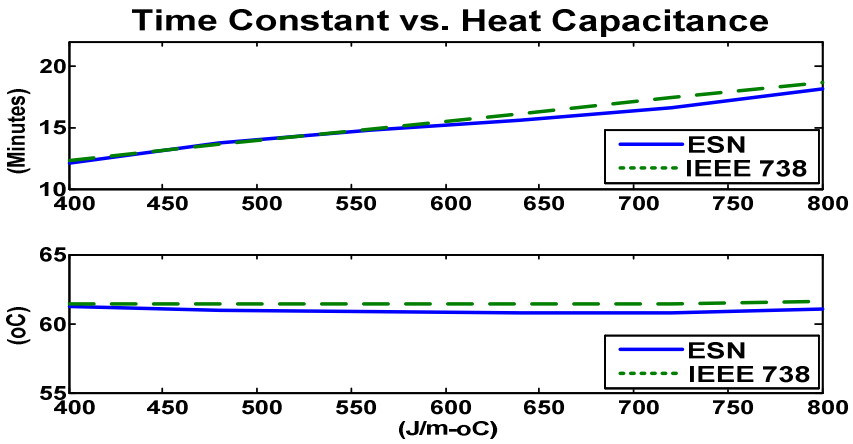

(b)

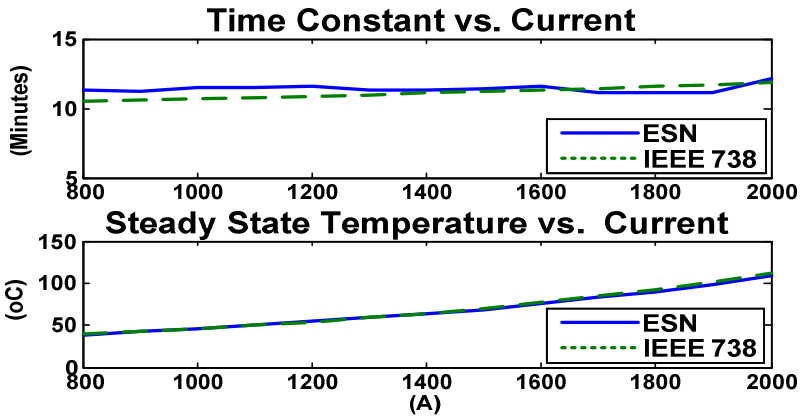

(c)

Figure 6.4. Steady state and time constant evaluation of and weather condition estimation based on ESN identifier output.

6.4 Online Adaptation of Echo State Networks

In the previous sections, the ESN-based identification for overhead conductor thermal dynamics has been conducted in an offline batch learning mode, and the capability of the ESN model to predict the complete transient behavior of the conductor temperature has been validated in the simulation environment. This section extends the research by investigating the ESN's ability to continuously adapt itself to time-varying ambient

weather conditions on a continuous base, so that the on-line updated ITLC of an overhead conductor can be obtained subjected to any variation of ambient weather conditions.

With reference to Figure 6.2, the online adaptation of the ESN model requires both of the two operation modes of ESNs, i.e., I-Mode and P-Mode as introduced in Section 6.3. Similar to the off-line batch learning process, two ESNs (but of the same structure) exist to support the ESN operating in the two modes independently, namely ESN Identifier (ESN-Idf) operating in the I-Mode and ESN Predictor (ESN-Prd) operating in P-Mode. In the online adaptation context, the ESN-Idf is continuously trained (in the I-Mode) as the training sequence data passes through the network thus to continuously **adapt** itself to any time-varying changes in the conductor thermal dynamics $f_c(.)$ caused by the weather condition variations. At any instant of time, once the ESN-Idf is updated, the most recent weights are exported to the ESN-Prd, which in turn operates in the P-Mode. To evaluate the dynamic line rating (or ITLC) on a continuous base, the ESN-Prd functions as a conductor temperature predictor driven by a set of different, assumed overload conditions of the conductor during every ESN update period.

As discussed in [103], the training of an ESN is essentially a linear regression problem. If the online adaptation of an ESN is desired, standard recursive algorithms known from adaptive linear signal processing, e.g. the Least Mean Squares (LMS) algorithm or the Recursive Least Squares (RLS) algorithm [110], can be used. This makes the ESN-based dynamic system identification an attractive solution for real-time implementation. However, online adaptation with ESNs has its unique issues and challenges, one of which is the stability issue. Especially when a well-trained ESN is expected to operate independently, the recurrent connectivity between neurons inside the network potentially amplify any small errors, thereby causing the network output to possibly diverge from its desired value. To overcome this problem, a Sliding-Window (SW) based learning algorithm is proposed for the online adaptation of the ESN in this section.

6.4.1 Issues and Challenges in Online Adaptation with ESNs

As a linear regression problem, the "linear least squares" fitting technique is the most commonly applied method to train an ESN in a batch learning mode. In the ESN context, the regression problem can be phrased as solving $\boldsymbol{W}^{out} \cdot \boldsymbol{M} = \boldsymbol{Z}$ with respect to $\boldsymbol{W}^{out}$. $\boldsymbol{M}$ $((K+N+1)\times Q)$ is denoted as the state-collection matrix consisting of all $M(k) = [U(k) \quad X(k) \quad 1]$, for $k = 1,\ldots,Q$, where Q is the size of the training sequence. $\boldsymbol{Z}$ $(L\times Q)$ is the teacher-collection matrix consisting of all $Z(k) = f_{out}^{-1}(D(k))$. Both matrices, $\boldsymbol{M}$ and $\boldsymbol{Z}$, are collected while the training data sequence, $<U(k), D(k)>$, passes through the ESN during the training period. One direct solution to $\boldsymbol{W}^{out}$ is to calculate the pseudoinverse $\boldsymbol{M}^{+}$ of $\boldsymbol{M}$, given by [111],

$$W^{out} = \boldsymbol{Z} \cdot \boldsymbol{M}^{+} \tag{6.11}$$

in order to minimize the error expressed in the mean square sense, i.e. $MSE = (\sum_{k=1}^{Q} \| \tanh^{-1} D(k) - \tanh^{-1} Y(k) \|^2) / Q$. This method exhibits high numerical stability, and has been utilized for the batch-mode training of the ESN as presented in Section 6.2.

For online adaptation with ESNs, the network training algorithm typically minimizes an error that is exponentially discounted going back in time [105],

$$MSE(n) = \sum_{k=-\infty}^{n} \lambda^{n-k} \cdot \| \tanh^{-1} D(k) - \tanh^{-1} Y(k) \|^2 \tag{6.12}$$

where $\lambda < 1$ is the forgetting factor. To minimize $MSE(n)$, for $n = 1, \ldots, \infty$, standard recursive algorithms for mean-square-error minimization, known from adaptive linear signal processing, can be applied, e.g. the Least Mean Squares (LMS) algorithm and the "Recursive Least Squares" (RLS) algorithm.

The LMS algorithm (also known as the stochastic gradient descent algorithm) with an ESN has been outlined in [111]. It is easy to implement, requires low computational complexity, and has robust performance. However, the LMS algorithm is sensitive to the eigenvalue spread (EVS, the ratio of the maximal eigenvalue to the minimal eigenvalue [110]) of the correlation matrix $\boldsymbol{R} = \boldsymbol{M} \cdot \boldsymbol{M}^T$. For the online adaptation of an ESN by LMS, a small EVS is necessary [107]. However, in this ESN application, the EVS sometimes reaches 10^{12} or even higher, which makes the use of the LMS training unfeasible.

The RLS algorithm is a second-order method and known as an alternative to LMS in many applications. Ref. [111] has derived a recursive set of equations conjoining ESNs with the RLS algorithm. Because the RLS algorithm is independent of the EVS of the correlation matrix $\boldsymbol{R}$, it is capable of tracking the signal variations on a continuous basis with high quality in convergence speed and residual error. The downside is that RLS is computationally expensive (order $O(N^2)$ instead of $O(N)$ for LMS) and notorious for numerical stability issues.

Nevertheless, through careful selection of recursive learning algorithms, a high-quality tracking performance of an ESN during the training process (I-Mode) can normally be obtained, as demonstrated by many applications [104] [112]. However, this high-quality tracking performance unfortunately does not guarantee an equally good performance when the ESN needs to run freely, i.e. to operate in the P-Mode as depicted in Section II. On the other hand, a trained ESN, when running in the P-Mode, generally tends to experience numerical stability issues (even though its DR has ESP properties). The reason can be explained as follows.

For an ESN structure shown in Figure 6.1, the network has its output *Y(n)* looped back to the network through $\boldsymbol{W}^{back}$. During the ESN training process (I-Mode), however, the network is normally trained on "one-step" signal prediction using teacher forcing (i.e. with the desired outputs *D(n),* instead of *Y(n),* fed to the network as the feedbacks). Therefore, the states of the network are updated by the following rule [103],

$$X(n) = f(\boldsymbol{W}^{in} \cdot U(n) + \boldsymbol{W} \cdot X(n-1) + \boldsymbol{W}^{back} \cdot D(n-1)) \tag{6.13}$$

instead of the rule depicted in (6.3). During the training process (in I-Mode), the network is then represented by $Y(n) = f_{ESN}(D(n-1), U(n))$ instead of by (6.5).

When the network is later run freely in its P-Mode, looping its own outputs *Y(n)* back to the network through $\boldsymbol{W}^{back}$ (as depicted in Figure 6.1) and operating based on (6.3)-(6.5), any small errors, e.g. quantization errors, get amplified through the feedback connection $\boldsymbol{W}^{back}$ potentially causing *Y(n)* to diverge from the desired *D(n)*. Even if the network has been trained for the best one-step ahead prediction with good accuracy in its I-Mode, the use of the recursive learning algorithm for the one-step ahead prediction usually causes the ESN's output to have a sharp change from one step to the next (This change is called the "sharpness"). Even though the variation can be small, it still potentially causes numerical instability when the network runs in the P-Mode. This phenomenon is demonstrated later in Section IV.B.

To smooth out the sharpness, a classical remedy is to add some noise to the states *X(n)* during the training as suggested in [103]. The research conducted for this application finds that, by introducing a semi-batch-mode learning scheme into the recursive training procedure, the network is able to learn how to reach the desired next step output *D(n)* from a neighborhood of the current state *X(n)*, and tends to improve the numerical stability of the network. Therefore, to obtain a balance between the sharpness and accuracy in the I-Mode and stability in the P-Mode of the ESN operation, a **Sliding-**

Window (SW) based algorithm is proposed for the ESN online adaptation for the conductor thermal dynamics.

6.4.2 Online Adaptation of ESN-based Conductor Thermal Dynamics Identifier

The SW-based learning algorithm is not a truly iterative process as usually required in online adaptation learning. The online learning algorithm operates on the basis of a constant length sliding window composed of Q training data pairs, $<U(k), D(k)>$, for k = 1, …, Q, sampled at every 6 seconds from the immediately preceding two-hour time-varying profiles of I, T_a and T_c. At every time instant, the oldest training data pair is discarded, and the most recent pair is added to the sliding window. The weights of the ESN, i.e. W^{out}, are updated every 5 minutes based on the latest training set in the sliding window. The system data sampling rate and the ESN updating rate are summarized in Table 6.2.

Table 6.2 SYSTEM DATA SAMPLING AND ESN UPDATING RATE

Training Data Sampling rate ΔT	6 seconds
Size of the Sliding Window *Q*	1200 samples (2 hours)
ESN (or I-T Curve) Updating Rate ΔT_{ESN}	5 minutes

During each ESN updating interval, i.e. every ΔT_{ESN} = 5 minutes, the new output matrix $\boldsymbol{W}^{out}$ can be calculated by (6.11). However, direct pseudoinverse calculations are expensive memory-wise for large state-collection matrices $\boldsymbol{M}$. This issue can be solved in the normal equation of this problem [110], and the $\boldsymbol{W}^{out}$ is then obtained by solving,

$$\boldsymbol{W}^{out} = \boldsymbol{Z} \cdot \boldsymbol{M}^{T} \cdot (\boldsymbol{M} \cdot \boldsymbol{M}^{T})^{-1} \tag{6.14}$$

Since the matrices $\boldsymbol{P} = \boldsymbol{Z} \cdot \boldsymbol{M}^T$ $(L \times (K+N+1))$ and $\boldsymbol{R} = \boldsymbol{M} \cdot \boldsymbol{M}^T$ $((K+N+1) \times (K+N+1))$ do not depend on the length of the training set, Q, they can be calculated incrementally through time while the training data passes through the ESN, given by,

$$\boldsymbol{P} = \boldsymbol{P} + Z(n) \times M(n)^T \tag{6.15}$$

$$\boldsymbol{R} = \boldsymbol{R} + M(n) \times M(n)^T \tag{6.16}$$

so that the solution complexity of (6.11) does not depend on Q any more, and the computational burden is relieved.

In this research, the ridge, or Tikhonov, regulation [113] is also applied to improve the numerical stability of (6.11), given by,

$$\boldsymbol{W}^{out} = \boldsymbol{P} \cdot (\boldsymbol{R}^T + \delta^2 \boldsymbol{I})^{-1} \tag{6.17}$$

where $\boldsymbol{I}$ $(N \times N)$ is the identity matrix and $\delta < 1$ is a regularization factor. The ridge regulation is an alternative form of adding noise to *X(n)* but with much less computation required. This weights updating rule is a highly promising solution for training the ESN with improved numerical stability but reduced computational cost. This Sliding-Window (SW) based online adaptation algorithm for the conductor thermal dynamics identification is summarized in Figure 6.5.

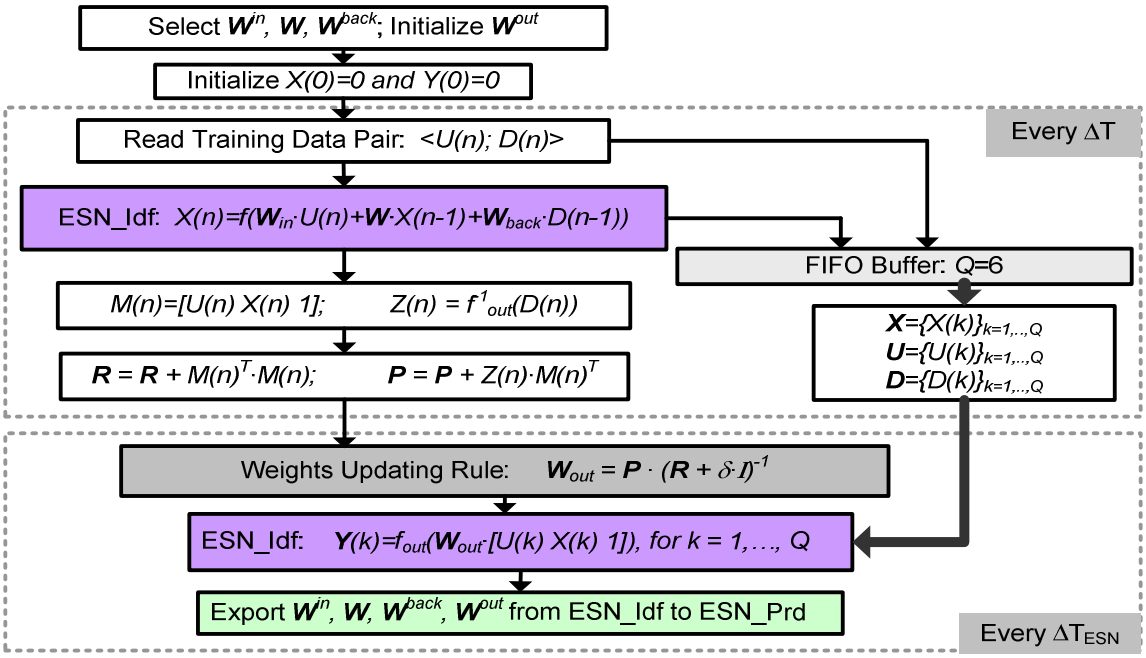

Figure 6.5. Sliding-Window (SW) based Online Adaptive Algorithm Flow Chart.

During each ESN updating interval, after the ESN-Idf is successfully updated, the most recent weight matrices are exported to the ESN-Prd that in turn functions as a **predictor** of T_c under the present ambient weather condition. In the following subsection, the performance of the online adaptation algorithm with the ESN-Idf and the ESN-Prd is validated in the simulation environment.

6.4.3 Performance Validation of the Online Adaptation of ESN-Idf/ESN-Prd

In this study, a 795 kcmil 26/7 ACSR (Drake) conductor is evaluated as the base case. The training sequence for the ESN-Idf is prepared based on the IEEE standard 738-2006 model [24]. To introduce time-varying behavior of the conductor thermal dynamics, a set of time-varying weather conditions and loading conditions of the conductor for a period of two days is prepared and depicted in Figure 6.6.

To validate the performance of ESN online adaptation algorithms for this application, two recursive learning algorithms are tested: the ESN_RLS algorithm introduced in [111],

and the proposed SW-based algorithm. To provide an objective evaluation of the algorithm performances, the Normalize Mean Square Error (NMSE) is used as follows,

$$NMSE(n) = \| Y(n) - D(n) \|^2 / \| D(n) \|^2 \tag{6.18}$$

Figure 6.7 firstly shows the tracking performance of the RLS learning algorithm. Under the weather and loading conditions of Figure 6.6, the ESN-Idf is continuously trained based on an RLS algorithm specifically derived for online adaptation of ESNs (for details see [111]). Figure 6.7 (a) compares the output of the ESN-Idf versus the actual conductor temperature. Figure 6.7 (b) depicts the NMSE as defined in (6.18). The simulation results validate the tracking performance of the ESN-RLS algorithm to signal variations with excellent quality in convergence speed and residual error (in an order of 1e-10).

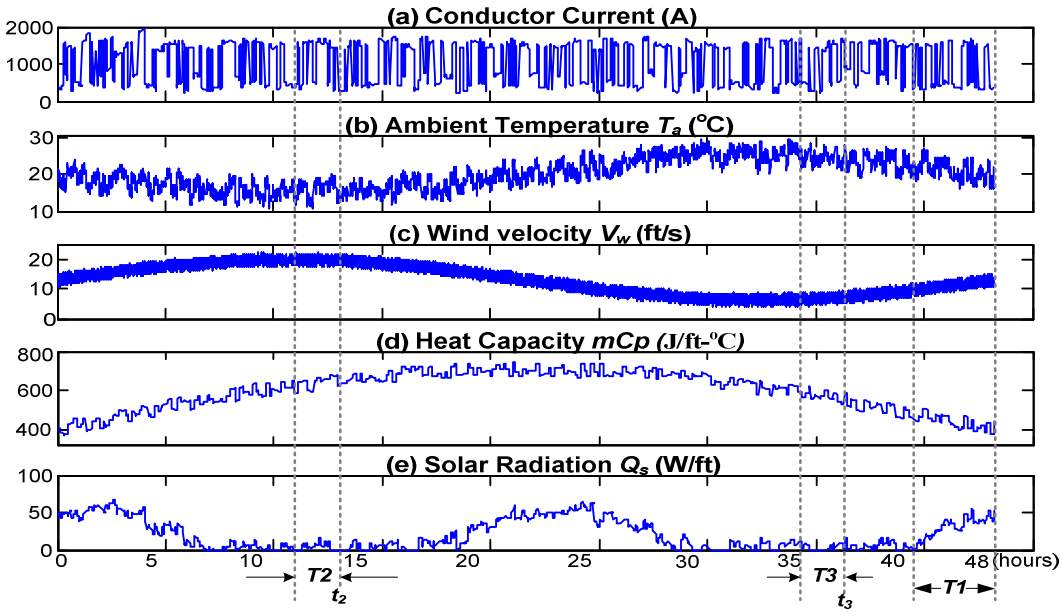

Figure 6.6. Time-varying weather and loading conditions of the conductor for two days: (a) Joule heat gain; (b) ambient temperature Ta; (c) wind velocity; (d) conductor heat capacity; (e) solar radiation.

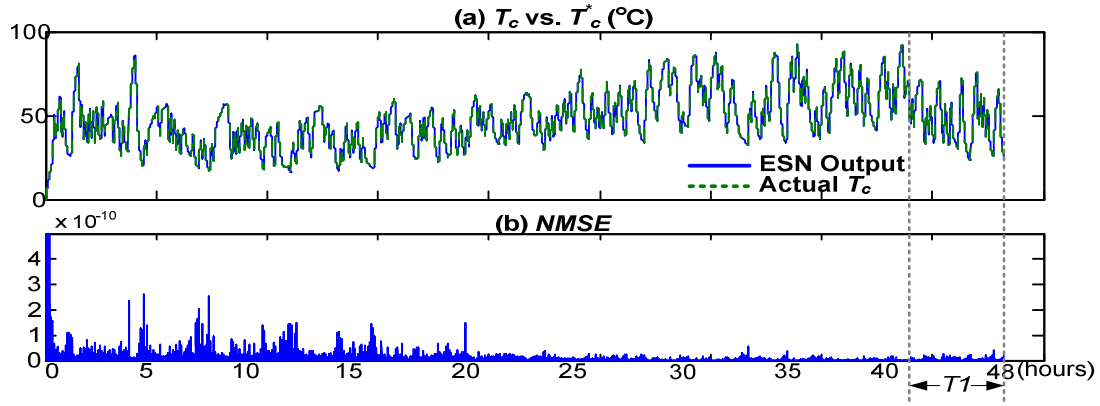

Figure 6.7. The RLS algorithm's tracking performance with ESN-Idf in I-Mode: (a) the ESN-Idf's output vs. Tc; (b) Normalized Mean Square Error (NMSE) in (6.18).

To demonstrate the performance of the ESN operation in the P-Mode, the weights of the ESN-Idf, after training on two days of data, are exported to the ESN-Prd. The ESN-Prd is then run freely (P-Mode), driven by an input sequence the same as the input sequence during the period T1 as shown in Figure 6.6 (the last six hours of the two-day training process). Figure 6.8 (a) compares the ESN-Prd's output versus the actual conductor temperature, with the NMSE depicted in Figure 6.8 (b). The well-trained ESN with the RLS algorithm unfortunately fails to repeat/mimic the conductor thermal behavior that has just been learned, when it operates independently in its P-Mode. The simulation results in Figure 6.7 and Figure 6.8 clearly indicate that, an excellent tracking performance of the network in I-Mode does not ensure the same level of performance when the network has to operate in its P-Mode.

Similar tests are conducted to evaluate the performance of the proposed SW-based learning algorithm. Under the same weather and loading conditions of Figure 6.6, the ESN-Idf is again continuously trained based on the SW-based algorithm for a duration of two days. Figure 6.9 (a) compares the ESN-Idf's output versus the actual conductor temperature, with the NMSE depicted in Figure 6.9 (b). The simulation results in Figure

6.9 indicate that, although the tracking performance of the SW algorithm is inferior to that of the ESN-RLS, it still offers fast convergence speed and low residual error (in the order of 1e-6).

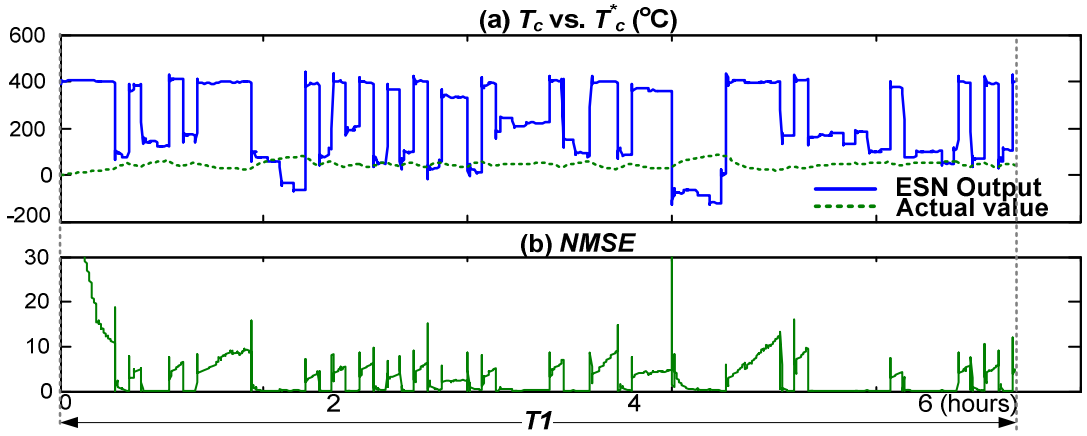

Figure 6.8. The RLS algorithm's performance with ESN-Prd in P-Mode: (a) the ESN-Prd's s output vs. Tc; (b) Normalized Mean Square Error (NMSE) in (13).

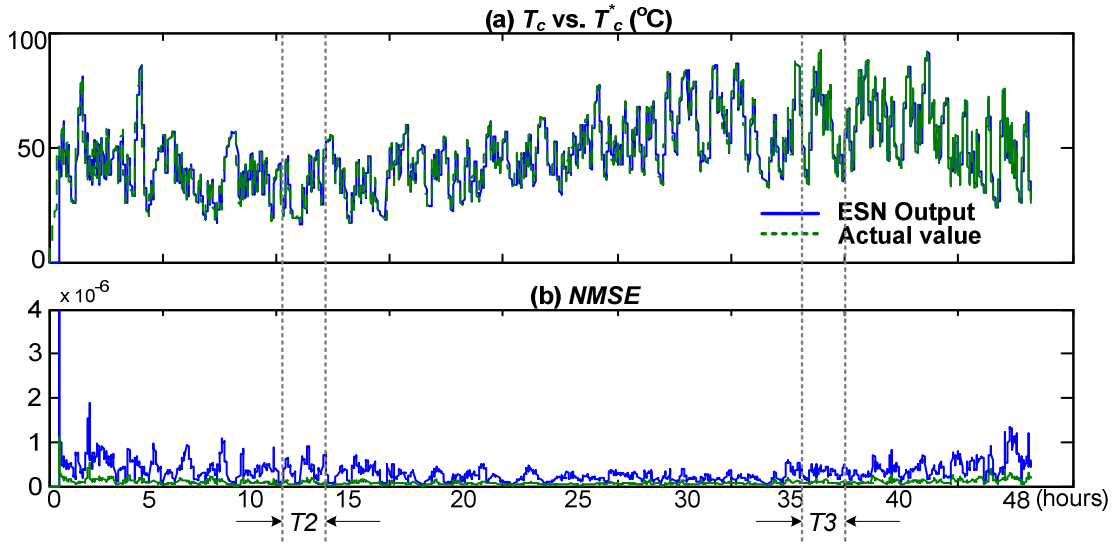

Figure 6.9. The SW algorithm's tracking performance with ESN-Idf in I-Mode: (a) the ESN-Idf's output vs. Tc; (b) Normalized Mean Square Error (NMSE) in (6.18).

Figure 6.10 demonstrates the performance of the SW training algorithm, when the ESN-Prd operates in the P-Mode. Since the ESN-Prd (or ESN-Idf) is updated every ΔT_{ESN} throughout the two-day simulation period, the ESN-Prd's performances at two network-updating instants of time are sampled, i.e. t_2 and t_3 as shown in Figure 6.6 and Figure 6.9. At the instant of time t_2, i.e. the last step of the two-hour period $T2$, the weights of the ESN-Idf (trained based on the training sequence over the period $T2$) are exported to the ESN-Prd. The ESN-Prd is then run freely (in P-Mode) driven by an input sequence the same as the input sequence for the period $T2$. A similar test is conducted when the ESN online adaptation runs through the time period $T3$. Figure 6.10 (a) compares the output of the ESN-Prd versus the actual conductor temperature during the two testing periods, with the NMSE depicted in Figure 6.10 (b). The simulation results validate that, with the SW learning algorithm, the continuously updated ESN-Prd manages to mimic the conductor thermal behavior with quite high accuracy under various ambient conditions, and the stability of the network operating in its P-Mode is also retained throughout the adaptation process.

Besides, it is observed from Figure 6.10 that, during each testing period, the initial error between the network's output and the desired output resulting from the effects of the initial network states eventually washes out over time. The results indicate that, given the echo state property, the network converges asymptotically to a state dependent only on the input history.

The simulation results in Figure 6.9 and Figure 6.10 show that, the proposed SW algorithm offers a satisfactory performance of the ESN operating in both I-Mode and P-Mode. The stability of the ESN operating in P-Mode ensures that the continuously updated ESN-Prd functions as a conductor-temperature predictor under time-varying weather conditions and in turn helps evaluate the dynamic thermal rating of the line.

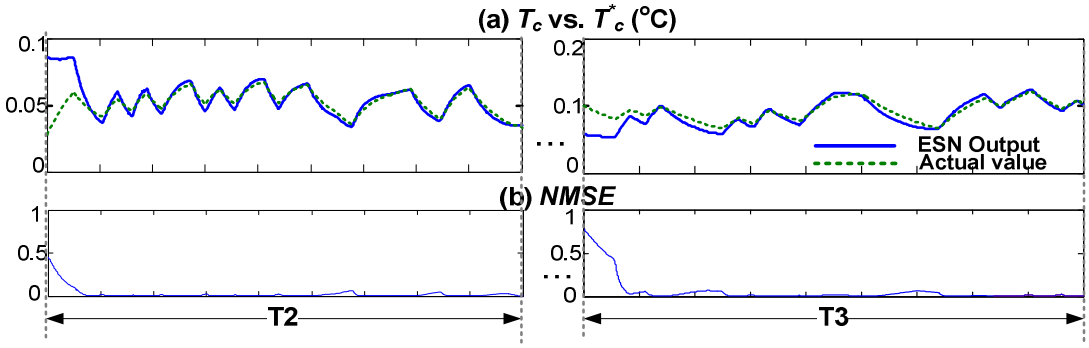

Figure 6.10. The SW algorithm's performance with ESN-Prd in P-Mode: (a) the ESN-Prd's s output vs. Tc; (b) Normalized Mean Square Error (NMSE) in (6.18).

6.5 Real-Time Dynamic Thermal Rating Evaluation and On-line Update of I-T Thermal Limit Curve

This section presents the procedure to obtain the continuously updated I-T Thermal Limit Curve, with help from the online adaptive ESN-Prd.

6.5.1 Overhead Power Line I-T Thermal Limit Curve

This section describes how the ESN-Prd is utilized to help the operator determine the RDTR (I-T Thermal Limit curve) of the line under certain weather conditions. An example, shown in Figure 6.11, depicts the performance of the ESN-Prd to predict T_c up to half an hour ahead of time for a series of step increases in current. The ambient weather conditions are shown in Figure 6.11. The preload current I_i is 500 A and T_c is 95°C at time t_0=*101* minutes. The set of thirteen curves in Figure 6.11 illustrate how the T_c would rise if the 500 A were to be increased to thirteen different final values varying from 800 A to 2000 A for I_f. The oblique arrow across the curves indicates direction of higher final current values.

In this work, the maximum allowable conductor temperature T_{cMax} is defined to be 110 °C. Under each of the thirteen overload conditions, the intersection between the ESN

step response and T_{cMax} determine the duration for which the conductor could operate before reaching its maximum temperature. The relation of the overload current to the overload duration forms an I-T Thermal Limit curve given in Figure 6.12. For instance, the point A, in both Figure 6.11 and Figure 6.12, tells the operator that the current in this line could be increased from the present 500 A to 1300 A for a duration of 5 minutes before the maximum allowable temperature T_{cMax} would be reached.

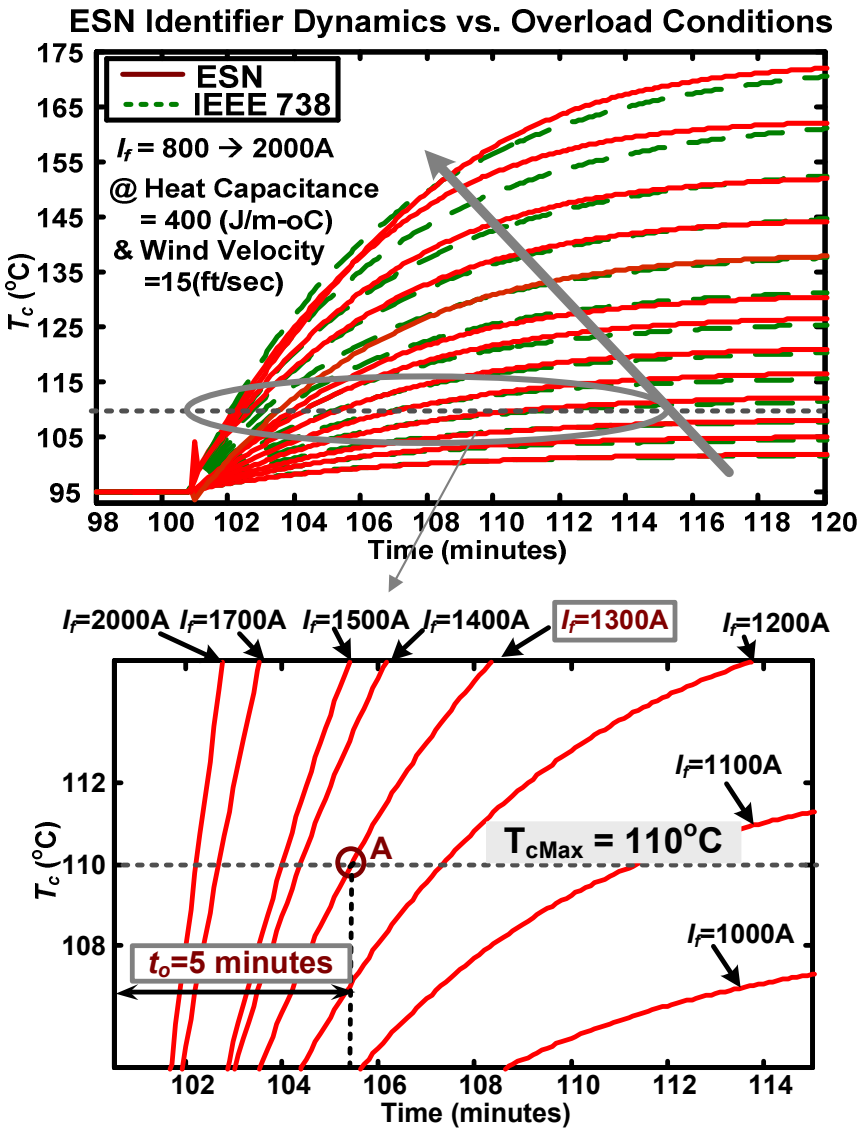

Figure 6.11. ESN identifier behaviors under various overload conditions.

6.5.2 Online Adaptation of I-T Thermal Limit Curve

In the online adaptation scenario, during every ESN updating interval, i.e. every ΔT_{ESN}, a similar procedure is repeated. Figure 6.13 summarizes the procedure, where an I-T thermal limit curve is generated based on the latest updated ESN-Prd.

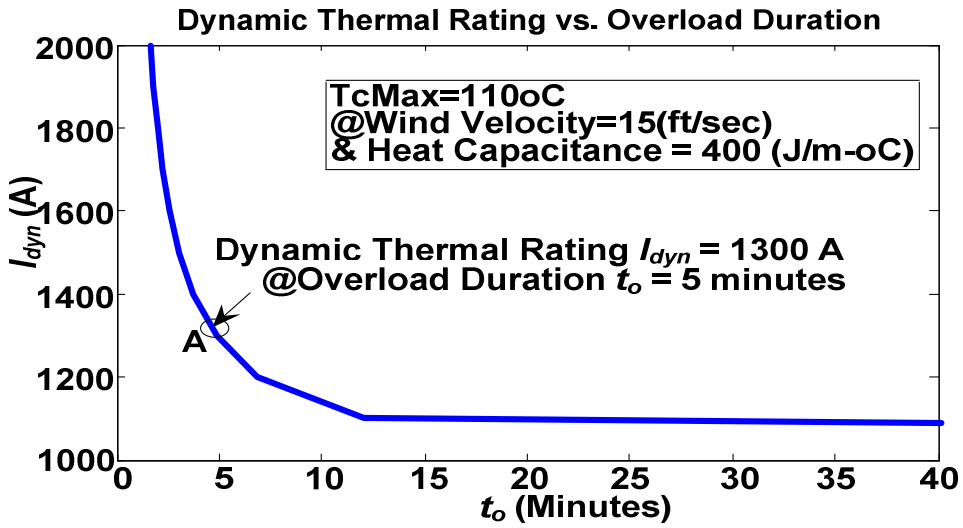

Figure 6.12. I-T Thermal Limit curve of one line segment

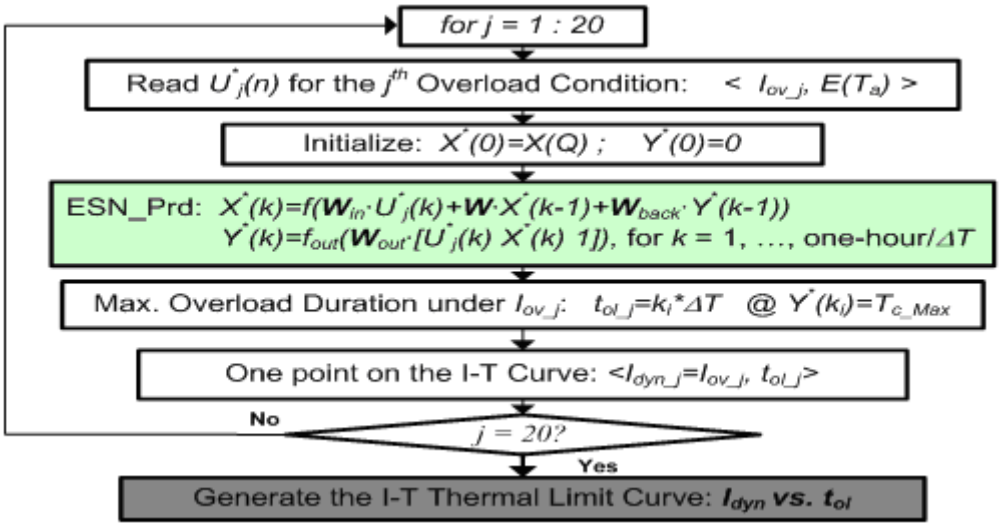

Figure 6.13. Flow Chart of Online Updating of the I-T Thermal Limit Curve.

During each network updating period, after the ESN-Prd is updated, the predictor network is run in its P-Mode, from the state of the last training step driven by 20 overload currents, i.e. $I_{dyn\_j} = 400 + 100 \cdot (j - 1)$, for j = 1, …, 20. These 20 currents represent a set of overload conditions ranging from 400 A to 2300 A (with increments of 100 A), which sufficiently cover the overload conditions of interests with enough resolution in this example. The maximum allowable overload duration t_{ol_j} under the jth overload condition I_{dyn_j}, for which the conductor can operate before its temperature reaches the maximum allowable value (T_{cMax} = 90 ^{o}C), is then determined by the output of the ESN-Prd (i.e. the predicted conductor temperature). The resultant twenty pairs of information, $<I_{dyn\_j}, t_{ol\_j}>$, then form the I-T thermal limit curve under the present weather conditions, which is updated every ΔT_{ESN} = 5 minutes.

Figure 6.14 depicts how the I-T thermal limit curve is updated continuously through time based on the weather and loading conditions as depicted in Figure 6.6. For demonstration purposes, the examples shown in the figure are the I-T curves sampled every 5 hours. The I-T curve is then sent from the local PLS module to a control center providing the operator with an effective guideline to determine the maximum allowable short term overload capacity under the present ambient conditions for the local line segment where the PLS module is mounted.

Of course, for a long power line, the I-T curves from all the PLS modules have to be considered, since each one represents the safe operating margin of each line segment. A composite 'worst case' I-T capacity (CWIT) curve can thus be obtained by superimposing the I-T curves of all individual line segments [10]. An example of a CWIT curve as a result of two line segments under different weather conditions is shown in Figure 6.15. A similar process can be applied for a line with multiple segments. This composite I-T curve therefore provides the operator an ongoing real time estimation of the 'worst case' contingency capacity for the line, factoring in conditions over the entire

length of the line, and most importantly, it is continuously updated in the presence of time varying ambient weather conditions.

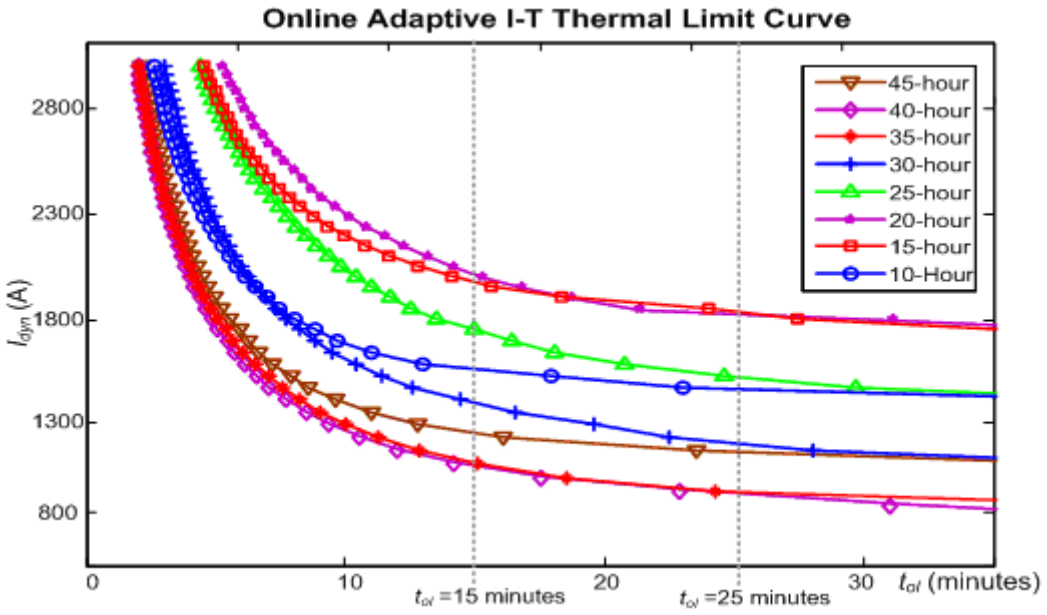

Figure 6.14. I-T thermal limit curve updating through time

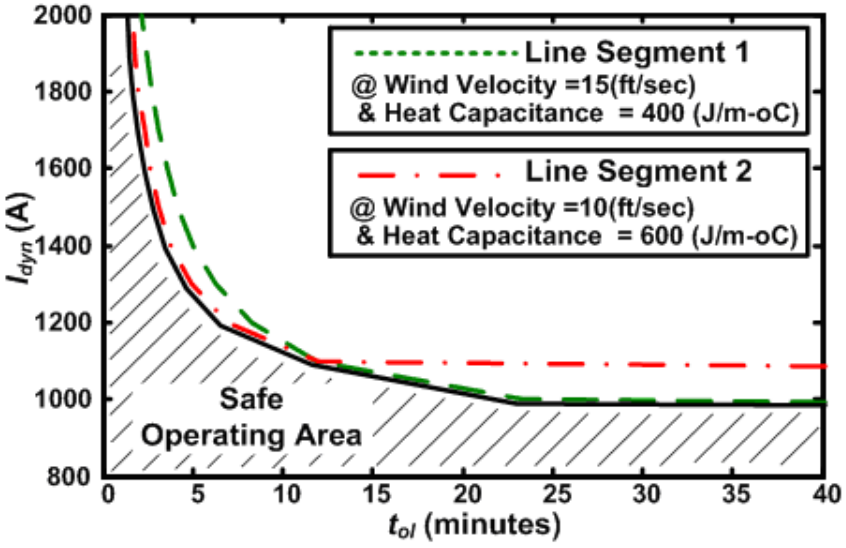

Figure 6.15. Dynamic thermal rating I-T curve for multiple line segments

6.5.3 Real-time Thermal Rating over a Pre-allotted Overload Duration

If the power utility wants to see a continuous profile of the RDTR over the duration of an overload, the information can be obtained with help from the continuously updated I-T curve, e.g. the I-T curves shown in Figure 6.14. Figure 6.16 (a) shows the RDTR over an overload duration of 25 minutes, $I_{dyn@25minutes}$, under the same conditions as shown in Figure 6.6 for two days. Similarly, Figure 6.16 (b) shows the dynamic thermal rating over an overload duration of 15 minutes, $I_{dyn@15minutes}$. For comparison purposes, the corresponding dynamic thermal ratings based on the IEEE std. 738 model are also shown in the figure. The simulation results show an encouraging agreement of these two rating methods.

The grey solid lines in both Figure 6.16 (a) and (b) represent the Real-time Steady State Thermal Rating (RSTR), I_{RS}, without taking the thermal inertia of the conductor into account. Figure 11 also depicts that the conventional Static Steady State Thermal Rating (SSTR), I_{SS} = 780 A (grey dotted line), determined by a set of conservative weather parameters (i.e. T_a = 40 ^{o}C; V_w = 2.1 ft/s; Q_s = 100 W/ft^2).

The results in Figure 6.16 clearly indicate that, including the real-time weather conditions, the actual steady state thermal capacity (RSTR) of the line segment is higher than the rating determined by the SSTR for most of the time. During favorable weather conditions, e.g. during the simulation period from 10 to 15 hours, when the wind speed is high, the ambient temperature is low, and the solar radiation is almost zero, as indicated in Figure 6.6; the RSTR even doubles the value defined by the conventional rating (i.e. SSTR). If the short-term (dynamic) thermal capacity is considered, the increment of the available line capacity is even more obvious. Comparing $I_{dyn@25minutes}$ to $I_{dyn@15minutes}$ in Figure 6.16, reveals that the shorter the overload duration, the more the maximum short-time overload current is allowed to flow through the conductor. This additional short-term capacity of the conductor is especially meaningful, when an emergency happens and the utility needs to temporally overload a particular line for a short duration. This short-

time safe operating margin of a line can help the operator make an optimized load management decision and utilize the lines more effectively.

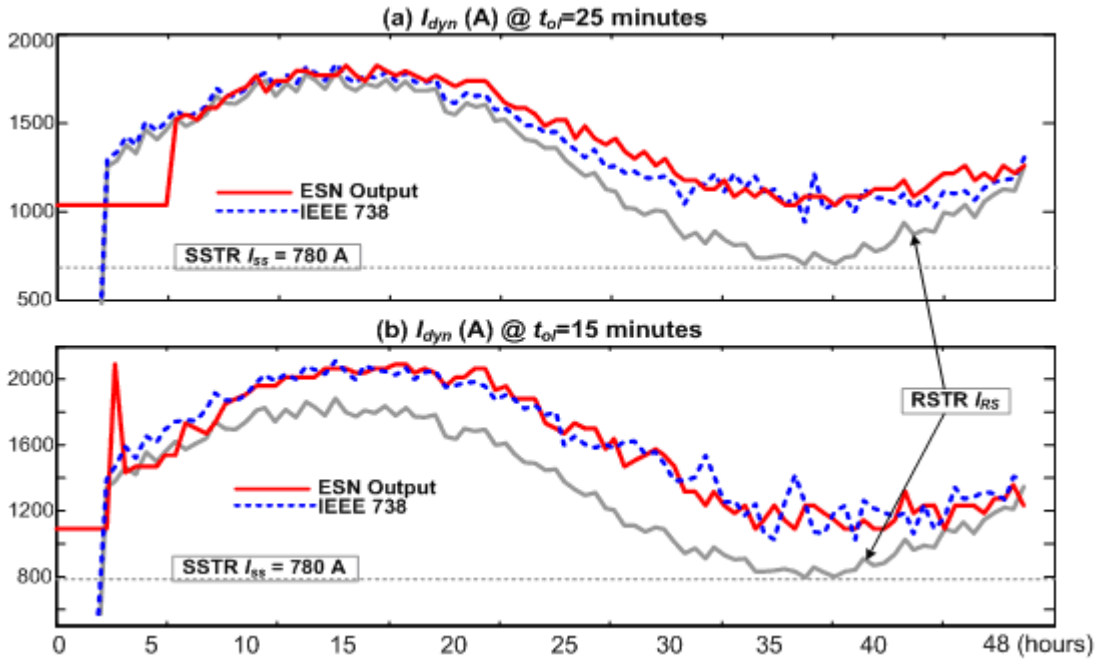

Figure 6.16. Real-time dynamic thermal rating over an allotted overload duration: (a) tol = 20 minutes; (b) tol = 10 minutes.

From 10 to 15 hours in Figure 6.16 (a), the dynamic rating $I_{dyn@25minutes}$ appears to be almost equal to its steady state value, i.e. I_{RS}. This coincides with a period of time in Figure 6.6 when the wind speed is high, the ambient temperature is low, and the solar radiation is almost zero; the conductor therefore has high heat-removal capability (i.e. small thermal resistance). Also during this period the time constant of the conductor thermal dynamics is only about 15 minutes, so that the conductor temperature almost reaches its steady state at 25 minutes after the conductor is overloaded, and $I_{dyn@25minutes}$ is therefore close to the steady state rating I_{RS}. On the other hand, during the period from 35 to 40 hours when the wind speed is low and the ambient temperature is high, the conductor has low heat-removal capability (i.e. high thermal resistance). The time

constant of the thermal dynamics therefore increases to around 30 minutes because of the increased thermal inertia. Since it takes longer than 25 minutes for the conductor to reach its steady state value, the conductor allows more current to flow temporarily than that determined by the steady state rating I_{RS}.

6.6 Experimental Validation

The performance of the ESN online adaptation has also been validated in a laboratory environment. A laboratory Power Line Sensor Network (PLSN), including a prototype Power Line Sensor (PLS) module, has been set up in the Intelligent Power Infrastructure Consortium (IPIC) lab at the Georgia Institute of Technology. A 795 kcmil 26/7 ACSR (Drake) conductor has been evaluated as the base case. Figure 6.17 (a) shows the experimental test set-up for the thermal testing of the Drake conductor. The set-up is powered through a 0-480 V feeder of controlled voltage. A step-down transformer, with a turns ratio of 10:1, is used to provide increased current on the secondary side. The ASCR Drake conductor closes the loop on the secondary with an inductive load of 120 μH connected in series, and the system is capable of delivering up to 1500 A of continuous current through the conductor. The prototype PLS module is clamped around the ASCR Drake conductor as shown in Figure 6.17 (b) (Chapter 9 provides more details on the PLS module functionalities).

Figure 6.18 shows a set of time-varying loading conditions of the conductor, wind speed, ambient temperature and the conductor temperature for a period of 6 hours. To introduce the time-varying weather conditions, a wind-tunnel has been built to generate wind passing across the conductor with varying velocities, ranging from 3 ft/s to 9 ft/s. The ESN-Idf is then continuously trained based on the proposed SW-based learning algorithm through time.

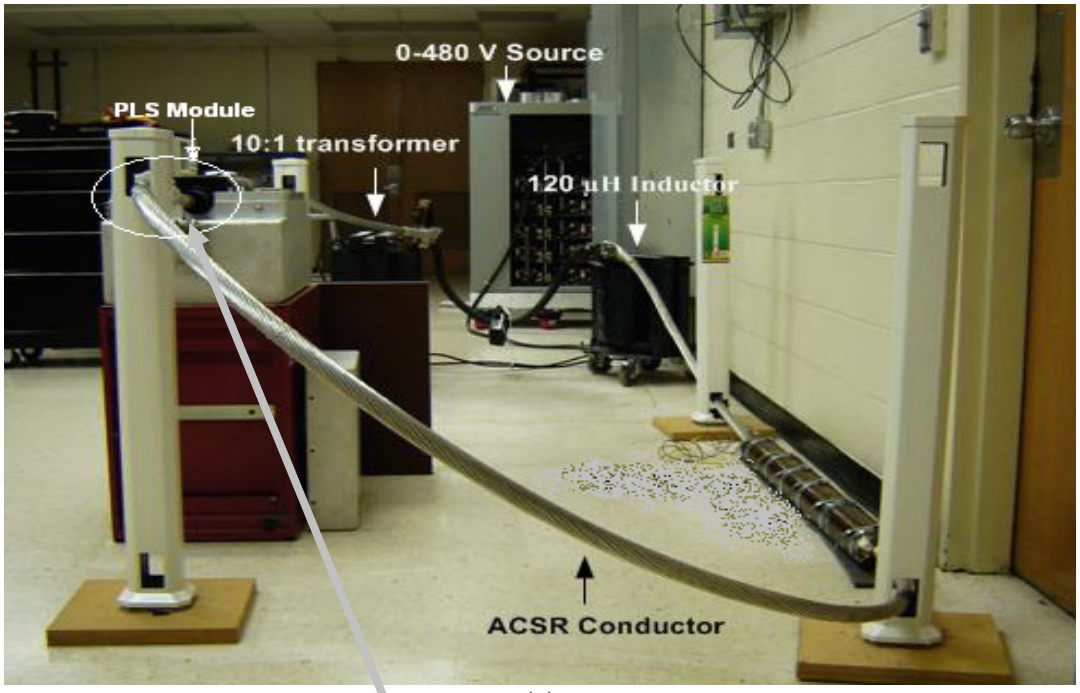

(a)

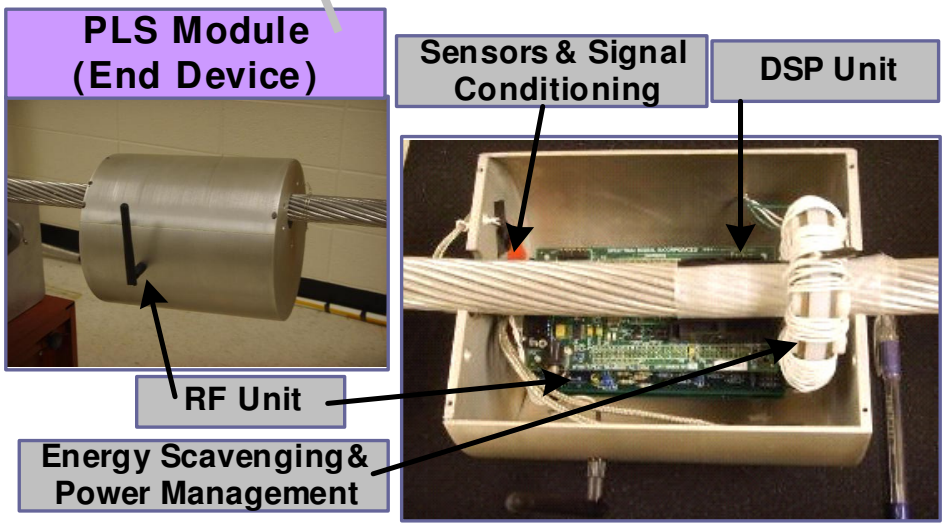

(b)

Figure 6.17. IPIC Lab set-up for experimental testing: (a) 795 kcmil 26/7 ACSR (Drake) conductor experimental test set-up; (b) Prototype PLS module.

Figure 6.19 shows how the I-T thermal limit curve is updated continuously through time based on the weather and loading conditions as depicted in Figure 6.18. For demonstration purposes, the examples shown in the figure are the curves as updated every half hour. The I-T curve is continuously sent from the local PLS module to a

control center providing the operator with an effective guideline to determine the maximum allowable short term overload capacity under the latest ambient conditions for the line segment where the PLS module is mounted.

Figure 6.20 depicts two continuous profiles of the Real-time Dynamic Thermal Rating (RDTR), I_{dyn}, over an overload duration of 10 minutes and 20 minutes. Similar to simulation results, the comparison of $I_{dyn@20minutes}$ to $I_{dyn@10minutes}$ demonstrates that the shorter the overload duration, the more the maximum allowable short-term overload current is allowed to flow through the conductor in the laboratory environment.

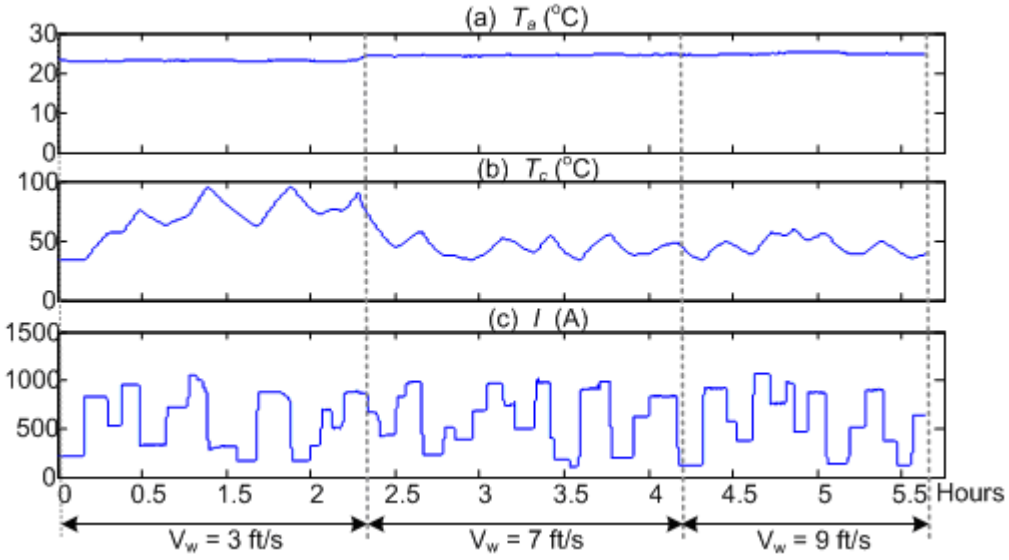

Figure 6.18. Time-varying weather and loading conditions of the conductor for two days: (a) ambient temperature Ta; (b) conductor temperature; (c) conductor current.

The experimental results validate that the ESN model is able to identify the conductor thermal dynamics, and adapt itself to time-varying ambient weather conditions. The experimental results show that the proposed ESN-based method can help evaluate the safe operating margin (thermal rating) of a line segment where the PLS module is mounted under the present ambient condition on a continuous base. The low cost solution of the proposed PLSN makes the widespread and distributed deployment of such PLS

modules feasible. Collaborating the safe operating margin from all PLS modules along a power line, the operator can obtain the accurate operational margin, factoring in conditions over the entire length of the line, down to a granularity of one span. This helps the operator make an optimized load management decision and to utilize the lines (assets) more effectively, particularly during emergency conditions.

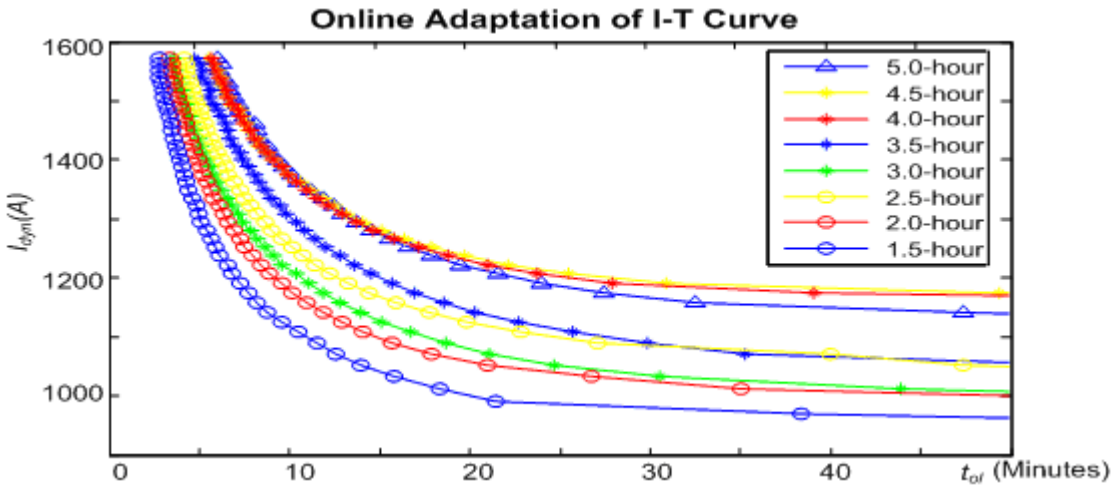

Figure 6.19. I-T thermal limit curve updating through time

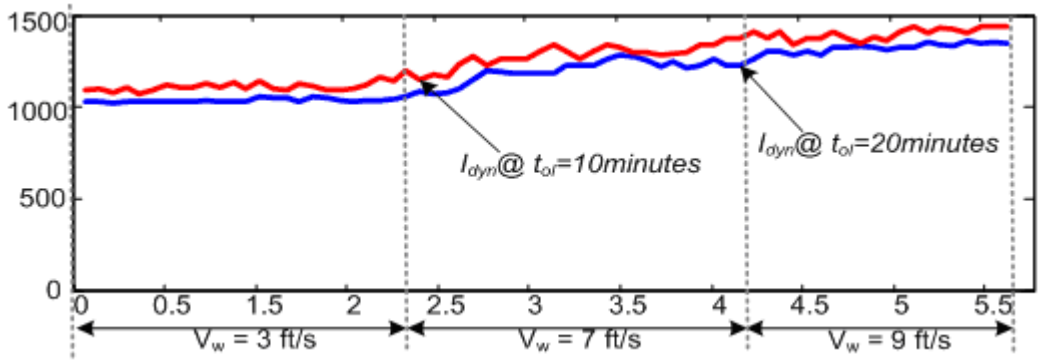

Figure 6.20. Real-time dynamic thermal rating over an allotted overload duration: (a) tol = 20 minutes; (b) tol = 10 minutes.

6.7 Chapter Summary

This chapter has presented a novel and simple method to provide the Real-time Dynamic Thermal Rating (RDTR) evaluation of an overhead power line down to the 'per span' granularity. An Echo State Network (ESN) model has been proposed to learn the overhead conductor thermal dynamics in real time, and in turn to predict the conductor temperature up to 40 minutes ahead of time. In this way, the direct complex and time consuming traditional IEEE recommended way of calculating the conductor temperature and evaluating the RDTR is avoided. Moreover, this chapter has also validated the ESN's capability to adapt itself to **changes** in ambient weather conditions on a **continuous base**. A Sliding Window (SW)-based online adaptation algorithm has been proposed to ensure the stability of the ESN model in the online adaptation context. The online ESN-based adaptive identification of the conductor thermal dynamics has been validated in both the simulation and experimental environment. The online adaptation of the ESN-based temperature predictor has also been demonstrated as a useful tool to help evaluate the dynamic thermal rating of a line segment in real-time.

As the second major potential application of the proposed Power Line Sensor Network (PLSN), the function of the Power Line Sensor (PLS) module to monitor and characterize the electric field in the vicinity of an overhead power line is presented in the following Chapter 7.

CHAPTER 7

POWER LINE VICINITY MONITORING VIA ELECTRIC FIELD DETECTION

Apart from investigating the capability of the proposed Power Line Sensor Network (PLSN) to help evaluate the real-time thermal rating of an overhead power line as introduced in Chapters 5 and 6, the PLSN concept is also proposed to conduct power line vicinity monitoring via detecting and analyzing Electromagnetic (EM) signatures around overhead conductors.

This chapter presents the function of the PLS module for power line vicinity monitoring via electric field (E-field) analysis. A novel Multiple Displacement Current Sensor (mDCS), as a part of the PLS module, is proposed to capture the spatial mapping of the E-field distribution around an overhead conductor, thus to sense the presence of incipient insulation failure between power conductors to ground, and/or to other nearby conducting objects.

In stead of considering total induced equivalent electric charge, this research considers the distribution of the electric charge density induced on the mDCS surface. A new concept of Distributed Capacitance Density (D_cap) is proposed, and a space-phasor model of the conductor electric field (E-field) is developed in a 3-Φ (3-phase) overhead power line system. A DQ-axis decomposition technique is applied to the E-field space-phasor, and thus to separate the capacitive coupling effects between the conductor, where the mDCS is mounted, and other adjacent conducting objects in different directions. The decomposed DQ-axis components enable independent measurement of conductor-to-ground clearance and overhead conductor voltage.

Simulation results are presented to validate the proposed idea. An experimental test setup is built to prove the feasibility of measuring the conductor E-field displacement

current variations caused by any changes in either conductor-to-ground or overhead conduct voltage.

7.1 Dielectric Coupling between Overhead Conductors to Ground

Overhead power lines are suspended above the ground, and the line conductors are separated from each other and from ground by air, which is a dielectric. Thus there is dielectric (capacitive) coupling between line conductors and ground. Even though the capacitive current (displacement current) from conductor to conductor and conductor to ground is negligible in comparison to the total 60 Hz load current in lines, a good understanding of the dielectric circuit around conductors has drawn great interest for decades for a comprehensive study of the electrical environment in the vicinity of overhead power lines [114].

In an overhead power line system, the distance between phase conductors is normally much larger than the diameter of the phase conductors themselves. Therefore, the conventional E-field analysis assumes that, the electric charge induced on each conductor is **uniformly distributed** on its surface, and only the total equivalent charge induced on each conductor is considered, while the location of the charge is assumed to be at the mean center of the conductor.

If an overhead power line system is assumed to have *n* conductors, including line conductors, overhead neutral/ground wires (OHGW), the earth, and other vicinity conducting objects such as vegetation nearby, the total induced electric charge on conductor 1 (any conductor in the system) can be expressed [115] by,

$$q_1(t) = \sum_{j=2}^{n} C_{1j}(t) \cdot v_{1j}(t) \tag{7.1}$$

where $v_{1j}(t)$ is the voltage difference between conductor 1 and any adjacent conductor j, for $j = 1, \ldots, n$. C_{1j} represents the mutual capacitance between conductor 1 and conductor j, which is a function of the distance between conductor 1 and the other conductor; if the geometry configuration of the power line system remains unchanged, i.e., C_{1j} is constant, the induced charge on conductor 1 (or E-field around conductor 1) is a function of only conductor voltages. The assumption of unchanged line geometry configuration has been widely assumed, when an overhead conductor E-field is detected to measure overhead conductor voltage [116].

However, for an overhead power line system, geometry variations around line conductors are not uncommon. The gradual intrusion of tree limbs to conductors and galloping conductors have been reported to happen frequently. Besides, conductor steel cores can overheat in conditions of peak electrical demand, causing the conductor to stretch and sag below acceptable ground clearance. All these phenomena also change the amount of charge induced on a conductor, and alter the electric field intensity around that conductor. Therefore, if the E-field around an overhead conductor is analyzed based only on (7.1), it is difficult to decouple the effects on the E-field from the conductor voltage and line geometry variations. This fact prevents either an accurate measurement of conductor voltage, or a reasonable assessment of the vicinity environment of the line to detect the presence of possible failures along the line.

In this research, the E-field around an overhead conductor is no longer analyzed based on the assumption that the electric charge induced on the conductor surface is uniformly distributed. The effects from adjacent conductors in different directions on the E-field spatial distribution are also included in the analysis. In another word, not only is the total equivalent charge induced on a conductor considered, but the distribution of the surface charge density around the conductor is also analyzed.

To capture the spatial mapping of the E-field distribution around a line conductor, a novel Multiple-Displacement-Current-Sensor (mDCS) scheme, as a part of the PLS module, is proposed in this work. The analysis of the E-field spatial mapping enables the separation of the capacitive effects between the conductor, where the mDCS is mounted, and its adjacent conducting objects in different directions, and thus to allow independent measurements of conductor voltage and line geometry variations.

7.2 Multiple Displacement Current Sensor (mDCS) Scheme

Figure 7.1 shows the cross-section view of a 3-Φ overhead power line system, where a PLS module is clamped around the phase C conductor. The PLS module metallic housing is assumed to be a cylindrical shape and coaxially around conductor C. The proposed mDCS consists of two coaxial, metallic cylinders separated by a layer of dielectric material. The PLS housing is used as the mDCS inner layer. The outer layer consists of six metallic arc plates 60° apart from one another, which are clamped together around the dielectric material and form the other cylinder. As shown in Figure 7.1, with this configuration, six capacitors C_i, for i = 1,…, 6, are formed between the PLS module housing and the mDCS outer layer.

Table 7.1 summarizes the proposed mDCS dimension with the prototype PLS module as the platform.

Table 7.1 PROPOSED MDCS DIMENSION

Diameter of the cylinder housing	0.3 meter
Length of the sensor	1 meter
Surface area of each sensor capacitor S_i	$\frac{\pi D_{sr}}{6} = 0.157\ m^2$
Material of the housing	Aluminum
Thickness of the dielectric material	2 mm
Material of the dielectric	Relative permittivity = 2~6 (Plastic material)

The PLS housing is electrically connected to conductor C; therefore the inner layer of the mDCS has the same potential as conductor C. The induced electric charge on the mDCS surface is thus affected in the same way as the induced charge on conductor C is by the conductor voltage and the line vicinity environments, such as the conditions of conductor separation and conductor-to-ground clearance, and proximity of tree limbs, etc.

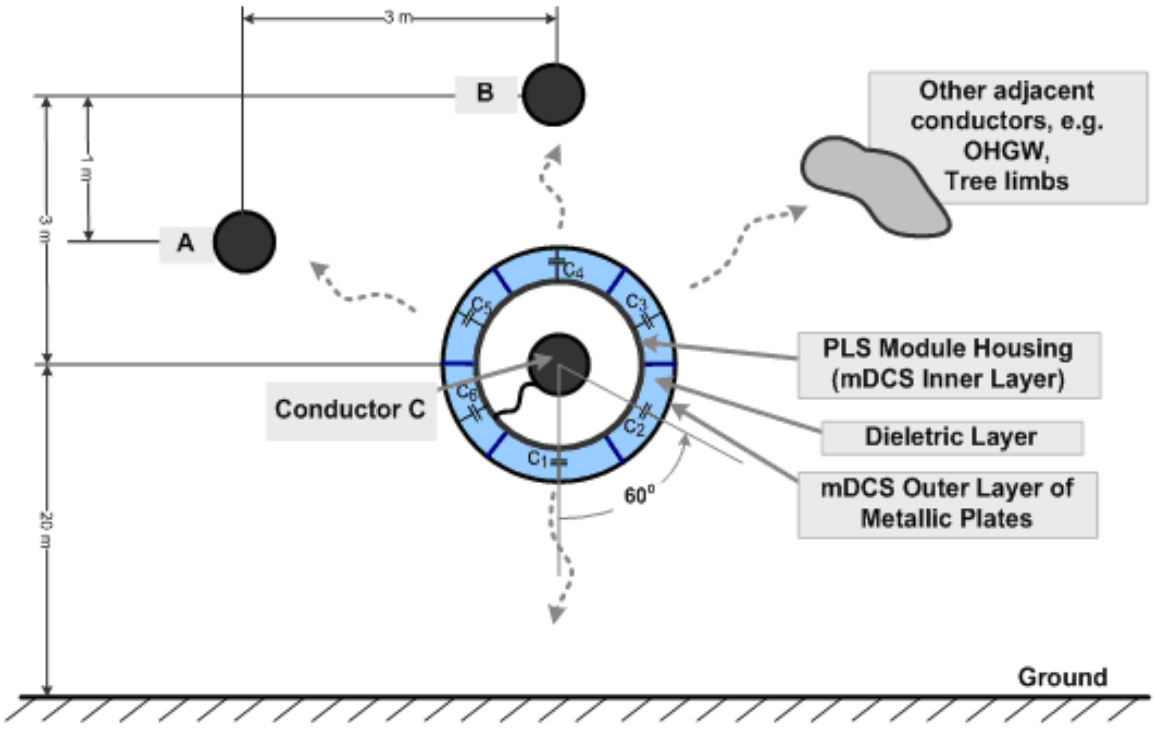

Figure 7.1. Multiple Displacement Sensor (mDCS) as a part of the PLS Module mounted around a Overhead Conductor

By measuring the six displacement currents $i_{d\_i}(t)$ flowing through the mDCS's six capacitors C_i, for i = 1~6, the distribution of the electric charge density induced on the mDCS surface can be captured in real time. In this application, the success of this proposed method highly relies on the accuracy and sensitivity of the displacement current measurement subject to the line geometry variation. In Section 7.6, the feasibility of

measuring the displacement current in a scale-down single-phase 60 Hz AC system is validated in the laboratory environment.

It is well known that, displacement current results from a time-varying electric flux density $\boldsymbol{D}$ [115]. If $\boldsymbol{D}_i$ is the average electric flux density on the metallic surface of capacitor C_i, the total displacement current crossing the capacitor is $i_{d\_i}(t) = (\partial \boldsymbol{D_i} / \partial t) \cdot S_i$, where S_i is the metallic arc surface area of C_i. On a metallic surface, the electric flux leaves the conductor in a direction normal to the surface, and the value of electric flux density is numerically equal to the surface charge density, i.e. $\boldsymbol{D_i} = \rho_i = \varepsilon_0 \cdot |\boldsymbol{E_i}|$. $\varepsilon_0 = (1/36\pi) \times 10^{-9} F/m$ is the permittivity of air. The magnitude of the electric field intensity vector $\boldsymbol{E_i}$ on the metallic plate surface of C_i can then be expressed by,

$$|\boldsymbol{E}_i(t)| = \rho_i(t)/\varepsilon_0 = \int_0^t i_{d\_i}(t) \cdot dt / (\varepsilon_0 S_i) \tag{7.2}$$

Therefore, the E-field distribution around the mDCS surface can be approximated by measuring six displacement currents in the six capacitors of the mDCS. Of course, the accuracy of the E-field distribution approximation can be improved if more metallic arc plates are used. The six-capacitor scheme is considered to be sufficient to capture the field distribution for this application. Since the surface charge density on a metallic surface is proportional to the magnitude of electric field intensity vector, therefore the surface charge density on a conductor and the spatial E-field distribution around the conductor surface may be exchanged in the rest of the chapter.

To validate the capability of the proposed mDCS to capture the E-field distribution around its surface, the 3-Φ overhead power line system shown in Figure 7.1 is analyzed in the Maxwell Electrostatic 2D simulation environment. The line configuration is based on the clearance requirement for a 115 kV transmission line, and the detailed dimensions are depicted in Figure 7.1. The conductor type is Drake ACSR. Figure 7.2 shows three

examples of the average surface charge density ρ_i induced on the metallic surface of each of the six capacitors C_i (i = 1,…6), at one particular moment, say t_0. The 3-Φ line voltages are $v_A(t_0)$ = -100 kV, $v_B(t_0)$ = -100 kV, and $v_C(t_0)$ = 115 kV respectively, i.e. the phase angle of phase-C voltage $\theta_C = 0^o$. Case 1 has the same line geometry as shown in Figure 7.1. In Case 2, the distance between the conductor and the ground decreases from 20 to 16 meters. In Case 3, the conductor separation between C and A changes from 3 to 4 meters.

Figure 7.2 indicates that, with the same conductor voltage values, variations of line geometry do cause changes in E-field distribution around the mDCS surface. Via measuring and analyzing the spatial mapping of the E-field distribution in real time, it is therefore possible to determine the physical reasons that may cause any changes in the E-field distribution, and thus to detect and predict the presence of incipient faults in the vicinity of the mDCS along the line.

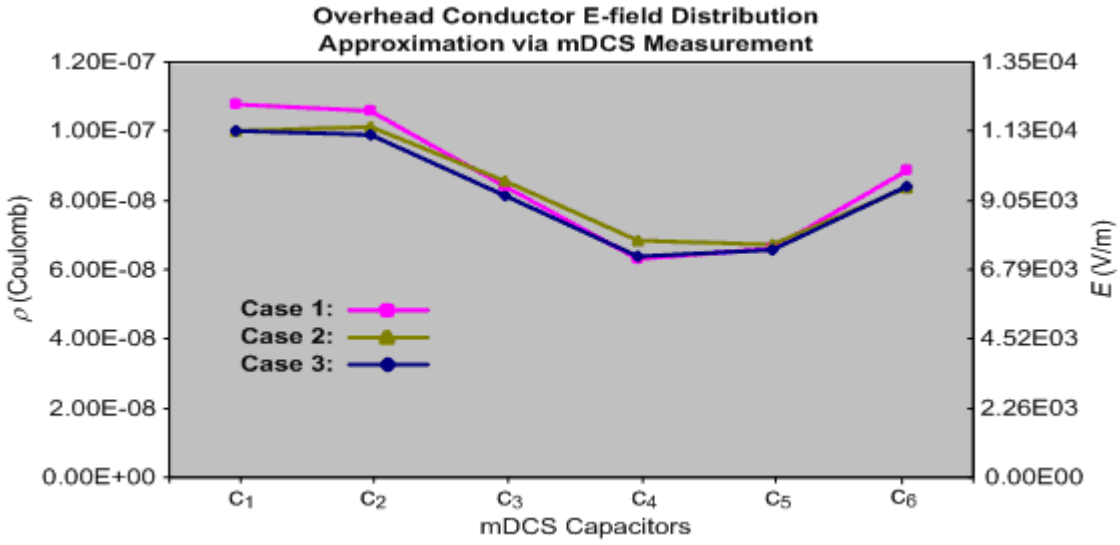

Figure 7.2. Overhead conductor E-field distribution approximation via mDCS measurement

In addition, Figure 7.2 also shows that the magnitude of the E-field deviation is about 10% of its mean value. The resolution of low cost Analog-to-Digital Convertors (ADC) is sufficient to capture this variation. This makes the proposed mDCS scheme a feasible solution to monitor the spatial distribution of the E-field around overhead conductors. Of course the diameter of the mDCS cylinder affects E-field magnitude deviation, i.e. the larger the diameter, the greater the E-field deviation. However, a larger diameter of the proposed mDCS sensor may potentially create corona effects between conductors. A tradeoff has to be considered in the future work.

In the following two sections, an analytical model of the E-field distribution around the mDCS surface in a 3-Φ power line system is developed. The resultant model is then used to extract useful information to characterize the environment of a power line.

7.3 Introducing the Concept of Distributed Capacitance Density (D_cap)

To develop an analytical model of the electric charge density induced on the mDCS surface in a 3-Φ overhead power line system, a new concept of **Distributed Capacitance Density (D_cap)** between two conductors is first introduced in this section.

7.3.1 Introduction to Distributed Capacitance Density

In an isolated two-conductor system, if only total electric charge is considered, the dielectric coupling between the two conductors is represented by conventional capacitance, which is the ratio of the magnitude of **the total charge** on either conductor to the potential difference between the two conductors [115]. In this work, however, an important concept of **Distributed Capacitance Density (D_cap)** between two conductors is defined, which is driven by the need that the dielectric coupling between two conductors can be depicted not only in terms of strength, but also (more importantly) in terms of spatial distribution.

Denote c_{12} to be the D_cap of conductor 1 subject to conductor 2. By definition, c_{12} is the ratio of the surface **charge density** on conductor 1, $\rho_{s\_1}(xx)$, induced by conductor 2 to the potential difference between these two conductors, V_{12}. It can be formulated by,

$$c_{12}(xx) = \rho_{s\_1}(xx)/V_{12} \ \textbf{(F/m}^2\textbf{)} \tag{7.3}$$

where *xx* denotes any position on conductor 1 surface.

The distributed capacitance density is not a fixed value, but a function of the position on the surface of the conductor under study. It does not only provide capacitive coupling capability between two conductors, but also describe how the coupling is distributed on one conductor subject to another.

To apply this D_cap concept to this application, a simple two-conductor system where the electric charge around mDCS surface is induced by only **one** adjacent conducting object is first studied as follows.

7.3.2 mDCS Surface Charge Density in a Two-Conductor System

Figure 7.3 (a) shows the cross-section view of an isolated two-conductor system, consisting two long and parallel power conductors C and B. The mDCS is clamped around conductor C, and has the same potential as C.

The center of the mDCS (coaxial with conductor C) is at *(x, y)=(0, 0)* with radius of *r*. Conductor B is represented by its equivalent line charge ρ_L concentrated along an infinitesimal filament coincident with the wire axis *(x, y)=(R,0)*. By solving the 2D Laplace's equation for this problem [115], the charge density of the mDCS surface can be approximated to be a sinusoidal distribution with a constant bias, given by,

$$\rho_C(r,\varphi) = \rho_{C\_m} + \Delta\rho_C \cdot \cos(\varphi) \tag{7.4}$$

where φ is measured in the counter-clockwise direction with respect to the x-axis ρ_{C_m} and $\Delta\rho_C \cdot \cos(\varphi)$ are defined to be the common and differential modes of mDCS surface charge density, as expressed by,

$$\rho_{C\_m} = V_{CB} \cdot \frac{\varepsilon_0(R^2 - r^2)}{2r(R^2 + r^2)\ln(R/r)} \tag{7.5}$$

$$\Delta\rho_C = V_{CB} \frac{\varepsilon_0 \cdot R(R^2 - r^2)}{(R^2 + r^2)^2 \ln(R/r)} \tag{7.6}$$

where V_{CB} is the potential difference between conductor C and B. The charge distribution around the mDCS surface peaks along the x-axis and distributes sinusoidally around the sensor surface, as shown in Figure 7.3 (a). The x-axis is denoted as "**CB Electric Axis (CB-axis)**". Appendix D gives the derivation procedure in details.

By the definition of D_cap shown in (7.3), the D_cap of the mDCS subject to conductor B can be expressed by,

$$c_{CB}(\varphi) = \frac{\rho_C(r,\varphi)}{V_{CB}} = c_{CB\_m} + \Delta c_{CB} \cdot \cos(\varphi) \tag{7.7}$$

where c_{CB_m} represents the **common-mode** component of the D_cap, and Δc_{CB} is the D_cap **differential-mode** component. The CB-axis (φ=*0*) shown in Figure 7.3 (a) represents the direction with the strongest capacitive coupling between the mDCS and conductor B, and the coupling strength is distributed sinusoidally around the mDCS surface, as a function of φ.

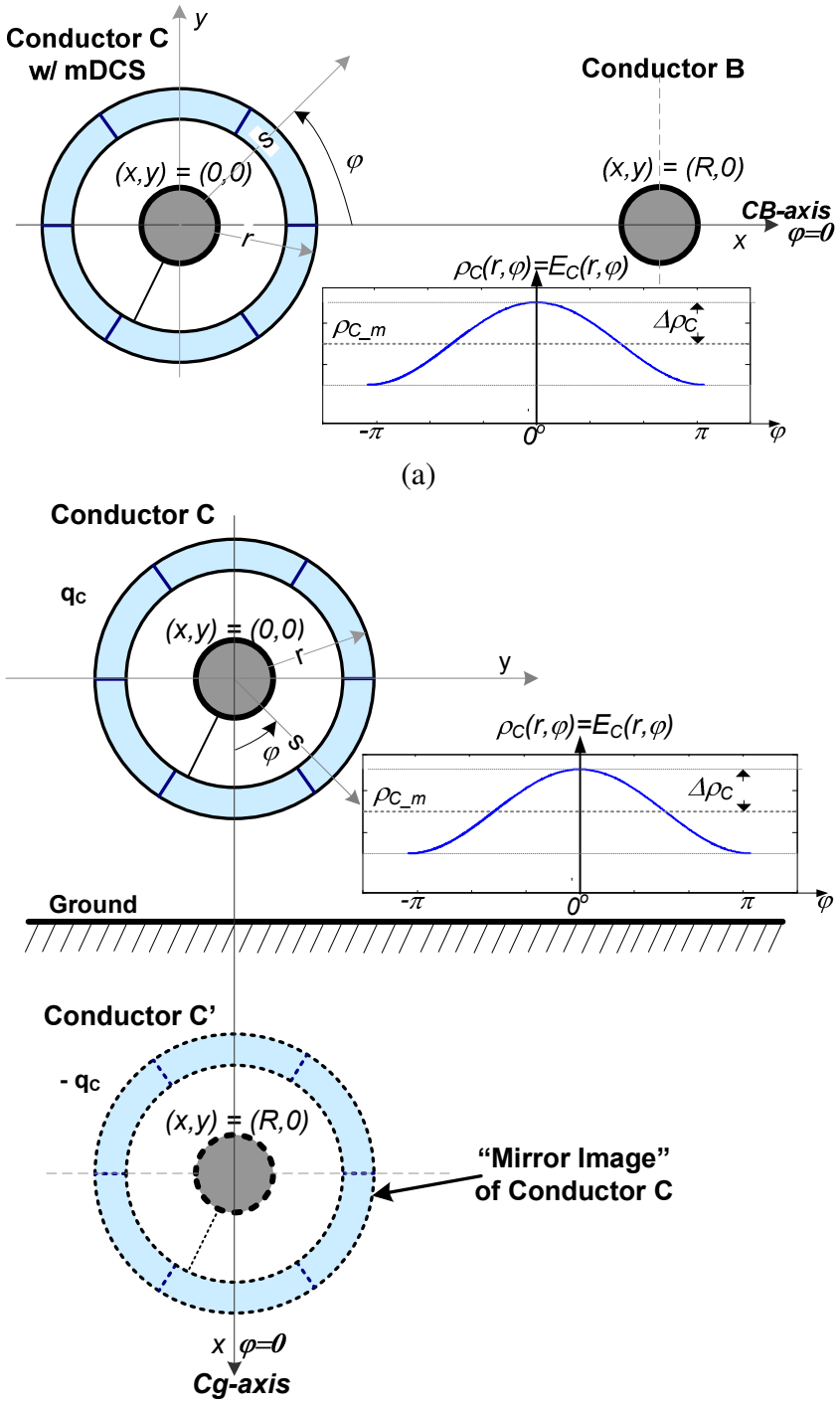

Figure 7.3. Electric charge density (E-field distribution) over mDCS surface subject to (a) conductor B; (b) earth.

Similarly, Figure 7.3 (b) shows another type of isolated two-conductor system, where conductor C (with mDCS mounted) is suspended above the ground. Similarly, the mDCS surface charge distribution peaks along the x-axis, as shown in Figure 7.3 (b), and distributes sinusoidally around the sensor surface. In this case, the x-axis is denoted as "**Cg Electric Axis (Cg-axis)**". Appendix D gives the derivation procedure in details.

Introducing the concept of D_cap is intrigued by the concept of "distributed windings", which has been widely utilized in AC machine magnetic field analysis [117]. In this work, the concept of D_cap plays a critical role in developing the mathematical model of the E-field distribution around the mDCS surface in a 3-Φ power line system, as presented in next section.

7.4 mDCS Surface Charge Density in a 3-Φ Power Line System

Figure 7.4 shows the cross-section view of the same 3-Φ overhead power line system as depicted in Figure 7.1. Applying the concept of D_cap, the capacitive coupling between the mDCS and other adjacent conductors, i.e. phase conductors A and B, ground, and other grounded objects, etc, can be represented by several D_caps, i.e. $c_{CA}(\varphi)$, $c_{CB}(\varphi)$, $c_{Cg}(\varphi)$, $c_{CW}(\varphi)$, as shown in Figure 7.4. As indicated in the previous section, each D_cap at every instant produces a sinusoidal charge distribution (E-field distribution) on the mDCS surface peaking along its electric axis. These electric axes, i.e. Cg-axis, CW-axis, CB-axis, and CA-axis, are displaced from each other based on the inherent power line geometry configurations, as shown in Figure 7.4. To generalize the problem, other grounded objects may represent OHGW, proximity of tree branches or any other conductors with ground potential, whose capacitive coupling to the mDCS is generically represented by $c_{CW}(\varphi)$.

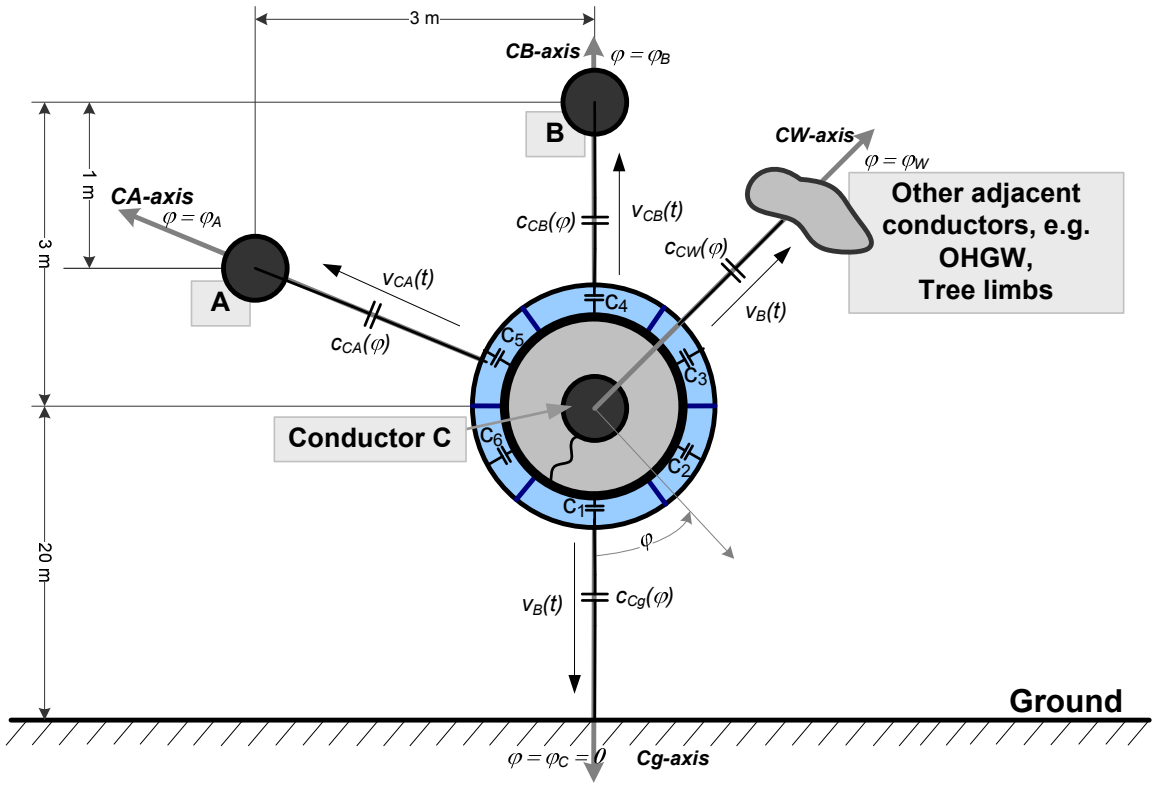

Figure 7.4. Cross-section of a 3-Φ Power Line System with mDCS installed on Conductor C.

The four D_caps appeared in Figure 7.4 can be expressed in terms of two different modes, i.e. common and differential modes, given by

$$c_{Cg}(\varphi) = c_{Cg\_m} + \Delta c_{Cg} \cdot \cos(\varphi) \tag{7.8}$$

$$c_{CW}(\varphi) = c_{CW\_m} + \Delta c_{CW} \cdot \cos(\varphi - \varphi_W) \tag{7.9}$$

$$c_{CB}(\varphi) = c_{CB\_m} + \Delta c_{CB} \cdot \cos(\varphi - \varphi_B) \tag{7.10}$$

$$c_{CA}(\varphi) = c_{CA\_m} + \Delta c_{CA} \cdot \cos(\varphi + \varphi_A) \tag{7.11}$$

where φ is measured in the counter-clockwise direction with respect to the Cg-axis ($\varphi = 0$). φ_B, φ_A and φ_W are the displacement angles of CB-axis, CA-axis and CW-axis respectively.

With reference to (7.1), if the conventional mutual capacitances are replaced by their D_cap alternatives, the electric charge density induced on the mDCS surface can be formulated by,

$$\rho_C(\varphi,t) = c_{Cg}(\varphi)v_C(t) + c_{CW}(\varphi)v_C(t) + c_{CB}(\varphi)v_{CB}(t) + c_{CA}(\varphi)v_{CA}(t) \tag{7.12}$$

where $v_C(t)$ is phase C voltage, and $v_{CB}(t)$ and $v_{CA}(t)$ are the line-to-line voltages. If the three phases are symmetric and balanced, the three voltage values are given by

$$\begin{aligned} v_C(t) &= V_\Phi \cos(\omega t + \theta_C) \\ v_{CB}(t) &= \sqrt{3}V_\Phi \cos(\omega t + \theta_C - \theta_B), \\ v_{CA}(t) &= \sqrt{3}V_\Phi \cos(\omega t + \theta_C + \theta_A) \end{aligned} \tag{7.13}$$

where V_ϕ is the peak value of phase voltage. θ_C is the phase angle of phase C voltage, and $\theta_B = \theta_A = \pi/6$.

Equation (7.12) analytically describes the electric charge density $\rho_C(\varphi,t)$ induced on the mDCS surface in a generalized 3-Φ power line system. It is noted that, $\rho_C(\varphi,t)$ is a function of both time and the location on the mDCS surface in terms of φ. Substituting equations (7.8) - (7.11) into (7.12), the mDCS surface charge density can be expressed in two different modes, as follows,

$$\rho_C(\varphi,t) = \rho_{C\_m}(t) + \Delta\rho_C(\varphi,t) \tag{7.14}$$

where $\rho_{C\_m}(t)$ and $\Delta\rho_C(\varphi,t)$ are the common and differential modes of mDCS surface charge density (E-field distribution), which are contributed by the common and differential components of D_caps respectively. In the following two sub-sections, these two different modes will be analyzed in details.

7.4.1 Common-Mode mDCS Surface Charge Density (E-field Distribution)

With reference to (7.12) and (7.14), the common mode surface charge density $\rho_{C\_m}(t)$ is expressed by,

$$\rho_{C\_m}(t) = c_{Cg\_m} \cdot v_B(t) + c_{CW\_m} \cdot v_B(t) + c_{CB\_m} \cdot v_{CB}(t) + c_{CA\_m} \cdot v_{CA}(t), \tag{7.15}$$

The common-mode charge density is not a function of position around the mDCS surface, but only a function of time; at any instant of time, its magnitude is linearly proportional to the product of phase voltage and common-mode D_caps. The analysis for $\rho_{C\_m}(t)$ is fairly straightforward. The multiplication of $\rho_{C\_m}(t)$ and the surface area of mDCS simply results in the total charge induced on the mDCS surface. By using complex notation, $\rho_{C\_m}(t)$ can be expressed by,

$$\begin{aligned} \rho_{C\_m}(t) &= \mathrm{Re}\{V_\Phi \cdot (c_{Cg\_m} + c_{CW\_m} + \sqrt{3}c_{CB\_m} \cdot e^{-j\theta_B} + \sqrt{3}c_{CA\_m} \cdot e^{j\theta_A}) \cdot e^{j\omega t}\} \\ &= \mathrm{Re}\{\tilde{\rho}_{C\_m} \cdot e^{j\omega t}\} \end{aligned} \tag{7.16}$$

where $\tilde{\rho}_{C\_m} = V_{\Phi} \cdot (c_{Cg\_m} + c_{CW\_m} + \sqrt{3}c_{CB\_m} \cdot e^{-j\theta_B} + \sqrt{3}c_{CA\_m} \cdot e^{j\theta_A}) = \hat{\rho}_{C\_m} \cdot e^{-j\theta_{Cm}}$ is the phasor of the common-mode charge density. $\hat{\rho}_{C\_m}$ and θ_{C_m} are the phasor's magnitude and angle respectively.

If the phase C voltage phasor is denoted by $\tilde{V}_C = V_{\phi} \cdot e^{j\theta_c}$, with reference to (7.15), then the phasor angle θ_{C_m} is,

$$\theta_{C\_m} = \theta_C + \theta_{\Delta} \tag{7.17}$$

where $\theta_{\Delta} = \tan^{-1}(\frac{\sqrt{3}/2 \cdot (c_{CB\_m} - c_{CA\_m})}{c_{Cg\_m} + 1.5 \cdot (c_{CB\_m} + c_{CA\_m})})$.

7.4.2 The Space-Phasor Model of Differential-Mode mDCS Surface Charge Density (E-field Distribution)

Similarly, with the reference to (7.12) and (7.14), the differential mode surface charge density $\Delta\rho_C(\varphi,t)$ is given by,

$$\begin{aligned}\Delta\rho_C(\varphi,t) = {} & v_C(t) \cdot \Delta c_{Cg} \cdot \cos(\varphi) + v_C(t) \cdot \Delta c_{CW} \cdot \cos(\varphi - \varphi_W) \\ & + v_{CB}(t) \cdot \Delta c_{CB} \cdot \cos(\varphi - \varphi_B) + v_{CA}(t) \cdot \Delta c_{CA} \cdot \cos(\varphi + \varphi_A)\end{aligned} \tag{7.18}$$

$\Delta\rho_C(\varphi,t)$ is the part of the electric charge induced the mDCS surface that is contributed by differential components of D_caps. It is a function of both time and angle position φ. Re-arranging (7.18), $\Delta\rho_C(\varphi,t)$ yields two components, expressed by,

$$\Delta\rho_C(\varphi,t) = \Delta\rho_{CP}(\varphi,t) + \Delta\rho_{CN}(\varphi,t) \tag{7.19}$$

where,

$$\Delta\rho_{CP}(\varphi,t)=\frac{V_{\Phi}}{2}(\ \Delta c_{C_g}\cdot\cos(\omega t-\varphi)+\Delta c_{CW}\cdot\cos(\omega t-\varphi+\varphi_W)$$
$$+\sqrt{3}\Delta c_{CB}\cdot\cos(\omega t-\varphi+(\varphi_B-\theta_B)) \tag{7.20}$$
$$+\sqrt{3}\Delta c_{CA}\cdot\cos(\omega t-\varphi-(\varphi_A-\theta_A)))$$

and,

$$\Delta\rho_{CN}(\varphi,t)=\frac{V_{\Phi}}{2}(\ \Delta c_{C_g}\cdot\cos(\omega t+\varphi)+\Delta c_{CW}\cdot\cos(\omega t+\varphi-\varphi_W)$$
$$+\sqrt{3}\Delta c_{CB}\cdot\cos(\omega t+\varphi-(\varphi_B+\theta_B)) \tag{7.21}$$
$$+\sqrt{3}\Delta c_{CA}\cdot\cos(\omega t+\varphi+(\varphi_A+\theta_A)))$$

$\Delta\rho_{CP}(\varphi,t)$ represents a sinusoidal distribution of the charge around the mDCS surface, and rotates in the positive (counter-clock wise) direction in space with the synchronous speed ω. Similarly, $\Delta\rho_{CN}(\varphi,t)$ represents another sinusoidal distribution, but rotates in the negative (clock wise) direction the synchronous speed ω. The differential modes of the charge density distribution on the mDCS surface are depicted in Figure 7.5.

By using complex notation, the two rotational distributions can be expressed by,

$$\Delta\rho_{CP}(\varphi,t)=\mathrm{Re}\{\vec{\rho}_{CP}\cdot e^{-j\varphi}\} \tag{7.22}$$

$$\Delta\rho_{CN}(\varphi,t)=\mathrm{Re}\{\vec{\rho}_{CN}\cdot e^{j\varphi}\} \tag{7.23}$$

where

$$\vec{\rho}_{CP}(t) = \frac{V_\Phi}{2}(\Delta c_{Cg} + \Delta c_{CW} \cdot e^{j\varphi_W} + \sqrt{3}\Delta c_{CB} \cdot e^{j(\varphi_B - \theta_B)} + \sqrt{3}\Delta c_{CA} \cdot e^{-j(\varphi_A - \theta_A)}) \cdot e^{j\omega t} \\ = \hat{\rho}_{CP} \cdot e^{j\theta_P} \cdot e^{j\omega t} \tag{7.24}$$

$$\vec{\rho}_{CN}(t) = \frac{V_\Phi}{2}(\Delta c_{Cg} + \Delta c_{CW} \cdot e^{-j\varphi_W} + \sqrt{3}\Delta c_{CB} \cdot e^{-j(\varphi_B + \theta_B)} + \sqrt{3}\Delta c_{CA} \cdot e^{j(\varphi_A + \theta_A)}) \cdot e^{j\omega t} \\ = \hat{\rho}_{CN} \cdot e^{j\theta_N} \cdot e^{j\omega t} \tag{7.25}$$

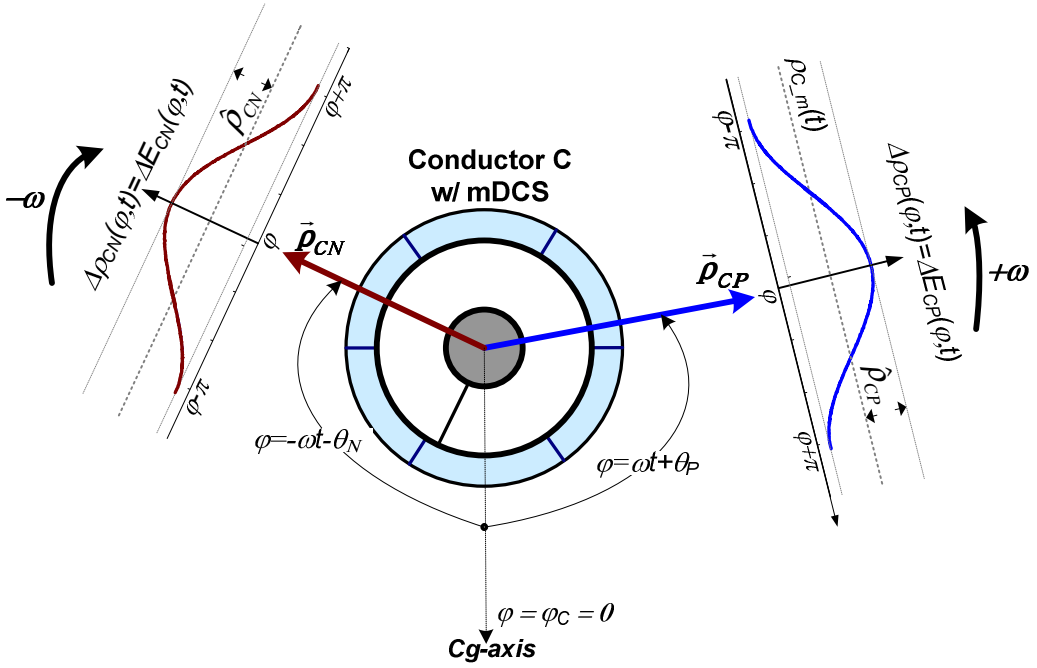

Figure 7.5. Differential-mode mDCS surface charge density distribution

$\vec{\rho}_{CP}(t)$ and $\vec{\rho}_{CN}(t)$ are the space phasors of $\Delta\rho_{CP}(\varphi,t)$ and $\Delta\rho_{CN}(\varphi,t)$. Physically, these two space phasors determine the instantaneous magnitudes and spatial displacements of the peaks of the two sinusoidal surface charge distributions around the mDCS surface, which are depicted in Figure 7.5. In equations (7.24) and (7.25) $\hat{\rho}_{CP}$ and $\hat{\rho}_{CN}$ are the moduli of the two space-phasors. θ_P and θ_N are their phase angles with respect to the real axis defined by phase C voltage $v_C(t)$.

To summarize, the three different modes of mDCS surface charge density $\rho_C(\varphi,t)$ (E-field distribution) are listed in Table 7.2.

Table 7.2 MDCS SURFACE CHARGE DENSITY $\rho_C(\varphi,t)$

Common Mode $\rho_{C\_m}(t)$	Differential Mode $\Delta\rho_C(\varphi,t)$	
	Positively Rotating Mode $\Delta\rho_{CP}(\varphi,t)$	Negatively Rotating Mode $\Delta\rho_{CN}(\varphi,t)$

The concept of D_cap helps to build a **space-phasor model** of the differential-mode E-field distribution around the mDCS surface. This analysis is similar to that when the space-phasor model of magnetic field (M-field) is analyzed for AC machines [117]. For better understanding, Table 7.3 gives the analogy between AC machines M-field and the mDCS E-field in a 3-Φ power line system.

Table 7.3 ANALOGY BETWEEN AC MACHINE M-FIELD AND MDCS E-FIELD IN A 3-Φ POWER LINE SYSTEM

	AC Machine	**mDCS in a 3-Φ Power Line System**
Source	Winding current $i(t)$	Conductor voltage $v(t)$
Media	Sinusoidally distributed winding conductor density $n(\varphi)$	Sinusoidally distributed capacitance density (D_cap) $c(\varphi)$
Field	Magnetic flux (density) Φ ($B(\varphi,t)$) Or mmf $F(\varphi,t)$	Electric flux (density) Q ($\rho(\varphi,t)$)
	Magnetic field intensity $H(\varphi,t)$	Electric field intensity $E(\varphi,t)$
Conditions	$i_a(t)+i_b(t)+i_c(t)=0$	$v_a(t)+v_b(t)+v_c(t)=0$

With the help from the concept of D_caps, the space-phasor model of the E-field distribution concisely but yet comprehensively describes any changes in the charge density around the mDCS surface in real time, subject to any instantaneous variations either in conductor voltage or line geometry, or both. More importantly, the theories and methods that have been widely used for AC machines magnetic field analysis can be applied to analyze the mDCS E-field distribution.

7.5 Information Extraction from mDCS Surface E-field Distribution

This section briefly presents the procedure to approximate the E-field distribution around the mDCS surface based on the six displacement current measurements, and how the information can be extracted to allow independent measurements of both conductor-to-ground clearance and conductor voltage. Figure 7.6 shows the block diagram of the proposed information extraction procedure. A DQ-axis decomposition technique is applied to the approximate E-field distribution. The potential of the decomposed DQ-axis components to separate the capacitive coupling effects between the mDCS and its adjacent conducting objects in different directions is validated in the MAXWELL 2D simulation environment.

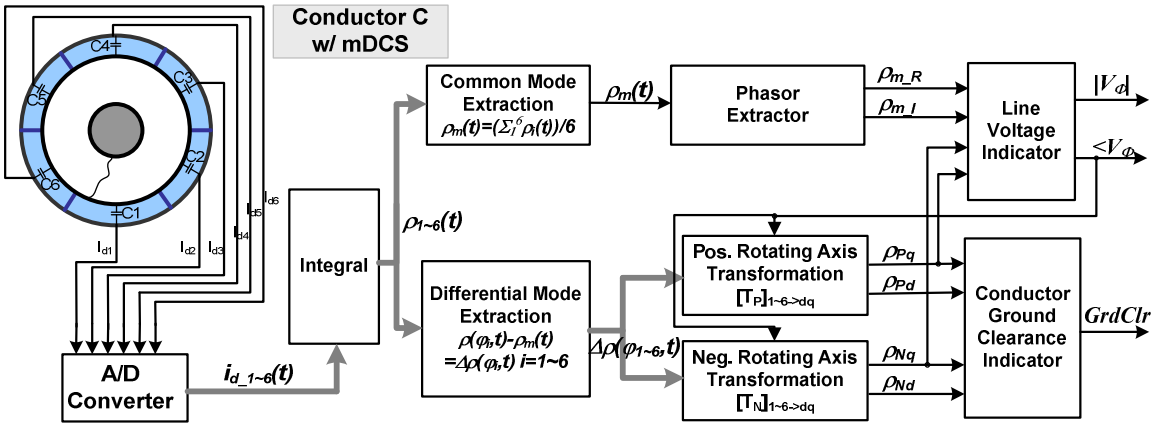

Figure 7.6. Overhead power line voltage and conductor ground clearance measurement based on mDCS scheme

7.5.1 E-field Distribution Approximation by mDCS

The procedure to capture and construct the spatial mapping of the E-field distribution around the mDCS surface is summarized as follows,

1. Six displacement currents, $i_{di}(t)$, for i = 1~6, flowing through the six capacitors are measured. The center position of the capacitor i is located at $\varphi_i = (i-1)\cdot\pi/3$, and denotes the direction of i-axis. $\varphi_0 = 0$ also denotes the direction of the Cg-axis.
2. The average electric charge density on the ith capacitor surface, $\rho_i(t)$, is obtained as follows,

$$\rho'(\varphi_i,t) \approx \rho_i(t) = (\int_0^t i_{d\_i}(t)\cdot dt)/S \tag{7.26}$$

where S is the metallic plat surface area of each capacitor, and $\rho_i(t)$ is the approximate mDCS surface charge density along i-axis , i.e. $\rho'(\varphi_i,t)$.

3. $\rho_i(t)$s' differential mode and common mode are extracted.

The common mode of $\rho_i(t)$ is,

$$\rho_m(t) = \frac{1}{6}\sum_{i=1}^{6}\rho_i(t)\,. \tag{7.27}$$

The differential mode of $\rho_i(t)$ can be obtained by,

$$\Delta\rho'(\varphi_i,t) = \Delta\rho_i(t) = \rho_i(t) - \rho_m(t)\,. \tag{7.28}$$

The differential-mode charge density around the mDCS surface can also be represented in a vector form, given by $\Delta\Upsilon'(t) = [\Delta\rho'(\varphi_1,t)\ \ ...\ \ \Delta\rho'(\varphi_6,t)]'$. $\Delta\Upsilon'(t) + \rho_m(t)$

which provides the real-time approximation of the charge density around the mDCS surface $\rho_C(\varphi,t)$, as depicted in (7.12).

In the following subsection, two rotational reference frame transformations are applied to convert the six displacement current measurements to four DQ-axis components.

7.5.2 Rotational Reference Frame Transformation from 1~6-axis to DQ-axis Coordinates

With the condition of $\sum_{i=1}^{6}\Delta\rho_i(t)=0$, the differential mode mDCS E-field distribution can be represented by a space phasor constructed by the six surface charge measurements, given by,

$$\Delta\vec{\rho}'(t)=\frac{1}{3}\sum_{i=1}^{6}\Delta\rho'(\varphi_i,t)\cdot a^{i-1} \tag{7.29}$$

where $a=e^{j\pi/3}$ is the space operator.

It is an important consequence of the approximated **sinusoidal surface charge distribution**, as indicated in (7.7), that the space phasor of the six measurements can be added together. The space phasor in (7.29) acts as an intermediary, where the differential mode surface charge density $\Delta\Upsilon'(t)=[\Delta\rho'(\varphi_1,t)\ \ ...\ \ \Delta\rho'(\varphi_6,t)]'$ in 1~6-axis quantities can be transformed into equivalent quantities in two rotational reference frames: positively rotational reference frame (Pdq-axis frame, rotating counter-clockwise); negatively rotational reference frame (Ndq-axis frame, rotating clockwise).

In positively rotational frame, the direct axis (Pd-axis) is coaxial to a space phasor denoted as $\vec{\rho}_{Cg}(t)=e^{j\omega t+\theta_C}$, and the quadrature axis (Pq-axis) is selected to be orthogonal

to the Pd-axis (leading Pd-axis by 90°). Similarly, in the negatively rotational frame, the direct axis (Nd-axis) is also coaxial to the space phasor $\vec{\rho}_{Cg}(t) = e^{j\omega t+\theta_C}$ but rotating negatively, and the quadrature axis (Nq-axis) is selected to be orthogonal to the Nd-axis (leading Nd-axis by 90°).

The decomposed Pdq- and Ndq-axis components by applying two revised Park's transformations are given by,

$$\left[\rho'_{CP\_d} \quad \rho'_{CP\_q}\right]' = [T_P]_{1\sim 6\to dq} \cdot \Delta\Upsilon'(t) \tag{7.30}$$

$$\left[\rho'_{CN\_d} \quad \rho'_{CN\_q}\right]' = [T_N]_{1\sim 6\to dq} \cdot \Delta\Upsilon'(t) \tag{7.31}$$

where

$$[T_P]_{1\sim 6\to dq} = \frac{1}{3}\begin{bmatrix} \cos(\varphi_{Pd}) & \cos(\varphi_{Pd}-\pi/3) \ldots \cos(\varphi_{Pd}-5\pi/3) \\ -\sin(\varphi_{Pd}) & -\sin(\varphi_{Pd}-\pi/3) \ldots -\sin(\varphi_{Pd}-5\pi/3) \end{bmatrix}_{(2\times 6)} \tag{7.32}$$

is used to transform the 1~6-axis quantities to the Pdq-axis frame, and $\varphi_{Pd} = \omega t + \theta_C$.

The matrix $[T_N]_{1\sim 6\to dq}$ is then used to transform the 1~6-axis quantities to the Ndq-axis frame, given by,

$$[T_N]_{1\sim 6\to dq} = \frac{1}{3}\begin{bmatrix} \cos(\varphi_{Nd}) & \cos(\varphi_{Nd}+\pi/3) \ldots \cos(\varphi_{Nd}+5\pi/3) \\ -\sin(\varphi_{Nd}) & -\sin(\varphi_{Nd}+\pi/3) \ldots -\sin(\varphi_{Nd}+5\pi/3) \end{bmatrix}_{(2\times 6)} \tag{7.33}$$

where $\varphi_{Nd} = \omega t + \theta_C$.

The DQ-axis decomposition technique requires accurate assessment of voltage phase angle θ_C, which can actually be obtained from the phase angle of the common mode

surface charge density $\rho_{C\_m}(t)$, as shown in (7.17). Note that the angle difference between phase voltage V_c and $\rho_{C\_m}(t)$ is θ_Δ, ranges from 3° to 5°, which is determined by the inherent line conductor configurations.

Correct utilization and combination of these four DQ-axis components in (7.30) and (7.31) potentially leads to separate the capacitive couplings between the mDCS and its adjacent conductors in different directions. This helps to distinguish and characterize the physical reasons that cause the variations in the mDCS E-field distribution, and thus to detect and predict the presence of line incipient faults. The importance of the components' decomposition is that it also allows an accurate assessment of conductor voltage variation. To validate the proposed idea, preliminary simulation studies are conducted in the Maxwell Electrostatic 2D simulation environment.

7.5.3 Maxwell^{TM} Electrostatic 2D Simulation Validation of DQ-axis Decomposition

The equations (7.30) and (7.31) indicate that the four decomposed DQ-axis components all are functions of conductor voltage V_Φ, as well as line geometry configuration that can be described generically by the D_caps in Figure 7.4, i.e. $c_{CA}(\varphi)$, $c_{CB}(\varphi)$, $c_{Cg}(\varphi)$, and $c_{CW}(\varphi)$. The ratio between these DQ-axis components can then effectively remove the effect of conductor voltage, and the resultant value is able to reflect the variations in line geometry only. Figure 7.7 and Figure 7.8 give two examples of how to utilize these four DQ-axis components to separate the capacitive coupling effects of between the conductor, where the mDCS is mounted, and its adjacent conductors in different directions.

The first case is to verify the behaviors of the four DQ-axis components when the conductor-to-ground clearance changes from 5 to 16 meters. Two ways of combining the

DQ-axis components are tested, where $N\rho'_{CQ} = \frac{\rho'_{CP\_q} + \rho'_{CN\_q}}{\rho'_{CP\_d} + \rho'_{CN\_d}}$ and $N\rho'_{CD} = \frac{\rho'_{CP\_d} + \rho'_{CN\_d}}{\rho'_{CP\_d} - \rho'_{CN\_d}}$. As shown in Figure 7.7, $N\rho'_{CQ}$ remains almost constant as the conductor-to-ground clearance changes from 5 to 16 meters. On the other hand, the variation of $N\rho'_{CD}$ subject to the change in the conductor-to-ground clearance is almost 10 times larger than that of $N\rho'_{CQ}$, which makes $N\rho'_{CD}$ a good indicator to the conductor-to-ground clearance.

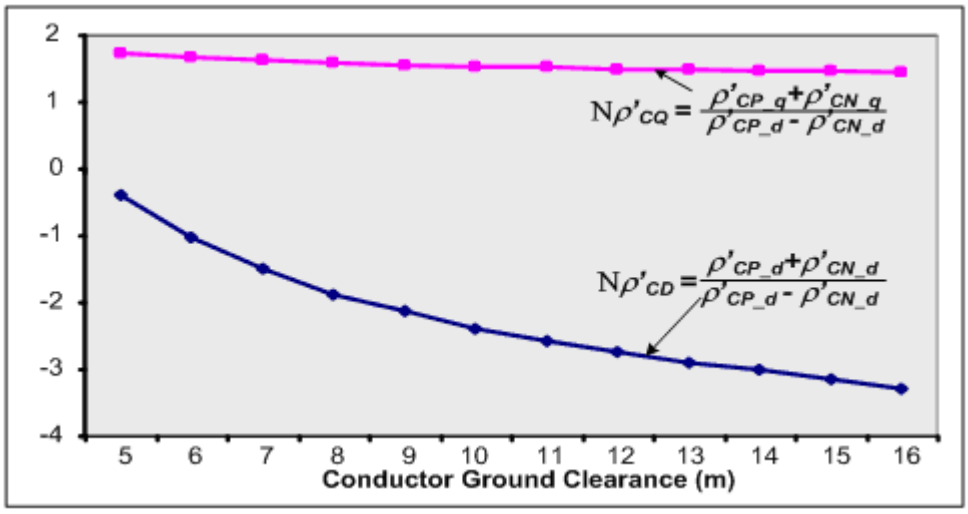

Figure 7.7. DQ-axis components subject to conductor-to-ground clearance variation

Figure 7.8 shows another example of how the DQ-axis components change, subject to relative motion between phase conductors, as a result of galloping conductors for instance. In this case, the clearance between conductors C and A in Figure 7.4 decreases from 3.6 to 2.4 meters, while the clearance between C and B increases from 3 to 4.2 meters. Even though $N\rho'_{CQ}$ is insensitive to conductor-to-ground clearance variation as shown in Figure 7.7, it is sensitive to variations in conductor separations. This makes

$N\rho'_{CQ}$ a promising indicator to those conductor movements that may cause changes in conductor separation, such as conductor galloping.

To verify that the DQ-axis components' decomposition can also help measure the conductor voltage even when the overhead power line is subjected to changes in line geometry, Figure 7.9 shows the third example of how the DQ-axis components can be utilized. As depicted in Figure 7.9, $\rho'_{CP\_d} - \rho'_{CN\_d}$ remains almost constant compared to $\rho'_{CP\_d} + \rho'_{CN\_d}$ as the conductor-to-ground clearance changes from 5 to 16 meters. If there is no relative motion between phase conductors (mainly caused by conductor gallop), $\rho'_{CP\_d} - \rho'_{CN\_d}$ is a function of conductor voltage only, which makes it a promising indicator to conductor voltage variation.

With the help of the above analysis, two indicators to detect the variations in both conductor voltage and conductor-to-ground clearance are proposed and presented in the following two subsections.

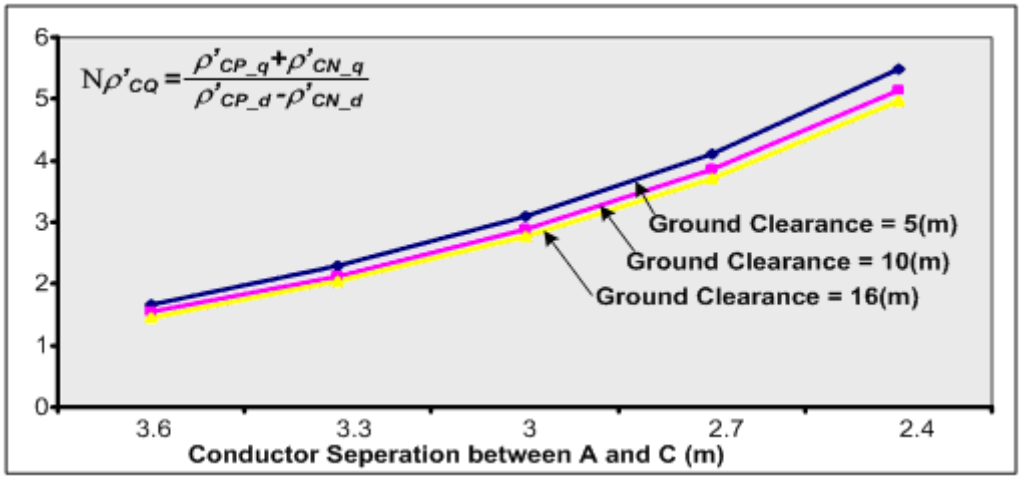

Figure 7.8. DQ-axis components subject to conductor separation variation

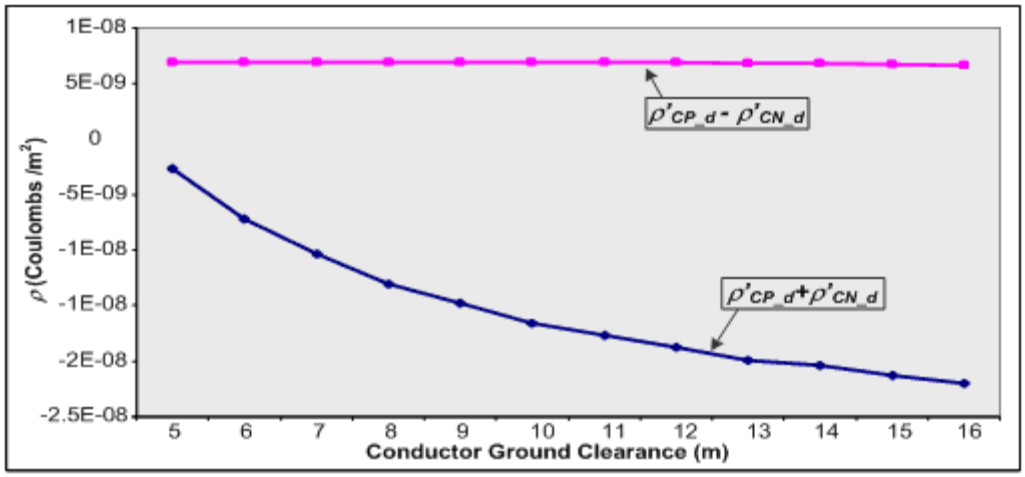

Figure 7.9. DQ-axis components variation subject to conductor-to-ground clearance variation

7.5.4 Line Voltage and Conductor Ground Clearance Indicators

Conductor Voltage Indicator:

With reference to the analysis shown in Figure 7.9, a conductor voltage magnitude indicator is proposed as follows,

$$V'_{\phi} = k_1 \cdot (\rho'_{CP\_d} - \rho'_{CN\_d}) \tag{7.34}$$

where k_1 is an unknown scalar, which can be calibrated using historical data. If it is assumed that $|\tilde{V}_{\phi}|'$ shares the same probability distribution to real voltage magnitude V_{Φ}, and the mean value of $|\tilde{V}_{\phi}|'$ is equal to the nominal value of the line voltage magnitude, the value of k_1 can therefore be determined.

The voltage phase angle is determined the following equation,

$$\angle \tilde{V}_{\phi}' = \angle \tilde{\rho}_{m}' + \theta_{\Delta} \tag{7.35}$$

where $\angle \tilde{\rho}_{m}'$ is the common mode E-field phase angle. The angle difference θ_{Δ} can be determined by (7.17), which can be evaluated based on priory information of the common mode capacitance.

Overhead Conductor-to-Ground Clearance Indicators:

With reference to the analysis shown in Figure 7.7, a conductor-to-ground clearance indicator is proposed as follows,

$$GrdClr' = k_{s1} \cdot \exp\left(\frac{\rho_{CP\_q}' + \rho_{CN\_q}'}{\rho_{CP\_d}' + \rho_{CN\_d}'}\right) + k_{s2} \tag{7.36}$$

where k_{s1} and k_{s2} are the two scalars needed to map the term exp(.) to the actual ground clearance value. Again, historical data can be used to calibrate these two scalars. The strong correlation between the conductor sag and the conductor temperature can be used for calibration [30], which forms an interesting topic for future work. The work presented in this thesis, however, focuses on the principle that the DQ-axis components can be used to formulate the conductor voltage and ground clearance indicators. The performances of the two proposed indicators are validated in the Maxwell Electrostatic 2D simulation environment as follow.

The 3-Φ overhead power line system depicted in Figure 7.4 is again used as the base case for the simulation validation. The simulation conditions are set up to mix the variation of conductor voltage magnitude and conductor-to-ground clearance. For a duration of 10 minutes, the conductor voltage magnitude varies sinusoidally at 0.0233 Hz, with the magnitude deviation up to ±10% of the nominal voltage. At the same time,

the conductor-to-ground clearance changes from 5 to 16 meters, as shown in Figure 7.10. The Parametric Analysis module provided by Maxwell 2D is used to sweep the conductor voltage and ground clearance values during the simulation.

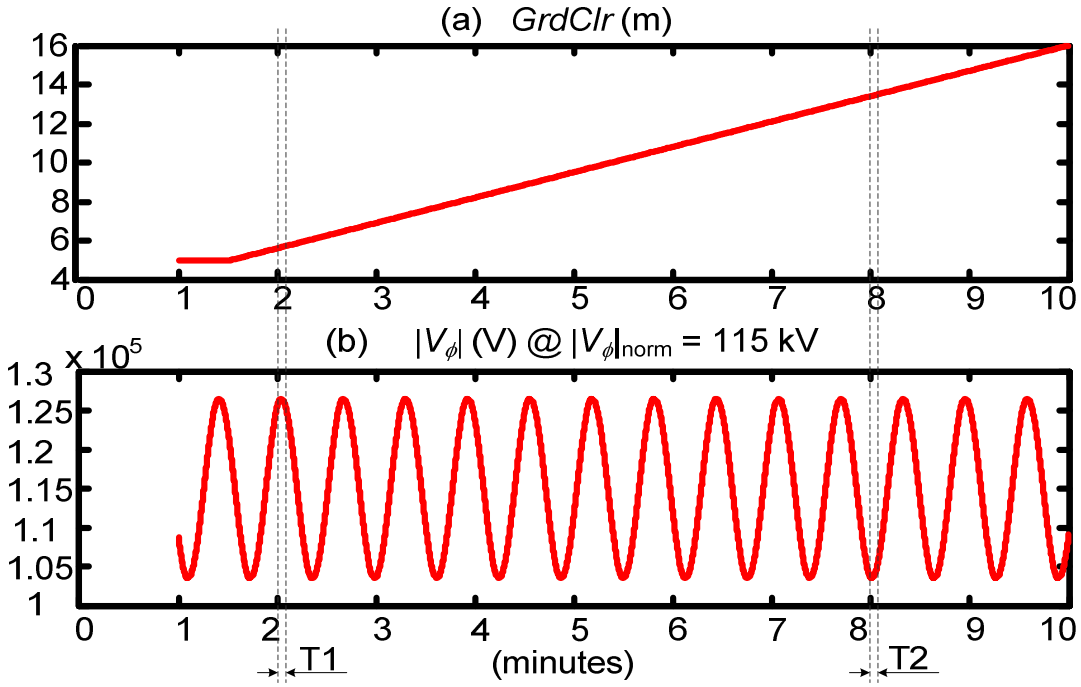

Figure 7.10. Conductor-to-ground clearance varying from 5 to 16 meters; (b) line phase voltage magnitude varying sinusoidally at 0.0233 Hz.

For demonstration purposes, Figure 7.11 (a) shows the real-time measurements of the mDCS surface charge density for two short periods of time: at about 2 minutes after simulation starts (period T1 in Figure 7.10, from 120.6 to 120.66 sec), and at about 6 minutes later (period T2 in Figure 7.10, from 480.6 to 480.66 sec). Each waveform in Figure 7.11 (a) indicates that the average charge density $\rho_i(t)$ induced on each capacitor C_i (for i=1,…,6) varies sinusoidally at 60 Hz, but the magnitude decreases from T1 to T2 mostly due to the variation in the 0.0233 Hz voltage magnitude and somewhat due to the conductor-to-ground clearance variation. Figure 7.11 (b) indicates the common mode of

the mDCS surface charge density, $\rho_m(t)$, which represents the average induced charge on the mDCS, and the waveforms have similar changes from T1 to T2 as in Figure 7.11 (a) due to the same reasons. Figure 7.11 (c) shows the differential mode of the mDCS surface charge density $\Delta\rho_i(t)$ and at any instant of time, the magnitude of $\Delta\rho_i(t)$ induced on each capacitor C_i differs from one to the other. This explains how the six capacitors are able to capture the different capacitive coupling strength to the mDCS from all its adjacent conductors in different directions, from which the spatial mapping of the E-field distribution can be obtained in real time, as explained in Section III.B. The same effects from T1 to T2 also appear in Figure 7.11 (c).

By applying the DQ-axis transformation to the six surface charge density values, four decomposed DQ-axis components are obtained and utilized to formulate the voltage magnitude and conductor to ground clearance indicators, as introduced in the previous subsection.

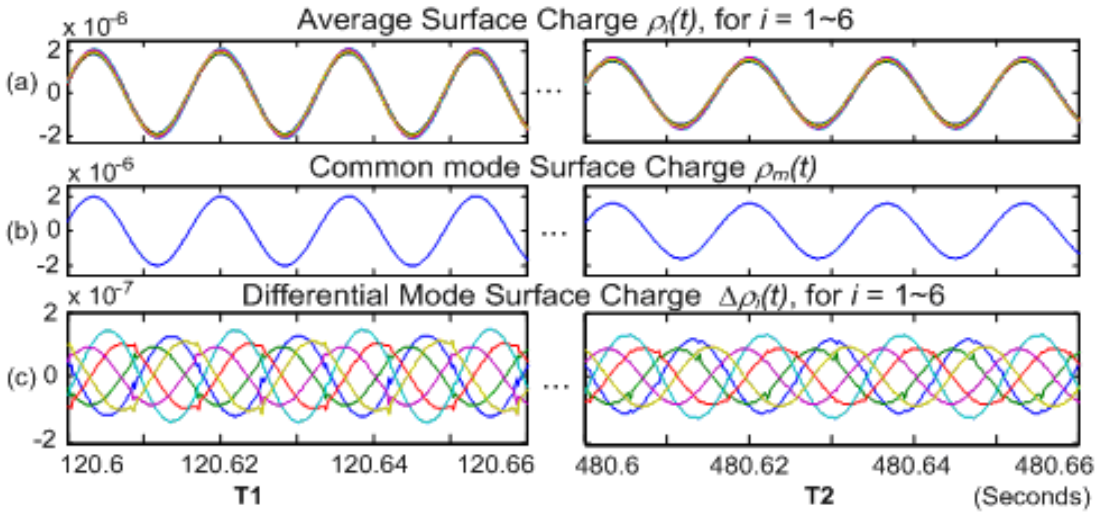

Figure 7.11. $\rho_i(t)$, for $i = 1, \ldots, 6$: (a) $\rho_m(t)$; (b) $\Delta\rho_i(t)$.

Figure 7.12 depicts the performance of the conductor voltage magnitude indicator $|\tilde{V}_{\phi}|'$, as defined in (7.34). For comparison purposes, the original phase C voltage excitation $|V_{\phi}|$, with reference to Figure 7.10 (b), is also presented. The simulation results show an encouraging match between the estimated voltage magnitude and its actual value. This validates that the voltage indicator in (7.34) provides an accurate measurement of conductor voltage variation, even while the conductor-to-ground clearance is varying from 5 to 16 meters at the same time.

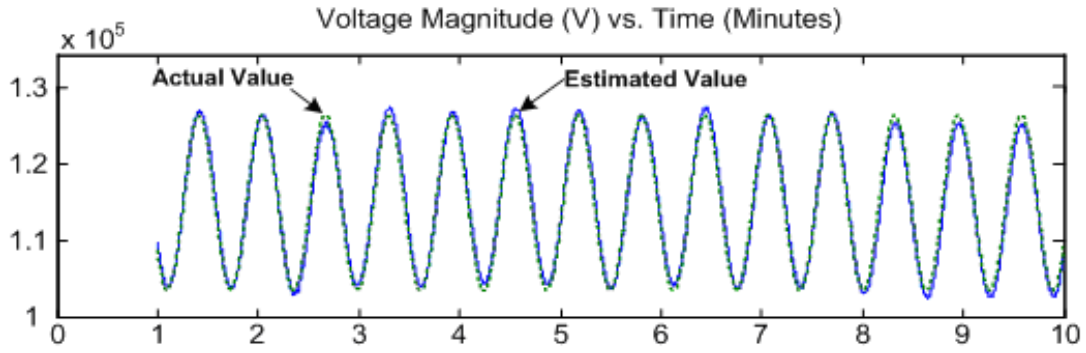

Figure 7.12. Conductor voltage Estimation with the reference of (7.34).

To assess the measurement accuracy of the proposed voltage indicator, Figure 7.13 shows the error between the estimated voltage magnitude and its actual value, with respect to variation in conductor-to-ground clearance *GrdClr* . The maximum value is within ±3% of its actual value. The accuracy is lower than the traditional voltage measurement devices, but it is acceptable for monitoring the voltage magnitude for system security purposes. The accuracy of the proposed voltage indicator may be affected by any relative motion between phase conductors, which is discussed again in Chapter 10.

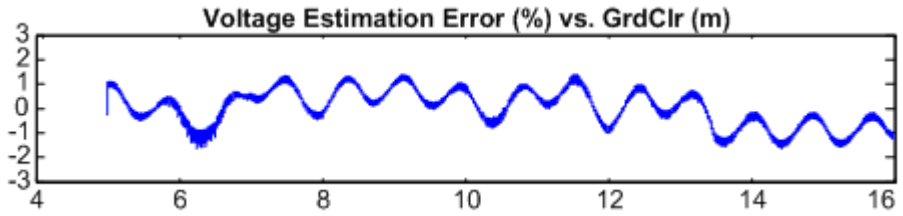

Figure 7.13. Conductor voltage estimation accuracy assessment with respect to conductor-to-ground clearance variation.

Figure 7.14 indicates the performance of the conductor-to-ground clearance indicator, as defined in (7.36). The actual conductor-to-ground clearance is also presented for comparison purpose, with reference to Figure 7.10 (a). The simulation results show an encouraging match between the estimated ground clearance and its actual value. The results validate that the indicator in (7.36) provides an accurate assessment of the clearance between the conductor where the mDCS is mounted and ground. The maximum error is less than 1 meter.

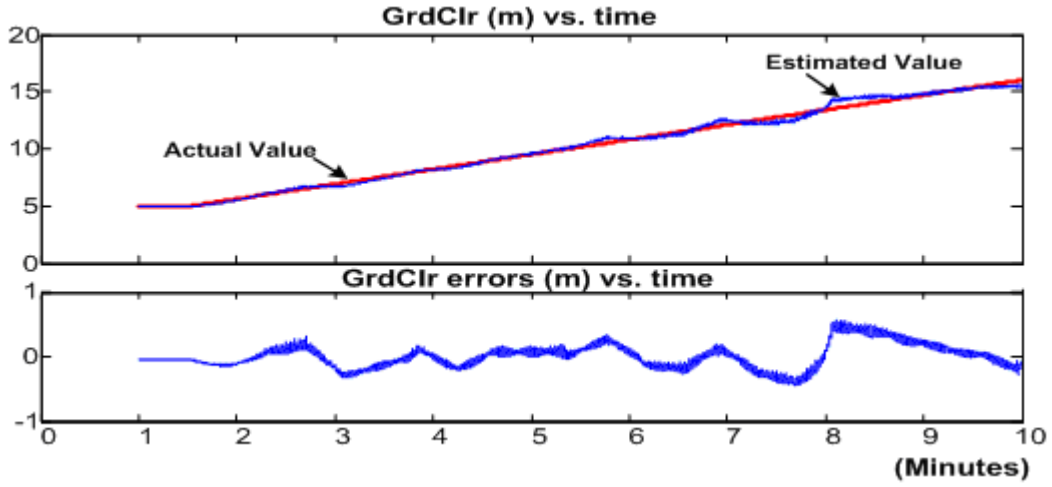

Figure 7.14. Conductor-to-ground clearance estimation.

So far, a mathematical space-phasor model of the E-field distribution around the mDCSs surface in a 3-Φ overhead power line system has been established by using the

concept of distributed capacitance density (D_cap). The novel and original mDCS, with six capacitors, has been proposed to capture the E-field spatial distribution around an overhead conductor, by measuring the six displacement currents $i_{d\_i}(t)$ flowing through the mDCS's six capacitors C_i, for i = 1~6. The simulation results have shown the proposed method as a promising solution to enable independent measurements of conductor-to-ground clearance as well as overhead conductor voltage.

However, the success of this proposed method depends on a reliable and accurate measurement of the displacement currents, which are typically in the order of 0.x μA for a 3-Φ overhead power line system. The following section, therefore, presents an effort to validate the feasibility of measuring the displacement current in a scaled-down, single-phase, 160V @ 60 Hz system in a laboratory environment.

7.6 Displacement Current Measurement and Experimental Validation

As discussed in Section 7.1, the displacement current flowing from an overhead conductor to its surroundings is affected by the capacitive coupling strength between the conductor and its adjacent conductors. This capacitive coupling is represented by the D_caps in a 3-Φ power line system as shown in Figure 7.4. The D_cap concept forms the foundation in developing the mathematical model of the E-field distribution around the mDCSs surface. Therefore, this section starts with an evaluation of the actual D_cap values for the 3-Φ power line system shown in Figure 7.1. The results consequently provide a guideline to determine/design a laboratory testing arrangement, so that the experimental setup can provide the capacitive coupling on a similar scope of that in the 3-Φ overhead power line system shown in Figure 7.1.

7.6.1 Displacement Current Sensing around an Overhead Power Conductor

To understand the range of the D_cap values, the 3-Φ overhead power line system shown in Figure 7.1 is analyzed in the Maxwell Electrostatic 2D simulation environment. For example, the D_cap of the mDCS subject to ground can be expressed by (with reference to Figure 7.3 (b)),

$$c_{Cg}(\varphi) = \frac{\rho_C(r,\varphi)}{V_{Cg}} = c_{Cg\_m} + \Delta c_{Cg} \cdot \cos(\varphi) \tag{7.37}$$

where c_{Cg_m} represents the **common-mode** component of the D_cap, and Δc_{Cg} is the **differential-mode** component. Figure 7.15 shows that both c_{Cg_m} and Δc_{Cg} subject to conductor-to-ground clearance varying from 5 to 16 meters.

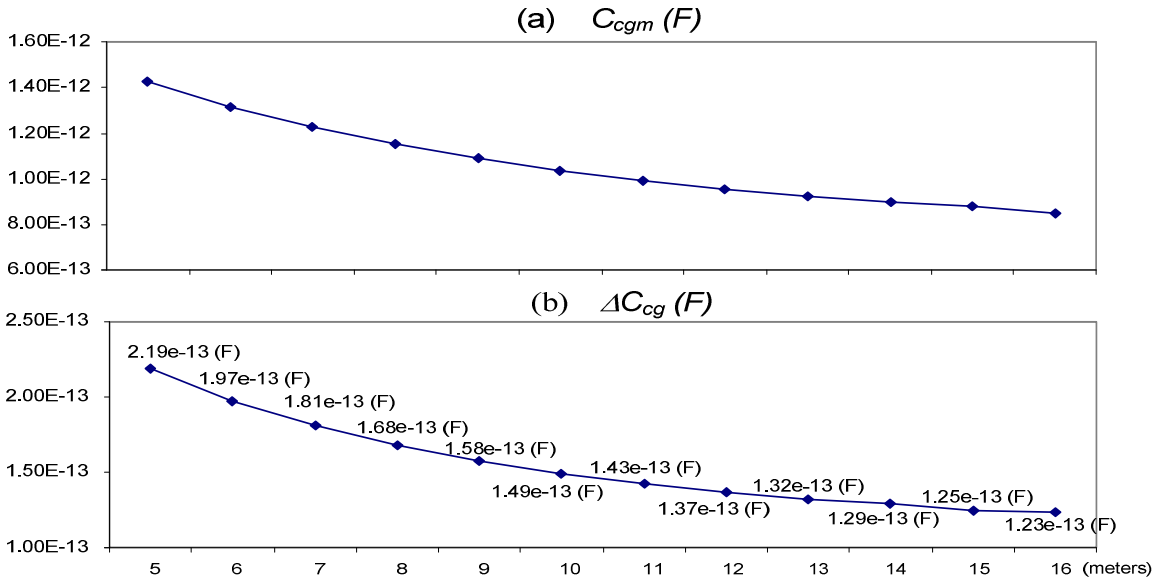

Figure 7.15. D_cap of mDCS subject to ground vs. conductor-to-ground clearance: (a) Common-mode component c_{Cg_m}; (b) Differential-mode component Δc_{Cg} (Maxwell Electrostatic 2D).

As discussed in the previous sections, the D_cap differential-mode components play an important role in this proposed method. Being able to detect the capacitance variation in the differential-mode components is therefore essential. If only the differential-mode D_cap is considered, the analytical results in Figure 7.15 indicate that, to detect a change in conductor-to-ground clearance with a resolution of 1 meter, the mDCS is required to measure a capacitance value in the order of 0.x pF, but with a resolution of around 0.00x pF. In a 115 kV power line system, the sensing circuit should be able to measure the displacement current flowing from the overhead conductor to its adjacent conductors in the order of x0 μA with a resolution of 0.0x μA. This is a challenging low current measurement problem.

Figure 7.16 gives a generic representation of the proposed mDCS sensing scheme in an overhead power line system. The figure only indicates the measurement for the displacement current i_{d_1} flowing through the metal arc plate S-1 as an example. The current sensor is denoted to be Displacement Current Sensor – 1 (DCS-1) as shown in the figure.

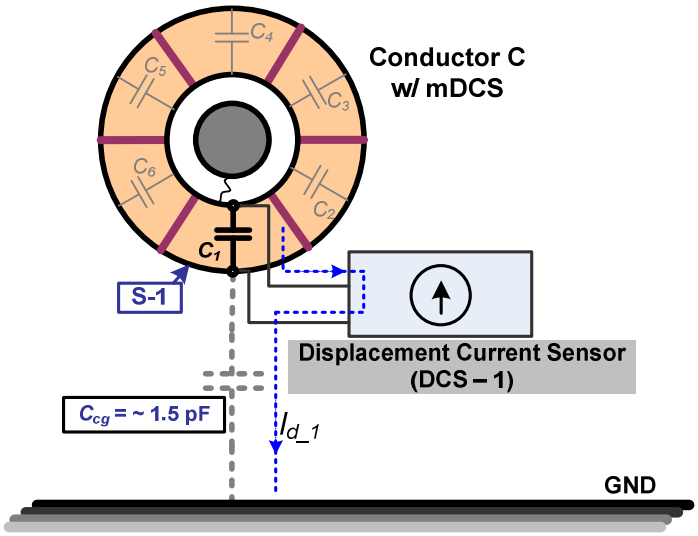

Figure 7.16. Generic representation of mDCS sensing scheme in an overhead power line system, with i_{d1} measurement as an example

One of the main objectives and challenges in the experimental validation presented in this section is to design a Displacement Current Sensor (DCS) that is capable of measuring small current (in the order of x0 μA with the resolution of 0.0x μA as discussed above). Another challenge in this experiment is to design a proper experimental arrangement in the laboratory environment, so that the testing setup can provide the capacitive coupling in the order of the differential-mode D_cap as shown in Figure 7.15.

The following subsection firstly introduces a laboratory testing arrangement specifically designed for this experiment, which is driven by a scaled-down, single-phase, 160 V @ 60 Hz voltage source. Then, a Displacement Current Sensor (DCS) is proposed and tested in the lab setup with experimental results validation.

7.6.2 Displacement Current Sensor Experimental Validation in a Scaled-Down 160 V Single-Phase System

The physical laboratory testing setup is depicted in Figure 7.17, and Figure 7.18 shows the schematic of the setup. For the convenience of installation, this laboratory setup adopts a parallel-plates capacitor arrangement, where a wooden frame is used to separate the metal plates, i.e., Plate-1 and Plate-2, as shown in Figure 7.17. This arrangement is supplied by a 160 V @ 60 Hz, single-phase voltage source power supply, where the metal Plate-1 that is suspended at the top of the frame has the potential of 160 V with respect to the Ground-Plane at the bottom of the frame, as shown in Figure 7.17 and Figure 7.18. Plate-2 is separated from the Ground-Plane by a layer of dielectric material, which forms a sensing capacitor C_s, as illustrated in Figure 7.18. C_s is used to facilitate measuring the displacement current I_d following from Plate-1 to Plate-2. It is noted that, the sensing capacitor C_s plays the similar role as the C_1 in Figure 7.16. At the

same time, the tested capacitor C_t between Plate-1 and Plate-2 in Figure 7.18 is designed to be equivalent to the capacitor C_{og} as indicated in Figure 7.16.

The dimensions of the parallel-plate arrange are shown in Figure 7.16. For this arrangement, because the distance between the two metal plates, *h,* is large with respect to the area of the metal plates, the "fringing effects" at the edges of the capacitor can not be ignored. At the same time, in the laboratory environment, the parasitic couplings between the testing setup and any conducting surfaces in close proximity form stray capacitances and introduce errors into the measurement.

In this experiment, the influence of fringe fields and stray capacitive couplings are reduced via the use of a Kelvin guard-ring geometry [118] [119], in which the inner Plate-1 is shielded by a Grounded Guard-Ring (G-GR), as shown in both Figure 7.17 and Figure 7.18. There is a small air gap between the outer edge of Plate-1 and the inner edge of the G-GR. The gray lines in Figure 7.18 give a generic representation of the resultant E-field distribution among Plate-1, Plate-2 and G-GR under this arrangement, which effectively reduces the measurement errors and uncertainties that are caused by the other conductors in the lab in the proximity of the experimental setup.

Figure 7.18 also shows the schematic of the proposed displacement current sensor (DCS), where a transimpedance amplifier is used to convert the small displacement current I_d into a measurable voltage V_{out} via the feedback resistor R_f. The current is measured from the point **A** as shown in both Figure 7.17 and Figure 7.18. This is the configuration of a typical feedback-type transimpedance, and the transfer function is given by,

$$V_{out} = I_d \cdot R_f \tag{7.38}$$

However, to obtain a reliable and accurate measurement of a small current in the order of x0 µA with the resolution requirement of 0.0x µA as discussed above needs careful design of the circuit with special techniques for prototype board layout.

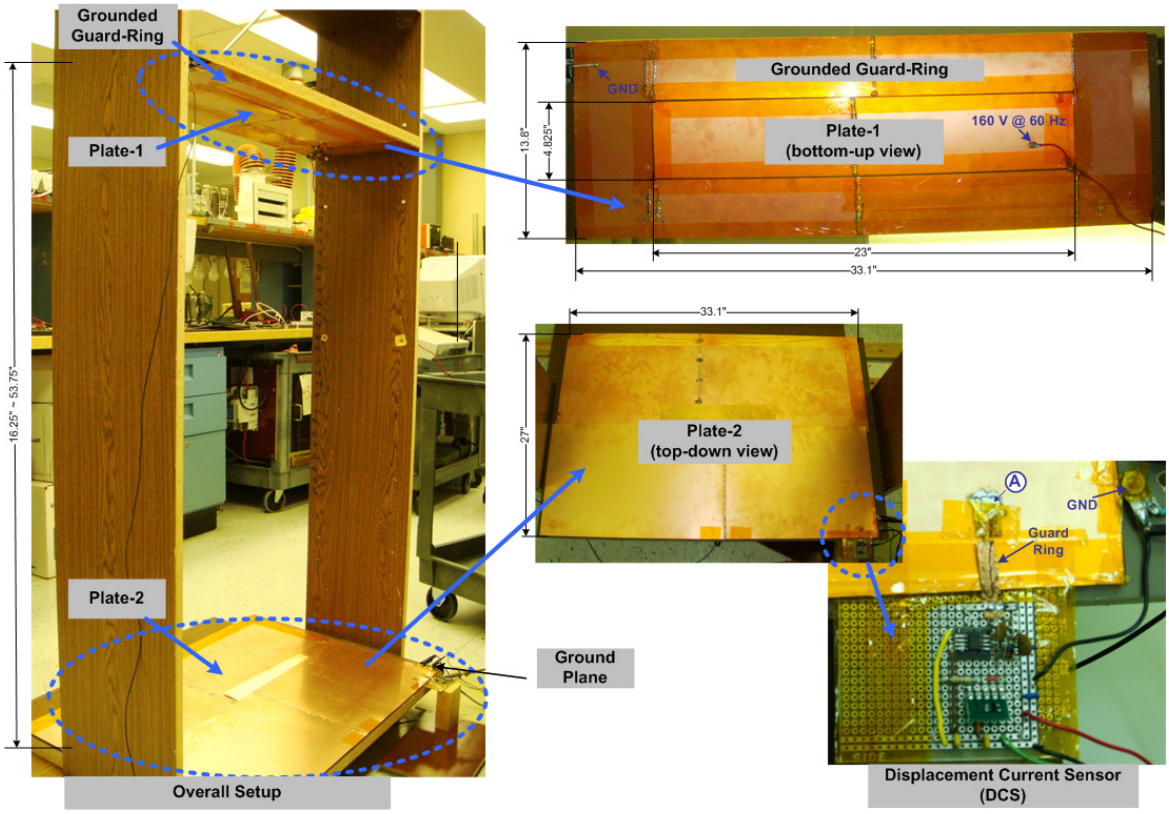

Figure 7.17. Laboratory testing arrangement for displacement current measurement.

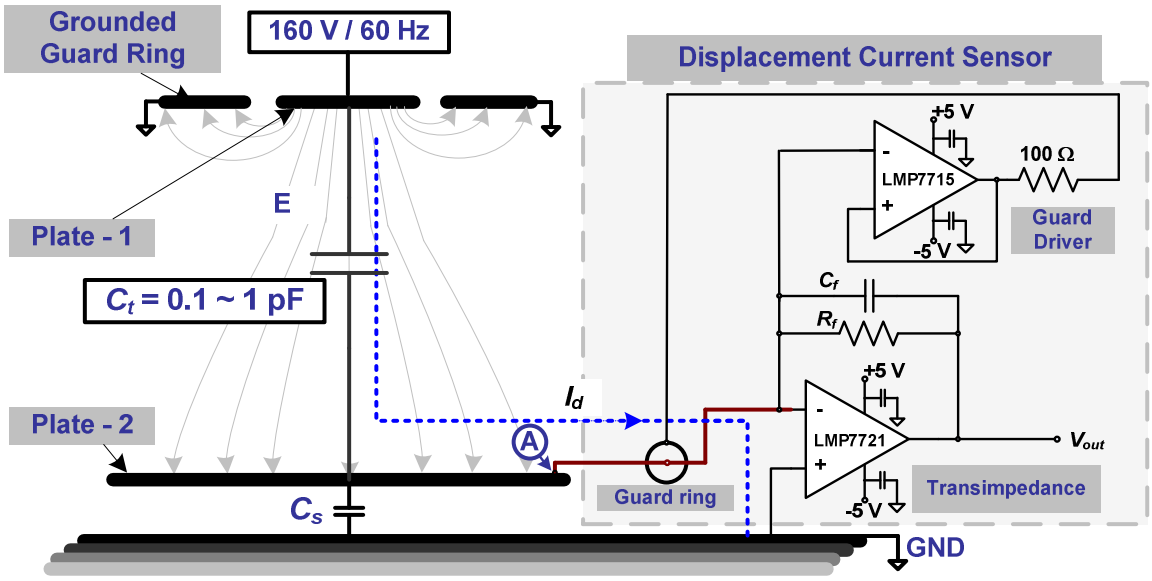

Figure 7.18. Schematic of the experimental setup and the displacement current sensing scheme.

With reference to Figure 7.18, I_d flows from Plate-1 to Plate-2. The inverting input of the transimpedance is connected to point A on Plate-2 via an input conductor lead (highlighted in red in Figure 7.18 and denoted as the "sensitive current path") to pick up the measured current I_d. In the prototype board layout, there are always high resistance paths, between this "sensitive current path" and near by voltage sources or ground, which can cause significant leakage currents. These leakage currents in turn introduce the errors in the current measured by the transimpedance or even mask the real current value. In this proposed DCS, this effect is eliminated through guarding techniques. As shown in both Figure 7.17 and Figure 7.18, a guarding conductor is driven by a low impedance source, denoted as the Guard Driver, and remains at the same potential as the "sensitive current path". The guarding conductor totally surrounds the "sensitive current path" and prevents leakage from the various circuit elements in the proximity.

Besides, because the amount of the measured current is small in this application, it requires a large gain from the amplifier to transform the miniscule current into easily

detectable voltage. A large value R_f is often needed and a 25 MΩ feedback resistor is used in this application. However, such a large feedback resistor potentially introduces large errors caused by the amplifier bias current. To minimize this effect, the proposed DCS utilizes an ultra low input bias current amplifier, i.e., LMP7721, with the input bias current of 3 fA and a guaranteed limit of +/-20 fA at 25 ^{o}C [120].

With reference to the schematic shown in Figure 7.18, the output voltage of the DCS, V_{out}, is related to the tested capacitor between Plate-1 and Plate-2, i.e., C_t, as follows,

$$V_{out} = \frac{V_{source}}{2\pi f \cdot C_t} \cdot R_f \tag{7.39}$$

where V_{source} = 160 V and f = 60 Hz.

To validate that the DCS is able to measure the displacement current flowing from Plate-1 to Plate-2, i.e., I_d, subject to any change in C_t, the distance between Plate-1 and Plate-2, h, changes from 16.25 to 53.75 inches, with an increment of 2.5 inches, as shown in Figure 7.17. The DCS's output, V_{out}, for each case is measured, and corresponding C_t is estimated based on (7.39). Figure 7.19 shows the resultant $C^{\wedge}_t$ via the direct displacement current measurement. For comparison purposes, the capacitance of the lab arrangement in Figure 7.17 is also evaluated analytically by using the approximation suggested in [121], where Hegg proposes a capacitance correction of a parallel-plate arrangement considering the fringing effect The resultant analytical C^{*}_t for each distance arrangement between plates is also presented in Figure 7.19. The result shows a promising match between the measured and analytical values. Because the analytical evaluation considers a ground plane being infinitively large, the resultant C^{*}_t is on average larger than $C^{\wedge}_t$.

When the distance, between Plate-1 and Plate-2, increases, the difference becomes even more obvious. However, the main purpose of evaluating C_t analytically is to help

validate that the lab setup shown in Figure 7.17 is able to provide the capacitance in the order of 0.x pF, with fine enough granularity (i.e., 0.00x pF), as depicted in Figure 7.19. The exact difference will depend on the accuracy of the measurement system. At this early stage on the research, the fact that the trend in the measured curve agrees with that of the analytical curve is more important than absolute values. As the most interesting information is the change in the displacement, any systematic errors will be cancelled out.

To show that the DCS's output voltage V_{out} is able to provide enough sensitivity to detect the capacitance variation of 0.00x pF, Figure 7.20 depicts the measured V_{out} with respect to the distance between Plate-1 and Plate-2 varying from 16.25 inches to 53.75 inches (Refer to Figure 7.17). Two conditions are particularly marked as an example representing the most challenging case, when the plates' distance changes from 51.25 inches to 53.75 inches. The figure indicates that the measured V_{out} changes from 240 mV to 236 mV correspondingly. With reference to Figure 7.19, this 4 mV voltage variation represents a capacitance change of 0.002 pF from 1.59e-13 F to 1.57e-13 F.

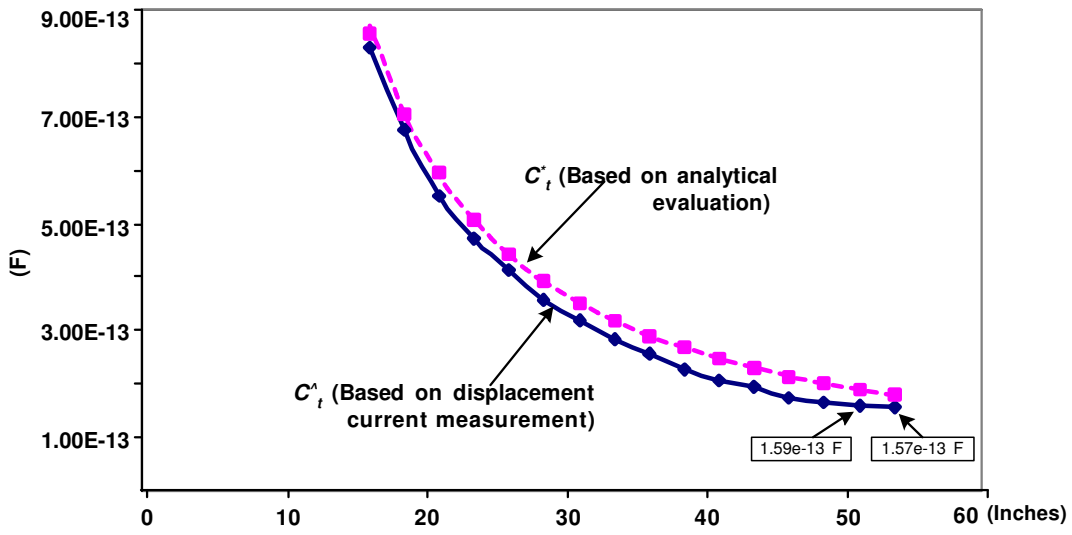

Figure 7.19. C_t evaluated by the direct displacement current measurement vs. C_t simulated in the Maxwell electrostatic 2D environment

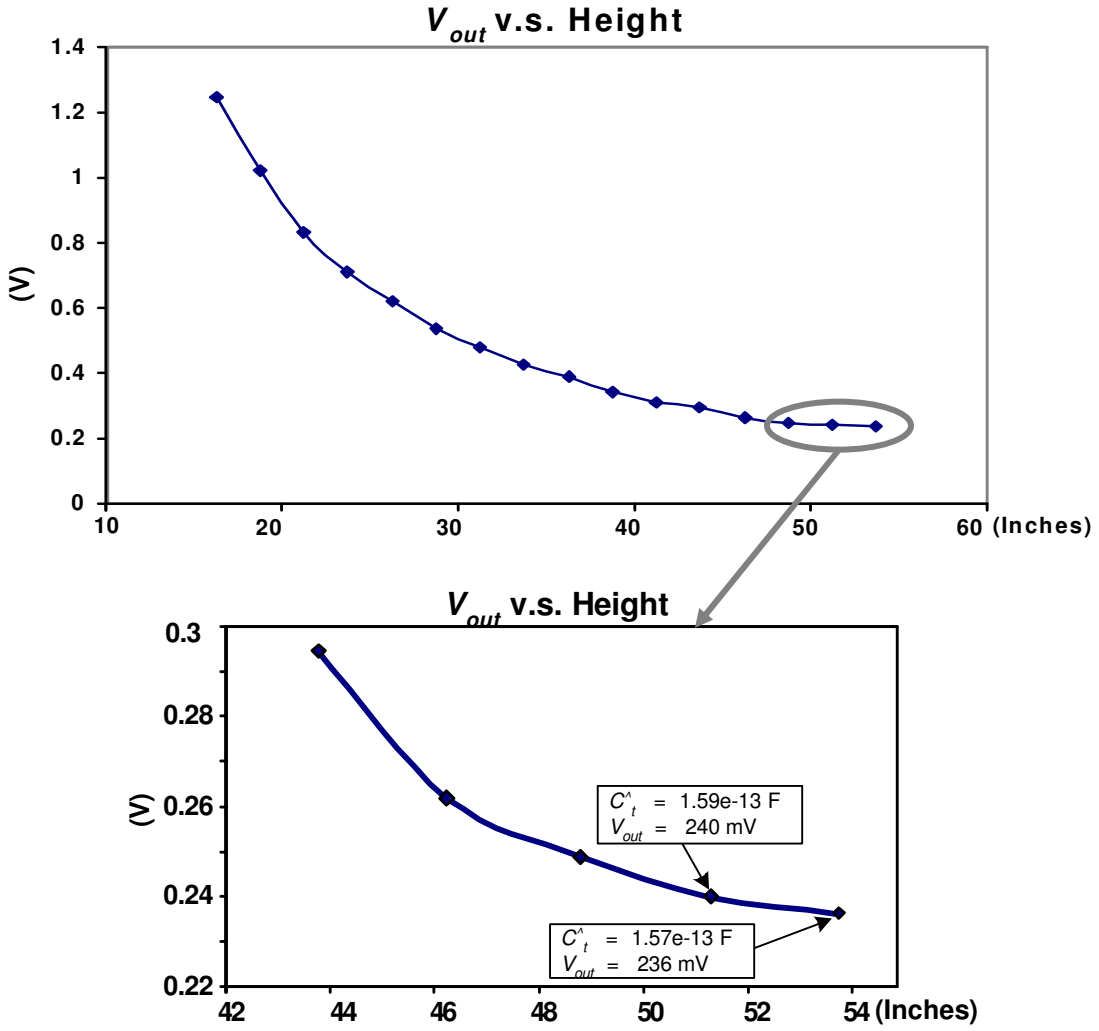

Figure 7.20. DCS's output voltage V_{out} vs. parallel plates distance

The experimental results presented in this section validate that the proposed DCS is able to detect small capacitance variations (i.e., 0.00x pF) with fairly high sensor output sensitivity up to x mV. One of the advantages of the proposed sensing scheme is that the DCS implements the direct displacement current measurement, in stead of measuring voltage signals across sensing capacitors as normally adopted in the literature [114]. The ultra-low input impedance of the transimpedance in Figure 7.18 bypasses the sensing

capacitor C_s (i.e., *C1~C6* in Figure 7.16), the displacement current I_d, therefore, directly flows through the DCS, and the value of C_s does not affect the measured result. This fact especially benefits, when the DCS scheme is applied to the mDCS scheme for the 3-Φ overhead power line system. As shown in Figure 7.16, six DCSs are needed to capture the displacement currents in different directions around the overhead conductor. The performance (or circuit parameters) of the six sensors must be close to each other in order to capture the realistic mapping of the E-field distribution around the conductor. This direct displacement current sensing scheme allows higher tolerance to the difference among the six capacitors. This greatly relieves the precision requirement when the sensor is designed and manufactured, and consequently reduces the cost.

7.7 Chapter Summary

This chapter has proposed a novel mDCS, as a part of the PLS module, for overhead power line vicinity monitoring. The mDCS is capable of measuring the spatial mapping of the E-field distribution around overhead conductors. A DQ-axis decomposition technology is used to analyze the spatial E-field distribution, and thus to separate the capacitive coupling effects from mDCS adjacent conductors in different directions. The decomposed DQ-axis components show their potential to enable independent measurements of conductor-to-ground clearance as well as overhead conductor voltage.

The proposed mDCS scheme is a passive sensing solution. It only requires a simple capacitor add-on to the existing PLS module, which is low cost, robust, and easy to implement. The importance of this result is that this method does not only provide a promising solution to measure the conductor-to-ground clearance, but also allows assessment of the clearance between line conductors thus to detect possible abnormal conductor movements, such as conductor gallop. At the same time, this method has shown the potential to measure the voltage magnitude of an overhead power line. It

eliminates the needs for high voltage isolation, which is normally required by conventional expensive and bulky high-voltage measurement solutions, and provides a low-cost solution for high-voltage measurement in power system application.

This chapter has also presented a preliminary experimental validation of the proposed method in a scale-down, single-phase, 160 V @ 60 Hz system. The experimental results have indicated that the proposed displacement current sensing scheme is able to detect a small capacitance variation (on the scope of 0.00x pF as required by the application) with the sensor output sensitivity of x mV. The results have greatly encouraged the further investigation by applying the sensing scheme to the proposed mDCS in a 3-Φ overhead power line system, and consequently the experimental validation of the theory developed in this chapter.

However, there are several drawbacks to this method. First of all, since the length of the proposed mDCS sensor is limited (say 1 meters), the method only shows its benefit to detect the variations in conductor separation or conductor-to-ground clearance caused by the conductor inherent movements, such as conductor sag or conductor gallop. Any other discrete line disturbances, such as proximity of tree branches, may not be detected effectively, unless the disturbance happens close to the sensor itself. Nevertheless, the proposed mDCS sensing scheme shows as a promising low cost, simple solution for overhead power line vicinity monitoring, as well as high voltage measurement.

So far, the two functions of the PLSN from the end-user perspective have been introduced. In the following chapter, the design and implementation of a prototype PLSN are introduced with preliminary experimental results validating its basic performance.

CHAPTER 8

PROTOTYPE POWER LINE SENSOR NETWORK AND EXPERIMENTAL VALIDATION

The design and implementation issues of the proposed PLSN are addressed in this chapter. As the platform of the proposed work, a prototype PLSN has been developed in the Intelligent Power Infrastructure Consortium (IPIC) lab at the Georgia Institute of Technology. A prototype PLS module has been built with four functions integrated, which have been validated in a laboratory environment. Experimental results are presented to validate the feasibility of the proposed scheme. The lab PLSN shows its capability as a platform to demonstrate more advanced functions in future work.

8.1 Power Line Sensor Module Design and Its Implementation

Overhead power lines operate in hostile environments, with high electrical and magnetic fields, extreme temperatures and weather conditions. The issues concerning the PLS module design are greatly driven by the unique aspects of the environment. Some important design considerations are addressed about the following aspects:

- Energy Scavenging and Power Management Unit: converting sufficient power to meet the module internal needs over a wide range of current levels, including fault currents and lightning strikes.
- Sensing and Signal Conditioning Units: providing accurate, cost effective, and reliable measurement, considering mechanical mounting difficulties, electromagnetic interference from the power line conductor, etc.
- Wireless Communication Unit: providing simple but reliable communications between sensor modules, self-organizing/healing network capabilities, and multi-hopping solutions for wide area monitoring in particularly hostile high-voltage environment.

- Digital Signal Processor (DSP) unit: sufficiently fast to handle real time monitoring, diagnostic, and communication, etc., simultaneously, with enough memory space for local computation.

The proposed PLS module consists of the four sections stated above. Figure 8.1 gives a general representation of such an implementation.

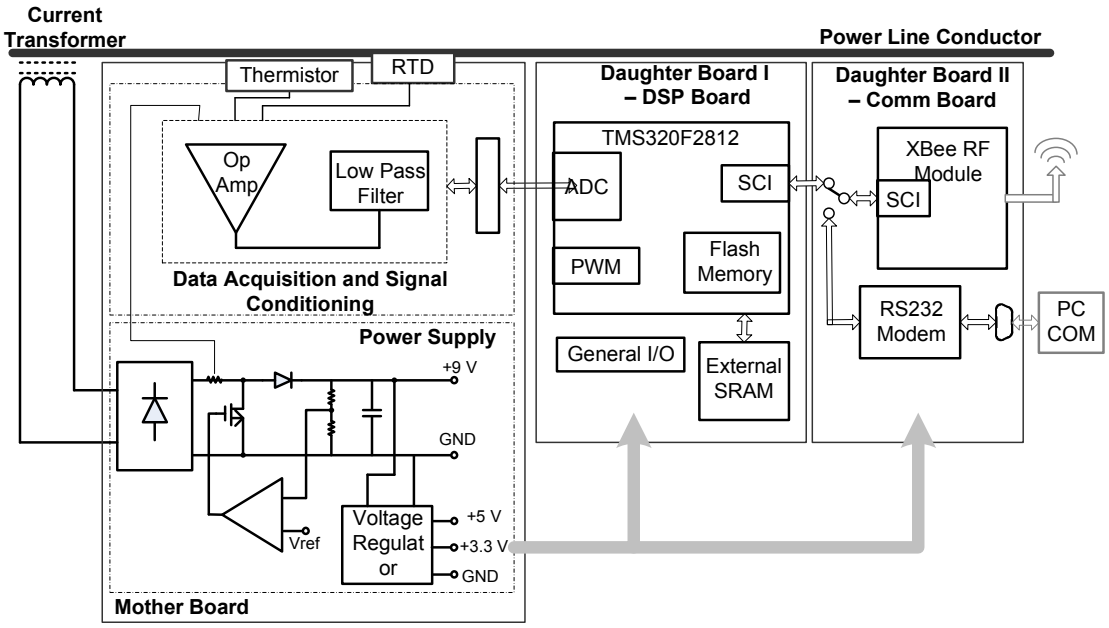

Figure 8.1. Power Line Sensor (PLS) Module Schematic

While the power line sensor concepts can be extended across the entire transmission and distribution domain, the initial targets are for power lines rated at 69 kV and higher. For a typical transmission and distribution line operating at 138 kV level, the line parameters are shown in Table 8.1, which are used as a reference when the sensor module is designed.

Table 8.1 LINE PARAMETERS [126]

Operating Line Voltage	Thermal Capacity	Outside radius
138 kV	750 A	30 mm

8.1.1 Energy Scavenging and Voltage Regulation Unit

The energy scavenging and voltage regulation unit is perhaps the most critical design issue for the PLS module. The proposed sensor modules are placed in a high-voltage area, and massively deployed in a wide geometrical area of the power grid, therefore being autonomous and self-sustained is important to each sensor module. Each module is able to convert energy from its surroundings to support its internal electrical circuitry, with no battery/replacement and minimum maintenance.

The PLS module energy scavenging function is accomplished by a single turn current transformer, of which the cylindrical core consists of two parts that can be physically clamped around the power conductor forming a complete magnetic circuit. The power line itself acts as the primary side windings of the transformer. The secondary winding is wound on the cylindrical core with multiple turns to transform the operating line amperes to an appropriate lower value sustainable for the subsequent voltage regulation circuitry.

The single turn current transformer core uses the same design as the series D-FACTS devices in [126]. Most of the design considerations apply to the trade-off criteria for this application such as the weight of the core, mechanical clearance, and magnetizing inductance value of the transformer seen from the power line side, etc. The main properties of the core appear in Table 8.2.

Table 8.2 TRANSFORMER CORE GEOMETRY [126]

Mechanical Clearance	Inner Radius	Outside Radius	Length	Weight of Iron
5 mm	25 mm	45 mm	15m m	0.4 Kg

For the particular application of coaxial transformers considered here, the magnetic path of the core will always have a small air gap, as a result of the separable cores needed

for clamp-on. The air-gap is desired and can be tuned to maximum power capacity of the transformer without causing saturation of the core.

Considering the general functionalities shown in Figure 8.1, the power requirement for such a PLS module can be estimated, as shown in Table 8.3.

Table 8.3 PLS MODULE POWER REQUIREMENT

	Typical Power Requirement		
	V(volts)	**I_{max}(mA)**	**P(watts)**
Comm. Transmit Power	3.3	300	100 m
Comm. Receiving Power	3.3	100	50 m
DSP	3.3	30	100 m
Sensing & Signal Conditioning	5	100	500 m
Available Capability			4

Silicon steel with a relative permeability of 5000 is used as the core material. The peak flux density of 1.55 T is observed at the inner circumference [126]. The current transformer is capable of delivering power up to 6 W from the power line to the sensor module's internal circuitry, which is sufficient to meet the requirement in this application.

The module is designed for a line current of up to 1000 A. The design of the secondary windings is primarily governed by the open circuit voltage that the secondary side circuit components can withstand, and the maximum current under normal and faulted conditions. The electrical rating of the voltage regulation circuitry has a direct bearing on the module's size and weight. Under an operating line current of 1000 A, the turns ratio of 100:1 brings the open circuit voltage to 20 V on the secondary, and the continuous secondary side current is 10 A. This design can be used with the commercially available power electronic devices, thereby keeping the size and weight acceptable.

Figure 8.2 shows the voltage regulation circuit used in this application. A full bridge rectifier is directly connected to the current transformer secondary side winding, followed by a boost switching regulation circuit. The switching signal, I_g, as shown in Figure 8.2,

is the output of a comparator U02 with a reference signal V_{ref} and the regulated voltage feedback V_{fb} as inputs. I_g serves as the gate signal of the switching device Q1, which is used to regulate the DC voltage V_o to around 9 V. The cascaded voltage regulation stages provide 5 V and 3.3 V respectively for the communication, DSP, and signal conditioning circuit. Appendix H.1 describes the components values of PLS module power supply circuitry in details.

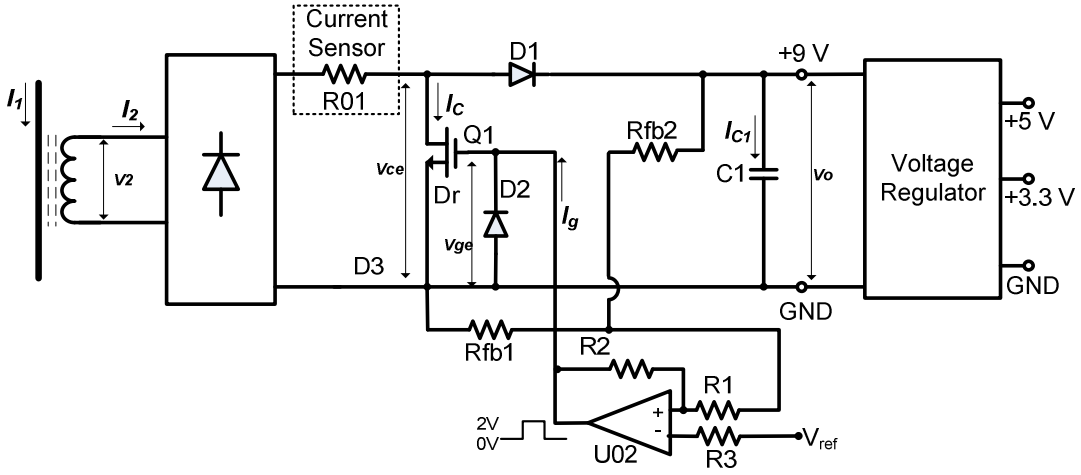

Figure 8.2. PLS Module power supply circuit

Under power line fault conditions, fault currents can be as high as 50 kA, which can cause large voltage spikes on the secondary of the transformer. These voltage transients can be damaging for the module internal circuitry and it is desirable to bypass it once the fault is detected. Reference [126] addresses the design considerations on the issue of secondary protection under high fault current conditions.

8.1.2 Sensing and Signal Conditioning Unit

The proposed sensor module specifically targets the use of passive sensing technologies, with a primary focus on evaluating the dynamic capacity of a specific span

of the power line under current weather conditions. The design of the sensing and signal conditional circuitry only focuses on real-time monitoring of the line current, ambient temperature and conductor temperature at this stage of this research. The other two applications for power line vicinity monitoring via electromagnetic field measurement require additional hardware design sensing and signal conditioning functionality, but these are interesting topics for future work.

Cost-effective, accurate and reliable real-time measurement is important in the sensor module design, especially under the hostile environment of high-voltage power lines. In this application, a Resistance Thermal Detector (RTD) is selected to measure the conductor surface temperature, and a thermistor is used to measure the ambient temperature. The applications of both thermal sensors are based on their resistance-temperature characteristics. In order to reduce the electromagnetic interference caused by the high current flowing through the power line conductor, twisted pair cabling needs be used for any voltage signal measurement. For the current measurement, a low value high precision resistance is connected in series to the output of the full-bridge rectifier, as shown in Figure 8.2. The average value of the voltage across the resistance is proportional to the RMS value of the conductor current, if the current transformer is assumed to be ideal.

When the PCB board is designed, a grounding loop has to be cautiously avoided; otherwise, a substantial voltage of up to 500 mV is induced on the grounding system because of the high magnetic field near the power line.

8.1.3 IEEE 802.15.4 RF Unit

In this work, an off-the-shelf communication approach is adopted based on Wireless Sensor Network (WSN) technologies. Digi's XBee-PRO RF Module [76] is selected to provide the wireless communication function for the PLS module. The XBee PRO is

engineered to meet IEEE 802.15.4 standards and support the unique needs of low-cost, low data rate, simple connectivity, and low-power WSNs. It operates at the ISM 2.4 GHz frequency band, with a maximum over-the-air data rate of 250 kbps. Due to the overhead of the protocol the actual theoretical maximum data rate is approximately half of the theoretical maximum. IEEE 802.15.4 specifies the use of Direct Sequence Spread Spectrum (DSSS) and uses an Offset Quadrature Phase Shift Keying (O-QPSK) to modulate the RF carrier [62]. This helps to enhance the communication immunity to ambient noises, especially to those with wide frequency bandwidth, such as impulse noises commonly observed in the high-voltage power line environment.

Besides, the RF module can operate at different modes under various conditions, each of which has a different power requirement. Correct design of the switching scheme between modes can help to reduce a module's power consumption.

8.1.4 DSP Unit

The DSP unit is the core of the PLS module, coordinating the module internal sensors and integrating all the functions. This upgrades the PLS module from just a sensory device to a 'smart' alternative which is capable of accomplishing higher level monitoring and diagnostic tasks.

A Texas Instrument TMS320F2812 DSP [127] is used. The F2812 is a fixed point, low power consumption DSP. Its 32-bit high performance CPU offers up to 150 MIPS operating speed. It consists of up to 128K words on-chip Flash memory for program storage, and 64K word off-chip SRAM memory space for data storage. It is efficient in DSP math tasks, and is capable of handling high numerical resolution problems that would otherwise demand a more expensive floating point processor solution.

The F2812 offers an extensive peripheral interface, such as analog-to-digital converter (ADC); synchronous/asynchronous serial interface (SPI/SCI), up to 48 general

purpose I/Os, and two event-manager modules. The integrated peripherals of the F2812 make the device capable of servicing and coordinating many asynchronous events with minimal latency. In this work, four Channels of 12-bit ADC are used to capture the analog signals from the sensors, and a SCI port connects the DSP device to the XBee RF module.

Asynchronous external events are handled by peripheral Interrupt Service Routines (ISRs), such as analog signals acquisition, communication requests, and abnormal operation interrupt, etc. Periodical ISRs are governed by the CPU-Timer 0, with the basic sampling rate of 10 kHz, which is designed as Multi-Task-Handler (MTH). Multiple tasks are assigned into different time slots based on their variant priorities and sampling rate requirements, such as sensor calibration, communication application interface, and other application level tasks. This design increases the system flexibility and scalability, and simplifies the procedure when more advanced monitoring and diagnostic tasks are added to the system in future, such as line dynamic thermal rating evaluation, power line environment monitoring, artificial intelligent learning process, etc. The integrated multiple tasks scheme is illustrated in Figure 8.3.

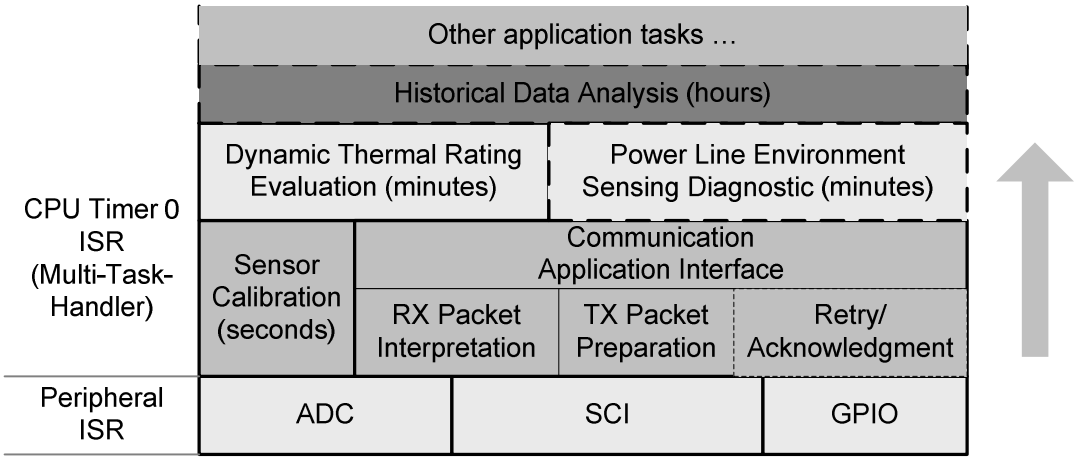

Figure 8.3. CPU Multi-Task Handler

8.2 Prototype PLSN and Experimental Validation

As the platform of the proposed work, a prototype PLSN has been developed in the Intelligent Power Infrastructure Consortium (IPIC) lab at the Georgia Institute of Technology.

8.2.1 Prototype PLS Module

Integrated with all the functionalities discussed above, a prototype PLS module has been build and tested on a laboratory power line system in IPIC lab, as shown in Figure 8.4.

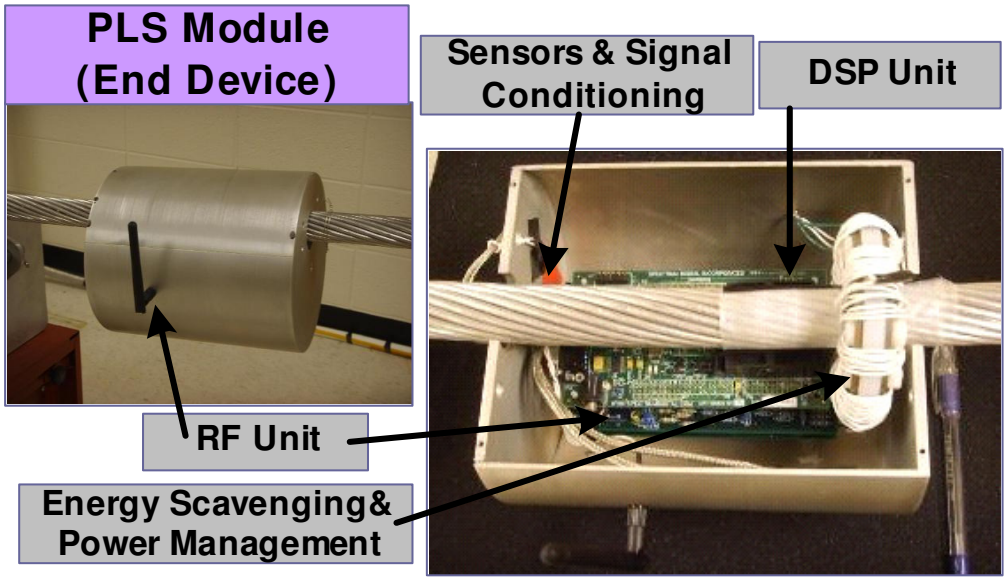

Figure 8.4. Prototype Power Line Sensor Module in IPIC lab

Table 8.4 summarizes the prototype PLS module's functionalities, and its implementation. The low cost of each module is one of the critical issues for the success of the distributed power line sensing concept. The design of the prototype PLS module suggests a primary price point of each module for around $100~200, which meets the target price point suggested by the survey results in [4].

Table 8.4 PLS MODULE FUNCTIONALITIES

Functions		Implementation
Communication Unit		MaxStream XBee-Pro based on ZigBee/IEEE 802.15.4
Sensing Unit	Current	High precision resistor
	Temperature	RTD; Thermistor
Signal Conditioning Unit		High-impedance differential Op-Amps
DSP Board		TMS320F2812
Energy Scavenging		C-core Current Transformer

8.2.2 PLS Module Stand-alone Performance Test

The prototype module has been tested in the lab on a Drake power line conductor, which is capable of carrying current of up to 1100 A. Preliminary results show that the module can be autonomously powered with the primary side power conductor current ranging from 100 A to 1000 A.

The sensor module is able to measure the line current with an accuracy up to 1.3%. The error mainly comes from the non-linear characteristics of the current transformer caused by core saturation especially under high current conditions. However, in this application, in which the power conductor thermal capacity estimation is of primary concern a 1% error of the current measurement is considered to be acceptable.

The sensor module offers a temperature measurement with an accuracy up to 1 ^{o}C. However, because of the wind shielding and thermal resistance between the thermal sensor and the conductor, as discussed in Chapter 5, the measured conductor temperature is normally lower than its actual value, and the error could be up to 5 ^{o}C. Therefore temperature-compensation needs to be included accordingly in future work.

8.2.3 IEEE 802.15.4 Data Transfer Performance

To test the communication protocol performance an indoor loopback test between the PLS module and host PC has been performed in the lab. A host PC is used to transmit the data stream (32 bytes/packet) continuously to the PLS module, and communication performance is evaluated via receiving the same data stream looped back from the remote PLS module clamped over the power line with current flowing through up to 1000A. Two criteria are evaluated, as shown in Table 8.5:

- RSSI: Received Signal Strength;
- PSR: Percentage of successful receiving.

Table 8.5 IEEE 802.15.4 PERFORMANCE TEST IN HC ENVIRONMENT (INDOOR)

Current (A)	Range (m)	RSSI (dBm)	PSR
1000	50	-70~-75	100%
	100	~-92	~45%
500	10	-45~-50	100%
	50	~-73	100%
	100	~-93	~45%

In order to evaluate the maximum transmission distance supported by this RF device, an outdoor test at Georgia Tech campus has also been done without considering the effect from high current/high voltage environment. Performance up to a distance of up to 700 meters, between two RF nodes, is evaluated, and Table 8.6 contains the results.

The test results show that a high current does not affect the performance of the communication. However, the obstacles between two communication nodes affect the performance dramatically. Even though the communication performance is degraded, an outdoor transmission distance of up to 400 meters is achieved with a successful transmission rate as high as 80%. The effect of high voltage, mainly due to the corona effect, will be evaluated in the future.

Table 8.6 IEEE 802.15.4 PERFORMANCE TEST IN OUTDOOR (@GT CAMPUS)

Range (m)	RSSI (dBm)	PSR	Conditions
200	~-76	~95%	Close to line of sight
400	~-83	~80%	Trees
500	-92	~35%	Trees & Buildings

8.2.4 IPIC Laboratory PLSN and Experimental Validation

To validate the system's performance, a laboratory PLSN has been set up in the IPIC lab as shown in Figure 8.5. The PLS module monitors thermal conditions and the current of the conductor locally, and sends the aggregated information to a remote host PC, with a RF data rate up to 250 kbps, located 5 meters away in the lab. The network performance is summarized in Table 8.7.

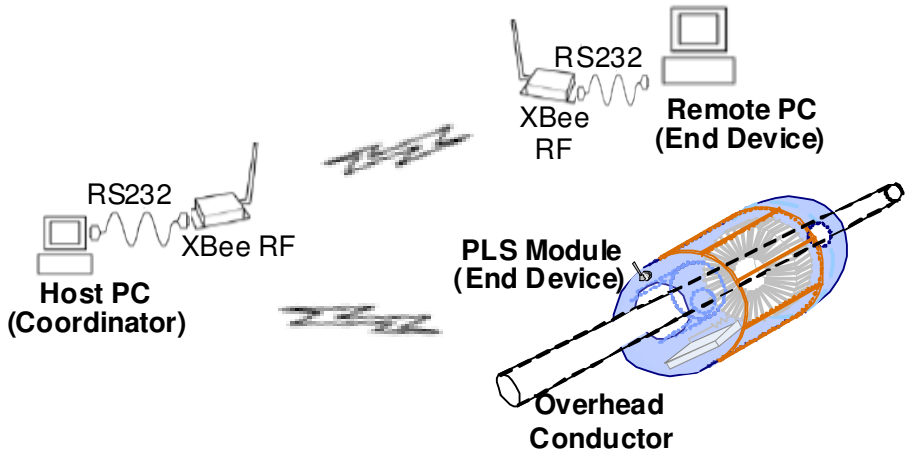

Figure 8.5. IPIC Laboratory Prototype Power Line Sensor Network

Table 8.7 IPIC LABORATORY POWER LINE SENSOR NETWORK PERFORMANCE

PLSN Networking Performance	
Outdoor RF Range	1.6 km
RF data rate	250 kbps
Packet TX rate	20 msec (100-byte)
Sensing Channel	Up to 8

Figure 8.6 presents four channels of signals received by the host PC every 0.2 ms continuously for two hours showing the communications performance of the prototype PLSN. The signals include the conductor temperature, the line current, the estimated cooling condition around the conductor, and the estimated thermal rating. The four channels of signals are transmitted from the PLS module clamped over the lab power line around 5 meters away from the host PC, as shown in Figure 8.5. The preliminary experimental results validate the prototype PLSN's capability to do the continuous real-time monitoring over the transmission line. A more advanced ZigBee networking performance will be tested in the lab as part of future work.

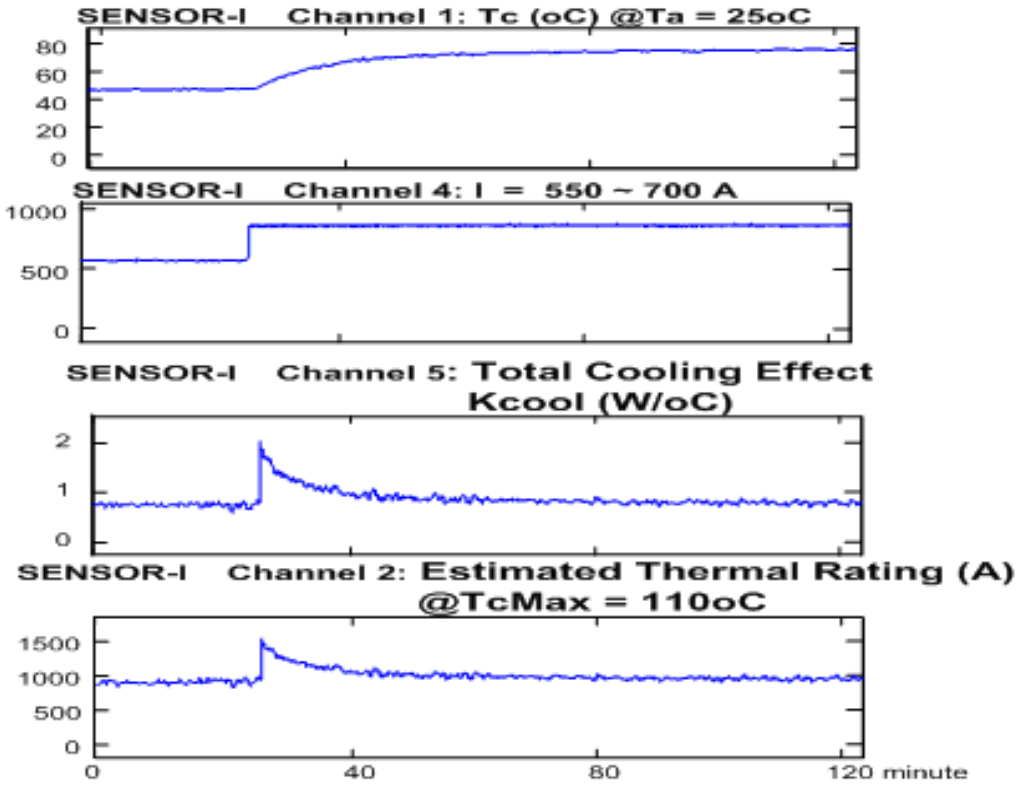

Figure 8.6. IPIC Prototype PLSN Experimental Results

8.3 Chapter Summary

This chapter has presented the design and implementation issues of the proposed PLSN. Its fundamental performance has been demonstrated in the laboratory environment, showing that the realization of such a distributed network can provide distributed and continuous on-line monitoring of transmission lines. The prototype PLS module and network using commercially available low power devices, offer the potential to dramatically reduce the cost of power grid monitoring. PLS modules require no change in utility infrastructure and operate autonomously, with no battery replacement requirement and minimum maintenance.

The laboratory PLSN provides a platform for the further evaluation of the functionality and performance of the proposed network.

CHAPTER 9

CONCLUSIONS AND CONTRIBUTIONS

9.1 Overview

This chapter summarizes the conclusions and lists the major contributions of this work. Recommendations for future work in the areas of overhead power line monitoring to assess a transmission line's safe maximum thermal capacity as well as a line's vicinity conditions are also presented.

9.2 Conclusions

This dissertation has proposed a distributed Power Line Sensor Network (PLSN) to provide continuous on-line monitoring of the power grid by using large amounts of low-cost Power Line Sensor (PLS) modules, and it has investigated the underlying technologies for implementing the PLSN that can enhance the utilization and reliability of the existing system.

Chapter 1 has introduced the background information and stated the objective of this research work.

In Chapter 2, a comprehensive literature survey has been presented to summarize the state of the art of existing sensing technologies, with a focus on two areas: real-time thermal condition monitoring of overhead power lines; electromagnetic (EM) signature measurement/analysis in the vicinity of overhead power lines. The existing communications technologies for power system applications have been summarized in Chapter 3, including wireless communications and power line communications, with a focus on the Wireless Sensor Network (WSN) technology. In addition, as one of the most important aspects for the successful implement of the proposed PLSN, the existing energy scavenging technologies have also been summarized in this chapter.

Chapter 4 has introduced the conceptual PLSN, including the principles of the basic PLSN operation. Three functions of the PLSN from the end-user perspective have also been briefly introduced.

The primary function of the PLSN is to evaluate the safe maximum thermal capacity of an overhead power line under various weather conditions in real time. Chapter 5 has proposed a Multilayer Perceptron Neural Network (MLPN) based method to evaluate the line real-time thermal rating of the line segment where the PLS module is mounted. The use of artificial neural networks helps to estimate the heat-removal capability of the conductor under present line loading and weather conditions, with only three real-time measurements, i.e. conductor temperature, ambient temperature, and conductor current. Simulation results have been presented to validate the proposed idea. However, the successful implementation of this proposed method still needs an analytical model of the conductor dynamics. The simplification of the model neglects several important conductor-thermal effects, and results in inaccurate thermal rating estimates. In addition, the complexity of the MLPN training process prevents the proposed method being a promising solution to real-time implementation.

To overcome the shortcomings of the MLPN-based method, another real-time dynamic thermal ratings strategy by using an Echo State Network (ESN)-based identifier has been proposed and presented in Chapter 6. This method adopts an ESN model to learn the overhead conductor thermal dynamics in real time, and in turn to predict the conductor temperature ahead of time up to 40 minutes. The ESN-based method eliminates the need for analytical models and relieves the difficulty to measure and quantify metrological parameters as required by traditional methods as well as the MLPN based method. This chapter has also validated the ESN's capability to adapt itself to changes in ambient weather conditions on a continuous base. A Sliding Window (SW)-based online adaptation algorithm has been proposed to ensure the stability of the ESN model in the online adaptation context. The online adaptive identification of the

conductor thermal dynamics based on an ESN has been validated in both the simulation and experimental environment. The results have shown that the proposed ESN-based method can help evaluate the safe operating margin (thermal rating) of a line segment where the PLS module is mounted under the present ambient condition on a continuous base. Coordinating the local safe operating margins from all the PLS modules along a power line, the operator can obtain an accurate operating margin, factoring in conditions over the entire length of the line, down to a granularity of the number of spans between adjacent sensors.

In Chapter 7, another ancillary function of the PLSN has been addressed, where the presence of incipient failures along an overhead power line needs to be detected and located by sensing and analyzing the EM signatures in the vicinity of the line with the PLS module as the platform. The electric field (E-field) around overhead conductors has been studied, and a Multiple Displacement-Current Sensor (mDCS), as a part of the PLS module, has been proposed. A DQ-axis decomposition technique has been applied to the E-field around the mDCS surface, in order to enable independent measurement of conductor-to-ground clearance and overhead conductor voltage. Simulation results have validated the proposed idea. The proposed mDCS scheme is a passive sensing solution. It only requires a simple capacitor add-on to the existing PLS module, which is low cost, robust, and easy to implement. The importance of this result is that this method provides a promising solution not only to measure the conductor-to-ground clearance, but also to assess the clearance between line conductors in order to detect possible abnormal conductor movements, such as conductor galloping. At the same time, this method has shown the potential to provide a low-cost solution for high-voltage measurement in power system application. This chapter has also presented a preliminary experimental validation of the proposed method in a scaled-down, single-phase, 160 V @ 60 Hz system. The experimental results have indicated that the proposed displacement current sensing scheme is able to detect a small capacitance variation (on the scale of 0.00x pF as

required by the application) with the sensor output sensitivity of x mV. The results have greatly encouraged further investigation by applying the sensing scheme to the proposed mDCS in a 3-Φ overhead power line system, and consequently the experimental validation of the theory developed in this chapter.

In Chapter 8, the prototype PLSN, developed in the Intelligent Power Infrastructure Consortium (IPIC) lab at the Georgia Institute of Technology, has been introduced. The PLSN fundamental performance has been demonstrated in the laboratory environment, showing that the realization of such a distributed network can provide distributed and continuous on-line monitoring of power lines. The lab PLSN has also shown its capability as a platform to demonstrate more advanced functions in the future.

9.3 Contributions

A comprehensive survey of the existing sensing technologies for power system applications has been presented and carefully analyzed. A complete survey of the state of the art in the fields of the existing communications technologies and the existing energy-scavenging technologies has also been prepared. These two sets of surveys have led to a good understanding of the full scope of potential applications, concerns, constraints and issues for the wide-scale deployment of distributed sensor networks for power grid monitoring.

A novel concept of a Power Line Sensor Network (PLSN) has been proposed to provide cost-effective, continuous and distributed large area monitoring of the power grid. By deploying low cost sensing technologies, and exploiting cost effective wireless communication technologies, i.e. WSN, it allows a dramatic reduction in cost and enables a grid-wide, distributed deployment of the PLSN.

As one of the main contributions in this research, the ability of artificial neural network technologies has been investigated and validated to estimate the heat-removal

capability of the line span where the PLS module is mounted, without the need for direct measurement of line ambient weather conditions. Two methods have been proposed. The Multilayer Perceptron Neural Network (MLPN) based method has been proposed to estimate two weather-related parameters that are in turn used to evaluate the real-time thermal rating of the line segment under different line loading and weather conditions.

To eliminate the need for an analytical model and relieve the difficulties to measure and quantify metrological parameters as required by traditional methods and the MLPN-based method, a novel Echo State Networks (ESN)-based method has been proposed. An ESN-based identifier has been proposed to learn the overhead conductor thermal dynamics in real time with only conductor current, ambient temperature and conductor temperature as inputs. The proposed ESN-based method enables the real-time evaluation of the safe operating margin (thermal rating) of a power line down to a granularity of the number of spans between adjacent sensors. It eliminates the need for direct measurement of line ambient weather conditions as often required by conventional methods. The low cost solution ensures the widespread and distributed deployment of the proposed PLSN and PLS modules. Coordinating the local thermal ratings from all PLS modules helps utility operators make an optimized load management decision and to utilize the lines (assets) more effectively, particularly during emergency conditions.

This research has also proposed and investigated two power line vicinity monitoring technologies to detect the health of overhead power lines and to predict incipient faults via sensing and analyzing the EM environment around an overhead power line.

A novel Multiple Displacement Current Sensor (mDCS), as a part of the PLS module, has been proposed to capture the spatial mapping of the E-field distribution around an overhead conductor, thus to sense the presence of incipient insulation failure between power conductors to ground, and/or to other nearby conducting objects. The analysis of the E-field distribution enables the independent measurements of both conductor-to-ground clearance and conductor voltage. The proposed mDCS scheme is a passive

sensing solution. It only requires a simple capacitor add-on to the existing PLS module, which is low cost, robust, and easy to implement. It enables a low-cost solution for high-voltage measurement in power system application.

The second part of the research in this dissertation has initiated a comprehensive investigation and development of practical and effective power line vicinity monitoring techniques, with the PLSN as the platform, via EM field monitoring and analyzing around overhead power lines. This part of the research has established a theoretical foundation that potentially leads to a cost-effective power line vicinity monitoring solution for real-time implementation.

A prototype PLSN has also been developed in the Intelligent Power Infrastructure Consortium (IPIC) lab. A prototype PLS module has been built with four functions integrated, which have been validated in a laboratory environment. The lab PLSN shows its capability as a platform to demonstrate more advanced functions in future work.

The research presented in this dissertation has resulted in several publications in electric power, computational intelligence, and diagnostic areas, listed as follows:

Conference Papers

- Y. Yang, D. M. Divan, R. G. Harley, and T. G. Habetler, "Power Line Sensornet – A New Concept for Power Grid Monitoring," in *Proc. 2006 IEEE Power Engineering Society General Meeting*, Montreal, Canada, June 2007.

- Y. Yang, F. Lambert, and D. M. Divan, "A Survey on Technologies for Implementing Sensor Networks for Power Delivery Systems," in *Proc. 2007 IEEE Power Engineering Society General Meeting*, Tampa, USA, June 2007.

- Y. Yang, R. G. Harley, D. M. Divan, and T. G. Habetler, "MLPN based Parameter Estimation to Evaluate Overhead Power Line Dynamic Thermal Rating," in *Proc. of the 15th International Conference on Intelligent System Applications to Power Systems (ISAP)*, Curitiba, Brazil, Nov. 2009.

- Y. Yang, R. G. Harley, D. M. Divan, and T. G. Habetler, "Adaptive Echo State Network to Maximize Overhead Power Line Dynamic Thermal Rating," in *Proc.*

IEEE Energy Conversion Congress and Exposition (ECCE'09), San Jose, CA, USA, Sept. 2009.

- Y. Yang, R. G. Harley, D. M. Divan, and T. G. Habetler, " Thermal Modeling and Real Time Overload Capacity Prediction of Overhead Power Lines," in *Proc. IEEE Symposium for Electrical Machines, Power Electronics & Drives 2009 (SDEMPED'2009)*, Cargese, France, Aug. 2009. (First Price Paper Award)

- Y. Yang, D. R. G. Harley, M. Divan, and T. G. Habetler, "Overhead Conductor Thermal Dynamics Identification by using Echo State Networks," in *Proc. 2009 International Joint Conference on Neural Networks (IJCNN'09)*, Atlanta, USA, June 2009.

- Y. Yang, D. M. Divan, R. G. Harley, and T. G. Habetler, "Design and Implementation of Power Line Sensornet for Overhead Transmission Lines," in *Proc. 2009 IEEE Power and Energy Society General Meeting*, Calgary, Canada, July 2009.

- Y. Yang, D. M. Divan, and R. G. Harley, "Power Line Vicinity Monitoring via Multiple Displacement Current Measurement," in *Proc. 2010 IEEE Power and Energy Society General Meeting, Minneapolis*, USA, July 2010.

Journal Papers

Y. Yang, R. G. Harley, D. M. Divan, and T. G. Habetler, "Adaptive Echo State Network to Maximize Overhead Power Line Dynamic Thermal Rating," submitted to *IEEE Trans. on Industry Electronics*.

R. Moghe, Y. Yang, F. Lambert, and D. M. Divan, "Design of a Low Cost Self Powered "Stick-on" Current and Temperature Wireless Sensor for Utility Assets," *submitted to IEEE Trans. on Power Electronics*.

CHAPTER 10

RECOMMENDATIONS FOR FUTURE WORK

The research presented in this dissertation advances a new concept of enhancing the utilization and reliability of the existing overhead power line systems. The concept has been proven with simulation studies on realistic models of overhead power lines. Detailed designs and experimental validations of the PLS module as well as the proposed sensing schemes have also been presented. However, further research work is required on various aspects of the technology.

10.1 Distributed Sensing for Overhead Power Lines and Utility Assets

The design and deployment of distributed sensor devices for power grid monitoring must consider the facts that their installation should have the least effects on the existing system. In addition, the implementation of such sensor devices should require a minimum of additional maintenance and human intervention. Therefore, exploring practical and useful energy scavenging technologies is critical in electric power utility applications for powering distributed sensor devices.

Magnetic fields around power assets have been shown to be the most promising and convenient energy source that is available for the distributed sensors in power system applications. Traditional high-permeability current transformer (CT) based methods have been used by others in many occasions to provide energy for unattended sensor devices, which has been utilized for the prototype PLS module in this research. However, this scheme requires the sensor devices to be clamped around the power assets, which potentially creates installation difficulty. To overcome this drawback, an easily-installed concept to harness inductive energy from utility assets is needed. As part of the future

work, Ref. [89] has proposed a novel solution, where a flux-concentrator sticks on to the surface of an asset. By loosely coupling the magnetic field through the use of the flux-concentrator, inductive energy is converted into useful electrical energy. This scheme limits the amount of energy that can be harnessed from the magnetic field around power assets, but it greatly simplifies the device installation and reduces the sensor cost. The preliminary study in [89] shows that a maximum power of 257 mW can be obtained with a primary current of 200 A. New design techniques of energy harvesting circuits are needed to support the sensor to operate over a wide operating range. Technical challenges pertaining to energy storage, communication networks, temperature and current sensing have to be addressed given the constraints of low cost.

10.2 Overhead Power Line Real-time Thermal Rating Evaluation

Much work has been done to address the issue of real-time dynamic thermal ratings of overhead power lines in the electric industry. Among the different kinds of line rating systems, the Conductor Temperature Model (CTM)-based method is the most promising candidate to evaluate the real-time thermal ratings of overhead power lines based on a distributed monitoring scheme, since only low-cost temperature and current sensors are needed in the CTM-based line rating systems. The MLPN-based and ESN-based line thermal rating systems proposed in this research belong to the category of the CTM-based line rating systems.

However, the performance of a CTM-based line rating method relies on the accuracy of the measured temperature, which is compromised by the heat-sink effect caused by the sensor itself. The issue of eliminating the heat-sink effect and improving the conductor temperature measurement accuracy needs to be addressed in more details.

At the same time, the implementation of a CTM-based system normally requires physical contact with a power conductor, and consequently increases the difficulty and

cost of device installation. The proper hardware design of sensor devices that can support low-cost and convenient installation is another interesting topic for future work.

10.3 Power Line Vicinity Monitoring via Overhead Conductor E-field Analysis

The space-phasor based mathematical model of the spatial mapping of the E-field around the mDCS surface has been established in this research. An information extraction scheme based on the DQ-axis decomposition technology has also been validated to separate the capacitive coupling effects from mDCS adjacent conductors in different directions. The experiment and the preliminary results presented in Chapter 7 have validated that the proposed DCS is able to detect small capacitance variations (i.e., 0.00x pF) with fairly high sensor output sensitivity up to x mV. The results have greatly encouraged the further investigation by applying the sensing scheme to the proposed mDCS in a 3-Φ overhead power line system, and consequently the experimental validation of the theory developed in this chapter. As the next step of the research, the proposed DCS circuit should be applied to the mDCS scheme, where six DCSs are needed to capture the displacement currents in six different directions around the overhead conductor. In terms of the sensor hardware design, the performance (or circuit parameters) of the six sensors must be close to each other in order to capture the realistic mapping of the E-field distribution around the conductor, although the direct displacement current measurement scheme proposed in Chapter 7 allows higher tolerance to the difference among the six capacitors. Special attention is needed to maintain consistency between the six sensors, when the sensor is designed and manufactured.

10.4 Power Line Vicinity Monitoring via Overhead Line EM Wave Propagation

Even though the proposed Multiple Displacement Current Sensing (mDCS) method via sensing E-field shows as a promising low cost, simple solution for overhead power line vicinity monitoring, there are several limitations to this method. Since the length of the proposed mDCS sensor is limited (say 1 meters), the method only shows its benefit to detect the variations in conductor separation or conductor-to-ground clearance caused by the conductor inherent movements, such as conductor sag or conductor gallop. Any other discrete line disturbances, such as proximity of tree branches, may not be detected effectively, unless the disturbance happens close to the sensor itself.

In order to further identify the potential of extracting EM field signatures for low-cost power line vicinity monitoring solutions, another method has been investigated. In this part of the work, instead of the electric field around overhead conductors, the electromagnetic (EM) energy wave propagation along overhead power lines is investigated to detect the present of incipient faults in the vicinity of PLS modules. In this case, the PLS module does not work only as a passive sensing device as in the applications presented in Chapters 5-7, but also acts as a Time-Domain Reflectometer, from which a wide bandwidth frequency signal is injected into one conductor of a power line. By measuring the reflective travelling wave (echoed wave), the equivalent impedance "seen" by the PLS module is evaluated, which is used to characterize and locate the line incipient failures, especially those caused by shunt-impedance variations along the line. To obtain a profile of line disturbances at any point along the line, two transformations are applied, by which the equivalent impedance is transformed from Time Domain, to Frequency Domain, and then to Longitudinal Domain. The performance of the proposed method is tested in the PSCAD^{TM}/EMTP^{TM} environment with preliminary simulation validation results.

10.4.1 Motivation of Detecting EM Wave Propagation along Overhead Lines and Proposed Method

Overhead power lines are essentially transmission systems wherein EM wave energy is guided or constrained by the line conductors. At high frequency of excitation, the EM wavelength (e.g. 150 m at 5 MHz) is much shorter than the length of the line itself (typically in the order of x0 miles). Therefore, an overhead power line can be viewed as a distributed-parameter structure along the line, and the EM wave propagation along the line is defined by its line parameters, i.e. series impedances and shunt admittances in a typical distributed-parameter line model. Frequency dependent overhead power line models have been studied for decades [122] [123]. The per-unit-length model of an overhead power line is the basic structure, where the line can be broken into the union of electrically small substructures with a *dx* length. Each substructure can then be represented by a lumped circuit model as shown in Figure 10.1.

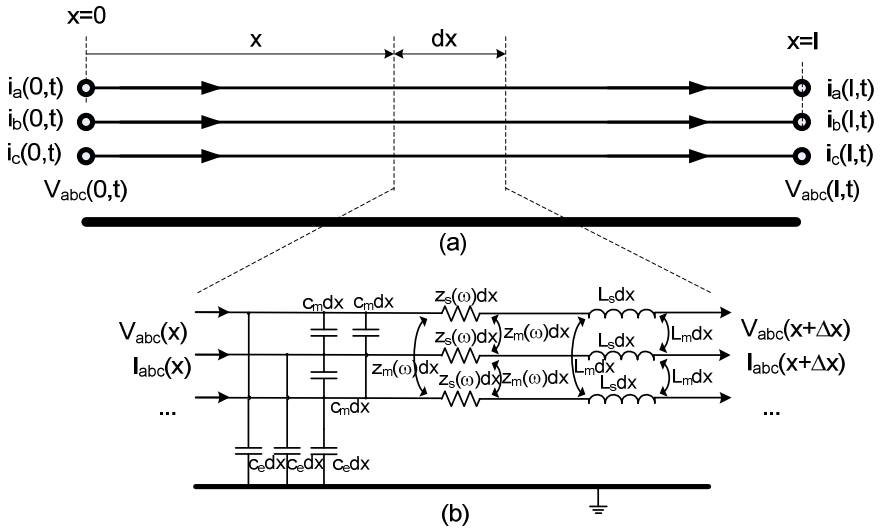

Figure 10.1 General representation of a 3-Φ overhead power line with earth return: (a) Schematic representation and notation; (b) equivalent circuits of an infinitesimal length.

In this small line substructure, EM wave propagation along the line can be described, in the frequency domain, by the following line equations [122],

$$\begin{aligned} \frac{d}{dx}\boldsymbol{V}_{abc}(\omega,x) &= -\boldsymbol{Z}(\omega,x)\cdot\boldsymbol{I}_{abc}(\omega,x) \\ \frac{d}{dx}\boldsymbol{I}_{abc}(\omega,x) &= -\boldsymbol{Y}(\omega,x)\cdot\boldsymbol{V}_{abc}(\omega,x) \end{aligned} \tag{10.1}$$

where $\boldsymbol{V}_{abc}(\omega,x)$ and $\boldsymbol{I}_{abc}(\omega,x)$ are line voltage and current vectors in the frequency domain at any point x along the line. The line per-unit series-impedance matrix $\boldsymbol{Z}(\omega,x)$ and the line per-unit shunt admittance matrix $\boldsymbol{Y}(\omega,x)$ are often functions of the position along the line x (because of the line discontinuity), as well as the excitation frequency ω (because of the skin effect developed inside the conductor and earth return path under high-frequencies). Appendix E depicts the frequency-dependent model of line parameters that are adopted in this study.

An overhead power line is a typical non-uniformly distributed transmission line system. Line parameter discontinuities occur along the line because of many reasons, such as the non-uniformly distributed terrain configuration, and varying tower heights. These line discontinuities are referred to as **inherent** line discontinuities. The line parameters can also be influenced by many other **time-varying and uncertain** factors, such as galloping and sagging conductors, gradual intrusion of tree limbs, skin and proximity affects of conductors and earth, insulation failure, etc. As discussed in the previous chapter, these phenomena are widely recognized by utilities as important factors to affect the reliability of the system. Since line discontinuities (inherent or time-varying) affect the EM wave propagation along a line, the accurate measurement and proper analysis of the wave propagation allows the detection of any variations in line parameters thus the sensing and locating of the presence of incipient faults along the line.

To obtain the line discontinuity information with acceptable granularity, the **high frequency characteristics** of the overhead power line needs to be obtained and analyzed. In this work, the PLS module is proposed to work as a Time-Domain Reflectometer, injecting a wide-bandwidth signal into an overhead power conductor. A novel information extraction procedure based on Time-Domain Reflectometry (TDR) technology is proposed to capture the impedance discontinuities along overhead power line, and therefore to detect and locate line disturbances in the vicinity of the PLS module along the line, and to detect the presence of the line incipient faults

10.4.1.1 A Brief Introduction to Time-Domain Reflectometry Technology

A typical Time-Domain Reflectometer is an electronic instrument widely used to characterize and locate faults in metallic cables, or to detect defects in certain materials, etc., in the Time Domain [124]. The TDR analysis begins with emitting an impulse of energy into an EM wave transmission system under study, and subsequently observes the energy reflected by each impedance discontinuity in the system. By analyzing the magnitude, duration and shape of the reflected waveform in the Time Domain, the nature of the impedance variation in the transmission system can be determined.

The magnitude of the reflection is referred to as the reflection coefficient $\Gamma = \frac{Z_t - Z_0}{Z_t + Z_0}$, where Z_0 is defined as the characteristic impedance of the transmission medium [124], and Z_t is the impedance of the termination at the far end of the transmission line. Note that, any discontinuity, e.g. abrupt changes in the characteristic impedance of the transmission medium, can be viewed as a termination impedance and substituted as Z_t. The distance to the reflecting impedance can be determined from the time that the injected pulse takes to return, since the wave propagation velocity is relatively constant for a given transmission medium.

For a homogenous medium, the EM wave travelling speed is determined by $v = 1/\sqrt{\mu\varepsilon}$, where μ is the permeability of transmission medium and ε is the medium's permittivity. The propagation velocity is primarily affected by the permittivity of the medium, which can vary greatly by the moisture content and temperature of the medium [124]. For overhead power line applications, the permeability and permittivity of air are given as $\mu_0 = 4\pi \times 10^{-7} H/m$ and $\varepsilon_0 = (1/36\pi) \times 10^{-9} F/m$. Note that, the relative permittivity of moist air does not change significantly, compared to that of dry air, which ranges from 1.00054 to 1.00078. The EM wave propagation velocity is, therefore, relatively constant at $v_0 = 3 \times 10^8 m/\text{sec}$ for an overhead transmission line, and the distance of the reflecting impedance can be expressed by, $len = v_0 \cdot t_r / 2$, where t_r is the time duration for the injected pulse to return.

10.4.1.2 Proposed TDR-based Method

Figure 10.2 shows a generic 3-Φ overhead power line system, with three power conductors suspended above the ground. In this work, the Power Line Sensor (PLS) modules are proposed to work as TDR devices. They are clamped over the phase B conductor, with a 2 km separation from one module to another, as shown in the figure. Every 5 minutes, a PLS module injects a short period of wide bandwidth frequency voltage signal into the phase B conductor. With reference to the PLS module *M* in Figure 10.2, V_{sB} denotes the injected voltage from module *M*, and I_{sB} is the corresponding echoed response subject to the excitation V_{sB}. By measuring and analyzing the injected voltage signal V_{sB} and the reflected current signal I_{sB}, the impedance discontinuities (line disturbances) along the overhead power line in the vicinity of PLS Module *M* are detected and located.

In this chapter, the analysis of EM propagation along the overhead power line is only based on one PLS module, say *M*, and other adjacent PLS modules are treated as passive components coupled onto conductor B. The presence of other modules inevitably causes line parameters discontinuities that can also be detected by the PLS module *M*, and consequently affects the accuracy and the effectiveness of the detection of the line disturbances of interests in this work, such as galloping and sagging conductors, gradual intrusion of tree limbs, etc. How to remove this effect will be discussed later in this section.

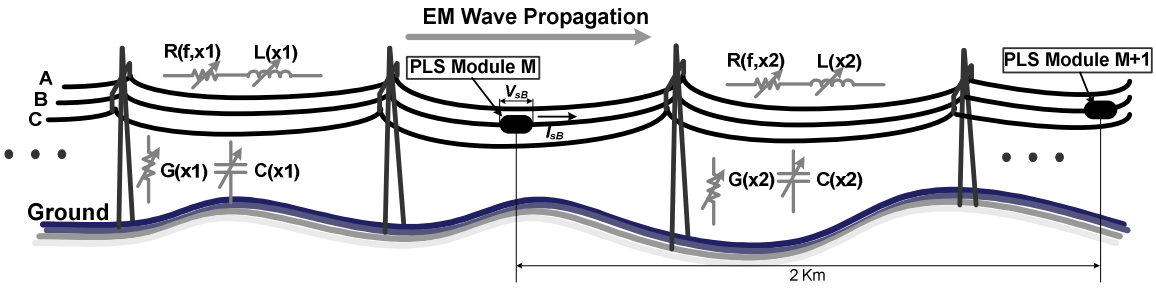

Figure 10.2 TDR based PLS power line vicinity monitoring

Even though, in this application, PLS modules act as TDR devices, there are several issues that make the proposed method different from the traditional TDR technology.

First of all, instead of an impulse signal, a chirp signal (a signal with gradual frequency sweeping from low values to high values) is emitted into the power conductor from the PLS module. Like impulse signals, chirp signals are also wide bandwidth frequency signals, but are more advantageous than impulse signals when practical implementation is considered. If an impulse signal is used in an echo-location system, the pulse is desired to be short enough to obtain a desired location resolution, but to have enough energy to be able to detect objects far way enough at the same time. The power needed to provide a pulse is equal to the energy of the pulse divided by the pulse length. The maximum power that the PLS module can handle without destroying itself forms a

constraint to satisfy both of the two requirements, i.e. more energy but short duration. Fortunately, chirp signals provide a way of overcoming this limitation. In this application, the chirp voltage signal injected onto the phase B conductor has frequency sweeps its frequency from 0 Hz to 5 MHz. The maximum frequency of 5 MHz provides a location resolution of up to 30 meters.

Secondly, in an echo-location system, the internal impedance of the injecting source affects the reflected waveform [122]. In this work, to eliminate the effects from the internal impedance, instead of the direct observation of the echoed signal I_{sB} as analyzed in conventional TDR systems, the equivalent impedance seen by the PLS module, given by $Z_{eq} = V_{sB} / I_{sB}$, is evaluated, and used as an indicator to capture the line discontinuities in the near vicinity of each PLS module.

As discussed above, overhead power line discontinuities can be grouped into two types, i.e. inherent line discontinuities and time-varying line discontinuities. The line vicinity disturbances that may affect the system reliability and need to be detected and located are mostly those that result in time-varying line discontinuities, such as galloping and sagging conductors, and gradual intrusion of tree limbs, etc. Therefore, in practice, not only does the equivalent impedance Z_{eq} itself, but also the **variations** in Z_{eq} have to be detected and analyzed, given by,

$$\Delta Z_{eq} = Z_{eq} - Z_{eq,Ref} \tag{10.2}$$

where $Z_{eq,Ref}$ is the reference equivalent impedance, which can be determined when PLS modules are initially installed. Z_{eq} is the equivalent impedance seen by each PLS module in real time, and is evaluated every 5 minutes. The detection of equivalent impedance variations ΔZ_{eq} eliminates the effects caused by the inherent line

discontinuities, such as non-uniformly distributed terrain configuration, or varying tower heights along the line. At the same time, the analysis of ΔZ_{eq} also helps to remove the interference from nearby PLS modules, since the line-parameter discontinuities caused by the present of other PLS modules are essentially time-invariant.

The third issue is that, if a chirp signal is injected into the power conductor through the PLS module, the reflected waveform can not be analyzed only in the **Time Domain** to characterize and locate line discontinuities, as it is done in conventional TDR systems. In this research, an "Anti-Chirp" process is proposed as shown in Figure 10.3, where the voltage and current signals measured in real time are firstly converted to quantities in the **Frequency Domain**. Then a modified **Inverse Fourier Transformation** (IFT) is applied to convert all values to the **Longitudinal Domain**.

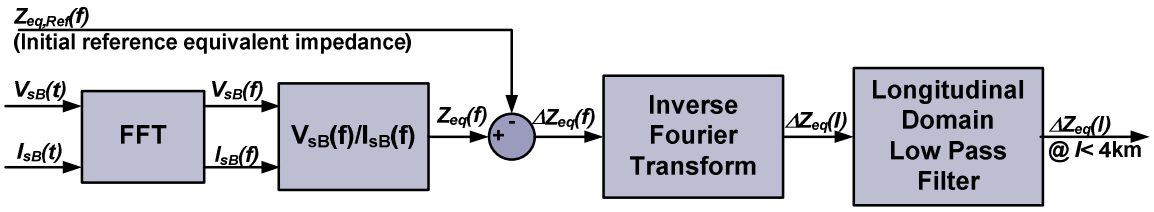

Figure 10.3 "Anti-Chirp" process for information extraction

As shown in Figure 10.3, the modified IFT [125] is used to convert $\Delta Z_{eq}(f)$ in the Frequency Domain into its Longitudinal Domain quantity, and the equivalent impedance variation "seen" by the PLS module in the Longitudinal Domain can be written by,

$$\Delta Z_{eq}(l) = L_M^{-1}\{\Delta Z_{eq}(f)\} = \int_{-\infty}^{\infty} \Delta Z_{eq}(f) \cdot e^{j2\pi(f/v_0)\cdot l} \cdot df \tag{10.3}$$

where the symbol $L_M^{-1}\{.\}$ denotes the IFT, and l denotes the distance from the PLS module. $\Delta Z_{eq}(l)$ provides the solution to the equivalent impedance variation in the

longitudinal variable l, and directly describes a profile of line discontinuity variations at any point l along the power line with reference to the PLS module location.

The visible range of each module is scoped to be 4 km (both sides of the module) in this work, considering the EM wave attenuation along the line caused by line losses. A Longitudinal-Domain Low-pass Filter is applied to filter out the longitudinal spectrum out of range of interests, which helps to remove the effects of line disturbances 4 km further away from the PLS module. The modified IFT is valid based on the assumption that the EM wave propagates in a homogeneous medium where the wave travelling speed is constant, i.e. the speed of light, v_o, in this application.

The above discussion shows that the success of the proposed method depends on an accurate detection of the equivalent impedance Z_{eq} (including its variations) seen by the PLS module. At the same time, an effective information extraction scheme based on Z_{eq} is critical to help characterize and locate the line vicinity disturbances and/or incipient failures. This requires an analytical study of the equivalent impedance Z_{eq} and a comprehensive understanding of the EM waveform propagation along a 3-Φ overhead power line system at high-frequency of excitation.

However, there are several factors that make analyzing overhead power line EM transmission system a difficult task. First of all, an overhead power line is a multi-conductor EM wave transmission system, including three phase conductors, overhead ground wire, and ground return path, which are all coupled with each other. Besides, under high-frequency conditions (say up to 5 MHz), the distributed parameters of an overhead power line are affected by skin effects of both overhead conductors and earth. This causes the line parameters to be highly frequency dependent [122] [123]. Moreover, the inherent discontinuity of the EM wave transmission system adds the complexity of building a mathematical model for overhead power lines.

Therefore, establishing an analytical model of the equivalent impedance Z_{eq} seen by the PLS module is a complex task. The following section starts with establishing the Thevenin Equivalent of a 3-Φ power line at the point of PLS module signal injection, and then a mathematical model of the equivalent impedance Z_{eq} seen by the PLS module is developed in terms of the natural modes of EM propagation along the line by applying the model decomposition technique.

10.4.2 Thevenin Equivalent of a 3-Φ Power Line at the Point of PLS Module Signal Injection

10.4.2.1 Overview

Figure 10.4 illustrates a 3-Φ overhead power line system with a PLS module, say module *M*, injecting a chirp voltage signal V_{sB} onto the Phase B conductor. The PLS module is modeled as an ideal voltage source, V_{sB}, with an equivalent internal impedance, Z_{sB}, both of which are connected in **series** to the power line circuit.

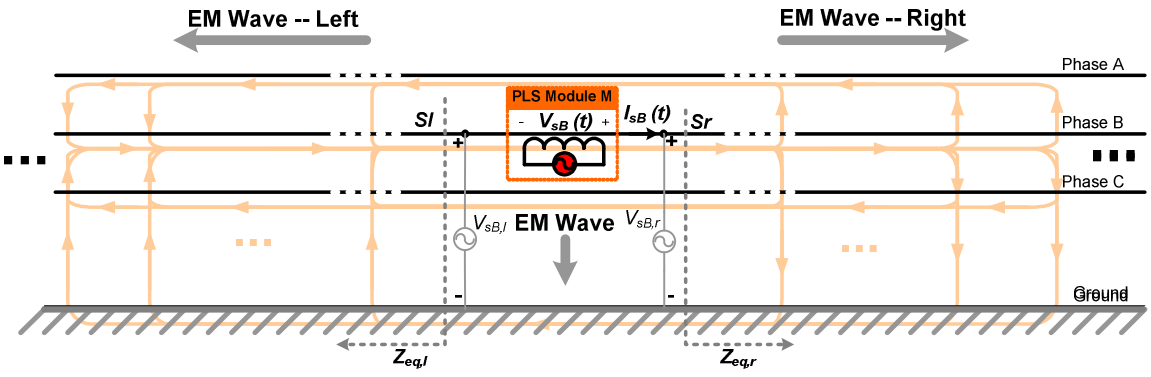

Figure 10.4 General representation of the induced current distribution subject to the V_{sB} injection.

Subject to the high-frequency injected voltage V_{sB} , the 3-Φ power line EM transmission system operates under **asymmetric** conditions. Because of the mutual coupling between different conductors and ground, the induced current I_{sB} as a result of V_{sB} flows in complex patterns and splits among various paths, i.e., phase wires, neutral wires, ground wires and the earth. The distribution of the current depends on the relative sizes of power line conductors, mutual coupling between conductors, line asymmetries, and resistances of the various system ground, etc. To simply the analysis, the line modal decomposition technique is often needed to decouple the mutual coupling between different conductors, and the resultant modal components are able to depict distinct natural modes of the EM wave propagation along the overhead power line independently.

Figure 10.4 also depicts that the injected voltage signal is coupled onto the system **in series**. The analysis of the EM wave propagation, as a result of the injected voltage in **series** to the power line circuit, is different from the case where the injection voltage is coupled into the circuit in **parallel**. In the case of **parallel** coupling, the EM energy wave propagates only horizontally in the direction guided by the overhead wires. However, in the case of **series** coupling, the EM wave propagates not only horizontally in the direction guided by the overhead wires, but also vertically in the direction guided by the conductive and capacitive path from overhead conductors to ground at signal injection point, as depicted in Figure 10.4. For a typical overhead power line construction, however, the conductor ground clearance is normally from 20 to 30 meters. If the injected signal has a bandwidth of 5 MHz, the minimum EM wavelength is 30 meters. The EM wave propagation in the vertical direction can, therefore, be represented by lumped parameters, i.e. the shunt admittance matrix $\boldsymbol{Y(\omega)}$ as depicted in (10.1) at the point of injection voltage (i.e. points *Sr* and *Sl* in Figure 10.4).

In this application, only the EM waves propagating horizontally in two directions (left and right as shown in Figure 10.4) guided by the overhead wires are considered. With reference to Figure 10.4, the injected voltage source V_{sB} can be expressed by

$$V_{sB} = V_{sB,r} + V_{sB,l} \tag{10.4}$$

where $V_{sB,r}$ and $V_{sB,l}$ are the potential differences from points *Sr* and *Sl* to ground respectively. These two potential differences can be considered as two virtual voltages that are coupled into the power line **in parallel**. Note that these two virtual voltages can not be obtained by direct measurement in this application. The introduction of the two quantities is for the convenience of analyzing the EM wave propagations guided by the overhead wires in both directions. In addition, the method to analyze the EM wave propagation based on the **parallel coupling** can be adopted.

In this application, the EM wave propagation is studied under the excitation frequencies swiping from 10 kHz to 5 MHz. Therefore, based on Thevenin theory, power generators (working at the power frequency of 60 Hz) in the system can be modeled as a passive element with impedance value of Z_{Gen}, and the far end load is modeled as equivalent load impedance Z_{load}.

10.4.2.2 Thevenin Equivalent of a 3-Φ Power Line at the Point of PLS Module Signal Injection

This sub-section develops the Thevenin equivalent of a 3-Φ overhead power line at the point of the PLS module signal injection, as shown in Figure 10.4. With reference to

(10.4), the injected voltage source V_{sB} can be expressed by two virtual parallel voltages, $V_{sB,r}$ and $V_{sB,l}$.

In a 3-Φ vector notation, the injected voltage $V_{abc,S}$ can be expressed by,

$$V_{abc,S} = \begin{bmatrix} 0 \\ V_{sB} \\ 0 \end{bmatrix} = V_{abc,r} + V_{abc,l} \tag{10.5}$$

where $V_{abc,r} = \begin{bmatrix} 0 \\ V_{sB,r} \\ 0 \end{bmatrix}$ and $V_{abc,l} = \begin{bmatrix} 0 \\ V_{sB,l} \\ 0 \end{bmatrix}$ are the two virtual 3-Φ voltage vectors that are coupled into the right- and left-side of the power line **in parallel**.

Subject to the injection voltage, the 3-Φ power line EM transmission system operates under the asymmetric conditions. The line modal decomposition technique is needed to decouple the mutual coupling between different conductors, and results in three distinct natural modes of the EM wave propagation along the overhead power line. In this application, a special case of modal decomposition is utilized, resulting in what is known as the sequence modes of a 3-Φ line, and the modal transformation matrix is also called symmetrical component transformation defined as follows,

$$\boldsymbol{T} = \frac{1}{\sqrt{3}} \begin{bmatrix} 1 & 1 & 1 \\ 1 & a^2 & a \\ 1 & a & a^2 \end{bmatrix} \tag{10.6}$$

where $a = e^{-j120^0}$.

The symmetrical sequence voltages $\boldsymbol{V}_{012,s}(x)=[V_{s0},V_{s1},V_{s2}]'$ and currents $\boldsymbol{I}_{012,s}(x)=[I_{s0},I_{s1},I_{s2}]'$ are related to their phase quantities by

$$\boldsymbol{V}_{abc,s}(x)=\boldsymbol{T}\cdot\boldsymbol{V}_{012,s}(x) \tag{10.7}$$

and,

$$\boldsymbol{I}_{abc,s}(x)=\begin{bmatrix} I_{sA} \\ I_{sB} \\ I_{sC} \end{bmatrix}=\boldsymbol{T}\cdot\boldsymbol{I}_{012,s}(x) \tag{10.8}$$

With reference to (10.8), the current following through conductor B, I_{sB}, can be represented in terms of its symmetric components, as follows,

$$I_{sB}=\frac{1}{\sqrt{3}}\cdot(I_{s0}+\alpha^2\cdot I_{s1}+\alpha\cdot I_{s2}) \tag{10.9}$$

Now, apply the inverse transformation $\boldsymbol{T^{1}}$ to $\boldsymbol{V}_{abc,s}$, and the injection voltage in symmetric sequence quantities can be expressed by,

$$\boldsymbol{V}_{012,s}=\boldsymbol{T}^{-1}\cdot\boldsymbol{V}_{abc,s}=\boldsymbol{T}^{-1}\cdot\begin{bmatrix} 0 \\ V_{sB} \\ 0 \end{bmatrix}=\frac{1}{\sqrt{3}}\begin{bmatrix} V_{sB} \\ \alpha\cdot V_{sB} \\ \alpha^2\cdot V_{sB} \end{bmatrix} \tag{10.10}$$

In sequence quantities, every symmetric sequence (modal) voltage is related to the current through the equivalent impedance of its own sequence mode. For instance, for zero sequence, the following relation holds,

$$I_{s0} = \frac{V_{s0}}{Z_{eq0}} = \frac{1}{\sqrt{3}} \frac{V_{sB}}{Z_{eq0}} \tag{10.11}$$

where Z_{eq0} is the equivalent impedance of zero-sequence power line network seen at the point of PLS module injection. Similar formulas can be obtained for positive and negative (i.e., "1" and "2" as denoted in (10.7) respectively) sequence, as follow,

$$I_{s1} = \frac{V_{s1}}{Z_{eq1}} = \frac{1}{\sqrt{3}} \frac{\alpha \cdot V_{sB}}{Z_{eq1}} \tag{10.12}$$

$$I_{s2} = \frac{V_{s2}}{Z_{eq2}} = \frac{1}{\sqrt{3}} \frac{\alpha^2 \cdot V_{sB}}{Z_{eq2}} \tag{10.13}$$

where Z_{eq1} and Z_{eq2} are the equivalent impedances of positive and negative sequence networks respectively, seen at the point of PLS module injection. Appendix F.1 gives more details on how to obtain the above equations (10.11)-(10.13).

Substitute (10.11) – (10.13) to (10.9), I_{sB} can be related to V_{sB} by,

$$I_{sB} = \frac{1}{3}\left(\frac{1}{Z_{eq0}} + \frac{1}{Z_{eq1}} + \frac{1}{Z_{eq2}}\right) \cdot V_{sB} \tag{10.14}$$

With reference to Appendix F.2, the equivalent impedance of each sequence network is a composition of equivalent impedances of both right- and left-side the networks, given

by $Z_{eq0} = Z_{eq0,l} + Z_{eq0,r}$, $Z_{eq1} = Z_{eq1,l} + Z_{eq1,r}$ and $Z_{eq2} = Z_{eq2,l} + Z_{eq2,r}$. For example, $Z_{eq0,l}$ represents the equivalent impedance of the left-side of the zero-sequence power line network. Based on the above analysis, the Thevenin equivalent circuit of the 3-Φ power line (in sequence networks) at the point of PLS voltage source injection is depicted in Figure 10.5 (a).

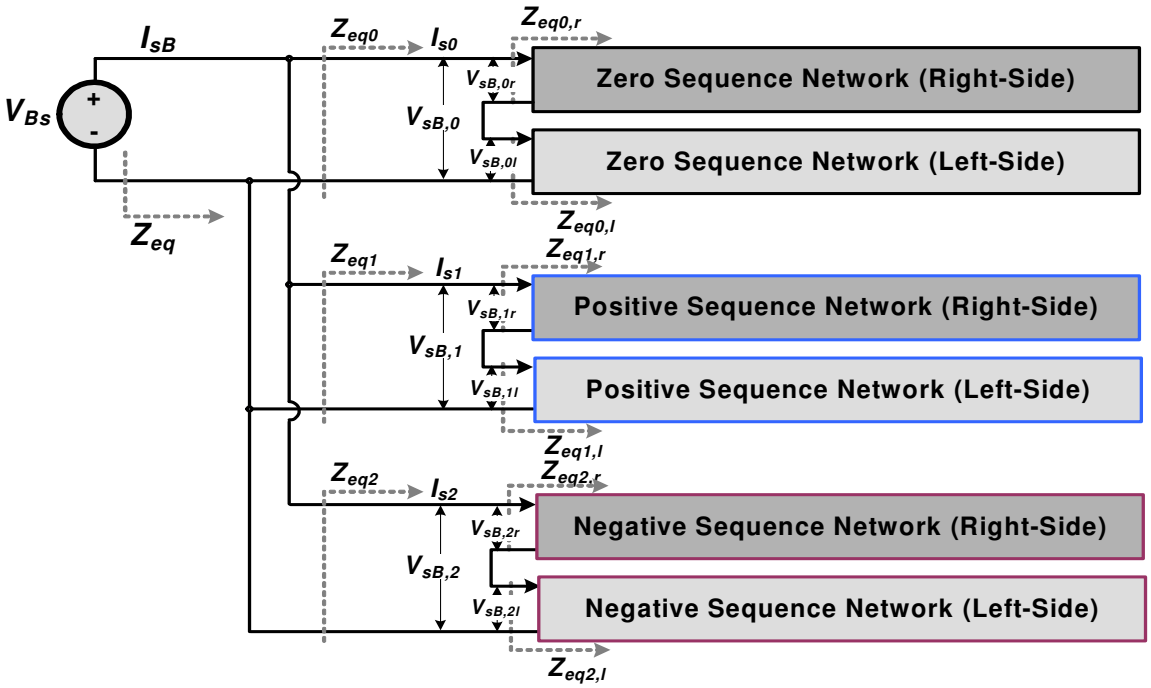

(a)

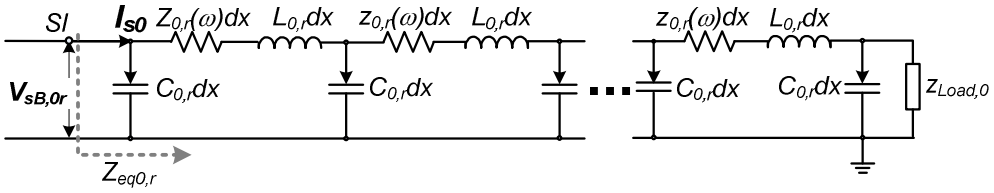

(b)

Figure 10.5 Thevenin equivalent network of a 3-Φ power line (in sequence networks) at the point of PLS voltage source injecting: (a) Generic representation; (b) Single-phase equivalent circuit of right side of zero-sequence network with respect to the voltage injection point.

The advantages of modal decomposition are obvious. It results in three independent natural modes (i.e., zero, positive, and negative sequences) of EM wave propagation along the line. Each natural mode has its own propagation functions and characteristic impedance, and can be represented by a single-phase distributed (per-unit) EM transmission line model, as shown in Figure 10.5 (b).

With reference to (10.14), the net equivalent impedance Z_{eq}, of the power line seen by the PLS module can be expressed in sequence quantities, as follow,

$$Z_{eq} = \frac{V_{sB}}{I_{sB}} = 3 \Big/ \left(\frac{1}{Z_{eq0}} + \frac{1}{Z_{eq1}} + \frac{1}{Z_{eq2}}\right) \tag{10.15}$$

The Thevenin equivalent analysis of the 3-Φ power line system indicate that the equivalent impedance/admittance seen by the PLS module is the composition of the effects from all three sequence modes. Figure 10.6 illustrates the physical meaning of these three sequence modes. For both positive and negative sequence modes shown in Figure 10.6 (a) and (b), the three phase currents are balanced, and the electric current in the earth is zero. For the zero sequence mode (also called ground mode) shown in Figure 10.6 (c), all three phase currents are identical and in phase, and the earth current will be the negative of the sum of the phase current.

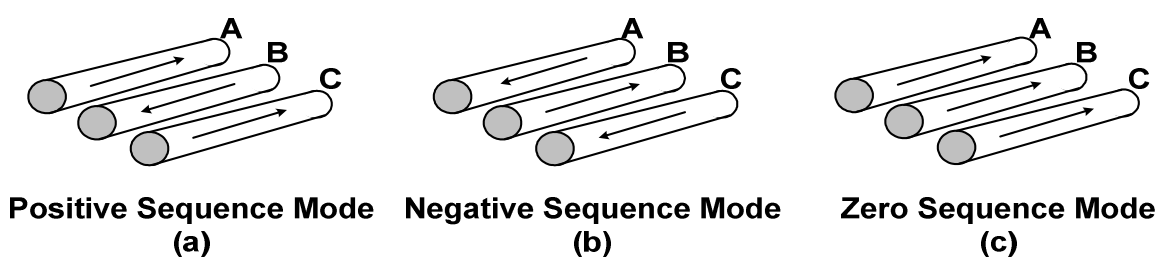

Figure 10.6 Illustration of the Symmetrical Components on a 3-Φ Power Line

So far, a Thevenin equivalent circuit of a 3-Φ power line at the point of the PLS module voltage injection has been established. The modal decomposition technique is used to extract the three independent, natural modes (i.e., sequence modes in this application) of EM propagation along the overhead power line. The equivalent impedance of the power line seen by the PLS module has been proved to be the composition of the equivalent impedances of the three natural modes.

An overhead power line in general spreads over several miles, which is a typical non-uniformly distributed transmission line. The line discontinuities may be caused by many reasons, such as different heights of line towers, variant terrain configurations, as well as variant conductor sagging conditions, vegetation proximity, etc. To capture the line discontinuity analytically, the single-phase non-uniformly distributed EM transmission line model for each natural mode (i.e., zero, positive, and negative) of the overhead power line needs to be established by a cascading procedure. The power line is divided into several segments, each of which is assumed to have constant line parameters. A concept of "Transmission Matrix" is applied to cascade all ling segments together. Appendix G provides the detailed description of a single-phase model of a non-uniformly distributed EM transmission line. The analytical models of both $Z_{eq0,l}$ and $\Delta Z_{eq,r}(l)$ for one natural EM wave propagation mode are also developed in Appendix G. The developed model indicates $\Delta Z_{eq,r}(l)$ as a promising indicator to the presence and location of line discontinuities along the line.

As discussed in Section 10.4.1, the important factors that create incipient faults along the line and consequently affect the reliability of the system are those associated with variations in the shunt admittances $\boldsymbol{Y}(\omega, x)$ along the line, e.g., overhead conductor-to-ground clearance, tree branches to intrusion, etc. For an overhead power line, however, there are other types of time-varying line parameter variations (line discontinuities) that

do not directly affect the system reliability. For instance, soil resistivity that varies along the length of the power line, as well as weather/season changes the skin-effect developed in the earth, and consequently affects the EM propagation in the zero-sequence mode. This phenomenon also generates a certain form of time-varying line discontinuity that can be detected by $\Delta Z_{eq,r}(l)$. Since the variation of soil resistivity does not potentially generate incipient faults along the power line, this type of line disturbances has to be distinguished from the line discontinuity caused by **shunt admittance variation**. With reference to the frequency-dependent model in (E.3) in Appendix E, the soil resistivity only affects the distributed **series impedance** $\boldsymbol{Z}(\omega, x)$ along the length of the power line. Therefore, in this work, how to distinguish the time-varying line discontinuities caused by different physical reasons, i.e., **shunt admittance** variation or **series impedance** variation, is another interesting issue to address.

To validate the proposed method and the performance of $\Delta Z_{eq}(l)$ as an indicator to capture, locate the line disturbances, as well as to distinguish the physical reasons behind the disturbances, a preliminary analysis is conducted in the PSCAD™/EMTP™ simulation environment.

10.4.3 Simulation Validation of the Proposed Method

10.4.3.1 PSCAD™ Frequency-Dependent Transmission Model

In this work, the PSCAD™/EMTP™ frequency-dependent line model based on a practical transmission line geometry configuration is used for simulation validation.

The test case is a 3-Φ overhead power line of 40 km length. Multiple PLS modules are mounted onto the line with 2 km separation. To simulate the **inherent** discontinuities of the line, the whole line consists of 40 cascaded elementary line sections, one of which is represented by a uniform PSCAD frequency-dependent line model. The line model of each section has its individual setup, reflecting its local conductor heights with respect to

ground, or local soil moisture level in terms of soil resistivity. This cascaded chain of uniform line sections provides a step-wise profile of impedance discontinuities along the whole line. This cascaded multiple-line-section setup also provides the flexibility of changing line parameters at a certain location along the line, which can be used to simulate the time-varying line disturbances along the line.

The geometry for the line under study is summarized in Table 10.1.

The Thevenin equivalent impedances at the load and generator end points of the line are defined to be 100 Ω. In fact, different values of end point impedance are tested, but they do not affect the simulation results.

Table 10.1 LINE CONFIGURATION UNDER STUDY

Transmission line length (mile)	50 miles
Conductor Type	Drake
Height of the tower	35 meter
Min. Ground Clearance	20 meter

10.4.3.2 Simulation Results

The PLS module *M* under study, with reference to Figure 10.2, is assumed to be located in the middle of the line. To validate that, the proposed PLS module is able to detect line disturbances in its vicinity, a base case of the transmission line with inherent line discontinuities located at several places along the line is simulated first. This base case serves as the reference providing the reference equivalent impedance $Z_{eq,Ref}$, as discussed in Section 10.4.1.2. A chirp voltage source signal V_{sB} with 5 MHz bandwidth is injected into the phase conductor of the line. Both V_{sB} and the corresponding echoed response I_{sB} under the reference line condition are shown in Figure 10.7 in the Time-Domain.

With reference to Figure 10.3, the signals measured in real time, V_{sB} and I_{sB}, are converted to quantities in the Frequency-Domain via the Fourier Transform. The resultant

frequency spectrum of the equivalent impedance of the reference power line case, $Z_{eq,Ref}(f)$, seen by the PLS module *M*, is shown in Figure 10.8.

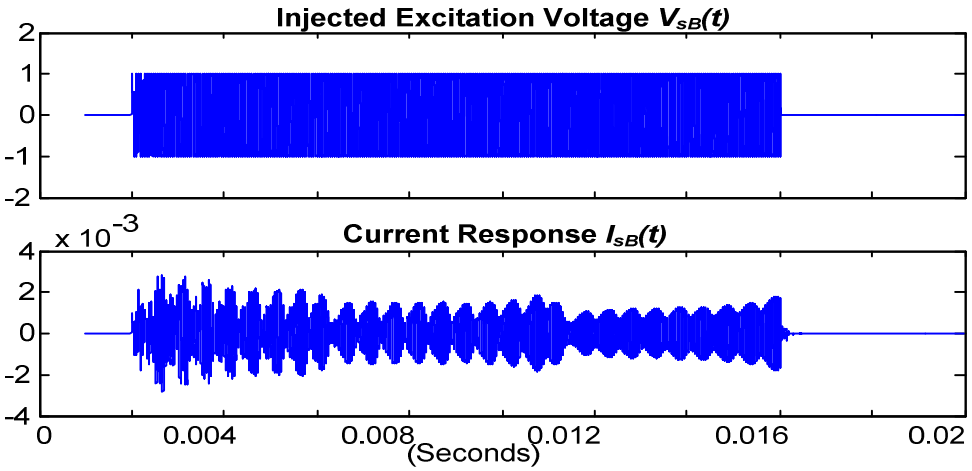

Figure 10.7 Injected voltage signal V_{sB} and reflected current signal I_{sB} in Time Domain

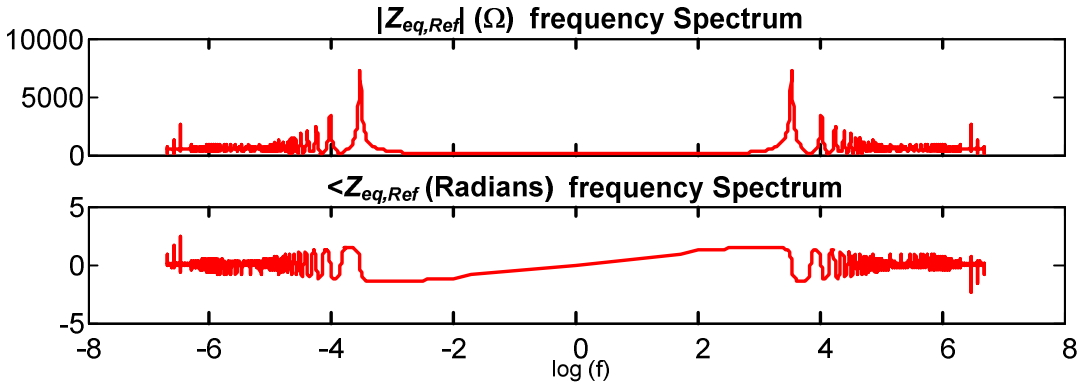

Figure 10.8 Frequency spectrum of the reference equivalent impedance $Z_{eq,Ref}$ seen by the PLS module *M*.

To simulate line disturbances, the configurations of two elementary line section models are changed from their original reference setups. On the right side of PLS module *M*, 1000 to 1500 meters away from it, the conductor-to-ground clearance (GrdClr)

decreases from 25 to 23 meters (by 2 meters). At the same time, on the left side of the PLS module, the conductor-to-ground clearance decreases from 20 to 16 meters at the location 2050 to 2080 meters away from the PLS module. Similarly, a chirp voltage source signal V_{sB} with 5 MHz bandwidth is injected into the line. The same procedure, as applied to $Z_{eq,Ref}(f)$, is conducted to evaluate the equivalent impedance $Z_{eq}(f)$ in the presence of the line disturbances mentioned above.

Applying the modified IFT, as depicted in (10.2), the difference between $Z_{eq,Ref}(f)$ and $Z_{eq}(f)$ is converted to the Longitudinal Domain, $\Delta Z_{eq}(l)$, as shown in Figure 10.9. Figure 10.9 indicates clear peaks on the magnitude of $\Delta Z_{eq}(l)$ at the locations where line disturbances happen. It also shows abrupt changes in the phase angle at the same locations. This result validates that, $\Delta Z_{eq}(l)$ is a promising indicator to the variations in shunt impedance of the line. It directly provides a profile of line disturbances at any point along the power line in the vicinity of the PLS module under study.

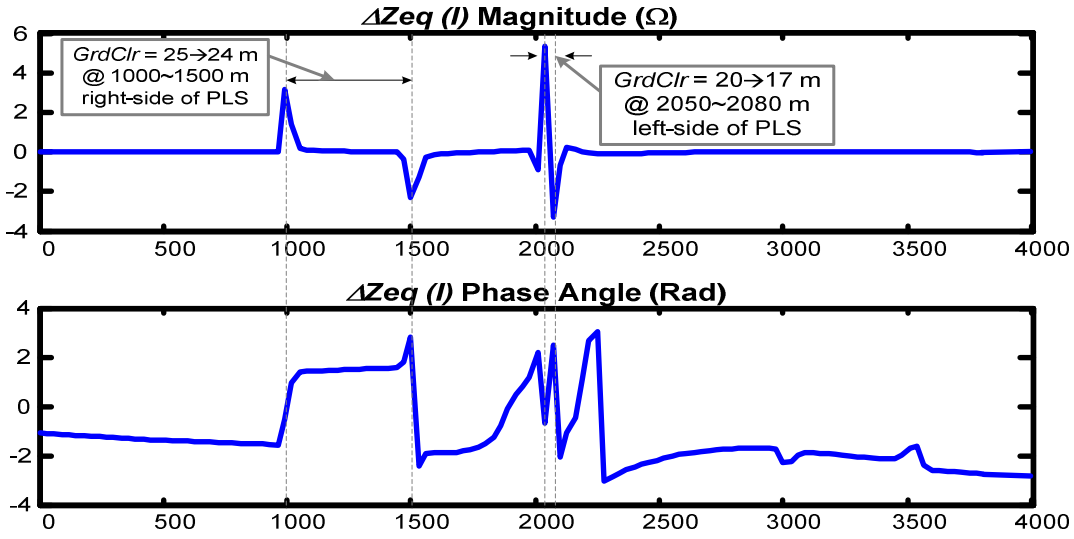

Figure 10.9 $\Delta Z_{eq}(l)$ subject to line disturbances with respect to shunt admittance variation.

To evaluate the sensitivity of $\Delta Z_{eq}(l)$ to detect the shunt admittance variation, additional line disturbances are created at four locations, i.e., 700 m, 1100 m, 1500 m and 1900 m away from the PLS module *M*. At each location, the *GrdClr* increases from 12 meters to 15 meters, with the increment of 1 meter. Figure 10.10 shows the detected peak value of $\Delta Z_{eq}(l)$ accordingly under all the disturbances. The results indicate that $\Delta Z_{eq}(l)$ is able to detect the *GrdClr* variation with fairly high sensitivity. For instance, the line disturbance at the location of 1500 meter, when the *GrdClr* changes from 12 meter to 13 meter, causes the peak of $\Delta Z_{eq}(l)$ increasing almost by 50%.

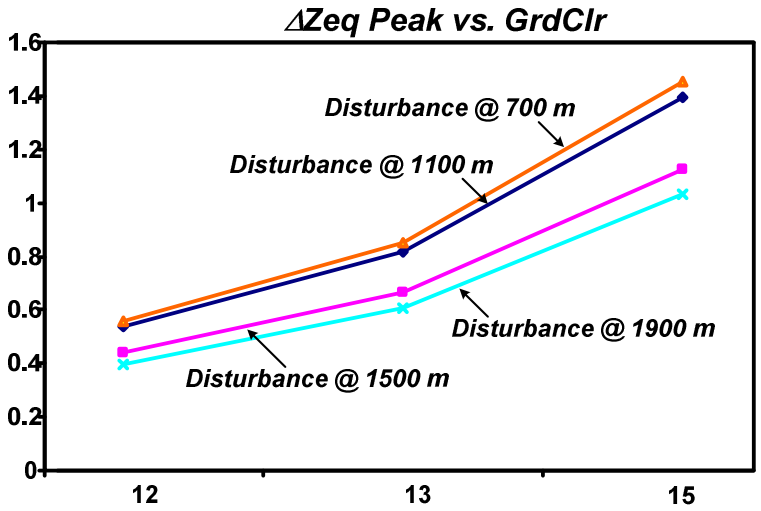

Figure 10.10 Sensitivity Analysis: $|\Delta Z_{eq}(l)|$ vs. conductor-to-ground clearance.

Figure 10.11 shows another example of validating the $\Delta Z_{eq}(l)$'s performance to distinguish the line disturbances caused by shunt admittance changes (e.g., caused by *GrdClr* variations) and series impedance variations (e.g., caused by changes in soil resistivity). In this case, on the right side of PLS module *M*, 850 to 1250 meters away from the PLS module, the *GrdClr* increases from 14 to 17 meters (by 3 meters). At the same time, on the left side of the PLS module, the soil resistivity changes from 100 to

150 at the location of 2750 to 3250 meters away from the PLS module. The result indicates clear changes on the magnitude of $\Delta Z_{eq}(l)$ at the locations where line disturbances happen. However, the shapes of $\Delta Z_{eq}(l)$'s profile along the length of the line, subject to these two types of line disturbances, are different. In addition, the *GrdClr* change causes an abrupt change in the phase angle, while the soil resistivity variation does not generate the same level of variation in the phase angle. The $\Delta Z_{eq}(l)$ has two distinct signatures for these two types of line disturbances, which can be used to indicate the physical reason of the detected line discontinuities.

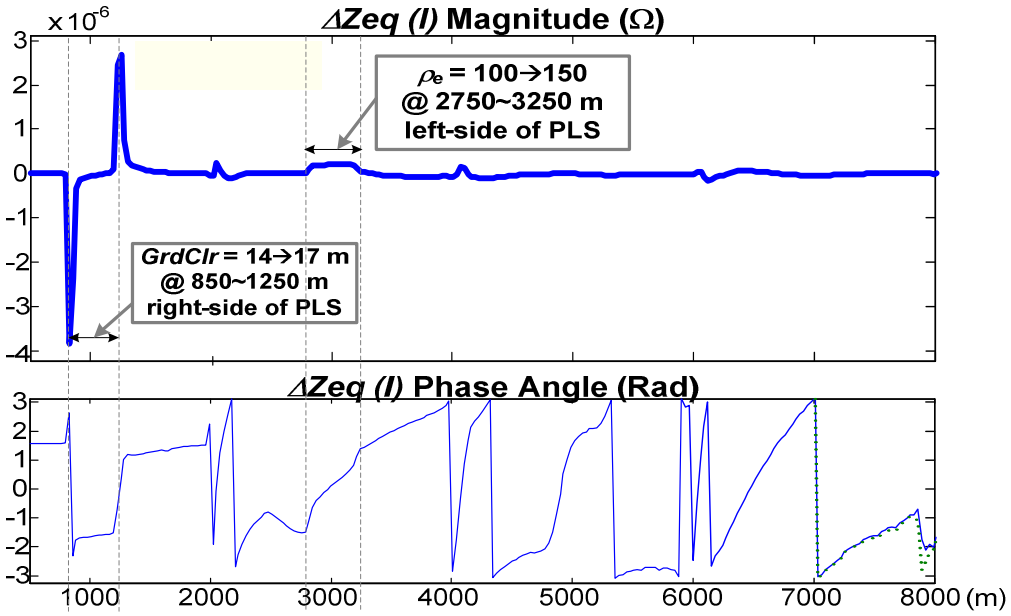

Figure 10.11 $\Delta Z_{eq}(l)$ subject to line disturbances with respect to both shunt admittance and series impedance variation.

10.4.4 Summary

Section 11.4 has described a power line vicinity monitoring, where the PLS module acts as a TDR equipment bursting a short period of wide-bandwidth chirp signal into an overhead conductor. The analysis of the equivalent impedance seen by the PLS module

helps to detect line disturbances, and thus to detect and locate the presence of incipient faults along the line. Preliminary simulation results have validated this proposed method as a promising solution to detect line disturbances with high sensitivity. Providing a profile of line disturbances at any location along the line, this method, unlike the mDCS based method, is able to detect the line disturbances caused not only by line inherent movements (i.e. conductor sagging or galloping), but also discrete line disturbances (i.e. proximity of tree branches).

This part of the work has initiated an analytical study of the equivalent impedance Z_{eq} and a comprehensive understanding of the EM waveform propagation along a 3-Φ overhead power line system at high-frequency of excitation with the PLS module as the platform. It has also established a mathematical model of the equivalent impedance Z_{eq} (including its variations) seen by the PLS module. This model provides a guideline for an effective information extraction scheme to help characterize and locate the line vicinity disturbances and/or incipient failures, as well as to distinguish the line disturbances caused by different physical reasons. However, before the proposed method can be applied successfully for real-time implementation, several issues need to be further addressed.

First of all, the line disturbances that happen on the right or left side of the PLS module need to be distinguished from one another. The simulation results shown in Figure 10.9 and Figure 10.11 indicate that the effects on $\Delta Z_{eq}(l)$ of line disturbances, either on the right or left side of the PLS module, overlap with each other along the longitudinal coordinate *l*. No matter on what side of the PLS module the line disturbances occur, the magnitude of $\Delta Z_{eq}(l)$ shares similar signatures. A further information extraction scheme is needed to address this issue.

Moreover, interference from external electromagnetic fields upon overhead power lines must be considered. These incident fields may be generated by distant transmitting

antennas or by nearby radiating structures. The induced current subject to external incident-field coupling may generate current waveforms that can be falsely identified as the sensing signal, thus causing misjudging of incipient fault detection. How to filter out the effects caused by incident fields is another interesting topic for future work.

Last but not the least, this TDR based method belongs to the category of intrusive sensing technologies, which potentially increases the cost and complexity of the PLS module. How to design a simple, cost-effective series-coupling circuit with a wide bandwidth of 5 MHz to inject the "chirp" signal onto the overhead conductor is the most challenging yet the most critical issue to be addressed, before the proposed TDR-based method can be successfully applied in the future.

10.5 Summary

Several technologies have been investigated in this research for developing the proposed Power Line Sensor Network (PLSN). Deployment of such a network can improve grid operations and utilization, and can provide improved situational awareness of the power grid. The results demonstrate that the developed power line thermal rating evaluation and vicinity monitoring methods are promising low-cost solutions that can improve power line reliability and utilization. The thesis has also briefly explored an interesting method for line monitoring using Time Domain Reflectometry principles. Although promising, the proposed techniques require significant level of validation. Significant work is needed to translate the design and development of distributed sensing technologies to an easy to use low-cost solution suitable for use in a realistic environment, thus enabling the successful implementation of such a PLSN for distributed power grid monitoring.

APPENDIX A

MLPN ON-LINE ADAPTIVE LEARNING ALGORITHM

A.1: Parameter Estimation Tester (PET) Model

$$\hat{T}_c(n) = \frac{\hat{\tau}_{tr}}{\Delta T + \hat{\tau}_{tr}} \hat{T}_c(n-1) + \frac{\Delta T}{\Delta T + \hat{\tau}_{tr}} (T_a(n-1) + \hat{R}_{tr} U_{tr}(n-1)) \tag{A.1}$$

$$\begin{aligned} \Delta\hat{T}_c(n) &= \hat{T}_c(n) - \hat{T}_c(n-1) \\ &= \frac{\Delta T}{\Delta T + \hat{\tau}_{tr}} (T_a(n-1) + \hat{R}_{tr} U_{tr}(n-1) - \hat{T}_c(n-1)) \end{aligned} \tag{A.2}$$

where ΔT is the sampling period. $\hat{T}_c$ is the predicted temperature.

$\hat{R}_{tr}(n) = 1/(\hat{K}_{\text{cov}}(n) + k1 + k2 \cdot T_a(n))$ is the thermal resistor, where $\hat{K}_{\text{cov}}$ is the estimated convection cooling factor and T_a is the ambient temperature. *k1* and *k2*, are constants associated with the conductor type under study [99]. $\hat{C}_{tr}(n) = m\hat{C}_P(n)$ is the effective thermal capacitor, and $\hat{\tau}_{tr}(n) = \hat{R}_{Tr}\hat{C}_{Tr}$ is the time constant of the overhead conductor thermal dynamics.

A.2: Sensitivity Matrix (SM)

Take the partial derivative of (5.7) with respect to $\underline{x}$ and use the chain rule to obtain the following equations,

$$\frac{\partial \hat{T}_c}{\partial \underline{x}}(n) = \delta_{TK}(n) \cdot \frac{\partial \hat{K}_{\text{cov}}}{\partial \underline{x}}(n) + \delta_{TC}(n) \cdot \frac{\partial m\hat{C}_P}{\partial \underline{x}}(n) \tag{A.3}$$

$$\frac{\partial \Delta \hat{T}_c}{\partial \underline{x}}(n) = \delta_{\Delta TK}(n) \cdot \frac{\partial \hat{K}_{\text{cov}}}{\partial \underline{x}}(n) + \delta_{\Delta TC}(n) \cdot \frac{\partial m\hat{C}_P}{\partial \underline{x}}(n) \tag{A.4}$$

where $\underline{x}$ is the vector of coefficients of the MLPN model, including its weights and biases. $\delta_{TK}(n) = \partial \hat{T}_c(n) / \partial \hat{K}_{\text{cov}}$, $\delta_{TC}(n) = \partial \hat{T}_c(n) / \partial m\hat{C}_P$, $\delta_{\Delta TK}(n) = \partial \Delta \hat{T}_c(n) / \partial \hat{K}_{\text{cov}}$ and $\delta_{\Delta TC}(n) = \partial \Delta \hat{T}_c(n) / \partial m\hat{C}_P$.

The Sensitive Matrix (SM) is defined as follows,

$$\prod_{RC}(n) = \begin{bmatrix} \delta_{TK}(n) & \delta_{TC}(n) \\ \delta_{\Delta TK}(n) & \delta_{\Delta TC}(n) \end{bmatrix} \tag{A.5}$$

A.3: SM Recursive Updating Model

Parameters A and B of the SM Recursive Updating Model in (5.14),

$$A = \begin{bmatrix} m\hat{C}_P & (\hat{T}_c(n) - T_a(n-1)) \cdot \Delta T \\ m\hat{C}_P & -1 \end{bmatrix} / (\Delta T \cdot \hat{K}_{cov} + m\hat{C}_P) \tag{A.6}$$

$$B = \begin{bmatrix} -\hat{K}_{\text{cov}} \cdot \Delta T & (\hat{T}_c(n) - T_a(n-1) - \Delta T_c(n)) \cdot \Delta T \\ -\hat{K}_{\text{cov}} \cdot \Delta T & -\Delta T_c(n) \end{bmatrix} / (\Delta T \cdot \hat{K}_{\text{cov}} + m\hat{C}_P) \tag{A.7}$$

APPENDIX B

DRAKE 795 KCM 26/7 ACSR CONDUCTOR PARAMETERS

Material	Aluminum	Steel
Weights per unit length (lb/ft)	0.750	0.344
Specific Heat (J/(lb-^{o}C))	433	216
Thermal Conductivity (W/(m.K))	200	16-50
Heat Capacity J/(ft-^{o}C)	325	74.3

Conductor Configurations [24]	
Outside Diameter r_0	1.11 in
Core Diameter r_s	0.41 in
Core Strand Diameter	0.14 in
Conductor Strand Diameter r_c	0.17 in
No. of Core Strands	7
No. of Conductor Strands n_c	26
No. of Outer Layer Conductor Strands	16
Conductor Fraction	0.951
Conductor Emissivity	0.75

APPENDIX C

BASE-CASE AMBIENT CONDITIONS OF AN OVERHEAD POWER LINE

Ambient temperature	0-40 ^{o}C
Wind speed	3 fps – 25 fps (perpendicular to line)
Latitude	30°
Azimuth of conductor	90°
Atmosphere	Clear
Solar Heating	On
Emissivity [24]	0.5
Absorptivity [24]	0.5
Elev. Above Sea Level	100 feet

APPENDIX D

CHARGE DENSITY DISTRIBUTION OVER MDCS SURFACE

For a long, straight, isolated round wire with electric charges, particularly if the length of the conductors is many times larger than the radius, the E-field around the conductor is in a radial direction, which is only a function of radius and angular, but not of z dimension. Therefore, all the following problems are studied in two dimensions, and the solutions do not depend on z.

Case 1: mDCS Surface Charge Density subject to earth

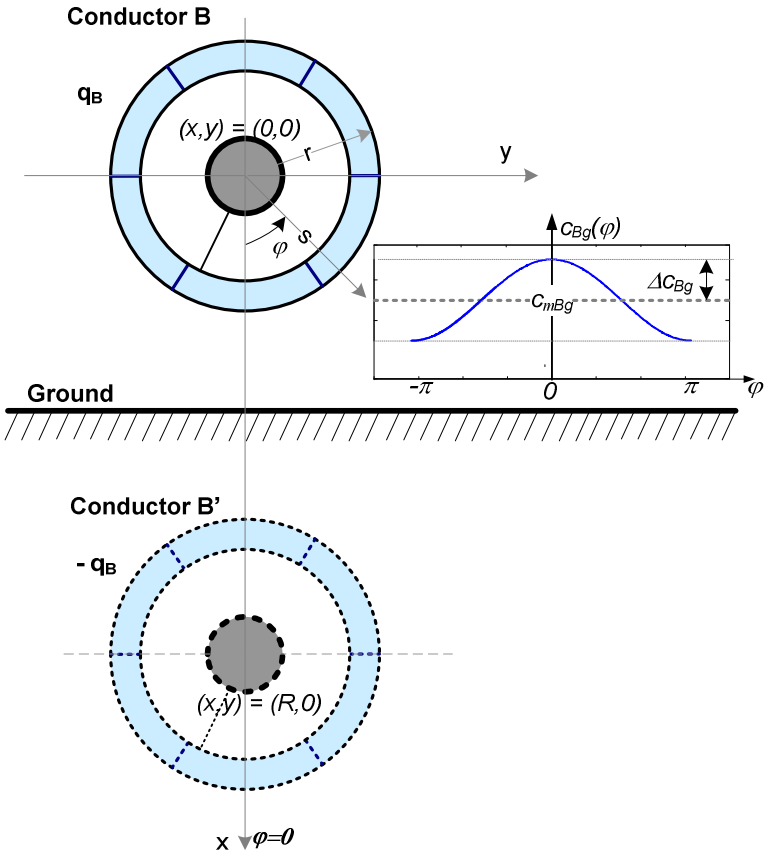

Figure D.1. mDCS surface charge density subject to earth

In this case, a configuration consisting of a long power line B suspended above earth is considered. The cylindrical metallic displacement current sensor is mounted and electrically connected onto line B, which is called Conductor B as one conducting body with the potential of V_B. Application of the theory of images results in the equivalent configuration as shown in Figure D.1. The center of Conductor B is at *(x, y)=(0,0)* with radius of *r*, and the center of its image Conductor B' is at *(x, y) = (R, 0)*.

The 2-D Laplace's equation in cylindrical coordinates [115] is given by,

$$\nabla^2\Phi(s,\varphi) = \frac{1}{s}\frac{\partial}{\partial s}(s\frac{\partial\Phi}{\partial s}) + \frac{1}{s^2}(\frac{\partial^2\Phi}{\partial\varphi^2}) \tag{D.1}$$

where Φ is the potential field. *s* is used for the radius, and φ is the angular dimension, which is measured in the counter-clockwise direction with respect to the *x*-axis (or the axis of $\varphi = 0$).

The boundary conditions are,

$$\Phi(s,\varphi) = V_B, \quad s = r \quad Conductor\,B \tag{D.2}$$

$$\Phi(s,\varphi) = -V_B, \quad s^2 + R^2 - 2sR\cos(\varphi) = r^2 \quad Conductor\ B' \tag{D.3}$$

where V_B is the potential Conductor B.

By solving this Laplace's equation (D.1), the potential at the position of *(s, φ)* is given by,

$$\Phi(s,\varphi) = \frac{V_B}{\ln(K1)}\ln\frac{s^2 + (h+a)^2 - 2s(h+a)\cos(\varphi)}{s^2 + (h-a)^2 - 2s(h-a)\cos(\varphi)} \tag{D.4}$$

where $h = R/2$, $a = \sqrt{(\frac{R}{2})^2 - r^2}$, $K1 = \frac{(h+a)^2}{r^2}$, and $\Delta h = h - a$.

The E-field intensity $\vec{E}(s,\varphi)$ can be found by taking the gradient of the potential field and its value at $s = r$ is normal to Conductor B surface, as given by,

$$\begin{aligned} \vec{E}(r,\varphi) &= E_N(r,\varphi) = -\nabla \cdot \Phi(r,\varphi) \\ &= \frac{V_B \cdot a}{\ln((h+a)/r) \cdot r} \cdot (\frac{R}{2} - r\cos(\varphi))^{-1} \cdot \vec{s} \end{aligned} \tag{D.5}$$

In a homogenous dielectric, the electric flux density on Conductor B is also normal to the surface, as given by $D_N = \varepsilon_0 E_N$. Considering the boundary conditions existing at the interface between a conductor and a dielectric, the surface charge density on Conductor B can be expressed [115] by:

$$\begin{aligned} \rho_{sB}(r,\varphi) &= |\vec{D}(r,\varphi)| = D_N = \varepsilon_0 E_N \\ &= \frac{\varepsilon_0 V_B \cdot 2a}{\ln((h+a)/r) \cdot rR} \cdot (1 - \frac{2r}{R}\cos(\varphi))^{-1} \\ &\approx \frac{\varepsilon_0 V_B \cdot 2a}{\ln((h+a)/r) \cdot rR}(1 + \frac{2r}{R}\cos(\varphi) - \frac{4r^2}{R^2}\cos^2(\varphi) - ...) \end{aligned} \tag{D.6}$$

Note that the third and higher order items in (D.6) are small and can be neglected when $R>>r$. Therefore, the surface charge density on Conductor B surface can be approximated to be a sinusoidal distribution with a constant bias, as given by,

$$\rho_{sB}(r,\varphi) = \frac{\varepsilon_0 V_B \cdot 2a}{\ln((h+a)/r) \cdot rR}(1 + \frac{2r}{R}\cos(\varphi)) = \rho_{sB\_m} + \Delta\rho_{sB} \cdot \cos(\varphi) \tag{D.7}$$

where φ is measured in the counter-clockwise direction with respect to the x-axis (it is also defined as "BG Electric Axis"). ρ_{sB_m} and $\Delta\rho_{sB}(\varphi)$ are defined to be the common and differential modes of Conductor *B* surface charge density, as expressed by,

$$\rho_{sB\_m} = V_B \cdot \frac{2a\varepsilon_0}{\ln((h+a)/r) \cdot rR} \tag{D.8}$$

$$\Delta\rho_{sB} = V_B \cdot \frac{4ar\varepsilon_0}{\ln((h+a)/r) rR^2} \tag{D.9}$$

Case 2: mDCS Surface Charge Density subject to an Adjacent Object

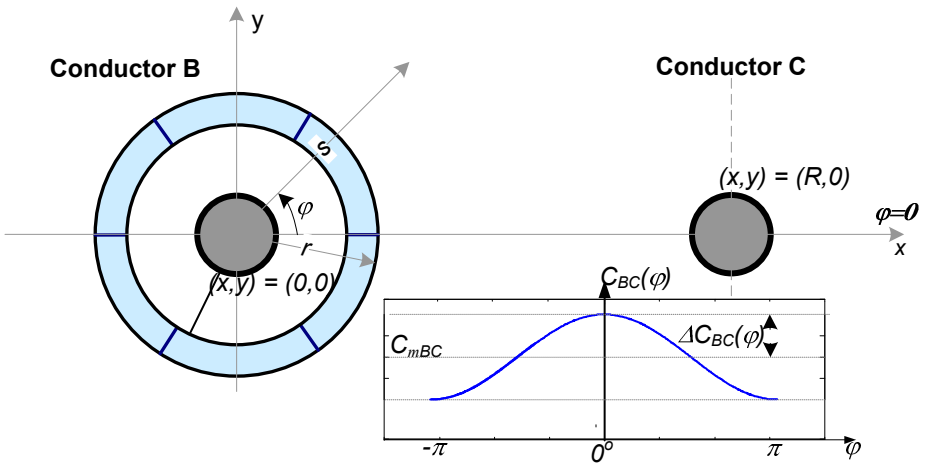

Figure D.2. mDCS surface charge density subject to one adjacent object

In this case, a configuration consisting of two long and parallel power line B and C is considered. Again, the cylindrical metallic sensor and the line B are called the Conductor B as one conducting body. Both of these two conductors have circular cross sections, as shown in Figure D.2. The center of Conductor B is at *(x, y)=(0, 0)* with radius of *r*. Conductor C is represented by its equivalent line charge ρ_L concentrated along an

infinitesimal filament coincident with the wire axis *(x, y)=(R,0)*, since its radius is much smaller than *R*.

The 2-D Laplace's equation in cylindrical coordinates [115] is given by,

$$\nabla^2\Phi(s,\varphi)=\frac{1}{s}\frac{\partial}{\partial s}(s\frac{\partial\Phi}{\partial s})+\frac{1}{s^2}(\frac{\partial^2\Phi}{\partial\varphi^2}) \tag{D.10}$$

where Φ is the potential field. *s* is used for the radius, and φ will be the angular dimension, which is measured in the counter-clockwise direction with respect to *x*-axis (or the axis of $\varphi=0$).

The boundary conditions are,

$$\Phi(s,\varphi)=0,\ \ s=R,\ \varphi=0^o\quad Conductor\ C; \tag{D.11}$$

$$\Phi(s,\varphi)=V_B,\quad s=r\quad Conductor\ B \tag{D.12}$$

where the potential difference between the two conductors is V_B, with Conductor C potentially equal to zero, and Conductor B potential of V_B.

By solving this Laplace's equation, the potential at the position of *(s, φ)* is given by,

$$\Phi(s,\varphi)=\frac{V_B}{2\ln(K1)}\ln\frac{s^2+R^2-2sR\cos(\varphi)}{s^2+\Delta h^2-2s\Delta h\cos(\varphi)} \tag{D.13}$$

where $K1=\frac{R^2}{r^2}$, and $\Delta h=\frac{r^2}{R}$

The E-field intensity can be found by taking the gradient of the potential field and its value at $s=r$ is normal to Conductor B surface, as given by,

$$\begin{aligned}\vec{E}(r,\varphi) &= E_N(r,\varphi) = -\nabla\cdot\Phi(r,\varphi) \\ &= \frac{V_B\cdot(R^2-r^2)}{2\ln(R/r)\cdot r}\cdot(r^2+R^2-2rR\cos(\varphi))^{-1}\cdot\vec{s}\end{aligned} \tag{D.14}$$

In a homogenous dielectric, the electric flux density on Conductor B is also normal to the surface, as given by $D_N = \varepsilon_0 E_N$. Considering the boundary conditions existing at the interface between a conductor and a dielectric, the surface charge density on Conductor B can be expressed by,

$$\begin{aligned}\rho_{sB}(r,\varphi) &= \vec{D}(r,\varphi) = D_N = \varepsilon_0 E_N \\ &= \frac{\varepsilon_0 V_B(R^2-r^2)}{\ln(R/r)\cdot r}\cdot(r^2+R^2-2rR\cos(\varphi))^{-1} \\ &\approx \frac{\varepsilon_0 V_B}{2\ln(R/r)}\frac{R^2-r^2}{r(R^2+r^2)}(1+\frac{2Rr}{r^2+R^2}\cos(\varphi)-\frac{4Rr}{(r^2+R^2)^2}\cos^2(\varphi)-...)\end{aligned} \tag{D.15}$$

Note that the third and higher order items in (D.15) are small and can be neglected when $R>>r$. Therefore, the surface charge density on Conductor B surface can be approximated to be a sinusoidal distribution with a constant bias, as given by,

$$\rho_{sB}(r,\varphi) = \frac{\varepsilon_0 V_B(R^2-r^2)}{2\ln(R/r)(R^2+r^2)r}(1+\frac{2Rr}{r^2+R^2}\cos(\varphi)) = \rho_{sB\_m} + \Delta\rho_{sB}\cdot\cos(\varphi) \tag{D.16}$$

where φ is measured in the counter-clockwise direction with respect to the x-axis (in this case, it is defined as "BC Electric Axis"). ρ_{sB_m} and $\Delta\rho_{sB}(\varphi)$ are defined to be the common and differential modes of Conductor B surface charge density, as expressed by,

$$\rho_{sB\_m} = V_B \cdot \frac{\varepsilon_0 (R^2 - r^2)}{2r(R^2 + r^2)\ln(R/r)} \tag{D.17}$$

$$\Delta\rho_{sB} = V_B \frac{\varepsilon_0 \cdot 2Rr(R^2 - r^2)}{2r(R^2 + r^2)^2 \ln(R/r)} \tag{D.18}$$

APPENDIX E

FREQUENCY DEPENDENT MODEL OF A 3-Φ TRANSMISSION LINE WITH GROUND RETURN CONSIDERED

Frequency dependent overhead power line models have been studies for decades [122] [123]. Under high frequencies excitation, the per-unit-length model of an overhead power line is the basic structure, where the EM wave propagation along the line can be described, in the frequency domain, by the following line equations,

$$\begin{aligned} \frac{d}{dx}\boldsymbol{V}_{abc}(\omega,x) &= -\boldsymbol{Z}(\omega,x)\cdot\boldsymbol{I}_{abc}(\omega,x) \\ \frac{d}{dx}\boldsymbol{I}_{abc}(\omega,x) &= -\boldsymbol{Y}(\omega,x)\cdot\boldsymbol{V}_{abc}(\omega,x) \end{aligned} \tag{E.1}$$

where $\boldsymbol{V}_{abc}(\omega,x)$ and $\boldsymbol{I}_{abc}(\omega,x)$ are line voltage and current vectors in the frequency domain at any point x along the line. $\boldsymbol{Z}(\omega)=\boldsymbol{R}(\omega)+j\omega\boldsymbol{L}(\omega)$ and $\boldsymbol{Y}(\omega)=\boldsymbol{G}(\omega)+j\omega\boldsymbol{C}(\omega)$ are the line per-unit-length impedance and admittance matrices, which are often functions of the position along the line, x, because of the line discontinuity. For imperfect conductors, the skin effect increases as the frequency increases. Therefore, line parameters $\boldsymbol{R}$ are constant at lower frequencies and increase as $\sqrt{f}$ at the higher frequencies. In 1929, Carson [129] published a method for determining the AC transmission line frequency-dependent impedance considering earth return, which is still the standard method for calculation of the frequency-dependent impedance of overhead transmission lines.

The line per-unit series-impedance matrix is normally approximated by $\boldsymbol{Z}(\omega)\cong\boldsymbol{A}+\boldsymbol{B}_s\sqrt{j\omega}+j\omega\boldsymbol{L}_e$, where $\boldsymbol{A}$ represents the dc per-unit-length resistance matrix.

The component $\boldsymbol{B}_s\sqrt{j\omega}$ represents the conductor resistance and internal inductive affect increasing as $\sqrt{\omega}$ at high frequencies, as the result of skin-effect developed inside the conductor and earth return path under high-frequencies. $\boldsymbol{L_e}$ represents the external inductive affect, which is independent of frequency and determined by the line geometry configuration, i.e. the conductor separation and ground clearance, etc. The line per-unit shunt admittance matrix is expressed by $\boldsymbol{Y(\omega) = G + j\omega C}$. Matrix $\boldsymbol{C}$ represents the capacitive coupling between conductors in the system. It is noted that, the loss introduced by imperfect conductors is usually more significant than the loss due to the medium for typical transmission line structures. It is for this reason that the surrounding medium is often assumed to be lossless, i.e., set $\boldsymbol{G} = 0$. References [129] [131] give a comprehensive description of each entry of above matrices, $\boldsymbol{Z}(\omega)$ and $\boldsymbol{Y}(\omega)$.

To decouple (E.1), the symmetrical component transformation is used, given by,

$$\boldsymbol{T} = \frac{1}{\sqrt{3}}\begin{bmatrix} 1 & 1 & 1 \\ 1 & a^2 & a \\ 1 & a & a^2 \end{bmatrix} \tag{E.2}$$

where $a = e^{-j120^0}$. The symmetrical sequence voltages $\boldsymbol{V}_{012}(x)$ and currents $\boldsymbol{I}_{012}(x)$ are related to their phase quantities by $\boldsymbol{V}_{abc}(x) = \boldsymbol{T} \cdot \boldsymbol{V}_{012}(x)$ and $\boldsymbol{I}_{abc}(x) = \boldsymbol{T} \cdot \boldsymbol{I}_{012}(x)$.

After applying the above symmetrical component transformation to (E.1), the EM wave propagation along the 3-Φ line can be described in symmetric sequence quantities, by the following line equations [123]

$$\begin{aligned} \frac{d}{dx}\boldsymbol{V}_{012}(x,s) &= -[\boldsymbol{A}_{012} + \boldsymbol{B}_{012}\sqrt{s} + s\boldsymbol{L}_{012}] \cdot \boldsymbol{I}_{012}(x,s) = -\boldsymbol{Z}_{012}(s) \cdot \boldsymbol{I}_{012}(x,s) \\ \frac{d}{dx}\boldsymbol{I}_{012}(x,s) &= -s\boldsymbol{C}_{012} \cdot \boldsymbol{V}_{012}(x,s) = -\boldsymbol{Y}_{012}(s) \cdot \boldsymbol{V}_{012}(x,s) \end{aligned} \tag{E.3}$$

References [132] [133] give a comprehensive description of the parameters in the above equation.

APPENDIX F

THEVENIN EQUIVALENT OF AN OVERHEAD POWER LINE SUBJECT TO 3-Φ VOLTAGE COUPLING

F.1. Equivalent Impedance of an Overhead Power Line subject to a 3-Φ "Parallel" Coupling

If it is assumed there are three phase voltages, in vector form $\boldsymbol{V}_{abc,r}(\omega,x)=[V_a \quad V_b \quad V_c]'$, that are coupled in parallel to the 3-Φ power line system at the position of *x=0*, as shown in Figure F.1, then the terminal voltages and currents at the position of the voltages inject can be expressed as follow,

$$\boldsymbol{V}_{abc,r}(\omega,0)=\boldsymbol{Z}_{\boldsymbol{eq,r}}(\omega)\cdot\boldsymbol{I}_{abc}(\omega,0) \tag{F.1}$$

where $\boldsymbol{Z}_{\boldsymbol{eq,r}}(\omega)$ is the equivalent impedance matrix of the power line seen from the point of *x=0* to the right. Because of mutual coupling between different conductors and ground, both series-impedance and shunt-admittance matrices, $\boldsymbol{Z}(\omega)$ and $\boldsymbol{Y}(\omega)$, are full matrices. So is $\boldsymbol{Z}_{\boldsymbol{eq,r}}(\omega)$, which results in (F.1) being a set of three coupled equations.

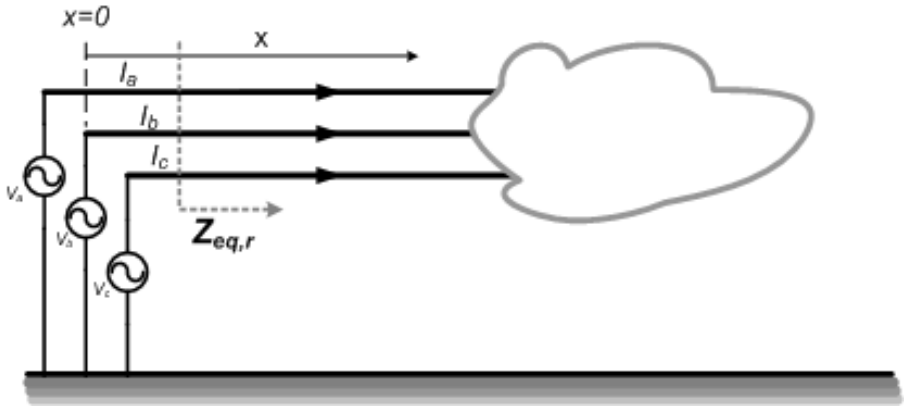

Figure F.1. 3-Φ Parallel Coupling

Apply the transformation $\boldsymbol{T}$ to (F.1), the following can be obtained,

$$\boldsymbol{T}^{-1} \cdot \boldsymbol{V}_{abc,r}(\omega, x) = [\boldsymbol{T}^{-1} \cdot \boldsymbol{Z}_{eq,r}(\omega) \cdot \boldsymbol{T}] \cdot \boldsymbol{T}^{-1} \cdot \boldsymbol{I}_{abc}(\omega, x) \tag{F.3}$$

$$\boldsymbol{V}_{012,r}(\omega, x) = \boldsymbol{Z}_{eq,r,012}(\omega) \cdot \boldsymbol{I}_{012}(\omega, x) \tag{F.4}$$

where $\boldsymbol{Z}_{eq,r,012}$ is the equivalent impedance matrix of the power line but in sequence quantities seen at the point of $x=0$ to the right. $\boldsymbol{V}_{012,r} = [V_{0,r} \quad V_{1,r} \quad V_{2,r}]'$, $\boldsymbol{I}_{012} = [I_0 \quad I_1 \quad I_2]'$, and $\boldsymbol{I}_{abc} = [I_a \quad I_b \quad I_c]'$.

If the overhead power line under study is assumed to be fully transposed, the matrix $\boldsymbol{Z}_{eq,r}$ is approximated to be symmetric. $\boldsymbol{Z}_{eq,r,012} = diag([Z_{eq0,r} \quad Z_{eq1,r} \quad Z_{eq2,r}])$ is therefore diagonal, where each diagonal element represents the equivalent impedance of the power line in each sequence network.

With reference to (F.4), the terminal voltage and current for every symmetric sequence can be related to each other through the equivalent impedance of its own natural mode of EM wave propagation along the line, as depicted as follow,

$$I_0 = \frac{V_{0,r}}{Z_{eq0,r}} \tag{F.5}$$

$$I_1 = \frac{V_{1,r}}{Z_{eq1,r}} \tag{F.6}$$

$$I_2 = \frac{V_{2,r}}{Z_{eq2,r}} \tag{F.7}$$

F.2. Equivalent Impedance of an Overhead Power Line subject to 3-Φ "Series" Coupling

Now, if it is assumed there are three phase voltages, in vector form $\boldsymbol{V}_{abc,s}(\omega,x)=[V_a \quad V_b \quad V_c]'$, which are coupled **in series** to the power line network, as shown in Figure F.2.

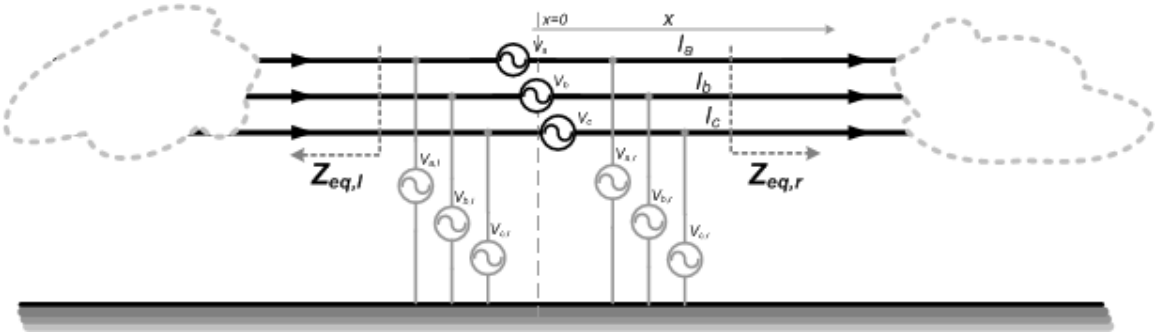

Figure F.2. 3-Φ Series Coupling

Applying the virtual parallel voltage concept, the series coupling voltage can be expressed by,

$$\boldsymbol{V}_{abc,s}(\omega,x)=\boldsymbol{V}_{abc,l}(\omega,x)+\boldsymbol{V}_{abc,r}(\omega,x) \tag{F.8}$$

where $\boldsymbol{V}_{abc,r}(\omega,x)=[V_{a,r} \quad V_{b,r} \quad V_{c,r}]'$ and $\boldsymbol{V}_{abc,l}(\omega,x)=[V_{a,l} \quad V_{b,l} \quad V_{c,l}]'$ are the vectors of the three phase virtual terminal voltages coupled **in parallel** to the right and left sides of the network respectively. With reference to (F.1), the terminal voltage and current can be expressed by, in terms of an equivalent impedance matrix,

$$\boldsymbol{V}_{abc,r}(\omega,x)=\boldsymbol{Z}_{\boldsymbol{eq,r}}(\omega)\cdot\boldsymbol{I}_{abc,s}(\omega,x) \tag{F.9}$$

$$\boldsymbol{V}_{abc,l}(\omega,x)=\boldsymbol{Z}_{\boldsymbol{eq,l}}(\omega)\cdot\boldsymbol{I}_{abc,s}(\omega,x) \tag{F.10}$$

where $\boldsymbol{Z}_{eq,r}(\omega)$ and $\boldsymbol{Z}_{eq,l}(\omega)$ are the equivalent impedance matrixes of the right and left sides of the network respectively, seen at the point of signal injection (where PLS module is mounted). $\boldsymbol{I}_{abc,s} = [I_a \quad I_b \quad I_c]'$.

Substitute (F.9) and (F.10) into (F.8), the following is obtained,

$$\begin{aligned} \boldsymbol{V}_{abc,s}(\omega, x) &= \boldsymbol{V}_{abc,l}(\omega, x) + \boldsymbol{V}_{abc,r}(\omega, x) \\ &= (\boldsymbol{Z}_{eq,l}(\omega, x) + \boldsymbol{Z}_{eq,r}(\omega, x)) \cdot I_{abc,s}(\omega, x) \end{aligned} \tag{F.11}$$

Apply the transformation $\boldsymbol{T}$ to (F.11) to obtain the following,

$$\boldsymbol{T}^{-1} \cdot \boldsymbol{V}_{abc,s}(\omega, x) = [\boldsymbol{T}^{-1} \cdot \boldsymbol{Z}_{eq,r}(\omega) \cdot \boldsymbol{T} + \boldsymbol{T}^{-1} \cdot \boldsymbol{Z}_{eq,l}(\omega) \cdot \boldsymbol{T}] \cdot \boldsymbol{T}^{-1} \cdot \boldsymbol{I}_{abc,s}(\omega, x) \tag{F.12}$$

$$\begin{aligned} \boldsymbol{V}_{012,s}(\omega, x) &= [\boldsymbol{Z}_{eq,r,012}(\omega) + \boldsymbol{Z}_{eq,l,012}(\omega)] \cdot \boldsymbol{I}_{012,s}(\omega, x) \\ &= \boldsymbol{Z}_{eq,012}(\omega) \cdot \boldsymbol{I}_{012,s}(\omega, x) \\ &= \boldsymbol{V}_{012,s,r} + \boldsymbol{V}_{012,s,l} \end{aligned} \tag{F.13}$$

where, $\boldsymbol{V}_{012,s} = [V_{s0} \quad V_{s1} \quad V_{s2}]'$, $\boldsymbol{V}_{012,s,r} = [V_{0,s,r} \quad V_{1,s,r} \quad V_{2,s,r}]'$, $\boldsymbol{V}_{012,s,l} = [V_{0,s,l} \quad V_{1,s,l} \quad V_{2,s,l}]'$, and $\boldsymbol{I}_{012,s} = [I_{s0} \quad I_{s1} \quad I_{s2}]'$

$\boldsymbol{Z}_{eq,012}$ are the equivalent impedances seen at the point of *x* in sequence modes of the power line, which is also a diagonal matrix based on the assumption that the overhead power line under study is symmetric. It is noted that, $Z_{eq0} = Z_{eq0,l} + Z_{eq0,r}$, $Z_{eq1} = Z_{eq1,l} + Z_{eq1,r}$ and $Z_{eq2} = Z_{eq2,l} + Z_{eq2,r}$ denoted as the equivalent impedances seen by the PLS module in the three sequence modes of EM wave propagation. $Z_{eq012,r}$ and $Z_{eq012,l}$ represent the equivalent impedance of the right and left side networks respectively.

With reference to (F.4), the terminal voltage and current for every symmetrical sequence can be related to each other through the equivalent impedance of its own natural mode of EM wave propagation along the line, depicted as follow,

$$I_0 = \frac{V_{0,s,r}}{Z_{eq0,r}} = \frac{V_{0,s,l}}{Z_{eq0,l}} = \frac{V_{0,s}}{Z_{eq0}} = \frac{1}{\sqrt{3}} \frac{V_{sB}}{Z_{eq0}} \tag{F.14}$$

$$I_1 = \frac{V_{1,s,r}}{Z_{eq1,r}} = \frac{V_{1,s,l}}{Z_{eq1,l}} = \frac{V_{1,s}}{Z_{eq1}} = \frac{1}{\sqrt{3}} \frac{\alpha \cdot V_{sB}}{Z_{eq1}} \tag{F.15}$$

$$I_2 = \frac{V_{2,s,r}}{Z_{eq2,r}} = \frac{V_{2,s,l}}{Z_{eq2,l}} = \frac{V_{2,s}}{Z_{eq2}} = \frac{1}{\sqrt{3}} \frac{\alpha^2 \cdot V_{sB}}{Z_{eq2}} . \tag{F.16}$$

APPENDIX G

NON-UNIFORMLY DISTRIBUTED TRANSMISSION LINE MODEL IN SINGLE PHASE MODEL REPRESENTATION

G.1. Per-unit Length Single Phase Model

An overhead power line is a multi-conductor EM wave transmission system, including three phase conductors, overhead ground wire, and ground return path, which are all coupled with each other. By applying modal decomposition techniques, three independent natural modes (denoted as zero-, positive-, and negative-sequence in this application) of the EM wave propagation along the line can be obtained. Each natural modal has its line parameters, and can be represented by a single-phase distributed (per-unit) EM transmission line model, as shown in Figure G.1. With reference to (E.1), the EM wave propagation of each natural mode along the line can be described by the following line equations, in the Laplace Domain,

$$\begin{aligned} \frac{d}{dx}V_{abc}(x,s) &= -[A + B\sqrt{s} + sL] \times I_{abc}(x,s) = -Z(s) \times I_{abc}(x,s) \\ \frac{d}{dx}I_{abc}(x,s) &= -sC \times V_{abc}(x,s) = -Y(s) \times V_{abc}(x,s) \end{aligned} \tag{G.1}$$

For convenient and simple notation, the single-phase model that is developed in this section removes the subscripts that have been used to indicate the sequence mode as presented in (E.3).

For each natural mode, the general solution to the single phase transmission line equation in (G.1) can be described as [122],

$$
\begin{aligned}
V(x+\Delta x,s) &= V^{+}(x+\Delta x,s)+V^{-}(x+\Delta x,s) \\
&= V^{+}(x,s)e^{-\gamma(s)\Delta x}+V^{-}(x,s)e^{\gamma(s)\Delta x} \\
I(x+\Delta x,s) &= I^{+}(x+\Delta x,s)-I^{-}(x+\Delta x,s) \\
&= \frac{1}{Z_C(s)}[V^{+}(x,s)e^{-\gamma(s)\Delta x}-V^{-}(x,s)e^{\gamma(s)\Delta x}]
\end{aligned}
\tag{G.2}
$$

where

$V^{+}(x+\Delta x,s)$ and $I^{+}(x+\Delta x,s)$ represent the forward-travelling waves, traveling in the $+x$ direction, and $V^{-}(x+\Delta x,s)$ and $I^{-}(x+\Delta x,s)$ represent the backward-travelling waves, traveling in the -x direction. $\gamma(s)=\sqrt{Z(s)/Y(s)}$ and $Z_C(s)=\sqrt{Z(s)\cdot Y(s)}$ are the **propagation constant** and **characteristic impedance** respectively.

If the transmission line under study is assumed to be uniformly distributed, and properly terminated, the EM wave propagation of one natural mode between two locations (x, $x+\Delta x$) along the line can be expressed by,

$$
\begin{bmatrix} V^{+}(x,s) \\ V^{-}(x,s) \end{bmatrix} = e^{\gamma(s)\Delta x}\begin{bmatrix} 1 & 0 \\ 0 & e^{-2\gamma(s)\Delta x} \end{bmatrix}\begin{bmatrix} V^{+}(x+\Delta x,s) \\ V^{-}(x+\Delta x,s) \end{bmatrix}
\tag{G.3}
$$

However, in actuality, an overhead power line, spreading for several miles, is a typical non-uniformly distributed transmission line. Its discontinuities may be caused by inherent line structure, such as different heights of line towers, or different terrain configurations, etc. The line discontinuities may also be caused by other reasons, such as variant conductor sagging conductions, vegetation proximity, or different earth soil resistivity conditions, etc.

Therefore, in the next section, the non-uniformly distributed overhead power line is modeled by a cascading procedure, where the line is divided into several segments, each of which is assumed to have a constant line impedance.

G.2. Non-uniformly distributed transmission line

Figure G.1 shows a generic presentation of a single-phase EM transmission system, e.g. the zero-sequence of an overhead power under study for this application. The power line is assumed to have length of *L*, and is divided into *M+1* line segments. Within each line segment, it assumes to have constant line parameters, denoted in terms of series impedance and shunt admittance, $< Z_j, Y_j >$, of the line segment *j*. However, the parameters of one line segment are different from the other, i.e., $< Z_j, Y_j > \neq < Z_{j\pm1}, Y_{j\pm1} >$.

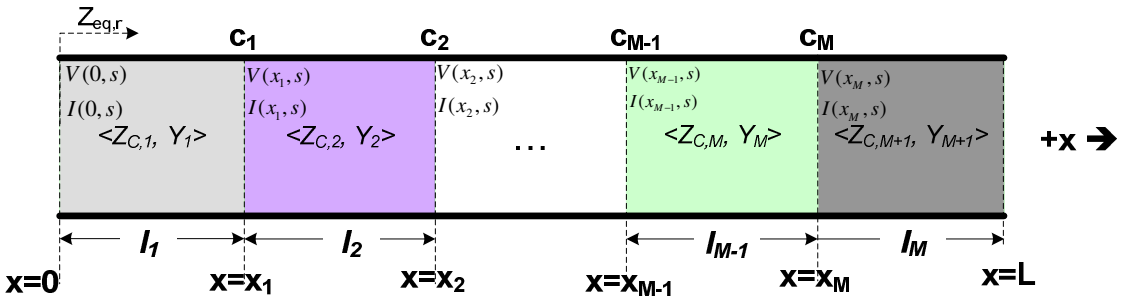

Figure G.1. General representation of a non-uniformly distributed EM wave transmission system – single phase model.

If the line parameters of all the line segments are the same, there is no wave reflection at the interface between the line segments. According to the wave propagation along a uniformly distributed line, as depicted in (G.3), the wave propagation in the jth line segment can be expressed as follows,

$$\begin{bmatrix} V^+(x_{j-1},s) \\ V^-(x_{j-1},s) \end{bmatrix} = e^{\gamma_j(s)l_i} \begin{bmatrix} 1 & 0 \\ 0 & e^{-2\gamma_j(s)l_i} \end{bmatrix} \begin{bmatrix} V^+(x_j,s) \\ V^-(x_j,s) \end{bmatrix} \tag{G.4}$$

where l_j is the length of the jth segment. $\begin{bmatrix} V^+(x_j,s) \\ V^-(x_j,s) \end{bmatrix}$ are the forward- and backward-travelling waves (travelling in $+x$ and $-x$ direction) respectively, at the interface between line segments j and $j+1$.

However, for non-uniform lines where the line parameters for each line segment are different from another, the line discontinuity at each line segment interface causes a wave reflection. With reference to Figure G.1, the wave propagation in the jth line segment can be expressed [122] as follows,

$$\begin{aligned} \begin{bmatrix} V^+(x_{j-1},s) \\ V^-(x_{j-1},s) \end{bmatrix} &= \frac{e^{\gamma_j(s)l_i}}{1+c_i} \begin{bmatrix} 1 & c_i \\ c_i e^{-2\gamma_j(s)l_i} & e^{-2\gamma_j(s)l_i} \end{bmatrix} \begin{bmatrix} V^+(x_j,s) \\ V^-(x_j,s) \end{bmatrix} \\ &= \boldsymbol{Tx}_j(s) \cdot \begin{bmatrix} V^+(x_j,s) \\ V^-(x_j,s) \end{bmatrix} \end{aligned} \tag{G.5}$$

where l_j is the length of the jth segment.

$c_j(s) = \dfrac{Z_{C,j+1} - Z_{C,j}}{Z_{C,j+1} + Z_{C,j}}$, for $j=0, 1, \ldots, M$, is the reflective coefficient at the location where line discontinuity happens.

With reference to (G.5), the **Transmission Matrix** for the line segment j is defined by,

$$\boldsymbol{Tx}_j(s) = \frac{e^{\gamma_j(s)l_i}}{1+c_i(s)} \begin{bmatrix} 1 & c_i(s) \\ c_i(s)e^{-2\gamma_j(s)l_i} & e^{-2\gamma_j(s)l_i} \end{bmatrix} \tag{G.6}$$

where $\gamma_j(s) = \sqrt{\frac{Z_j}{Y_j}}$ and $Z_{C,j}(s) = \sqrt{Z_j \times Y_j}$ are the propagation constant and characteristic impedance of the jth line segment respectively. Figure G.2 provides a generic Transmission Matrix representation.

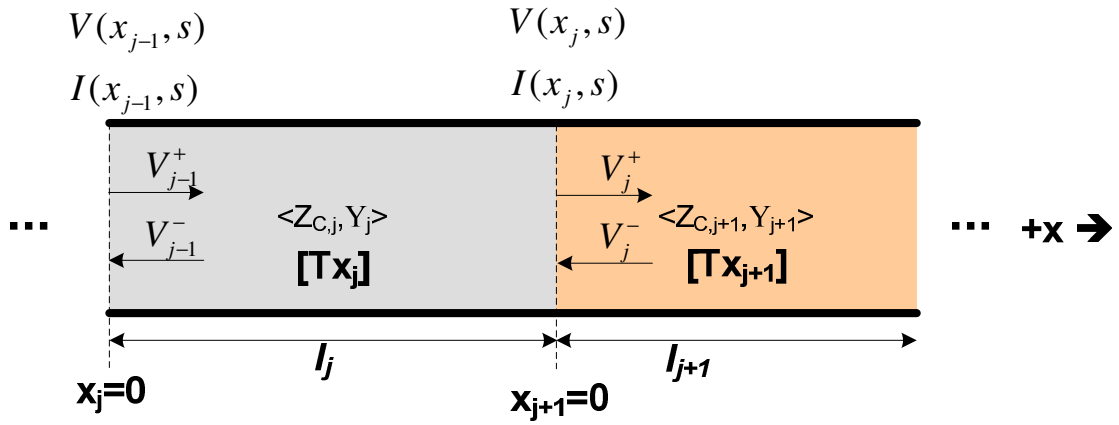

Figure G.2 Transmission Matrix representation.

Apply the **Transmission Matrix** in (G.6) for each line segment and cascade the line segment transition depicted in (G.5), and the wave propagation along the entire non-uniformly distributed power line can be described as follows,

$$\begin{bmatrix} V^+(x_0,s) \\ V^-(x_0,s) \end{bmatrix} = \frac{\prod_{j=0}^{M} e^{\gamma_j(s)\cdot l_j}}{\prod_{j=0}^{M}(1+c_j)} \left[\prod_{j=0}^{M} \boldsymbol{Tx}_j\right] \cdot \begin{bmatrix} V^+(x_M,s) \\ V^-(x_M,s) \end{bmatrix} \qquad \text{(G.7)}$$

The equivalent Transmission Matrix $\left[\prod_{j=0}^{M} \boldsymbol{Tx}_j\right]$ is obtained as the product, in the appropriate order, of the whole set of Transmission Matrices.

At the two terminals of the entire line, i.e., segments 0 and M, the boundary conditions are given by $V(x_0,s) = I(x_0,s) \cdot Z_{C,0}(s)$ and $V(x_M,s) = I(x_M,s) \cdot Z_{C,M}(s)$, where $Z_{C,0}(s)$ and $Z_{C,M}(s)$ are the two terminal impedances of the line. $<V(x_0,s),\ I(x_0,s)>$ and $<V(x_M,s),\ I(x_M,s)>$ are the two terminal voltages and currents.

Substitute the above line terminal conditions in to (G.7), the EM wave propagation along a non-uniform transmission line can then be depicted in terms of two terminal voltages and currents, given by,

$$\begin{bmatrix} V(x_0,s) \\ I(x_0,s) \end{bmatrix} = \frac{\prod_{j=0}^{M} e^{\gamma_j(s)\cdot l_j}}{\prod_{j=0}^{M}(1+c_j(s))} \boldsymbol{Y}_{C,0}(s) \cdot \left[\prod_{j=0}^{M} \boldsymbol{Tx}_j(s) \right] \cdot \begin{bmatrix} V(x_M,s) \\ 0 \end{bmatrix} \qquad \text{(G.8)}$$

where $\boldsymbol{Y}_{C,0} = \frac{1}{Z_{C,0}(s)} \begin{bmatrix} Z_{C,0}(s) & Z_{C,0}(s) \\ 1 & -1 \end{bmatrix}$.

Equation (G.8) gives a complete description of a single-phase, non-uniformly distributed transmission line model for one sequence (natural) model of EM propagation along a 3-Φ overhead power line. Combine (G.8) with Figure 10.5, and a complete mathematical model of the 3-Φ overhead power line at the location where the PLS module is mounted can be obtained. This model considers all the effects on wave propagation performance along the line, as discussed in Section 8.1, including line asymmetric operation (model decomposition), lossy earth return path (frequency dependent line parameters), and line discontinuity (cascaded transmission matrix).

This model defined by (G.8) provides the theoretical base to validate that the equivalent impedance seen by the PLS module is a useful indicator for the variation of line discontinuities caused by potential incipient insulation failure.

G.3. Equivalent Impedance of Single-Phase, Non-uniformly Distributed Line

Taking the right-side of the zero-sequence power line network shown in Figure 10.5, for instance, the boundary condition can be expressed by $V(x_0, s) = V_{s0,r}$ and $I(x_0, s) = I_{s0}$. For the simplest case, if the zero-sequence network of the line has a discontinuity only at the location $x = x_1$, as shown in Figure G.3, its equivalent impedance, at the point of x=0, can be derived with reference to (G.8).

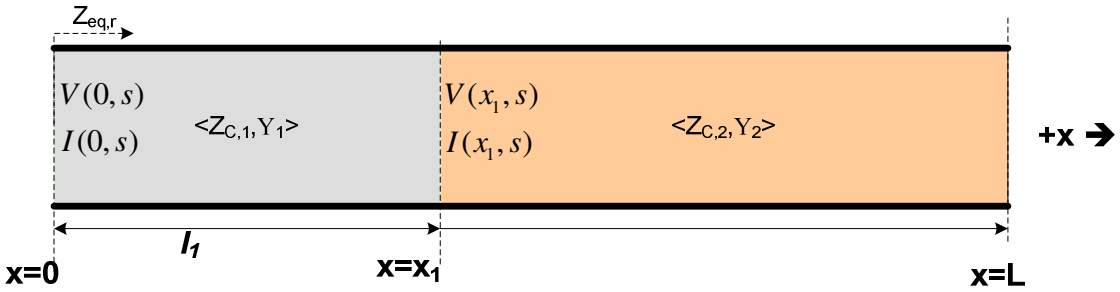

Figure G.3. An EM transmission line with one discontinuity at $x = x_1$

For a non-uniformly distributed transmission line with only one line discontinuity, (G.8) can be re-written by,

$$\begin{bmatrix} V_{s0,r}(0,s) \\ I_{s0}(0,s) \end{bmatrix} = \frac{e^{\gamma_1(s)\cdot l_1}}{(1+c_1)} \boldsymbol{Y}_{C,1} \begin{bmatrix} 1 & c_1 \\ c_1 e^{-2\gamma_1 x_1} & e^{-2\gamma_1 x_1} \end{bmatrix} \boldsymbol{Y}_{C,2}^{-1} \begin{bmatrix} V(x_1,s) \\ I(x_1,s) \end{bmatrix}$$
$$= \frac{e^{\gamma_1(s)\cdot l_1}}{(1+c_1)} \begin{bmatrix} 1+c_1 e^{-2\gamma_1 x_1} & c_1 + e^{-2\gamma_1 x_1} \\ Y_{C,1}(1-c_1 e^{-2\gamma_1 x_1}) & Y_{C,1}(c_1 - e^{-2\gamma_1 x_1}) \end{bmatrix} \begin{bmatrix} V^+(x_1,s) \\ 0 \end{bmatrix} \quad \text{(G.9)}$$

where the boundary conditions are given by $\boldsymbol{Y}_{C,1} = \begin{bmatrix} 1 & 1 \\ Y_{C,1} & -Y_{C,1} \end{bmatrix}$ and $\boldsymbol{Y}_{C,2}^{-1}(s) = \frac{1}{2}\begin{bmatrix} 1 & Z_{C,2}(s) \\ 1 & -Z_{C,2}(s) \end{bmatrix}$. Therefore, the equivalent impedance seen from location $x = 0$ is given by,

$$Z_{eq0,r} = \frac{V_{s0,r}(0,s)}{I_{s0}(0,s)} \approx Z_{C,1} + 2Z_{C,1} \cdot c_1 \cdot e^{-2\gamma_1 l_1} \tag{G.10}$$

where $c_1 = \frac{Z_{C,2} - Z_{C,1}}{Z_{C,2} - Z_{C,1}}$ is the reflective coefficient at the location of the load end.

If the above case is extended to a general case, where a non-uniform distributed transmission line with length of *L* has the line discontinuities at *M* locations along the line, its equivalent impedance seen from the location $x = 0$ can be described by

$$\begin{aligned} Z_{eq0,r}(s) &= \frac{V_{s0,r}(0,s)}{I_{s0}(0,s)} \\ &\approx Z_{C,1} + 2Z_{C,1} \cdot c_1 \cdot e^{-2\gamma_1 l_1} + 2Z_{C,1} \cdot (1 - c_1^2) \sum_{i=1}^{M} (c_i \cdot \prod_{k=1}^{i} e^{-2\gamma_k l_k}) \end{aligned} \tag{G.11}$$

The above derivation is based on the following assumption. If the maximum conductor-to-ground clearance is assumed to have a maximum variation of 10 meters from one line segment to another, or the soil resistivity changes by a maximum of two times, the reflection coefficient is normally within the range of $\pm 10\%$. Note the multiplication of reflection coefficients $\prod_{j=1}^{k} c_k \le 1\%$, if $k \ge 2$, so that any terms in (G.11) that contain this coefficient are assumed to be zero, and are ignored.

To illustrate how the equivalent impedance variation indicates the line discontinuity variation, Figure G.4 depicts a non-uniformly distributed line with multiple line discontinuities. Figure G.4 (a) shows Case-1, where two line discontinuities happen at the locations of $x = x1$ and $x = x4$. Compared to Case-1, Case-2 represent a different line condition when a disturbance happens somewhere between $x = x1$ and $x = x4$, where the line characteristic impedance changes to different values, i.e., $< Z_2, Y_2 > \Rightarrow \ < Z_3, Y_3 >$. This line disturbance creates another two line discontinuities at the locations of $x = x2$ and $x = x3$ along the line, as shown in Figure G.4 (b).

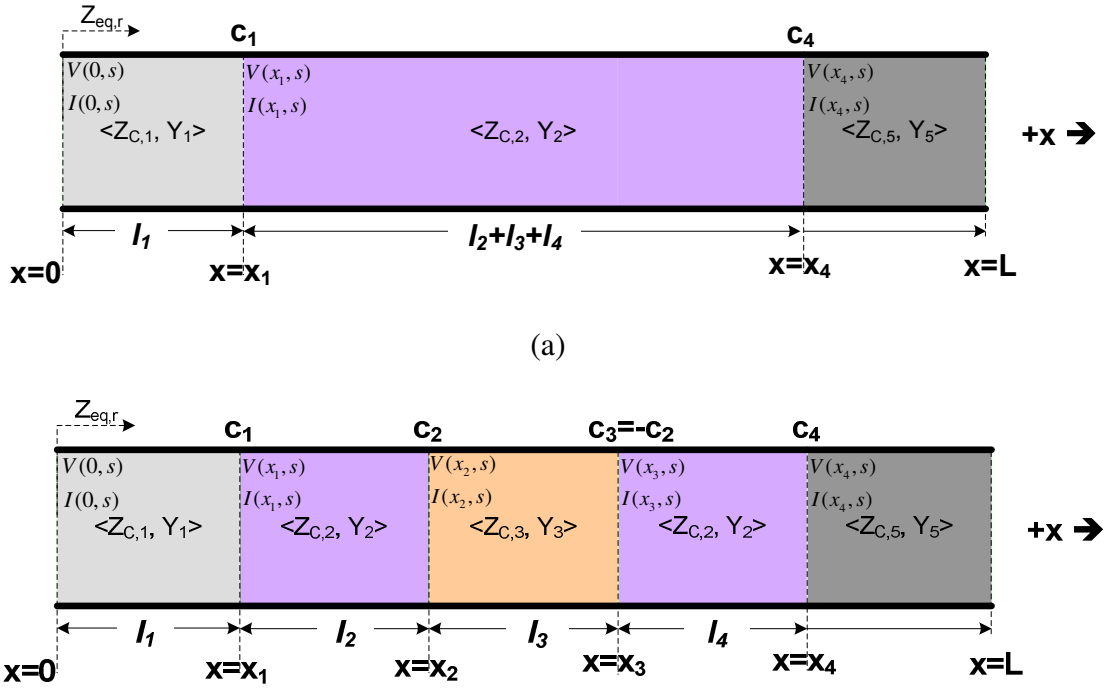

Figure G.4. Non-uniformly distributed line with multiple line discontinuities: (a) before disturbance; (b) after disturbance.

With reference to (G.11), the line equivalent impedance of Case-1 can be expressed by,

$$Z_{eq0,r}(s) = \frac{V_{s0,r}(0,s)}{I_{s0}(0,s)} \approx Z_{C,1} + 2Z_{C,1} \cdot c_1 \cdot e^{-2\gamma_1 l_1} + 2Z_{C,1} \cdot c_4 \cdot (1-c_1^2) e^{-2(\gamma_1 l_1 + \gamma_2 (l_2 + l_3 + l_4))} \quad \text{(G.12)}$$

Similarly the line equivalent impedance of Case-2 can be expressed by,

$$Z_{eq0,r}(s) = \frac{V_{s0,r}(0,s)}{I_{s0}(0,s)} \approx Z_{C,1} + 2Z_{C,1} \cdot c_1 \cdot e^{-2\gamma_1 l_1} + 2Z_{C,1} \cdot (1-c_1^2) \sum_{i=1}^{4} (c_i \cdot \prod_{k=1}^{i} e^{-2\gamma_k l_k}) \quad \text{(G.13)}$$

Subtract the equivalent impedance in (G.12) from (G.13) to obtain the equivalent impedance variation as follow,

$$\Delta Z_{eq,r}(s) \approx 2Z_{C,1} \cdot c_2 \cdot e^{-2(\gamma_1 l_1 + \gamma_2 l_2)} + 2Z_{C,1} \cdot c_3 \cdot e^{-2(\gamma_1 l_1 + \gamma_2 l_2 + \gamma_3 l_3)} \quad \text{(G.14)}$$

The above equation indicates that, by evaluating the equivalent impedance variations from Case-1 to Case-2 as shown in Figure G.4, the existing discontinuities of the line are successfully removed, but only the variations of the line discontinuity are captured. With reference to (G.12), the line discontinuity variations are represented by the two terms, in each of which the reflection coefficients, c_2 and c_3, represent how severe the discontinuities are, and the terms $e^{-2\gamma_1 l_1}$ and $e^{-2(\gamma_1 l_1 + \gamma_2 l_2)}$ tell the location of the discontinuities happened.

APPENDIX H

PROTOTYPE POWER LINE SENSOR MODULE

---LIST OF KEY COMPONENTS

H.1. PLS Power Supply Circuitry

Item	Part No. & Value	Description
Power Supply		
Q1	GBJ2502-BPMS-ND RECT BRIDGE GPP 25A 200V GBJ	Bridge rectifier
Q2	STP120NF10 MOSFET N-CH 100V 120A TO-220	Switch
Q3	L78S05CV IC REG POSITIVE 2A 5V TO-220	Voltage regulator 8V - 5V
D1, D2	V30100S-E3/45GI-ND DIODE SCHOTTKY 30A 100V TO-220AB	
D3	LM4040AIZ-2.5-ND IC REF PREC VOLT MICROPWR TO-92	
U01	IC Socket TLV2474AIN IC R-TO-R OP AMP QUAD 14-DIP	OpAmp
U02	IC Socket LM339ANNS-ND IC COMPARATOR QUAD LO PWR 14-DIP	Comparator
U03	TPS7333QP 5V→ 3.3V	Voltage regulator
R01	15FR200E-ND RES CURRENT SENSE .200 OHM 5W	Current sensing Feedback resistance
R02	60 kΩ	DC voltage fb resistor
R03	20 kΩ	DC voltage fb resistor
R04	2.5 kΩ potential meter	DC voltage fb resistor fine tune~~
R05	100 kΩ	Hysteresis comparator
R06	5 kΩ	Hysteresis comparator
R07	5 kΩ	Hysteresis comparator
R08	3 kΩ	Hysteresis comparator
R09	250 kΩ	U03 related
C01	50 V / 2200 μF	Main DC capacitor
C02	50 V / 33 μF	
C03	50 V / 33 μF	
C04,	0.1μF	IC chip capacitor

C05, C06		
C07	0.1μF	U03 related
C08	10 V / 10μF	U03 related

H.2. PLS ZigBee RF Circuitry

Item	Part No. & Value	Description
xBee RF section		
U11	xBee RF module	
U12	74LS04	For LED display
U13	TPS7333QP	Voltage regulator
LD1, 2, 3	LED	Comm. Status Display
R11, R12, R13	330	LED related
C11	50 V / 1μF	xBee related
C12	0.1 μF	xBee related

BIBLIOGRAPHY

[1] "The Smart Grid: An Introduction," The U.S. Department of Energy [Online]. Available: http://www.oe.energy.gov/DocumentsandMedia/DOE_SG_Book_ Single_ Pages (1).pdf

[2] F. Kreikebaum, D. Das, J. Hernandez, and D. Divan, "Ubiquitous power flow control in meshed grids," in *Proc. 2009 IEEE Energy Conversion Congress and Exposition (ECCE)*, pp:3907-3914.

[3] C. Y. Chong, and S. P. Kumar, "Sensor Networks: Evolution, Opportunities, and Challenges," *Proceedings of IEEE*, vol. 91, issue 8, pp. 1247-1255, Aug. 2003.

[4] Y. Yang, F. Lambert, and D. Divan, "A Survey on Technologies for Implementing Sensor Networks for Power Delivery Systems," in *Proc. 2007 IEEE Power Engineering Society General Meeting*, Tampa, USA, June 2007 p.:8.

[5] George J. Anders, *Rating of Electric Cables: Ampacity Computations for Transmission, Distribution, and Industrial Applications*, New York: Institute of Electrical and Electronics Engineers, 1997.

[6] J.L. Lilien (2008, June). Ampacimon as a tool for transmission line assets management. University of Liège, Belgium [Online]. Available: www.ampacimon .com.

[7] H. E. House and P. D. Tuttle, "Current carrying capacity of ACSR," *IEEE Trans. on Power Apparatus and Systems*, vol. 77, issue 2, pp. 1169-1178, April 1958.

[8] D. A. Douglass, D. C. Lawry, A.-A. Edris, and E. C. III Bascom, "Dynamic thermal ratings realize circuit load limits," *IEEE Computer Applications in Power*, vol. 13, issue 1, pp. 38-44, Jan. 2000.

[9] S. D. Foss, S. H. Lin, and R. A. Fernandes, "Dynamic Thermal Line Ratings, Part I, Dynamic Ampacity Rating Algorithm," *IEEE Trans. on Power Apparatus and Systems*, vol. 102, no. 6, pp. 1858-64, June 1983.

[10] S. D. Foss and R. A. Maraio, "Dynamic Line Rating in the Operating Environment," *IEEE Trans. on Power Delivery*, vol. 5, no. 2, pp.1832-1841, April 1990.

[11] P.J. Appelt and J.W. Goodfellow, "Research on How Trees cause Interruptions-Applications to Vegetation Management," in *Proc. 2004 Rural Electric Power Conference*, pp. C6-1-10.

[12] Y. Momomura, H. Marukawa, and T. Ohkuma, "Wind-Induced Vibration of Transmission Line Systems," *Journal of Wind Engineering and Industrial Aerodynamics*, vol. 43, pp. 2035-2046, Oct. 1992.

[13] T. O. Seppa, "Accurate Ampacity Determination: Temperature Sag Model for Operational Real Time Ratings," *IEEE Trans. on Power Delivery*, vol. 10, issue. 3, pp. 1460-1470, July 1995.

[14] L. Li and M.A. Redfem, "A Review of Techniques to Detect Downed Conductors in Overhead Distribution Systems," in *Proc. 2001 Developments in Power System Protection Conference*, no. 479, pp. 169-172.

[15] B. M. Aucoin and B. D. Russel, "Detection of Distribution High Impedance Faults using Burst Noise near 60Hz," *IEEE Trans. on Power Delivery*, vol. 2, no. 2, pp. 342-348, April 1987.

[16] K. L. Butler, B. D. Russell, C. Benner, and K. Andoh, "Characterization of Electrical Incipient Fault Signature resulting from Tree Contact with Electric Distribution Feeders," in *Proc. 1999 Power Engineering Society Summer Meeting*, vol. 1, pp. 408-413.

[17] Y. Yang, D. M. Divan, R. G. Harley, and T. G. Labeler, "Power Line Sensornet – A New Concept for Power Grid Monitoring," in *Proc. 2006 IEEE Power Engineering Society General Meeting*, p.:8.

[18] A. K. Deb, *Powerline ampacity system: theory, modeling, and applications*, CRC Press.

[19] M. W. Davis, "A New Thermal Rating Approach: The Real Time Thermal Rating System for Strategic Overhead Conductor Transmission Lines Part I: General Description and Justification of the Real Time Thermal Rating System," *IEEE Trans. on Power Apparatus and Systems*, vol. PAS-96, no. 3, pp. 803-809, May/June 1977.

[20] M. W. Davis, "A New Thermal Rating Approach: The Real Time Thermal Rating System for Strategic Overhead Conductor Transmission Lines Part II: Steady Sate

Thermal Rating Program," *IEEE Trans. on Power Apparatus and Systems*, vol. PAS-96, no. 3, pp. 810-825, May/June 1977.

[21] D. A. Douglass, "Weather-dependent versus static thermal line rating," *IEEE Trans. on Power Delivery*, vol. 3, no. 2, pp. 742-753, April 1988.

[22] J. F. Hall, "Wind tunnel studies of transmission line conductor temperatures," *IEEE Trans. on Power Systems*, vol. 3, no. 2, pp. 801-812, April 1988.

[23] S. D. Foss and R. A. Maraio, "Dynamic line rating in the operating environment," *IEEE Trans. on Power Delivery*, vol. 5, no. 2, pp. 1095-1105, April 1990.

[24] *IEEE Standard for Calculating the Current-Temperature of Bare Overhead Conductors*, IEEE Standard 738-2006, Jan. 2006.

[25] S. D. Foss, S. H. Lin, R. A. Maraio, and H. Schrayshuen, "Effect of variability in weather conditions on conductor temperature and the dynamic rating of transmission lines," *IEEE Trans. on Power Delivery*, vol. 3, issue 4, pp.1832-1841, Oct. 1988.

[26] J. S. Engelhardt and S. P. Basu, "Design, installation, and field experience with an overhead transmission dynamic line rating system," in *Proc. 1996 Transmission and distribution Conference*, pp. 366-370.

[27] P. M. Callahan and D. A. Douglass, "An experimental evaluation of a thermal line uprating by conductor temperature and weather monitoring," *IEEE Trans. on Power Systems*, vol. 3, issue. 4, pp. 1960-1967, Oct. 1988.

[28] T. O. Seppa, "A practical approach for increasing the thermal capabilities of transmission lines," *IEEE Trans. on Power Delivery*, vol. 8, issue. 3, pp. 1536-1550, July 1993.

[29] T. O. Seppa, "Factors influencing the accuracy of high temperature sag calculations," *IEEE Trans. on Power Delivery*, vol. 9, no. 2, pp. 1079-1089, April 1994.

[30] T. O. Seppa, "Accurate Ampacity determination: temperature-sag model for operational real time ratings," *IEEE Trans. on Power Delivery*, vol. 10, issue. 3, pp. 1460-1470, July 1995.

[31] P. R. N. Childs, *Practical temperature measurement*, Boston: Butterworth-Heinemann, 2001.

[32] G. Stranovsky, J. Koslosky, and B. Clairmont, "Backscatter Technology for Diagnostic Sensing," presented at the EPRI Increased Power Flow Conference, Boston, U.S.A, Step. 2008.

[33] A. Hartog, "Distributed Fiber-Optic Temperature Sensors: Technology and Applications in the Power Industry," *Power Engineering Journal*, vol. 9, no. 3, pp. 114-120, June 1995.

[34] Southwire, [On-line]. Available: www.southwire.com

[35] M. A. Romero, A. Jr. Calligaris, and M. T. C. Silva, "A Fiber-Optic Bragg-Grating Temperature Sensor for High Voltage Transmission Lines," in *Proc. 1997 Microwave and Optoelectronics Conference, 'Linking to the Next Century', (SBMO/IEEE MTT-S International)*, vol. 1, pp. 34-38.

[36] EPRI [On-line]. Available: www.epri.com.

[37] C. Mensah-Bonsu, U. F. Krekeler, G. T. Heydt, Y. Hoverson, J. Schilleci, and B. L. Agrawal, "Application of the Global Positioning System to the Measurement of Overhead Power Transmission Conductor Sag," *IEEE Trans. on Power Delivery*, vol. 17, issue. 1, pp. 273-278, Jan. 2002.

[38] R. M. Hayes, and A. Nourai, "Power Line Sag Monitor," U.S. Patent 6 205 867, March 27, 2001.

[39] R. G. Olsen and K. S. Edwards, "A New Method for Real-Time Monitoring of High Voltage Transmission Line Conductor Sag," *IEEE Trans. on Power Delivery*, vol. 17, issue. 4, pp. 1142-1152, Oct. 2002.

[40] EPRI. Space Potential Probe for Real-time Monitoring of Conductor Sag and Average Core Temperature, Project 1001820, Part 3 [On-line]. Available: www.epriweb.com

[41] California Energy Commission [On-line]. Available: http://www.energy.ca.gov

[42] EDM International, Inc. [On-line]. Available: http://www.edmlink.com

[43] M. Suojanen, J. Vehmaskoski, S. Kuusiluoma, P. Trygg, and L. Korpinen, "Effect of Spruce Forest on Electric Fields caused by 400 kV Transmission Lines," in *Proc. 2000 International Conference on Power System Technology (PowerCon 2000)*, vol. 3, pp. 1401-1405.

[44] K. L. Butler, B. D. Russell, C. Benner, and K. Andoh, "Characterization of Electrical Incipient Fault Signature resulting from Tree Contact with Electric Distribution Feeders," in *Proc. 199 Power Engineering Society Summer Meeting*, vol. 1, pp. 408-413.

[45] G. Diana, M. Bocciolone, F. Cheli, A. Cigada, and A. Manenti, "Large Wind-Induced Vibrations on Conductor Bundles: Laboratory Scale Measurements to Reproduce the Dynamic Behavior of the Spans and the Suspension Sets," *IEEE Trans. on Power Delivery*, vol. 20, issue. 2, part 2, pp. 1617-1624, April 2005.

[46] L. M. Wang, Y. Yin, X. D. Liang, and Z. C. Guan, "Study on Air Insulator Strength under Conductor Galloping Condition by Phase to Phase Spacer," in *Annual Report 2001 Conference on Electrical Insulation and Dielectric Phenomena*, pp. 617-619.

[47] Y. Tian, P. L. Lewin, and A. E. Davies, "Comparison of On-Line Partial Discharge Detection Methods for HV Cable Joints," *IEEE Trans. on Dielectrics and Electrical Insulation*, vol. 9, no. 4, pp. 604-615, Aug. 2002.

[48] H. Ora, and M. Ichihara, "Application of Advanced After-Laying Test to Long-Distance 275 kV XLPE Cable Lines", *IEEE Trans. on Power Delivery*, vol. 10, no. 2, pp. 567-579, April 1995.

[49] C.Y. Lee, S.H. Nam, S.G. Lee, D.W. Kim, and M.K. Choi, "High Frequency Partial Discharge Measurement by Capacitive Sensor for Underground Power Cable Systems," in *Proc. 2000 International Conference on Power System Technology (PowerCon 2000)*, vol. 3, pp. 1517-1520.

[50] C. Henningsen, K. Polster, B.A. Fruth, and D.W. Gross, "Experience with an On-Line Monitoring System for 400 kV XLPE Cables", in *Proc. 1996 Transmission and Distribution Conference*, pp.515-520.

[51] E. Ildstad, H. Faremo, O. Lillevik, and D. Linhjell, "Detection and Location of Partial Discharge Sources in XLPE Cables", in *Proc. 1997 10th ISH*, pp.8.

[52] N. H. Ahmed and N. Srinivas, “On-Line Partial Discharge Detection in Cables”, *IEEE Trans. on DEI*, vol. 5, pp. 181-188, 1998.

[53] A. Heirmann, T. Aschwandcn, H. Hahn, M. Laurent, and L. Ritter, "On-Site Partial Discharge Measurements on Premoulded Cross-Bonding Joints of 170 kV XLPE and EPR Cables", *IEEE Trans. on Power Delivery*, vol. 13, pp. 330-335, April 1998.

[54] N. Ahmed, O. Morel and N. Srinivas, "Partial Discharge Measurement in Transmission-Class Cable Terminations", in *Proc. 1999 IEEE Transmission and Distribution Conf.*, pp. 2-7.

[55] H. Zhang, T.R. Blackburn, B.T. Phung, and Z. Liu, "Application of Signal Processing Techniques to On-Line Partial Discharge Detection in Cables," in *Proc. 2004 International Conference on Power System Technology*, vol. 2, pp. 1780-1785.

[56] D. Zhu, A.J. McGrail, S. Swingler, D.W. Auckland, and B.R. Varlow, "Partial Discharge Detection in Cable Termination using Acoustic Emission Techniques and Adaptive Signal Processing," in *Proc. 1994 IEEE International Symposium on Electrical Insulation*, pp. 74-76.

[57] Y. Tian, P. L. Lewin, A. E. Davies, and G. Hathaway, “Acoustic Emission Techniques for Partial Discharge Detection within Cable Insulation”, in *Proc. 2000 8th DMMA,* pp. 503-508.

[58] E. Gulski, F.J. Wester, W. Boone, N. Schaik,, E.F. van Steennis, E.R.S. Groot, J. Pellis, and B.J. Grotenhuis, "Knowledge Rules Support for CBM of Power Cable Circuits," in *Proc. 2002 CIGRE Session*, pp. 1-12.

[59] F. Cleveland, “Use of Wireless Data Communications in Power System Operations,” in *Proc. 2006 Power System Conf. and Expo.*, pp. 631-640.

[60] IEEE Standard 802.11 Workgroup [Online]. Available: http://grouper.ieee.org/grups/ 802/11/main.html

[61] IEEE Standard 802.15 Workgroup [Online]. Available: http://www.ieee.org/15/ pub/ main.html.

[62] *IEEE 802.15.4: wireless medium access control (MAC) and physical layer (PHY) specifications for low-rate wireless personal area networks (LR-WPANs)*, IEEE Standard 802.15.4-2003.

[63] IEEE Standard 802.16 Workgroup [Online]. Available: http://standards. ieee.org/getie ee802 /802.16.html.

[64] GSM Tutorials. [Online]. Available: http://www.gsmfordummies.com.

[65] E. Callaway, P. Gorday, L. Hester, J.A. Gutierrez, M. Naeve, B. Heile, and V. Bahl, "Home Networking with IEEE 802.15.4: A Developing Standard for Low-Rate Wireless Personal Area Networks," *IEEE Communications Magazine*, vol. 40, issue 8, pp. 70- 77, Aug. 2002.

[66] ZigBee Alliance [Online]. Available: http://www.zigbee.org.

[67] IEEE Standard for Using Wireless Data Communications in Power System Operations, IEEE Standard P1777 (TM) [Online]. Available: http://standards.ieee.org/ announcements/pr_P1777new.html.

[68] H.C. Ferreira, H.M. Grove, O. Hooijen, and AJ. H. Vink, "Power line communications: An overview," in *Proc. 1996 IEEE AFRICON 4th*, vol. 2, pp. 558-563.

[69] O. Bilal, E. Liu, Y.P. Gao, and T.O. Korhonen, "Design of broadband coupling circuits for power line communication," in *Proc.2004 IS PLC*, pp. 8.

[70] R. Hills. (2001, July/Aug.) Sensing for danger. Sci. Technol. Rep. [Online]. Available: http://www.llnl.gov/str/JulAug01/Hills.html.

[71] D. Steere, A. Baptista, D. McNamee, C. Pu, and J. Walpole, "Research challenges in environmental observation and forecasting systems," in *Proc. 2000 6th Int. Conf. Mobile Computing and Networking (MOBICOMM)*, pp. 292–299.

[72] H. Edgar and Jr. Callaway, *Wireless Sensor Network*, CRC Press LLC, 2004.

[73] I.F. Akyidiz, W. Su, Y. Sankarasubramaniam, E. Cayirci, "Wireless Sensor Networks: A survey," *Computer Networks*, vol. 38, 2002, pp. 393-422.

[74] J. M. Kahn, R. H. Katz, and K. S. J. Pister, “Mobile networking for smart dust,” in *Proc. ACM/IEEE Int. Conf. Mobile Computing and Networking (MobiCom)*, 1999, pp. 271-278.

[75] Crossbow [Online]. Available: http://www.xbow.com

[76] Digi International®. [Online]. Available: http://www.digi.com.

[77] Tutorial-Reports [Online]. Available: http://www.tutorial-reports.com.

[78] D. Estrin, R. Govindan, J. Heidemann, and S. Kumar, “Next century challenges: Scalable coordination in sensor networks,” in *Proc. 1999 Int. Conf. Mobile Computing and Networking (MOBICOM)*, pp.263–270.

[79] T. Voigt, H. Ritter and J. Schiller, “Utilizing Solar Power in Wireless Sensor Networks,” in *Proc. 2003 IEEE International Conference on Local Computer Networks*, pp. 416-422.

[80] T.T. Le, H. Jifeng, A. von Jouanne, K. Mayaram, and T.S. Fiez, "Piezoelectric micro-power generation interface circuits", *IEEE Journal of Solid-State Circuits*, vol. 41, issue. 6, pp.1411-1420, June 2006.

[81] S. Roundy, E. Leland, J. Baker, E. Carleton, E. Reilly, E. Lai, B. Otis, J. Rabaey, V. Sundararajan, and P.K Wright. Vibration-Based Energy Scavenging for Pervasive Computing: New Designs and Research that Increase Power Output [Online]. Available: http://vertex.berkeley.edu/our_lab/publications/Pervasive Computing Final.doc.

[82] S. J. Roundy, “Energy Scavenging for Wireless Sensor Nodes with a Focus on Vibration to Electricity Conversion,” Ph.D. dissertation, Dept. Mech. Eng., Univ. California at Berkeley, Berkeley, 2003.

[83] J. Lee, S. Yuen, J. Wen, P. Leong, “Development of an AA Size Energy Transducer with Micro Resonators” in *Proc. 2003 IEEE Int. Sym. On Circuit Systems*, pp. 8.

[84] Sterken T, Fiorini P, Baert K, Puers R, and Borghs G, “An Electro-Based Electrostatic u-Generator,” *Transducers ’03*, June 2003.

[85] Stordeur M, Stark I (1997) Low Power Thermoelectric Generator – self-sufficient energy supply for micro systems. 16th International Conference on Thermoelectrics, 1997, p. 575 – 577.

[86] J.A. Paradiso, T. Starner, "Energy scavenging for mobile and wireless electronics," in *Prof. 2005 IEEE Pervasive Computing*, vol. 4, issue. 1, pp. 18-27.

[87] John G. De Steese, Donald J. Hammerstrom, and Lawrence A. Schienbein. Electric Power From Ambient Energy Sources. [Online]. Available: http://www.osti.gov/bridge/servlets/purl/764590-AeuPTN/webviewable/764590.pdf

[88] G. Zhang, SH.H. Li, ZH.P. Zhang, and W. Cao, "A Novel Electro-Optic Hybrid Current Measurement Instrument for High-Voltage Power Lines," *IEEE Trans. on Instrumentation and Measurement*, vol.50, no.1, pp:59-62, Feb. 2001.

[89] R. Moghe, Y. Yang, F. Lambert, D. Divan, "A scoping study of electric and magnetic field energy harvesting for wireless sensor networks in power system applications ," in *Proc. 2009 Energy Conversion Congress and Exposition (ECCE)*, pp. 3550-3557.

[90] Vanderelli at al., "Method and Apparatus for a Wireless Power Supply," U.S. Patent 7027311, Apr. 11, 2006.

[91] 47 CFR, PART 15 -Radio Frequency Devices, Federal Communications Commission (FCC), August 20, 2002.

[92] S. Nathan, J. Shenck, and A. Paradiso, "Energy Scavenging with Shoe-Mounted Piezoelectric," *IEEE Micro*, vol. 21, no. 3, pp. 30-42, May-June 2001.

[93] O Hunaidi, "Traffic Vibrations in Buildings, Construction Technology," National Research Council of Canada, Update No 39, 2000.

[94] M.Rahimi, H. Shah, G. Sukhatme, J. Heidemann, and D. Estrin, "Studying the Feasibility of Energy Harvesting in a Mobile Sensor Network," in *Proc. 2003 IEEE International Conference on Robotics and Automation*, pp. 19-24.

[95] N.P. Schmidt, "Comparison between IEEE and CIGRE Ampacity Standards," IEEE Trans. on Power Delivery, vol. 14, issue. pp.1555-1559, Oct 1999.

[96] V. T. Morgan, “Rating of Conductors for Short-Duration Currents,” in 1997 *Proc. IEE*, vol. 118, no. 3/4, pp. 555-69.

[97] S. D. Foss, S. H. Lin, and R. A. Fernandes, “Dynamic Thermal Line Ratings, Part I, Dynamic Ampacity Rating Algorithm,” *IEEE Trans. on Power Apparatus and Systems*, vol. 102, no. 6, pp. 1858-64, June 1983.

[98] *Thermal Behavior of Overhead Conductors*, CIGRE Standard ELECTRA No. 144, October 1992.

[99] W. Z. Black and R. L. Rehberg, “Simplified Model for Steady State and Real-time Ampacity of Overhead Conductors,” *IEEE Trans. on Power Apparatus and Systems,* vol. pas-104, no. 10, pp: 2942-2953, Oct. 1985.

[100] *Aluminum electrical conductor handbook*, 2nd ed. Washington, DC: The Aluminum Association, 1982.

[101] S. Haykin, *Neural Networks a Comprehensive Foundation*, Prentice-Hall, Inc. 1994.

[102] K. S. Narendra and K. Parthasarathy, "Gradient-methods for the optimization of dynamical systems containing neural networks," *IEEE Trans .on Neural Networks,* vol. 2, March 1991, pp. 252-262.

[103] H. Jaeger (2002). “Tutorial on training recurrent neural networks, covering BPPT, RTRL, EKF and the echo state network approach,” *GMD Report 159, Fraunhofer Institute AIS* [Online]. Available: http://www.faculty.iubremen.de/hjaeger/pubs /ESNTutorial.pdf.

[104] J. Mazumdar, R. G. Harley, T. G. Habetler, and F. Lambert, “Using a neural network to discriminate between the contributions of the power electronic load and the power system to harmonic pollution,” in *Proc. of the 5th International Power Electronics Conference (IPEC)*, April 2005, Niigata, Japan.

[105] H. Jaeger, “Adaptive nonlinear system identification with echo state networks,” in S. T. S. Becker & K. Obermayer, eds, ‘Advances in Neural Information Processing Systems 15’, MIT Press, Cambridge, MA, pp. 593-600, Oct. 2003.

[106] Y. Yang, D. M. Divan, R. G. Harley, and T. G. Habetler, "Design and Implementation of Power Line Sensornet for Overhead Transmission Lines," accepted for presentation at the *IEEE Power Engineering Society General Meeting* 2009, Alberta, July 2009.

[107] Lukosevicius M. and Jaeger H. (2009) Reservoir Computing Approaches to Recurrent Neural Network Training (draft version). *Computer Science Review*, to appear.

[108] R. J. Williams, "Backpropagation through time learning algorithm for continually running fully recurrent neural networks," *Neural Computation*, vol. 1, no. 2, pp. 270-80, June 1989.

[109] P. J. Werbos, "Backpropagation through time: what it does and how to do it," in *Proc. of IEEE*, Oct. 1990, vol. 78, issue 10, pp. 1550-1560.

[110] B. Farhang-Boroujeny. *Adaptive Filters: Theory and Applications*. Wiley, 1998.

[111] Ali U. Küçükemre, "Echo state networks for adaptive filtering." Master's thesis, University of Applied Sciences Bohn-Rhein-Sieg, Germany, 2006 [Online]. Available: http://www.faculty.jacobs-university.de/hjaeger/pubs/Kucukemre.pdf.

[112] J. Dai, G.K.Venayagamoorthy and R.G. Harley, "Harmonic identification using an Echo State Network for adaptive control of an active filter in an electric ship," in *Proc. 2009 International Joint Conference (IJCNN 2009)*, pp:634-640.

[113] A. Tarantola, *Inverse Problem Theory and Methods for Model Parameter Estimation*, 1st ed., SIAM, 2004.

[114] C.A. Gerrard and J.R. Gibson, "Remote Monitoring of Conditions on High Voltage Power Systems," *IEE Colloquium on Field Modeling: Applications to High Voltage Power Apparatus*, pp. 9/1-9/3, Jan 1996.

[115] W. H. Hayt and J. A. Buck, *Engineering Electromagnetics*, 6th ed., McGraw-Hill, 2001.

[116] W. R. Smith-Vaniz and R. L. Sieron, "Apparatus for measuring the potential of a transmission line conductor," U.S. Patent 4 714 893, Dec 22, 1987.

[117] D.W. Novotny and T.A. Lipo, *Vector control and dynamics of AC drives*, New York: Oxford University Press, 1996.

[118] By Roger F. Harrington, *Introduction to Electromagnetic Engineering*, Dover Publications, 2003.

[119] Kelvin, Lord F. "Contact Electricity of Metals," *Philosophical Magazine and Journal of Science*, S 5, v 46, n 278, July 1898, p 82-120.

[120] "LMP7721 3 Femtoampere Input Bias Current Precision Amplifier." National Semiconductor, Data sheet, 2008, [Online]. Available: http://www.national.com/ds/LM/LMP7721.pdf.

[121] Hegg, M.C. and Mamishev, A.V., "Influence of Variable Plate Separation on Fringing Electric Fields in Parallel-Plate Capacitors", in *Proc. 2004 International Symposium on Electrical Insulation*, Indianopolis, USA, September, 2004.

[122] C. R. Paul, *Analysis of Multiconductor Transmission Lines*, John Wiley & Sons, 1994.

[123] J. R. Carson, "Wave Propagation in Overhead Wires with Ground Return," *Bell System Technical Journal*, vol. 5, pp. 539-554, 1926.

[124] E. Pettinelli, A. Cereti, A. Galli, and F. Bella, "Time Domain Reflectometry: Calibration Techniques for Accurate Measurement of the Dielectric Properties of Various Materials," *Review of Scientific Instruments* 73, pp. 3553–3562.

[125] Ruel Vance Churchill , *Operational Mathematics*, 3d ed., New York: McGraw-Hill, 1971.

[126] H. Johal, D. Divan, "Design Considerations for Seriers-Connected Distributed FACTS Converters," *IEEE Trans. on Industry Applications*, vol. 43, no. 6, November/December 2007, pp: 1609-1618.

[127] Texas Instrument. [Online]. Available: http://www.ti.com.

[128] Hernandez Mejia, Jean Carlos, "Characterization of real power cable defects by diagnostic measurements." Ph.D. Dissertation, Georgia Institute of Technology,

USA, 2009 [Online]. Available: http://smartech.gatech.edu/bitstream/1853/31841/1/hernandezmejia_jean_c_200812_phd.pdf.

[129] J. R. Carson, "Wave Propagation in Overhead Wires with Ground Return." *Bell System Technical Journal*, vol. 5, pp. 539-554, 1926.

[130] T. Mine, "Attenuation and distortion of travelling waves on transmission lines due to skin effect," *Himeji Tech. Univ.*, Japan, 1952, Res. Rep. 2.

[131] K.R. Shah, "Analysis and detection of fault transients in power systems," *Ph.D. dissertation, Univ. of Michigan*, Ann Arbor, 1969 (microfilm).

[132] D. E. Hedman, "Propagation on Overhead Transmission Lines I – Theory of Modal Analysis," *Proc. of IEEE Winter Power Meeting*, New York, Jan. 31-Feb.5, 1965, pp: 200-205.

[133] D. E. Hedman, "Propagation on Overhead Transmission Lines II – Earth-Conduction Effects and Practical Results," *Proc. of IEEE Winter Power Meeting*, New York, Jan. 31-Feb.5, 1965, pp: 205-211.

[134] Y. Yang, R. G. Harley, D. M. Divan, and T. G. Habeler, "MLPN based Parameter Estimation to Evaluate Overhead Power Line Dynamic Thermal Rating," in *Proc. of the 15th International Conference on Intelligent System Applications to Power Systems (ISAP)*, Curitiba, Brazil, Nov. 2009.

[135] Y. Yang, R. G. Harley, D. M. Divan, and T. G. Habetler, "Adaptive Echo State Network to Maximize Overhead Power Line Dynamic Thermal Rating," in *Proc. IEEE Energy Conversion Congress and Exposition (ECCE'09)*, San Jose, CA, USA, Sept. 2009.

[136] Y. Yang, R. G. Harley, D. M. Divan, and T. G. Habetler, " Thermal Modeling and Real Time Overload Capacity Prediction of Overhead Power Lines," in *Proc. IEEE Symposium for Electrical Machines, Power Electronics & Drives 2009 (SDEMPED'2009)*, Cargese, France, Aug. 2009.

[137] Y. Yang, D. R. G. Harley, M. Divan, and T. G. Habetler, "Overhead Conductor Thermal Dynamics Identification by using Echo State Networks," in *Proc. 2009 International Joint Conference on Neural Networks (IJCNN'09)*, Atlanta, USA, June 2009.

[138] Y. Yang, D. M. Divan, and R. G. Harley, "Power Line Vicinity Monitoring via Multiple Displacement Current Measurement," *Proc. IEEE Power Energy Society Genertal Meeting (PESGM'2010)*, Minneapolis, USA, July 2010.

[139] Y. Yang, R. G. Harley, D. M. Divan, and T. G. Habetler, "Adaptive Echo State Network to Maximize Overhead Power Line Dynamic Thermal Rating," submitted to *IEEE Trans. on Industry Electronics*, Dec. 2009.